

Development of micron and submicron scale carriers for drugs and nutrients delivery



Cholpon Rustem kyzy

B.Sc. and M.Sc. Chemical Technology and Biotechnology

Thesis submitted for the degree of Doctor of Philosophy

University of East Anglia

School of Pharmacy

September 2018

© This copy of the thesis has been supplied on condition that anyone who consults it is understood to recognize that its copyright rests with the author and that no quotation from the thesis, nor any information derived therefrom, may be published without the author's prior, written consent.

Abstract

Formulating multiple nutrient supplements and better dosage forms for paediatric patients are still current needs and challenges. This study aims to develop a cost-effective novel delivery system capable of delivering water-soluble and oil-soluble nutrients or drugs to address paediatric compliance. Two ranges of micron and submicron scale carriers for nutrients and drugs were developed and characterized thoroughly. First, fast-dissolving orodispersible film was produced using an emerging electrospinning technique to deliver iodine, an essential micronutrient. PEO and KIO_3 were used in a formulation that ensures the safety and cost-effectiveness of the final product. Second, a novel structured oil system (SOS), capable of holding a large amount of oil, was designed as a carrier for fat-soluble vitamins and drugs. This SOS was produced using a freeze dryer that is suitable for heat sensitive vitamins and drugs. Gelatine/Xanthangum were used as emulsifiers due to the affinity of protein-polysaccharide complexes to form emulsions stable to environmental stresses such as freezing. In addition, a range of SOSs were formulated using Hypromellose/Xanthangum, Methylcellulose/Xanthangum, Tween 20/Xanthangum, and Gelatine/Carboxymethylcellulose in order to understand the formation of SOS, to prove the concept that any surface active and non-surface active polymers that can form electrostatic complexes can form SOS, and to find an alternative to Gelatine/Xanthangum emulsifiers. A thorough physicochemical characterisation of both the fast-dissolving orodispersible film and structured oil systems was conducted using a range of analytical techniques including imaging techniques (various optical and electron microscopes, and $X\mu\text{CT}$), ATR-FTIR, PXRD, DSC, TGA, a texture analyser, LD, and *in vitro* dissolution testing.

This study demonstrated that electrospinning technology has great potential to be used in formulating a dosage form for children, that liquid vegetable oil and fish oil can be encapsulated within fibres using emulsion electrospinning and introduced a novel solid structured oil system capable of holding large amounts of oil.

Acknowledgements

I would like to take the opportunity to express my sincere gratitude to those whose continuous support and guidance helped me to complete this research work.

First of all, I would like to thank my supervisors Dr. Sheng Qi and Prof. Peter Belton for giving me the opportunity to discover a world of pharmacy. Specifically, I am grateful to Prof. Peter Belton for his belief in me and for his offer to do my PhD in the school of PHA with Dr. Sheng Qi, and of course I am thankful to Dr. Sheng Qi who agreed to work with me.

I would never have had a chance to do a PhD in the UK without the financial support of the Islamic Development Bank Merit Scholarship Programme. I am endlessly grateful to the members of this programme for granting me a full scholarship and for their continuous support throughout my study. Particularly, I would like to thank Mr. A. M. Shaharuqul Huq, Dr. M. S. bin Mohd. Yusoff, Mr. L. M. Kadcadi, and Mr. H. M. Alsalahi. You are doing a great job to make the world a better place. Thanks to the IDB Merit Scholarship Programme, I met many interesting people from all over the world and found new friends. Dr. D. Dauletbekov, Dr. A. Seitkan, Dr. M. Normatova, Mr. A. Tolipov, Ms. G. Mamadjanova and Dr. R. Khalife: thank you for your inspiration and for offering so much valuable advice.

My research moved forward thanks to Dr. Inese Sarcevic (Eurofins Lancaster Laboratories Professional Scientific Services, LLC) who helped me to analyse PXRD data; Prof. Peter J. Wilde, Dr. Nikolaus Wellner, Mr. Mike Ridout and Ms. Kathryn Cross from the Institute of Food Research, Norwich, who gave their time for discussion about my project and helped me to conduct rheology and TEM analysis for SOS; the Bruker Corporation in Coventry that helped me to conduct X μ CT analysis and Dr. Mark Eddleston, University of Cambridge, who carried out some of the TEM experiments on the nanofibres.

Huge thanks to all of the staff members of the Drug Discovery and Drug Delivery Suite of the PHA and CHE schools and to all my friends and colleagues I met at UEA. Special thanks to Prof. Yaroslav Khimyak and his student Dr. Susana Ramalhete for helping me to explore the NMR instrument and for their strong support from the beginning of my study; to Dr. Andrew Mayes and his student Dr. Abdulrahman Saeed for kindly providing me with the DLS and conductivity

meter; to Dr. Pratchaya Tipduangta who first showed me how to work with the electrospinning technique, and to Prof. Arasu Ganesan, Prof. Mark Searcey and Prof. Maria O'Connell for support. Many thanks go to Dr. Colin Macdonald from PHA school, and Mr. Bertrand Leze and Dr. Paul Thomas from ENV school, who were always there ready to help me and instruct me on how to get better images on optical and electron microscopes.

My journey started in my home country, Kyrgyzstan, where I have people who were always with me with their hearts and thoughts. My special appreciation and thanks are given to Prof. T. Djunushalieva and Prof. T. Duishenaliev, from Kyrgyz Technical University named after I. Razzakov, who encouraged me to apply for a scholarship and supported throughout the application; to my friend Mr. M. Totobaev who supported and guided me when processing the scholarship application, and to Sharsheke uulu Zamirbek, Jamalbek baike and Dr. B. Akmatov (Bishkek Humanities University named after K. Karasaev) for inner and health support.

And finally, I wish to acknowledge my deepest gratitude to my beloved parents, Rustem Ryskulov and Zhibek Torobekova, to my elder brother Sultan and my elder sisters Jamilya and Rosa. I could not have completed everything I have achieved in my life without your powerful support, guidance and positivity. Last but not least, my very special warm thanks to my little prince and princesses, my nephew, Chingiz, and my nieces, Aiperi, Akylay, Ainazik, Ainur and Adilya. You are the rainbow in my life! I love you so much!

Table of Contents

TABLE OF CONTENTS	I
LIST OF ABBREVIATIONS	VI
1 CHAPTER 1. INTRODUCTION	1
1.1 Introduction	1
1.2 Nutritional Supplements	2
1.2.1 Iodine.....	4
1.2.2 Vitamin E	10
1.2.3 Polyunsaturated fatty acid	14
1.3 Active pharmaceutical ingredients (APIs).....	18
1.4 Main considerations when selecting the delivery systems for drugs or nutrients... 22	
1.4.1 Intrinsic physicochemical properties	22
1.4.2 Paediatric targeted group	23
1.4.3 Oral route of administration	24
1.5 Solid dispersion.....	26
1.6 Electrospinning	28
1.6.1 Emulsion and coaxial electrospinning.....	40
1.7 Structured oil systems	42
1.8 Motivations and aims of the study	45
2 CHAPTER 2. MATERIALS AND EXPERIMENTAL METHODS.....	48
2.1 Introduction.....	48
2.2 Materials	48
2.2.1 Nutritional supplements (KI and KIO ₃).....	49
2.2.2 Oils.....	51
2.2.3 Model drugs	54
2.2.4 Excipients.....	56
2.3 General introduction to preparation techniques	68
2.3.1 Electrospinning general set up.....	68
2.3.2 Homogenizing instruments	69

2.3.2.1	High-performance dispersing instrument (HPDI)	69
2.3.2.2	High pressure homogenizer (HPH)	70
2.3.3	Freeze drying	71
2.4	General introduction to characterization techniques	71
2.4.1	Imaging techniques	71
2.4.1.1	Optical microscopes	72
2.4.1.1.1	Upright microscope	73
2.4.1.1.2	Stereomicroscope	74
2.4.1.1.3	Confocal laser scanning microscope (CLSM)	74
2.4.1.2	Electron microscopes	75
2.4.1.2.1	Scanning electron microscope (SEM)	76
2.4.1.2.2	Cryo-scanning electron microscope (Cryo-SEM)	77
2.4.1.2.3	Transmission electron microscope (TEM)	78
2.4.1.3	X-ray micro computed tomography (X μ CT)	79
2.4.2	Energy-dispersive x-ray spectroscopy (EDS)	80
2.4.3	Powder x-ray diffraction (PXRD)	81
2.4.4	Attenuated total reflectance Fourier transform infrared spectroscopy (ATR-FT IR)	83
2.4.5	Differential scanning calorimetry (DCS)	84
2.4.6	Thermal gravimetric analysis (TGA)	85
2.4.7	Texture analyser	86
2.4.8	Particle size analysis	87
2.4.8.1	Dynamic light scattering (DLS)	87
2.4.8.2	Laser diffraction (LD)	88
2.4.9	In vitro dissolution testing	89
3	CHAPTER 3. DEVELOPMENT OF AN ORODISPERSIBLE FILM FOR DELIVERING HYDROPHILIC NUTRITIONAL SUPPLEMENTS	92
3.1	Introduction	92
3.2	Materials and methods	94
3.2.1	Materials	94
3.2.2	Methodology	94
3.2.2.1	Electrospinning	94
3.2.2.2	Wetting and dissolution testing	96
3.2.3	Characterization techniques	97
3.3	Results and discussions	98
3.3.1	Impact of KI and KIO ₃ incorporation on fibre formation	98
3.3.1.1	PEO loaded with KI	98
3.3.1.1.1	Effect of the solvent	99
3.3.1.2	PEO loaded with KIO ₃	101
3.3.1.2.1	Effect of the solvent	101
3.3.2	Formulation optimization	102

3.3.2.1	Effect of polymer concentration.....	102
3.3.2.2	Probing maximum loading of KIO_3	103
3.3.3	PVP and PVP/PEO polymer blend loaded with KIO_3	106
3.3.4	Processing parameters optimization	108
3.3.4.1	Distance between the needle and collector	108
3.3.4.2	Diameter of the needle.....	109
3.3.4.3	Applied DC voltage.....	110
3.3.4.4	Feeding rate	111
3.3.4.5	Type of collector	112
3.3.5	Characterization of PEO nanofibres loaded with KIO_3	115
3.3.5.1	Validation of the distribution of KIO_3 in the PEO fibres	115
3.3.5.2	Formation of KIO_3 nanocrystals in PEO nanofibres	117
3.3.5.3	Effect of processing and KIO_3 loading on the crystallization behaviour of PEO 122	
3.3.5.4	Ultra-rapid wetting and dissolution of PEO nanofibres loaded with KIO_3	124
3.4	Conclusion	126
4	CHAPTER 4. FEASIBILITY STUDY OF USING EMULSION ELECTROSPINNING FOR THE CO- DELIVERY OF MULTI-NUTRIENTS	128
4.1	Introduction	128
4.2	Materials and methods	129
4.2.1	Materials	129
4.2.2	Methodology	130
4.2.2.1	Emulsion preparation technique	130
4.2.2.2	Conventional emulsion electrospinning	130
4.2.2.2.1	Emulsions prepared using Tween 20 and TPGS	130
4.2.2.2.2	Emulsions prepared using Span 80 and TPGS	131
4.2.2.3	Coaxial emulsion electrospinning	132
4.2.2.3.1	Emulsions prepared using Tween 20/TPGS emulsifiers and PEO/ KIO_3 polymer solution	132
4.2.3	Characterization techniques	132
4.3	Results and discussion	132
4.3.1	Feasibility study of emulsion electrospinning.....	132
4.3.1.1	The effect of PEO and PEO/PVP continuous phase composition on fibre formation.....	134
4.3.1.2	The effect of emulsifier type on fibre formation: Tween 20 and TPGS.....	135
4.3.1.3	The effect of conventional and coaxial emulsion electrospinning on fibre formation.....	135
4.3.1.4	The effect of the type of collectors: stationary and rotating drum.....	135
4.3.2	Emulsion electrospinning using emulsions prepared using Span 80 and TPGS.....	136
4.3.2.1	Stability test of emulsions analysed by photographic study	136

4.3.2.1.1 The impact of oil type.....	139
4.3.2.1.2 The impact of emulsifier type	140
4.3.2.1.3 The impact of the HLB value of emulsifiers in the formulation	141
4.3.2.1.4 The impact of storage conditions.....	142
4.3.2.2 Particle size analysis.....	142
4.3.2.2.1 Particle size analysis of emulsions using DLS	142
4.3.2.2.2 Particle size analysis of emulsions prepared using sunflower oil by LD	146
4.3.2.3 Morphology of the emulsion electrospun films	147
4.4 Conclusion	150
5 CHAPTER 5. STRUCTURED OIL AS A PLATFORM FOR THE DELIVERY OF WATER-SOLUBLE AND OIL-SOLUBLE DRUGS	151
5.1 Introduction.....	151
5.2 Materials and methods	152
5.2.1 Materials	152
5.2.2 Methodology.....	152
5.2.2.1 Emulsions prepared using HPDI.....	152
5.2.2.2 Emulsions prepared using HPH.....	153
5.2.2.3 Producing structured oil systems	154
5.2.2.3.1 Freeze drying	154
5.2.2.3.2 Oven drying	154
5.2.2.4 Oil holding capacity under compression	154
5.2.3 Characterization techniques	155
5.3 Results and discussion.....	155
5.3.1 Emulsion formation development	155
5.3.1.1 The effect of processing parameters: HPDI and HPH	156
5.3.1.1.1 Stability of emulsions prepared using HPH	160
5.3.1.2 The effect of oil volume fraction	161
5.3.1.3 The effect of API: metoprolol succinate and ketoconazole.....	163
5.3.1.4 The effect of emulsifiers type: G/X, HPMC/X, MC/X, Tween 20/X, G/CMC	167
5.3.2 Producing structured oil systems.....	170
5.3.2.1 Impact of protein and polysaccharide ratio	170
5.3.2.2 Impact of dehydration method.....	171
5.3.2.3 Impact of oil volume fraction.....	172
5.3.2.4 Impact of processing parameters: HPDI and HPH	172
5.3.2.5 Impact of protein and polysaccharide: G and X.....	173
5.3.2.6 Impact of emulsifiers	173
5.3.3 Characterization of structured oil systems	175
5.3.3.1 Structured oil system under a fluorescence stereomicroscope	175
5.3.3.2 X-ray micro computed tomography (X μ CT).....	176
5.3.3.3 Cryo-SEM.....	178

5.3.3.4	TEM	180
5.3.3.5	ATR-FT IR.....	182
5.3.3.6	DSC.....	186
5.3.3.7	TGA.....	188
5.3.3.8	Mechanical properties and oil holding capacity under compression.....	189
5.3.3.9	Water uptake ability	190
5.3.3.10	Dissolution testing	192
5.4	Conclusion	194
6	CHAPTER 6. CONCLUDING REMARKS AND FUTURE PROSPECTS	195
6.1	Reflection on the key findings	195
6.2	Future outlook	197
7	APPENDICES	202
7.1	Appendix 1. The effect of Tween 20 surfactant on fibre morphology.....	202
7.2	Appendix 2. ATR-FT IR analysis of G/X SOS	202
7.3	Appendix 3. PXRD analysis of xanthan gum	208
7.4	Appendix 4. The new crystal modification of electrospun poly (ethylene oxide) under stretching.....	209
8	PUBLICATION.....	222
9	REFERENCES	223

List of Abbreviations

ADME Absorption, distribution, metabolism and excretion

ALA α -linolenic acid

API Active pharmaceutical ingredient

ARA Arachidonic acid

ATC Anatomical Therapeutic Chemical Classification system

ATR-FT IR Attenuated total reflectance Fourier transform infrared spectroscopy

BCS Biopharmaceutical Classification System

BP British Pharmacopoeia

CA Cellulose acetate

CCD Charge-coupled device

CLSM Confocal laser scanning microscope

Cryo-SEM Cryo-scanning electron microscope

DC Direct current

DDS Drug delivery system

DHA Docosahexaenoic acid

DLS Dynamic light scattering

DMA Dimethylacetamide

DSC Differential scanning calorimeter

EC/SCF European Commission/Scientific Committee on Food

EDS Energy-dispersive x-ray spectroscopy

EE Emulsion electrospinning

EFA Essential fatty acid

EM Electron microscope

EPA Eicosapentaenoic acid

EPP Electrospinning processing parameter

ER Extended-release

FDA Food Drug Administration

G Gauge

G Gelatine

G/CMC Gelatine and carboxymethyl cellulose

G/X Gelatine and xanthan gum

GI Gastrointestinal

GRAS Generally Regarded as Safe

GSH Glutathione

HLB Hydrophile-lipophile balance

HPDI High-performance dispersing instrument

HPH High pressure homogenizer

HPMC/X Hydroxypropyl methylcellulose and xanthan gum

IOM Institute of Medicine

IVIVC *in vitro-in vivo* correlation

LA linoleic acid

LD Laser diffraction

LM Light microscope

log P Partitioning coefficient

MC/X Methylcellulose and xanthan gum

o/w Oil-in-water

PEO Poly (ethylene oxide)

pKa Dissociation constant

PUFA Polyunsaturated fatty acid

PVA Polyvinyl alcohol

PVDF Poly (vinylidene fluoride)

PVP Polyvinylpyrrolidone

PXRD Powder X-ray diffraction

RDA Recommended Dietary Allowance

RH Relative humidity

SEM Scanning electron microscope

SOS Structured oil system

TEM Transmission electron microscope

Tg Glass transition

Tm Melting temperature

UNICEF United Nations Children's Fund

USP United States Pharmacopeia

UV-Vis Ultraviolet–visible

WHO World Health Organization

WHOCC World Health Organization Collaborating Centre for Drug Statistics Methodology

X Xanthan gum

X μ CT X-ray micro computed tomography

ω -3 or n-3 Omega-3 fatty acid

ω -6 or n-6 Omega-6 fatty acid

1 Chapter 1. Introduction

1.1 Introduction

In the human body, multiple micronutrient deficiency is more common than single nutrient deficiency because nutrients act synergistically or antagonistically relative to each other, with the lack or excess of one micronutrient affecting the absorption and metabolism of another. In infants and children, nutrition is one of the most important environmental factors influencing individual brain development. In addition, it is known that the brain grows rapidly within the first two years of a baby's life during which time it reaches 80 % of its adult weight [1]. It is therefore very important that in their early life children have sufficient nutritional intake. Prenatal, pregnant and lactating women are also susceptible to multiple micronutrient deficiency due to the extensive loss of vital vitamins and minerals during pregnancy. Multiple strategies for micronutrient supplementation and fortification of foods have been implemented by international organizations in partnership with government and public health officials, and the food and pharmaceutical industries, in order to prevent nutrient deficiency. Such examples include salt iodization and supplementation with iodized oil capsules, triple salt fortification, flour fortification with iron, iron-folic acid supplementation, periodic vitamin A supplementation and micronutrient powders to sprinkle on the foods being prepared at home. The United Nations Children's Fund (UNICEF) has been working with partners to develop and test a multiple micronutrient formulation to reduce anaemia, and is now working with partners to develop global guidance on intervention for the delivery of multiple micronutrient supplements [1-3]. In addition to salt, UNICEF supports national governments to develop food fortification programmes for vitamin A, iron and folic acid and they are advocating for legislation to make food fortification mandatory. Despite all these efforts, according to UNICEF and the World Health Organization (WHO) estimations, millions of children still suffer from stunted growth, cognitive delays, weakened immunity, and disease and even lose their life as a result of micronutrient deficiency. Often micronutrient deficiencies are also referred to as "hidden hunger", because they progress gradually over time without any evident symptoms until irreversible harm to health has been done. A child may go to sleep each night with a full belly; however, an imbalanced diet could mean that his

or her body is suffering from micronutrient deficiency. WHO prioritise four forms of hidden malnutrition and these are vitamin A, iodine, iron and zinc deficiencies [4]. Every year between 250,000 to 500,000 children become blind just because of vitamin A deficiency. In 2011, it was estimated that about 800 million children and women worldwide were affected with anaemia [5]. Over 740 million people have iodine deficiency disorders and 50 million people have some degree of mental retardation due to iodine deficiency disorders [6]. About 17.3% of the world's population is at risk of inadequate zinc intake [7].

1.2 Nutritional Supplements

Nutritional supplementation was first implemented as a main strategy to correct or prevent nutritional deficiencies in populations between the First and Second World Wars (1924–1945). During that period, salt iodization, margarine and milk fortification with vitamins A and D, and flours and bread fortification with vitamins B1, B2, niacin, and iron were introduced [8]. These micronutrients play a key role in the mental and physical development of the human body. For example, vitamin A is vital for the visual system, for growth and development [9]. Iodine is responsible for normal formation and function of the brain and thyroid gland, and for normal pregnancy and birth [10]. Zinc is a builder of the immune system, while iron deficiency causes anaemia [11].

The definition for dietary supplements slightly differs in different countries. In the UK it is defined as *“foods in unit dosage form, e.g. tablets, capsules and elixirs, taken to supplement the diet. Most are products containing nutrients normally present in foods which are used by the body to develop cells, bone, muscle, etc., to replace co-enzymes depleted by infection and illness, and generally to maintain good health”* [12].

In Europe, the definition is that *“food supplements are preparations including tablets, capsules, powders and liquids which are composed of, or contain, nutrients, micronutrients and/or other eligible substances consumed in unit quantities in addition to the normal food intake. Food supplements can be composed of vitamins, minerals and trace elements; peptides, amino acids and similar nitrogen-containing compounds; oils and fatty acids and*

their esters; fibres and other materials of plant or animal microbial origin as well as fermentation products, including those in dehydrated, concentrated or extracted form” [12].

In the United States, the Food and Drug Administration (FDA) includes herbs and other botanicals together with the items defined above.

The majority of dietary supplements existing in the UK are classified as foods and are not controlled as strictly as medicines. They are regulated by the Food Labelling Regulations (1996). Only the Medical and Healthcare Regulatory Agency, which includes the former Medicine Control Agency can determine whether a product is a medicine or not [12]. The majority of nutritional supplements are sold without prescription. Nevertheless, some nutritional products prescribed for specific conditions will be classified as medicines rather than food. Those prescriptions are offered to patients who have a chronic disease and may need special nutrients over a long period [13].

Vitamins and minerals. Vitamins and minerals play an essential role in the body's metabolic processes. They perform a function in enzymatic reactions and structure tissues such as bone and blood. Although the amount needed by the human body is very small, ranging from micrograms to milligrams, the effect of these nutrients is great. Most vitamins and minerals cannot be synthesized by the body, and therefore must be acquired from the outside, e.g. from the diet or from dietary supplements [14].

Vitamins are organic compounds, categorised as water or oil (fat) soluble. The fat-soluble vitamins are vitamins A, D, E and K. They are stored in the fatty tissue and sometimes can be secreted through bile. The water-soluble vitamins are thiamine (B₁), riboflavin (B₂), niacin (B₃), vitamin B₆, vitamin B₁₂, folate, vitamin C, pantothenic acid, biotin, and choline. The water-soluble characteristic limits their storage in the body for a long time [15].

Minerals are inorganic elements and fall into two categories: macrominerals and trace minerals. The macrominerals (calcium, phosphorus, magnesium, sodium, chloride, potassium and sulphur) exist in the body in larger amounts. The Dietary Reference Intake level for an adult is more than 100 milligrams per day. The Dietary Reference Intake level of trace minerals (iron, copper, iodine, manganese, fluoride, chromium, molybdenum, selenium, zinc and cobalt) is mostly less than 100 milligrams per day [16].

Essential fatty acids (EFAs) are unsaturated fatty acids that are essential to human health but are not metabolized by the body and must be acquired through the diet [17].

The doses for nutritional supplements depend on the individual needs and territory. For minerals and vitamins there is a recommended guideline developed by WHO that can be found on their official websites [18]. Some nutritional supplements may have some side effects, depending on personal hypersensitivity or intolerance to certain substances, or health conditions and dietary patterns. They may cause allergic reaction, nausea, headaches, sweating, or stomach upset [19].

1.2.1 Iodine

Iodine status in the world

Iodine deficiency is one of the key factors responsible for mental impairment worldwide and is easily preventable by supplementing the population using iodized salt [20-22]. Unfortunately, complete elimination of iodine deficiency in the world has not been achieved [23, 24]. It is still a major health problem in many developing countries, and it can easily re-emerge anywhere because of the socioeconomic situation and/or the circulation of iodine in nature. Iodine deficiency has occurred in some iodine-sufficient countries, including the UK (**Figure 1.1**) [25-31]. In an attempt to address this, the WHO and UNICEF urged all countries to control and monitor their iodine status every 3 years [32] and recommended oral iodine medicaments/supplements for the most vulnerable groups in the population, such as children, pregnant, and lactating women, in order to ensure they meet their required daily dose [9].

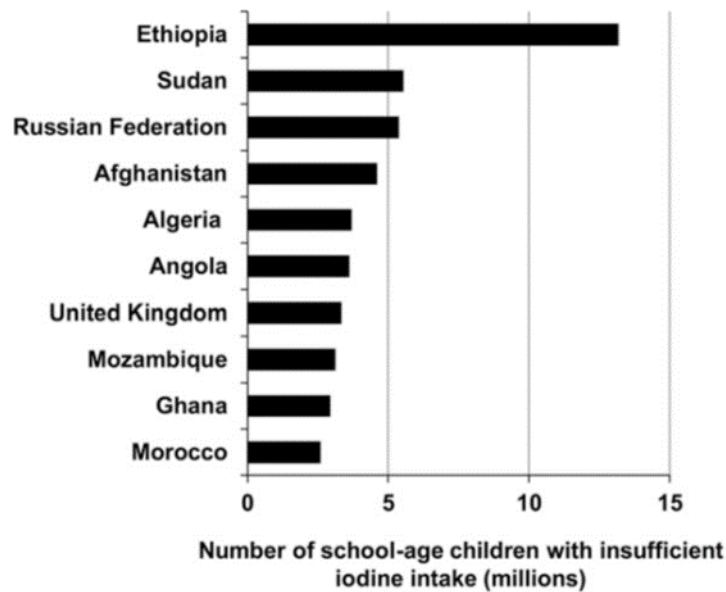


Figure 1.1. The top 10 iodine-deficient countries with the greatest numbers of school-age children with insufficient iodine intake in 2011. Adapted from [33].

Iodine prevention and control

Universal salt iodization (USI) is the main strategy to regulate and prevent iodine deficiency [33]. It was adopted in 1922 by the World Health Assembly as a highly effective and cheap method. However, a conflict between the two main goals of the health community, to reduce the average salt intake among the population due to the increase in hypertension and cardiovascular diseases and preventing iodine deficiency through salt iodization, suggests other means need to be developed to increase iodine intake. Thus, many other methods have been advanced and one of them is iodized oil. WHO recommends supplementation with iodized oil for women of reproductive age, children less than 2 years, pregnant women and people living in the areas with inadequate access to iodized salt [26]. The iodized oil can be prepared by esterification of the unsaturated fatty acids and adding iodine to the double bond [10]. The most popular iodized oils are Lipiodol® and poppy seed oil (where iodine content is 40 % per weight) or vegetable oils [26]. However, problems arising from the need for a distribution programme to deliver the supplement direct to the target population, and the potential for an unstable level of iodine in the body, makes iodized oil less attractive [34]. Other existing iodine medicaments and supplements are mostly in tablet form, which often cause serious difficulties in swallowing for paediatric and elderly patients. Although liquid iodine supplement formulations are available, such as Lugol's iodine (iodine and potassium

iodide dissolved in water, where the ratio of iodine to potassium iodide is 1:2) [19], there have been a number of drawbacks related with their reduced physical storage stability, increased manufacturing cost, and increased contamination risk for multiple dose formulations [26].

Bread fortification with iodine was successfully implemented in Australia, the Russian Federation and in some European countries. However, iodine intake remained insufficient; therefore, iodized salt has been introduced in bread making. Iodized water has been implemented in Thailand and Mali but it is costly. Iodized tea has been utilized in China. Indirect iodization methods in preventing iodine deficiency have also been developed. In Xinjiang, China, potassium iodate was successfully added into irrigation water; it has been reported that the infant mortality rate has fallen by 50 %. Finland, as a consequence of using iodized table salt to fortify animal fodder, is increasing the iodine intake through animal sources [26].

Functions of iodine in our body

Although iodine is accumulated in the ovary and other tissues [35], at present, the only physiological role known for iodine in the human body is in the synthesis of thyroid hormones by the thyroid gland [9]. The function of iodine is in the formation of the thyroid hormones thyroxine (T4) and triiodothyronine (T3), which are the main drivers for normal growth and development of brain tissues, the central nervous system, the body, as well as for energy production and oxygen consumption in cells [35]. **Figure 1.2** provides an illustration summarising the thyroid hormone production and regulation in the body. **Figure 1.3** provides an illustration of synthesis thyroid hormone.

When thyroid hormone secretion is insufficient, in the condition called *hypothyroidism*, the basal metabolic rate decreases and the level of activity of the affected person will fall. In *hyperthyroidism* the thyroid gland is active and produces an excessive amount of thyroid hormones that primarily affects the heart (cardiopalms) [36].

Table 1.1 represents the effects of iodine deficiency on human health at different life stages. A longitudinal study of parents and children in Avon, UK, has revealed that even in mild-to-moderate iodine deficiency of pregnant women there is an adverse influence on the cognitive

development of infants, and hence on their future study at school. Reporting such findings, Bath et al. [31] stated that the iodine situation in the UK needs urgent review. **Table 1.2** represents WHO recommendations for iodine intake by age and **Table 1.3** represents the tolerable upper intake level for iodine, estimated by the European Commission/Scientific Committee on Food (EC/SCF) and the Institute of Medicine (IOM).

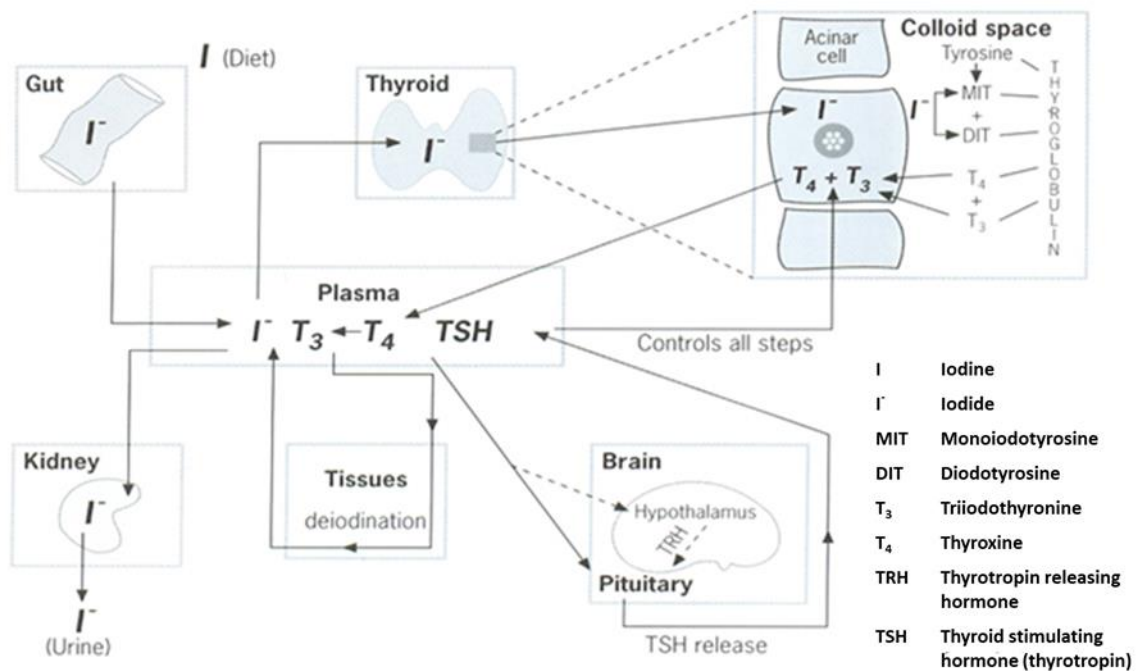


Figure 1.2. Summary of thyroid hormone production and regulation. Adapted from [9].

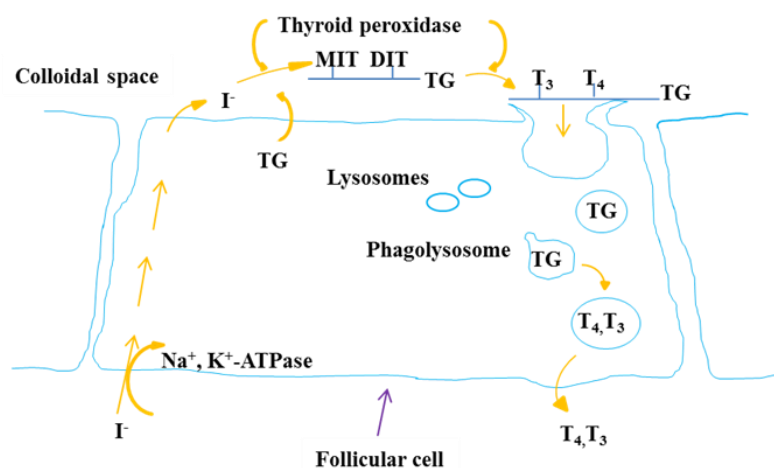


Figure 1.3. Synthesis of thyroid hormones. Adapted from [37].

Table 1.1. The impact of iodine deficiency on human health at different life stages. Adapted from [9].

Life stage	Effects
Foetus	Abortions Stillbirths Congenital anomalies Increased perinatal mortality Increased infant mortality Neurological cretinism: mental deficiency, deaf mutism, spastic diplegia, and squint Myxedematous cretinism: mental deficiency, hypothyroidism and dwarfism Psychomotor defects
Neonate	Neonatal goitre Neonatal hypothyroidism
Child and adolescent	Goitre Juvenile hypothyroidism Impaired mental function Retarded physical development
Adult	Goitre with its complications Hypothyroidism Impaired mental function Iodine-induced hyperthyroidism

Table 1.2. Recommended iodine intake by age and population group. Adapted from [22].

Age and population group	WHO ($\mu\text{m day}^{-1}$)
Children 0–5 years	90
Children 6–12 years	120
Adults \geq 12 years	150
Pregnant women	250
Lactating women	250

Table 1.3. Tolerable upper intake level for iodine ($\mu\text{g}/\text{day}$). Adapted from [26].

Age group	EC/SCF, 2002	IOM, 2001
1–3 years	200	200
4–6 years	250	300
7–10 years	300	300
11–14 years	450	300
15–17 years	500	900
Adult years	600	1100
Pregnant women >19 years	600	1100

Iodine absorption

Mostly, I_2 exists in foods as potassium or sodium iodide and as an organically bound complex, or as KIO_3 (a fortified compound used in bread and salt) [37, 38]. The majority of organic bound iodine releases iodine before absorption, which is reduced to iodide. As for iodate, it is reduced to iodide by glutathione (GSH) at pH 7.4 in GI within 2-3 min. The proposed stoichiometry of that reaction is $6\text{GSH} + \text{IO}_3^- \rightarrow 3\text{G-S-S-G} + \text{I}^- + 3\text{H}_2\text{O}$. Iodate can be also reduced to iodide when administered intravenously because red cells and most tissues contain GSH. More information about conversion of iodate to iodide *in vitro* and *in vivo* is given elsewhere [39]. Iodide is then absorbed rapidly by the stomach and the upper part of the small intestine [35] and it immediately appears in the blood stream. If iodine intake is sufficient, less than 10 % of iodide will be taken up by the thyroid gland, whereas in iodine deficiency it can reach up to 80 %, and the rest will be taken up by the kidney, where it will be excreted in the urine (**Figure 1.2**) [22].

Iodine interaction with other nutrients

The influence of selenium on thyroid functions is still being questioned due to the uncertainty of epidemiological surveys and clinical trial results. In Central Africa, where the iodine and selenium microelement intake is insufficient, myxedematous cretinism is the most common form; this leads to the assumption that selenium deficiency might subject the thyroid gland to free radical damage caused by hydrogen peroxide. However, the same iodine and selenium status in Tibet and in China has revealed no prevalence of myxedematous cretinism, suggesting that other factors can play a role [40].

There is strong evidence that iron supplementation or salt fortification along with iodine improve thyroid metabolism. Similarly, to iron, zinc [40], vitamin A [41] and copper deficiency is connected with hypothyroidism [42].

1.2.2 Vitamin E

Vitamin E is an essential micronutrient for humans and is obtained exclusively from the diet. The main biological role of vitamin E is its effective antioxidant properties in the cell antioxidant defence system that is attributed to the hydroxyl (-OH) group on the aromatic ring (**Figure 1.4**), which donates the hydrogen to free radicals, making them unreactive. Because vitamin E is mainly located within the phospholipid bilayer of cell membranes, it is particularly effective in preventing lipid peroxidation of polyunsaturated fatty acids (PUFAs), low-density lipoprotein and other components of cell membrane [9]. In addition, it has been reported that hypothyroidism is accompanied by an increase in oxidative stress, however, vitamin E supplementation, in this effect, could reduce oxidative damage [43]. Therefore, a water soluble source of vitamin E (discussed below) was used as a beneficial component for multiple micronutrient formulation to prevent iodine deficiency in **Chapter 4**. Besides, vitamin E has other multiple biological activities, including the regulation of inflammatory response, modulation of cellular signalling, membrane-bound enzymes, gene expression and cell proliferation [44], and it can be used therapeutically in doses of 200–400 mg/day to moderate some aspects of degenerative diseases such as Parkinson's disease, reduce the severity of neurological disorders such as tardive dyskinesia, prevent periventricular haemorrhage in pre-term babies, reduce tissue injury arising from ischemia and reperfusion during surgery, delay cataract development, and improve mobility in arthritis sufferers. However, very high doses (>1000 mg/day) may induce pro-oxidant damage; nevertheless, it has been reported in one study that a dose of 200 mg/day also causes an indication of a pro-oxidant effect in patients over 60 with respiratory tract infections.

The term vitamin E includes a group of eight naturally occurring homologues, classified into two classes, namely tocopherols that have a saturated 16-carbon phytyl side chain and tocotrienols that have three double bonds on the side chain. In turn, these classes each include four isoforms that differ in the number and position of methyl groups on the ring structure. The isoforms are *d*- α -, *d*- β -, *d*- γ -, and *d*- δ -tocopherol and *d*- α -, *d*- β -, *d*- γ -, and

d- δ -tocotrienol (**Figure 1.4**) [9]. They are a yellow viscous oil/liquid that oxidizes readily when exposed to light, oxygen and transition metal ions and they are fat soluble; however, they can be dissolved in alcohol and organic solvent too [45].

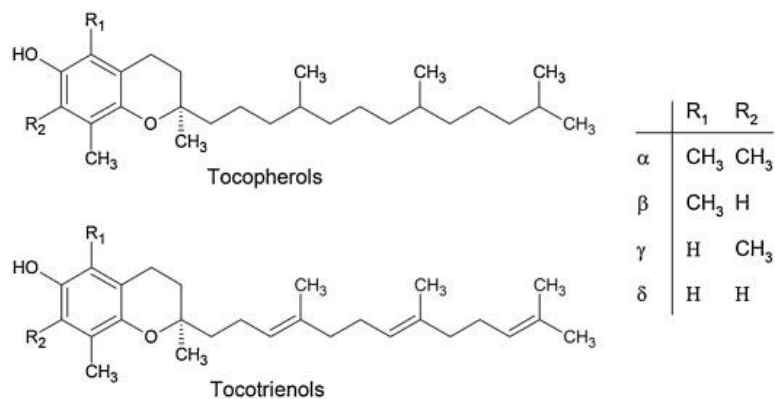


Figure 1.4. Chemical structures of tocopherol and tocotrienol. The value of the R groups for each isoform are listed in the table. Adapted from reference [46].

As the vitamin E family are all fat soluble, as with any other dietary lipid, they need to meet the following conditions to be absorbed: efficient emulsification, solubilization within mixed bile salt micelles, uptake by enterocytes and secretion into the circulation via the lymphatic system. Initially, emulsification occurs in the stomach and then in the small intestine in the presence of pancreatic and biliary secretions. As a result, vitamin E is solubilized and transported to the brush border membrane of the enterocyte, where it is incorporated into chylomicrons, then secreted into the intracellular space and lymphatic system, and subsequently into the blood stream. Tocopherol esters must be hydrolyzed in the small intestine before absorption. In the blood stream, vitamin E is transported via plasma lipoproteins and erythrocytes [9] from where it is transferred to the liver, which in turn separates out α -tocopherol and preferentially secretes it within very low-density lipoproteins and high-density lipoproteins into the bloodstream for distribution in the body. Therefore, α form predominates in blood and tissue, followed by γ -tocopherol [47], whereas a biodistribution study of tocotrienols shows an accumulation of them in peripheral tissues, such as the bones, brain, lung, muscle, and skin [44].

There is also available a water-soluble derivative of natural vitamin E, D- α -tocopheryl polyethylene glycol 1000 succinate (TPGS), that is widely used as a source of vitamin E

nutrients for foods and supplements. TPGS contains 27 % d- α -tocopherol, 65 % polyethylene glycol 1000 and 8 % succinic acid. The total α -tocopherol potency of this source is 260 mg/g TPGS (387 IU/g), after saponification of the esters. In addition, TPGS is used for special medical purposes in patients, mainly infants and children, with impaired vitamin E absorption due to fat malabsorption. For example, it can be utilized when insufficient amounts of bile are secreted, such as in cholestatic liver disease (at a dose level of 20–25 IU/kg bw/day (body weight per day) or 51.7–64.5 mg/kg bw/day), or when an insufficient amount of pancreatic enzymes are secreted, such as in cystic fibrosis, or in individuals with genetic anomalies in transport or binding proteins [9]. In addition, TPGS supplements have been given during post-surgical treatment in cardiac transplant recipients, as an oral coadministration with retinyl palmitate to improve vitamin A absorption in chronic cholestatic liver disease and to enhance vitamin D absorption in children with severe chronic cholestasis [48]. Moreover, TPGS has numerous applications in drug delivery systems (DDSs), and good reviews are given elsewhere [48-50]. Examples of commercially available supplements include NovaSOL[®] E (TPGS 100IU and 400 mg crystalline vitamin C), vitamin E solubilized liquid and oral tocofersolan [48]. The safety and bioavailability of TPGS was acknowledged by the European Food Safety Authority in 2007. From a toxicology study performed with rats and mice, the panel established an overall no-observed-adverse-effect level to be equivalent to 1000 mg TPGS/kg bw/day. However, the panel advised to avoid TPGS treatment in children with a severe impairment of kidney function and to apply fat-soluble vitamin E in healthy humans with normal fat absorption levels, because the administration of TPGS could only slightly elevate the plasma α -tocopherol level compared to fat-soluble vitamin E [51].

In dietary regulation, vitamin E activity is expressed as α -tocopherol equivalents (α -TEs), i.e. one α -TE is the activity of 1 mg d- α -tocopherol. In a mixed diet containing different natural forms of vitamin E, the α -TE is estimated as follows: the number of milligrams of β -tocopherols is multiplied by 0.5, γ -tocopherols by 0.1, and α -tocotrienols by 0.3. The synthetic *d,l*- α -tocopherols are multiplied by 0.74. One milligram of acetate form is equivalent to 1 IU of vitamin E [9]. The recommended intake for vitamin E in different countries varies between 3 and 15 mg/day. In the US, the Recommended Dietary Allowance (RDA) for both men and women adults from 14 years is 15 mg of α -tocopherol. Whereas, recently, the European Food

Safety Authority suggested replacing the present RDA for vitamin E with a newly defined Adequate Intake as follows: men 13 mg/day, women 11 mg/day, infants/children 5–13 mg/day (depending on the age) [47]. However, based on the evidence in different animals that low levels of vitamin E combined with an excess of PUFAs gives rise to a wide variety of clinical signs, the WHO published the best estimate of requirements of vitamin E by age, calculated using a suggested d- α -tocopherol/PUFA ratio of 0.4 mg/1 g. Nonetheless, WHO specifies that the diets high in PUFAs are also usually high in vitamin E, so the median intake of vitamin E will deviate considerably in most populations of industrialized countries. Therefore, they reported that the accumulated data about vitamin E deficiency was not strong enough to formulate a recommended nutrient intake for vitamin E and pointed out that the recommendation they provide can only represent the best estimate of requirements (**Table 1.4**). There are no specific recommendations for vitamin E requirements in pregnancy and lactation because there is no evidence that the vitamin E requirement is different from the standard adult requirement [9].

Table 1.4. The best estimate of Vitamin E requirement provided by WHO. Adapted from [9].

Group	Fat-soluble vitamin E (mg α-TE/day)	Group	Fat-soluble vitamin E (mg α-TE/day)
Infants		Adults	
0–6 m	2.7	Females 19–50 y (premenopausal)	7.5
7–12 m	2.7	Females 51–65 y (menopausal)	7.5
Children		Males 19–65 y	10.0
1–3 y	5.0	Elderly	
4–6 y	5.0	Females 65+y	7.5
7–9 y	7.0	Males 65+y	10.0
Adolescents		Pregnant women	–
Females 10–18 y	7.5	Lactating women	–
Males 10–18 y	10.0		

Vitamin E deficiency in humans causes muscle damage and neurological lesions. However, WHO published a book for mineral and vitamin requirements in 2005, where it says that there is very rare occurrence of clinical signs of deficiency (leakage of muscle enzymes into plasma, increased levels of lipid peroxidation products in plasma, and increased erythrocyte

haemolysis) in healthy individuals, suggesting that the average diet contains enough vitamin E to satisfy nutritional needs. In addition, they reported that the estimation of optimum intake, which may be implied when plasma concentration of vitamin E exceeds 25–30 $\mu\text{mol/L}$ of lipid-standardized α -tocopherol, should be treated with caution, because only 1 % of total tocopherol may be in the blood and its concentration is influenced by circulating lipid. Therefore, plasma vitamin E concentration does not necessarily reflect intake or tissue reserves. Thus, WHO recommended assessing vitamin E status by calculating a lipid-vitamin E concentration as $\mu\text{mol}/\text{mmol}$, e.g. a tocopherol-cholesterol ratio greater than 2.25 is believed to represent satisfactory vitamin E status and levels below this value should be taken as an indication of biochemical deficiency [9]. Whereas, the Institute of Medicine in the US established a status of serum- α -tocopherol concentration below 12 $\mu\text{mol/L}$ as deficient, because that concentration level was deemed sufficient to prevent peroxide-induced haemolysis and improve cell survival. Galli et al. [47] in a recent review of vitamin E, reported that vitamin E intakes in both developing and industrialized countries are below the RDA and the Estimated Average Requirements of 12 mg/day (the protective 12 $\mu\text{mol/L}$ serum α -tocopherol threshold level). For example, more than two-thirds of South Korean adults have suboptimal vitamin E status (12–30 $\mu\text{mol/L}$ (the optimum concentration is set at 30 $\mu\text{mol/L}$ and above by the German Federal Ministry of Health Consensus Statement) and almost one-quarter are deficient (<12 $\mu\text{mol/L}$). In rural Nepal, about one-third of pregnant women have severe vitamin E deficiency (<10 $\mu\text{mol/L}$), while in Bangladesh, almost two-thirds of the women in early pregnancy have more severe vitamin E deficiency (<9.3 $\mu\text{mol/L}$). American adults have suboptimal vitamin E status and about 90 % of the population has vitamin intakes below the Estimated Average Requirements. The low vitamin E intake is also observed in the United Kingdom (UK), Germany and the Netherlands.

1.2.3 Polyunsaturated fatty acid

Polyunsaturated fatty acid (PUFA) (used in this study in **Chapter 4**) is a class of fatty acid that contains more than one double bond in their backbone. PUFA includes a group of fatty acids that are essential to the human body because they cannot be synthesized by the body and, therefore, must be obtained from the diet. These are α -linolenic acid (ALA) (C18:3n-3) and linoleic acid (LA) (C18:2n-6), which are converted into long chain PUFA in the endoplasmic

reticulum of the liver and retina after they are taken in by dietary sources. ALA is a precursor for docosahexaenoic acid (DHA) (C22:6n-3) and its substrate eicosapentaenoic acid (EPA) (C20:5n-3), two key long chain ω -3 (n-3) EFAs. LA is a precursor for arachidonic acid (ARA) (C20:4n-6) a long chain ω -6 (n-6) EFA [52, 53].

In 2002, the Food and Nutrition Board, at the Institute of Medicine of the National Academies in the USA, established the Adequate Intake level for n-6 and n-3 fatty acids (**Table 1.5**).

Table 1.5. Adequate intake for n-3 and n-6 fatty acids, taken from [54]. m – Month, y – Year.

Life stage group	n-3 (source ALA) g/day	n-6 (source LA) g/day
Infants		
0–6 m	0.5	4.4
7–12 m	0.5	4.6
Children		
1–3 y	0.7	7
4–8 y	1.2	10
Males		
9–13 y	1.2	12
14–18 y	1.6	16
19–50 y	1.6	17
51 > y	1.6	14
Females		
9–13 y	1.0	10
14–18 y	1.1	11
19–50 y	1.1	12
51 > y	1.1	11
Pregnancy		
14–50 y	1.4	13
Lactation		
14–50 y	1.3	13

Omega-6 has important biological functions relating to growth, development and brain function as well as being a precursor of lipid mediators. It is especially important for ARA, which is found in breast milk and plays a crucial role in infant growth and mental development. A neuropsychological assessment study proposed that ARA supplementation might improve cognitive function and learning behaviour in the elderly [55]. Omega-3s, however, play an important structural role in cell membranes as components of phospholipids, especially DHA,

which appears in high levels in the retina, brain, and sperm [56]. The function of DHA in the brain was gleaned from animal experiments (young monkeys were given a diet deficient in n-3 fatty acids), which demonstrated poor visual acuity and an increase in stereotypical behaviour suggesting that brain development had been impaired. n-3 PUFA deficiency in humans has not been created because it is unethical; however, examinations of the cadavers of premature babies demonstrated a rapid accumulation of DHA and ARA in foetal brain tissue during the third trimester of pregnancy [57] and this accumulation continues throughout the first 2 years after birth. A similar finding was observed with the DHA concentration in the retina, in which accumulation is completed by birth [56]. The importance of dietary DHA and ARA intake during pregnancy and infancy for foetal growth and development has been recognised and has influenced the international food standards for infant formula. Thus, in 2007, the Codex Committee on Nutrition and Foods for Special Dietary Uses (the Codex Alimentarius international food standards meeting) recommended adding DHA and ARA to infant formula [55]. Moreover, omega-3s along with omega-6s serve as an energy supplier for the body and the energy is spent to form eicosanoids, which are signalling molecules that have a variety of effects on cardiovascular, pulmonary, immune and endocrine systems [56]. The UK dietary guidelines advocate the benefits of EPA and DHA consumption in improving cardiovascular risk factors.

A number of studies show the importance of the ratio of n-6/n-3 essential fatty acids intake. For example, a ratio of 4/1 resulted in a 70 % decrease in total mortality from cardiovascular disease; a ratio of 2.5/1 reduced rectal cell proliferation in patients with colorectal cancer, whereas a ratio of 4/1 had no effect; a ratio of 5/1 had a positive effect on patients with asthma, whereas a ratio of 10/1 had an adverse effect [58].

Deficiency of n-3 or n-6 PUFAs can affect the skin; for example, rough, scaly skin and dermatitis can be developed. In addition, if n-3 deficiency occurs, the DHA concentration in plasma and tissue decreases. However, there is no established critical concentration of DHA and EPA, which will affect the visual or neural function or the immune response [56].

Today industrialized societies are deficient in n-3 fatty acid and, particularly, Western diets are characterized by an increase in n-6 fatty acid and a decrease in n-3 fatty acid intake [58], with ratios at 7:1 and 17:1 for the UK and USA, respectively. In comparison, the Japanese diet,

which is a fish-eating diet, has a 4:1 ratio and has the lower risk of cardiovascular disease [57]. Therefore, supplementation strategies, which offer one of the approaches to improving PUFA consumption, mainly focus on the delivery of n-3 fatty acids. However, due to difficulties swallowing capsules or the unpleasant aftertaste, the rates of compliance are generally low. In addition, the use of gelatine, a main encapsulation material, makes supplementation strategies an unsuitable tool for most vegetarians and certain religious groups. Food-based strategies provide an alternative approach to improving omega-3 status and the population health. **Tables 1.6 and 1.7** represent a summary of n-3 fatty acid delivery systems and their production methods [59], and methods of incorporation of n-3 fatty acids into foods [60], respectively.

Table 1.6. Different encapsulation methods used to produce two types of delivery systems for n-3 fatty acid encapsulation, taken from [59].

Type of encapsulation	Method of encapsulation
Beads	Spray-, freeze-drying Emulsification/internal gelation Co-crystallization Emulsion extrusion Solvent evaporation Ionic gelation
Capsules	Coacervation Extrusion Condensation and interfacial polymerization Microfluidic devices

Table 1.7. Summary of methods used to incorporate n-3 fatty acids into foods, taken from [60].

Method	Example
Food fortification	Oat and soy based nutrition bar treatments Snacks bars and muffins Yogurt (as emulsion) Jalapeno or olive flavoured hummus type dip (as microemulsion) Powdered milk
Encapsulation	Soup powder Spray dried emulsions to form powders suitable to add to food matrices Milkshake Milk, yogurt and bread
Nanoemulsion	Yogurt

1.3 Active pharmaceutical ingredients (APIs)

There are two major classification systems for active pharmaceutical ingredients (APIs) that have been acknowledged and used in drug development. These are the Anatomical Therapeutic Chemical Classification system (ATC), regulated by the WHO Collaborating Centre for Drug Statistics Methodology (WHOCC), that were established in 1982 [61], and the Biopharmaceutical Classification System (BCS), proposed by Amidon et al. [62] that was introduced in 1995.

In the ATC classification system, the drugs are divided into groups at five different levels specifying the organ or system on which they act and their chemical, pharmacological, and therapeutic properties (**Table 1.8**) [63]. The first level has fourteen main anatomical/pharmacological groups (**Table 1.9**), which in turn are divided into pharmacological subgroups (2nd level). The 3rd and 4th levels are classified into chemical, pharmacological or therapeutic subgroups and the 5th level specifies the chemical substance.

Table 1.8. The structure of the code according to the ATC classification system. Adapted from [63].

A	anatomical main group (1 st level)
A10	therapeutic subgroup (2 nd level)
A10B	pharmacological subgroup (3 rd level)
A10BA	chemical subgroup (4 th level)
A10BA02	chemical substance (5 th level)

Table 1.9. The ATC system main groups or the 1st level of the classification. Adapted from [63].

A	Alimentary tract and metabolism	L	Antineoplastic and immunomodulating agents
B	Blood and blood forming organs	M	Musculo-skeletal system
C	Cardiovascular system	N	Nervous system
D	Dermatologicals	P	Antiparasitic products, insecticides, and repellents
G	Genito urinary system and sex hormones	R	Respiratory system
H	System hormonal preparations, excluding sex hormones and insulins	S	Sensory organs
J	Antiinfectives for systemic use	V	Various

The ATC assigns a unique ATC code for each drug that specifies its drug class within the ATC system; however, one drug may have more than one ATC code if the drug has two or more strengths or routes of administration with different therapeutic effects. For instance, metoprolol and ketoconazole, used in this study (**Chapter 5**) have several ATC codes (**Figure 1.5**), which can be found on the official website of the WHOCC (www.whooc.no).

C07AB02 metoprolol C07AB02 metoprolol C07FX03 metoprolol and acetylsalicylic acid C07FB13 metoprolol and amlodipine C07FB02 metoprolol and felodipine C07FX05 metoprolol and ivabradine C07CB02 metoprolol and other diuretics C07BB02 metoprolol and thiazides C07BB52 metoprolol and thiazides, combinations	C CARDIOVASCULAR SYSTEM C07 BETA BLOCKING AGENTS C07A BETA BLOCKING AGENTS C07AB Beta blocking agents, selective <table border="1"> <thead> <tr> <th>ATC code</th> <th>Name</th> <th>DDD</th> <th>U</th> <th>Adm.R</th> <th>Note</th> </tr> </thead> <tbody> <tr> <td>C07AB02</td> <td>metoprolol</td> <td>0.15</td> <td>g</td> <td>O</td> <td></td> </tr> <tr> <td></td> <td></td> <td>0.15</td> <td>g</td> <td>P</td> <td></td> </tr> </tbody> </table>	ATC code	Name	DDD	U	Adm.R	Note	C07AB02	metoprolol	0.15	g	O				0.15	g	P	
ATC code	Name	DDD	U	Adm.R	Note														
C07AB02	metoprolol	0.15	g	O															
		0.15	g	P															
D01AC08 ketoconazole G01AF11 ketoconazole J02AB02 ketoconazole	J ANTIINFECTIVES FOR SYSTEMIC USE J02 ANTIMYCOTICS FOR SYSTEMIC USE J02A ANTIMYCOTICS FOR SYSTEMIC USE J02AB Imidazole derivatives <table border="1"> <thead> <tr> <th>ATC code</th> <th>Name</th> <th>DDD</th> <th>U</th> <th>Adm.R</th> <th>Note</th> </tr> </thead> <tbody> <tr> <td>J02AB02</td> <td>ketoconazole</td> <td>0.2</td> <td>g</td> <td>O</td> <td></td> </tr> </tbody> </table>	ATC code	Name	DDD	U	Adm.R	Note	J02AB02	ketoconazole	0.2	g	O							
ATC code	Name	DDD	U	Adm.R	Note														
J02AB02	ketoconazole	0.2	g	O															

Figure 1.5. The ATC codes (on the right) and a description of one of the codes (on the left) of metoprolol (a) ketoconazole (b). DDD – defined daily dose, U – unit, Adm. R – route of administration, g – gram, O – oral, P – parenteral. Adapted from [61].

The BCS classification divides the drugs into four groups (class I, II, III, IV) according to their aqueous solubility and intestinal permeability (**Figure 1.6**). It is a useful tool at the early development stage of new drug products to establish a preliminary BCS classification for further improvement. For example, as shown in **Figure 1.6** the absorption of a class II drug can be improved by modification or changing the formulation design. The class III drug can be improved by adding absorption enhancer and class IV by a combination of approaches used for BCS class II and III. It can also be used to select suitable dissolution test conditions for new drugs and as a guide to determine whether *in vitro-in vivo* correlation (IVIVC) can be expected for an immediate release drug [62, 64].

According to the FDA, a drug is classified as highly soluble when its highest clinical dose strength is soluble in ≤ 250 ml of aqueous media over a pH range of 1–7.5 at 37.5 °C, and as highly permeable if the drug absorption, administered orally, is >90% in comparison to an intravenous reference dose or when determined using mass balance [65]. Thus, metoprolol and ketoconazole are classified as class I and class II drugs, respectively [66].

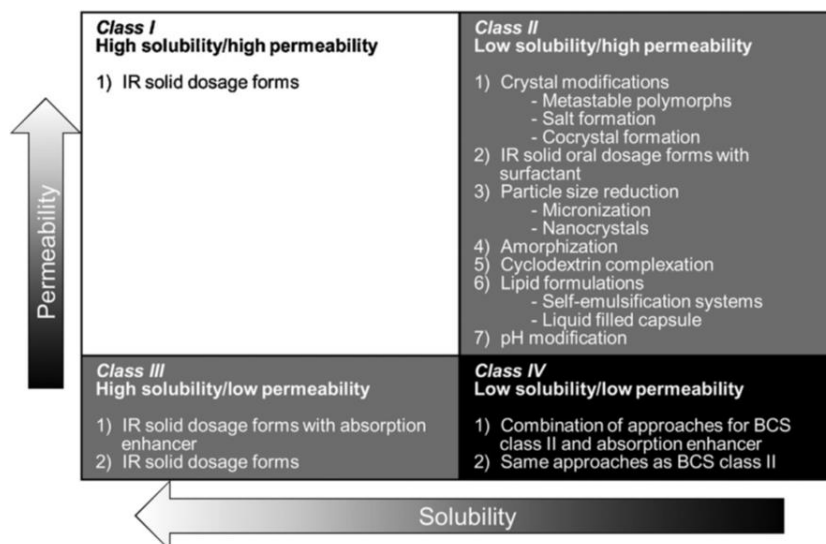


Figure 1.6. The Biopharmaceutical Classification System and possible formulation options based on the BCS. IR – immediate release. Adapted from [67].

Another sub classification of the drugs relates to the measurement of their physical nature. The dissociation constant, pK_a , is a measure of the strength of an acid or a base. It allows you to determine the ionization state with respect to pH. Strong acids and bases are those that are completely ionised in the pH range 0 – 14. Whereas weak acids and bases are those that are incompletely ionised in the pH range 0 – 14 [68]. An ionized drug is more aqueous soluble and less membrane permeable than a non-ionized form. The extent of ionization of a drug plays a crucial role in the characterization of its absorption, distribution, metabolism and excretion (ADME) profile [69]. The partitioning coefficient, $\log P$, is a measure of how well a substance dissolves in the water phase versus an organic phase, usually 1-octanol and water. Substances that are predominantly dissolved in the water phase are hydrophilic and those predominantly dissolved in lipids are lipophilic. The $\log P$ value of a drug provides a prediction of its behaviour in different environments and therefore it is an important property in drug development that helps to determine how to deliver a drug to specific sites and understand the behaviour of drug molecules in the body, i.e. its ADME properties [70].

1.4 Main considerations when selecting the delivery systems for drugs or nutrients

The selection and design of the delivery systems depends on the site of administration, the targeted group and the physicochemical properties of the active ingredient (either being a nutrient or a drug).

1.4.1 Intrinsic physicochemical properties

Drugs and nutrients have several characteristics, such as absorption in the intestine, the ability to change physiological processes and the possibility to cause toxicity in high doses.

One of the challenges of nutritional supplements is their high instability in nature. They are unstable and reactive substances, mostly susceptible to moisture, light, pH, and temperature. They can decompose and degrade during processing and storage depending on the surrounding conditions. In pharmaceutical formulations, vitamin and mineral degradation is related to micronutrient interaction with environmental conditions and the impact of gastric acidity (pH <2.0). Therefore, to provide protection from chemical and physical degradation and at the same time ensure bioavailability, encapsulation systems are commonly used as a carrier matrix [71]. In addition, by manipulating the structure of encapsulation systems, it is possible to deliver several substances with different chemical and physical properties simultaneously. However, considering their great probability to react with other ingredients and potential premature release, the challenging issues are to find an appropriate coating material as well as a suitable technology to produce a complex formulation. Secondly, the most problematic issue in nutrition supplementation is that the materials used as a carrier for nutritional supplements must be biodegradable, food grade, inexpensive, capable of protecting the internal phase from surrounding conditions and have high loading capacity to encapsulate a large amount of vitamins [72]. Furthermore, nutritional supplements are classified as food, yet the carrier materials accepted in pharmaceutical production have not been certified for food application. Thus, the available number of existing well-established carrier materials in the pharmaceutical industry is reduced significantly, leaving a limited number of possible carrier materials. However, all nutritional supplements may be treated and act as drugs, as mentioned earlier, i.e. the nutrient dosage must be a strictly accurate

amount. If the dose of micronutrient is higher than the tolerable upper intake level, it may have adverse health effects or even be toxic, or if it is less than the recommended dose then there is no effect. In addition, the selection of a delivery system for nutritional supplements is based on the same approach as in pharmaceutical formulation. Thus, when formulating a nutritional dosage form, the targeted group of population should be considered. Another aspect that should also be considered when formulating a nutritional dosage form is that the most vulnerable group of population affected by the deficiency of nutrients are women of reproductive age, pregnant women, lactating women, children and the elderly. The preference of these groups should be considered in the design, i.e. taste, appearance, dosage form, route of administration and so on. Finally, the majority of nutrient deficient people live in developing countries; hence, the cost of the end product is probably the most important challenge. There are numerous types of nutritional supplements available in the market; however, only a few of them have been adopted by the WHO in fighting nutrient deficiency on a mass scale. One of the main reasons behind this fact is simply the cost of these products. For instance, for the prevention of iodine deficiency, universal salt iodization was adopted as a cost-effective measure, in spite of knowing the direct adverse effect of table salt on a cardiovascular system and other organs in the body.

The main challenges with drugs are related to their poor aqueous solubility and dissolution rate, which limit formulation approaches, clinical application and marketability. At present about 40 % of the pipeline drugs are poorly soluble, i.e. belong to BCS II and IV compounds; hence, a delivery system that can improve the dissolution and/or apparent solubility of poorly soluble drugs should be selected for such compounds [73]. Whereas with highly water-soluble drugs it is difficult to achieve sustainable release, due to their high solubility, rapid dissolution and tachymetabolism; therefore, an appropriate loading system should be designed for them [74]. Other important properties of drugs are the Log P and pKa values, which help in many aspects of drug design.

1.4.2 Paediatric targeted group

A variety of different dosage forms are available for oral administration to paediatric and geriatric patients, such as solutions, syrups, suspensions, powders, tablets and capsules. However, despite extensive development of medicines for children for different types of

disease, and pharmaceutical companies bringing them to the market, according to a WHO report, the global mortality rate in children under five years due to the lack of appropriate paediatric dosage forms remains a significant problem for a group of diseases such as malaria, HIV (Human Immunodeficiency Virus), tuberculosis, pneumonia, diarrhoea and neonatal infections. In 2008, at the Informal Expert Meeting on Dosage Forms of Medicines for Children, WHO established the desirable criteria for dosage forms of medicines for children, with particular attention being paid to conditions prevailing in the developing countries and recommended preferred dosage forms of medicines for children (**Table 1.10**). Among the reported recommendations, a flexible solid dosage form, such as tablets that are orodispersible and/or that can be used for preparation of oral liquids (suspension or solution), was proposed to use for treating the diseases that are the major causes of mortality and morbidity of children under 5 years. In addition, solid formulations are the most convenient and acceptable forms in pharmaceutical formulations today since liquid formulations, although it is a preferred dosage form of paediatric patients, have short half-lives once opened, increased contamination risk for multiple dose formulations, are bulky to handle and store, and are relatively costly [75].

Table 1.10. Desirable requirements for dosage form of medicines for children identified by WHO. Adapted from [76].

-
1. Minimal administration frequency
 2. Minimal impact on life style
 3. Minimum, non-toxic excipients
 4. Convenient, easy, reliable administration
 5. Palatable
 6. Requiring minimal manipulation by health professionals or carers prior to use
 7. Transportable and low bulk/weight
 8. Easily produced, stable in a variety of climates
 9. Affordable
 10. Commercially viable
-

1.4.3 Oral route of administration

Drugs and nutrients can be administered via a number of routes, e.g. orally, topically, rectally, and intravenously. However, the oral route of administration remains the most popular and

preferred way of dosing by paediatric patients. This is because it is the easiest, painless and most convenient way of administering drugs/nutrients in contrast, for example, to intravenous administration which can be complicated with extravasation of the drug or blood, catheter infections, and thrombosis [77]. When a complex pharmaceutical dosage form is administered perorally, it sequentially breaks down into its elemental components in the GI tract and they are selectively absorbed/transferred in an organized manner from/through the gut and enter into blood circulation, where they are then distributed to various tissues [78, 79]. The human intestinal epithelium is highly absorptive due to numerous villi, which increase the total absorptive surface area of the gastrointestinal (GI) tract by up to 300–400 m² [80]. The factors that can limit the oral bioavailability of drugs/nutrients are the slow release of the drug/nutrient from the dosage form, instability of the drug/nutrient in the GI tract, poor permeability of the GI mucosa to the drug/nutrient, complexation with food and first-pass metabolism of the drug/nutrient [64]. In addition, drugs/nutrients administered orally experience a harsh environment when they pass through the GI tract, specifically, moving from 1.2 pH (in the stomach) to 6–7 pH (in the large intestine), which may cause the degradation or destruction of the drugs/nutrients [81, 82].

The oral trans-mucosal administration method offers some advantages over the peroral route of administration, such as avoiding the number of barriers a drug/nutrient must cross during GI transit. The oral mucosa includes the buccal (between the gum and cheek), the sublingual (under the tongue), the gingival, palatal and labial mucosa. The buccal and sublingual regions are the most commonly used routes for effective drug delivery [81]. The high vascularity and permeability of the sublingual and buccal mucosa allow the rapid transmucosal absorption of the drug/nutrient directly into systemic circulation, avoiding first-pass drug/nutrient metabolism and pre-systemic elimination of the drug/nutrient in the GI. This gives advantages over the peroral route, such as high bioavailability and almost immediate onset of action [72]. In addition, the oral cavity provides relatively consistent and friendly physiological conditions for dosage forms due to the continuous secretion of saliva, which is a relatively mobile fluid with less mucin, lower enzymatic activity and no proteases, making the oral trans-mucosal route favourable to protein and peptide delivery [81]. However, despite the attractive properties of the oral mucosa, it provides some limitations and challenges as well for researchers developing novel delivery systems. These are the relatively small surface area of

the oral cavity, poor drug/nutrient permeability through the oral mucosa, the fact saliva can wash away [72] and the fundamental limitation of this route of administration: the lack of cooperation of children and the risk of choking on or swallowing the delivery device or aspiration [83]. In addition, in order for a drug/nutrient to be formulated for delivery via the oral mucosa, the drug/nutrient should dissolve rapidly, produce the desirable therapeutic effects with a small amount of drug and have an agreeable taste [84].

Overcoming all these barriers and constraints related with each route of administration is an important aspect of the delivery systems development process.

1.5 Solid dispersion

Various approaches have been developed to overcome the solubility problem of poorly soluble drugs, including for example salt formation, prodrug formation, particle size reduction, complexation, solubilization (co-solvents, micelles, and emulsions), solid lipid nanoparticles and solid dispersion. However, of these approaches, a solid dispersion that is defined as “a dispersion of one or more API in an inert carrier or matrix at the solid state prepared by solvent, melting or solvent-melting method” [73] showed the most successful improvements in enhancing the dissolution profile of poorly soluble drugs. Its success is due to the combination of many advantageous properties, such as reducing particle size and changing the drug’s physical state, as dispersed molecules, amorphous or crystalline particles, enhancing wettability and porosity. For example, conventional particle size reduction techniques can reduce the size of particles down to 2-5 μm ; however, these particles can easily agglomerate in the formulation, dissolution process or during storage. While the solid dispersion method can reduce the drug particle size into molecular levels, the carrier or the matrix can also prevent the agglomeration of drug particles, and the drug is then released in a supersaturated state, which is advantageous for rapid absorption. However, if the drug is precipitated during supersaturation, the size of the precipitated drugs in the dissolution media is still at submicron level ($<1 \mu\text{m}$), hence the dissolution rate is still higher than that of microparticles. In addition, if the drugs exist in amorphous or more soluble polymorphic forms, the dissolution rate can be even faster because they have lower thermodynamic stability (a higher energy state) than drug particles. Moreover, solid dispersion can enhance

the drug wettability due to the high porous structure and increased surface area, particularly for those prepared using solvent evaporation methods. The fast removal of the solvent leaves many channels in the solid dispersion structure, which increases water absorption and the dissolution of carrier materials, which in turn increases the wettability of the drug. In addition, the wettability of the drug can also be improved by incorporating surfactants or emulsifiers or selecting polymers that can act as solubilizers to enhance drug solubility. These reduce the risk of agglomeration of drug particles in the dissolution media, hence increasing the dissolution rate of the drug. Besides, solid dispersion can be formulated in solid oral dosage forms that have more advantages than a liquid product produced by the solubilization method. Novel nanosizing approaches can also produce drug nanocrystals in a solid state; however, they have quite a long and complicated preparation process, and require stabilizers and special equipment. In contrast, the preparation process of solid dispersions is more simple and applicable.

The disadvantages of solid dispersion are related to the recrystallization of drugs from their amorphous state during solidification and storage, which will change a number of factors including the bioavailability of solid dispersion, the thermal instability of the drugs in the melting method, the solvent residue in the solvent method, the low IVIVC and the precipitation of the drugs in the dissolution media due to supersaturation. There are a number of strategies that have been implemented to overcome these common problems of solid dispersion. For example, the recrystallization of the drug can be inhibited by selecting polymers that have a higher glass transition (T_g) temperature than the drug, a strong interaction with the drug and low hygroscopicity. These can decrease the molecular mobility of the drug and hence decrease drug recrystallization. The addition of surfactants or emulsifiers into the formulation may also increase the miscibility of the drug-polymer due to their amphiphilic structure. Furthermore, surfactants or emulsifiers can reduce the process temperature in the melting method due to their plasticizing effect and, as mentioned earlier, improve wettability and inhibit the precipitation process as they can adsorb on the surface of the drug particles or form micelles that encapsulate the drugs. Finally, in the solid dispersion, the drugs can exist in a crystalline state as well, however, they still have better stability than if they are in pure crystalline form because the carrier or matrix still keeps the crystals separate and prevents them from agglomeration. For example, the *in vivo* bioavailability

study of crystalline drugs shows a significant increase in stability in comparison with a physical mixture [73, 85-88].

The solid dispersion based formulations can be prepared by using either the melting or solvent evaporation based method. **Figure 1.7** presents the list of techniques used to prepare solid dispersion. In this study, we used electrospinning to prepare solid dispersion based oral films. The detailed discussion on the electrostatic spinning techniques is presented in the next sections.

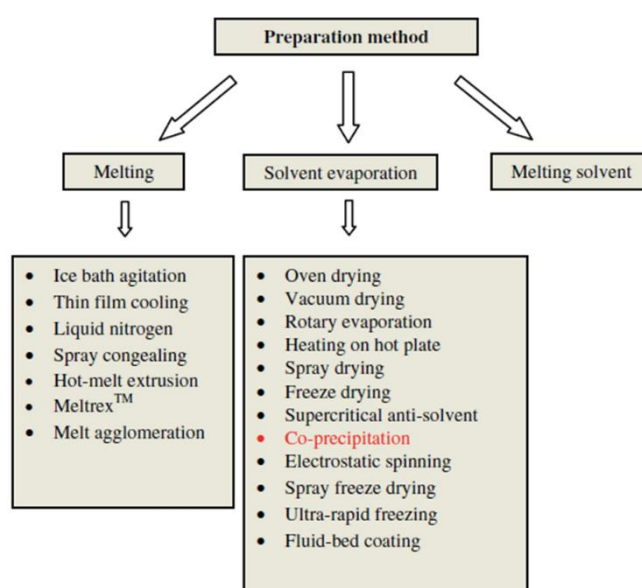


Figure 1.7. Preparation methods and techniques used to prepare solid dispersion. Adapted from [73].

1.6 Electrospinning

Electrostatic or electrohydrodynamic spinning or simply electrospinning is a simple and versatile technique used to fabricate nanofibres by using electrostatic forces, i.e. through an electrically charged polymer solution or polymer melt. In the study, which is discussed in **Chapter 3-4**, the electrospinning of a polymer solution is performed and therefore the process will be discussed in more detail here [89, 90].

The electrospinning system consists of a sample reservoir, which is a simple syringe with a needle, the syringe pumping special equipment, a high voltage power supply, two electrodes and a grounded collector (**Figure 1.8**). In electrospinning, high voltage is applied to the tip of the needle that contains the solution that is held by its surface tension. High voltage induces a charge on the surface of the liquid and further increasing the electric field, usually to a level more than 5–6kV, leads to the elongation of the hemispherical surface of the solution and forms a conical shape known as the Taylor cone. As the intensity of the electric field is increased at a critical voltage, when the repulsive forces are larger than its surface tension, the repulsive electrostatic forces overcome the surface tension and a charge jet would erupt from the tip of the Taylor cone. The jet undergoes a bending instability and elongation stage, with further stretching and thinning under the electrostatic forces as the solvent evaporates. Long and thin fibres are then collected at the opposite site, on the grounded collector.

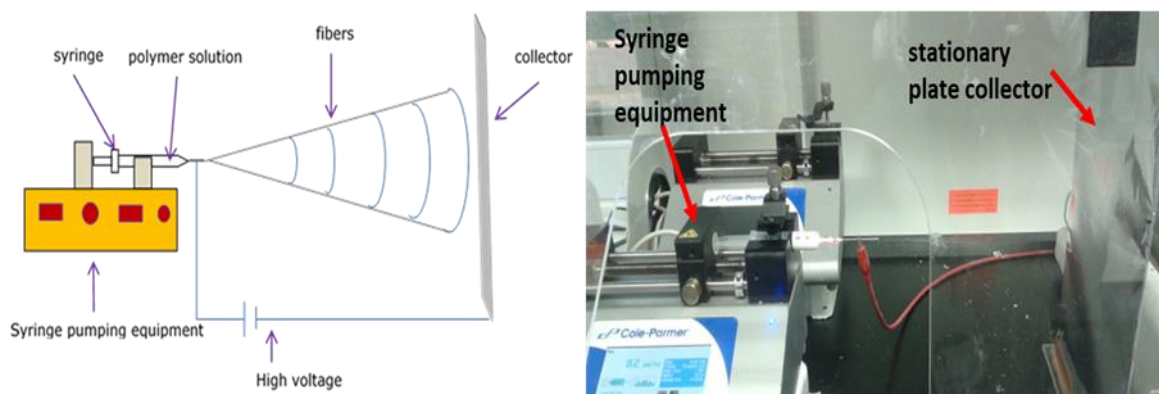


Figure 1.8. Schematic diagram of the set-up of the electrospinning apparatus (left). Adapted from [91]. The lab electrospinning set-up used in this study (right).

The diameter of the fibres created by the electrospinning process can range from nanometres to microns and the length can reach 1–3 metres. They are collected as non-woven fibrous mats that can be used in an oral dosage form by directly cutting them into pieces and then being packed in blister packs, or by milling and grinding or folding in many layers and further compressing into tablets or incorporating into capsules.

Electrospinning can be considered as a combination of solid dispersion technology and nanotechnology. The main advantages of this technique are the high surface area, high

porosity, high drug loading of produced delivery systems (e.g. 21 % w/w without changing the nanofibres morphology and up to 86 % w/w but with particulate beads as shown in this study **(Chapter 3)**, and 1:1 indomethacin:PVP and 4:1 aliskiren:PVP without changing the nanofibers morphology and forming a solid solution as reported by Brettmann et al. [92]) and the fast and efficient solvent evaporation, generally leading to the dispersion of the drug in the form of amorphous or nanocrystals and a more homogeneous distribution of API [73]. Yu et al. compared a polyvinylpyrrolidone (PVP) based solid dispersion of paracetamol (acetaminophen) prepared using electrospinning with other methods, namely vacuum drying, freeze drying, heat drying and pure paracetamol particles. *In vitro* dissolution testing was conducted in 900 ml 0.1 mol/L phosphate buffer solution with a rotating paddle at 50 rpm, 37 °C, and sink conditions $C < 0.2 C_s$. The results showed that the electrospun nanofibre-based solid dispersion had a faster dissolution profile followed by freeze-dried membrane and vacuum-dried membrane then heat-dried membrane and lastly pure paracetamol particles **(Figure 1.9)**. The authors reported that about 93-94 % of paracetamol was released in the first 2 min and completed within 5 min from electrospun nanofibres. Whereas the complete drug release from the freeze-dried membrane and vacuum-dried membrane was within 20 min, followed by heat-dried membrane, 30 min, all with zero-order kinetics. And it took 60 min for pure paracetamol for complete dissolution which in fact showed a fast release rate at the beginning but was followed later by prolonged tailing-off effect that is common for conventional tablets due to the large size of the drug particles. The solid dispersion membranes avoided the tailing-off effect due to the even distribution of the drug within PVP matrix and the amorphous state of the drug in electrospun, freeze-dried and vacuum-dried membranes. The drug in heat-dried membrane may have mixed amorphous, nano- and micro-particles.

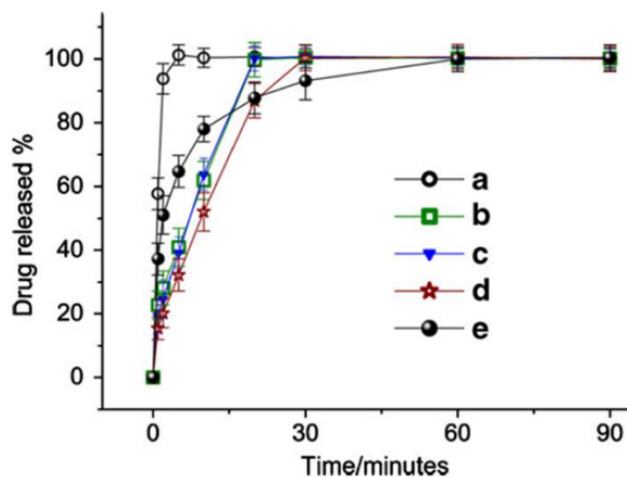


Figure 1.9. Paracetamol dissolution profile from membranes prepared by: a) electrospinning; b) freeze drying; c) vacuum drying; d) heat drying; e) pure paracetamol particles. Adapted from [87].

In addition, the fast disintegration and dissolution of electrospun prepared solid dispersions addresses the needs of paediatric, geriatric and dysphagic patients who often have difficulties in swallowing or taking medicines. Fast-dissolving electrospun solid dispersions, also known as oral fast-dissolving membranes or strips, or orodispersible films, can dissolve readily on the tongue and deliver drugs to a patient rapidly without the need to swallow and to take water [93]. The large surface area available in the strip dosage form allows rapid wetting and the moisture in the oral cavity is sufficient to dissolve it. The drug can be absorbed by the conventional gastrointestinal route and/or directly through the highly vascularized oral and buccal mucosa by entering the systemic circulation without undergoing first-pass hepatic metabolism, which in turn can improve the bioavailability of the drug and can reduce the dose of the drug. The fast-dissolving oral strip can be classified as an oral disintegrating tablet, which has been defined by the FDA as “solid oral preparations that disintegrate rapidly in the oral cavity, with an *in vitro* disintegration time of approximately 30s or less, when based on the United States Pharmacopeia (USP) disintegration test method or alternative” [94]. Other important advantages of the electrospinning process are that it does not employ thermal treatment and can be processed without using organic solvents. Therefore, it is perfectly suited for the production of heat sensitive nutritional supplements and APIs and can be considered as a green technology. Finally, yet importantly, the electrospinning technique involves a very compact and relatively cheap instrument that does not require special

conditions to maintain and which occupies a small space in the laboratory. The process is simple, fast, straightforward, and requires only a small amount of starting material. All these advantages make electrospinning technology relatively cost-effective.

Today, one of the leading research areas in electrospinning is to develop its industrial usage, due to its great potential in different applications. On the other hand, the industrial upscaling of electrospinning is still a challenging issue with a lot of space for further improvements. One of the main drawbacks of electrospinning is the low production rate. In academic research, electrospinning is performed with volumes in the range of millilitres and the production rate is several $\text{g}\cdot\text{h}^{-1}$. However, the production rate can be improved up to several $\text{kg}\cdot\text{h}^{-1}$ and is mainly based on the modification of the polymer injection system: 1) the introduction of multi-spinneret components (**Figure 1.10**) and 2) the development of free surface electrospinning methods (**Figure 1.11**) [95]. The multi-spinneret system can produce $1\text{ kg}\cdot\text{h}^{-1}$ for a typical spacing of 1–3 nozzles per cm^2 [96]. However, one of the main drawbacks of the multi-spinneret system is the alteration of the electric field (non-uniform electric field) profile due to the presence of another electrospinning jet nearby [95, 96]. Thus, if lab experimental studies, where a single spinneret is used, show good fibre production, transferring the lab processing parameters to industry may alter the fibre properties. Many approaches have been proposed to overcome this problem, including introducing a secondary electrode or an additional auxiliary electrode with charge of either the same polarity as the electrospinning jet or with opposite polarity, or increasing the collector dimension. However, all these modifications require additional studies and time to optimise the processing parameters, and operational and quality control to prevent nozzle clogging. The free surface electrospinning method is a very promising approach that can generate fibres two or three orders of magnitude higher than spinneret based methods. The principle of this method is based on generating jets from the rotating cylinder that are periodically dipped into the polymer solution, which is connected to a high voltage. The cylinder rotates slowly, at about 2.5 – 18 rpm, and the downward and upwards movement of the cylinder results in a thin layer of polymer solution on its surface. Upon applying a high voltage, an enormous number of jets are generated from that thin layer of polymer and collected conventionally on a collector [96]. Variations of an industrial electrospinning set up have been developed and are available commercially from Inovenso Ltd. and Elmarco Co.

Another drawback related to solvent electrospinning is the solvent residues that can be trapped inside the produced nanofibres. Therefore, novel formulations that can be processed by aqueous solutions should be developed [95].

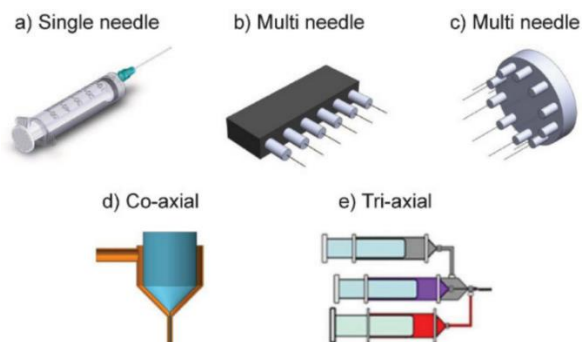


Figure 1.10. Schematic illustration of possible types of electrospinning spinneret. Adapted from [95].

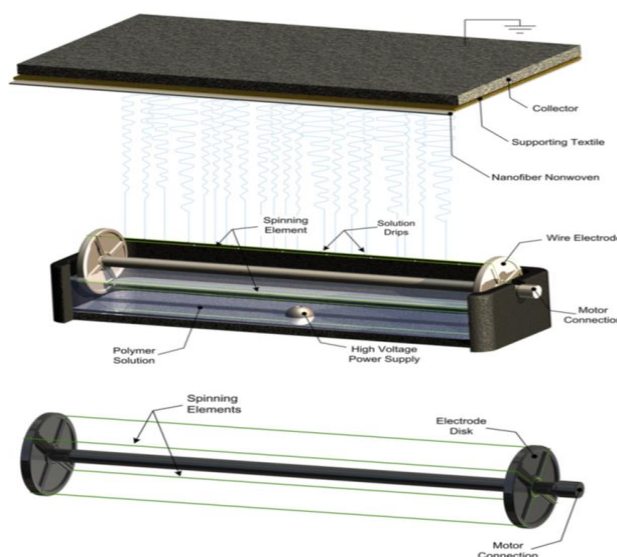


Figure 1.11. Schematic illustration of a free surface electrospinning apparatus. Adapted from [97].

Processing parameters influencing electrospinning

As with any other technological processes that are controlled by different parameters, the electrospinning process also involves many parameters that have an impact on the resultant fibres. Depending on the process parameters, the morphology of the end fibres might be varied, ranging from beaded fibres to porous nanofibres.

The primary aspects that affect fibre formation include:

- *Choice of electrospinning set up* (horizontal or vertical, one electrode set up or two electrode set up, type of collectors, single needle electrospinning or coaxial needle electrospinning);
- *Choice of materials* (type of polymer and its concentration and molecular weight, solution viscosity and conductivity, type of solvent, additional substances such as inorganic salts, surfactants, nanoparticles, drugs, carbon nanotubes, catalyst, liquid crystals, enzymes, emulsions);
- *Choice of spinning parameters* (feeding rate, distance between the needle and the collector, applied DC voltage, diameter of spinneret orifice) [98].

In order to obtain the fibres with the desired properties, the following are the key characteristics of the solution and the operational parameters:

- Suitable solvent to dissolve the polymer;
- The vapour pressure of the solvent should be appropriate so that it evaporates quickly enough to allow fibre formation before it reaches the target, but not too quickly to harden fibres before they reach the nanometre range;
- The viscosity and surface tension of the solvent should be neither too large to prevent jet formation nor too small to allow flowability of the polymer solution;
- The power supply should be sufficient to overcome the viscosity and surface tension of the polymer solution to form a stable jet;
- The distance between the tip of the needle and collector should be large enough to allow the solvent to evaporate, but not too large as this could lead to low yield. A small distance creates sparks between the electrodes;
- The optimum humidity is considered to be about 30–40 %, as the high humidity causes the formation of pores on the fibre surface and it is used successfully in the formation of porous nanofibres due to controllability [99].

Choice of electrospinning set up

There are two main electrospinning set ups used currently: vertical and horizontal. There is no difference on the resulting fibre morphology between the vertical and horizontal set up [91]. Another type of electrospinning set up was introduced by R. Jaeger et al. [100], which is the one electrode set up and two electrode set up. The one electrode set up is traditional electrospinning set up with one high voltage source, while the two electrode set up utilizes two high voltage sources, one conventional and the second a ring electrode, as shown in **Figure 1.12**. The second electrode in the two electrode set up is used to reduce the electrostatic field at the capillary tip. In the study described in **Chapters 3–4**, we used a horizontal one electrode set up.

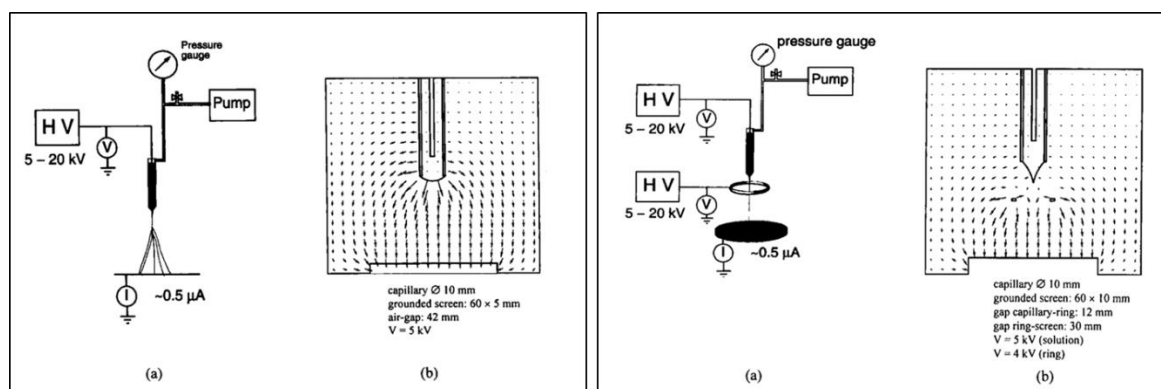


Figure 1.12. One electrode set up (left) and two electrode set up (right): a) experimental layout, b) electrostatic field. Adapted from [100].

There are more than 10 different types of collector designed nowadays and a comprehensive review on this aspect of electrospinning can be found elsewhere (**Figure 1.13**) [90]. In this project, the stationary plate and rotating drum collectors were used.

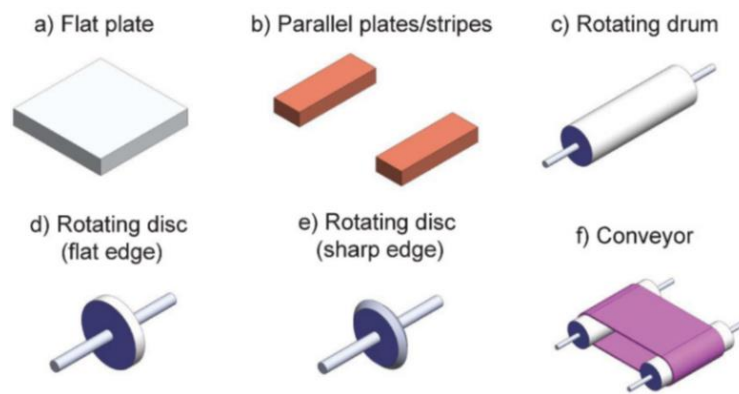


Figure 1.13. Schematic illustration of the main possible types of electrospinning collectors. Adapted from [95].

Choice of materials

There are many different types of polymer used in electrospinning. The selection of the material depends on the application, as some materials such as polymer and polymer nanofibre composites can be electrospun directly. For example, natural polymers such as chitosan, gelatine, collagen and cellulose, synthetic biodegradable polymers – poly (lactic acid) (PLA), poly (ϵ -caprolactone) (PCL), poly (ethylene oxide) (PEO), and copolymers, such as poly (L-lactide-co-caprolactone) (PCLA) and poly (lactic-co-glycolic acid) (PLGA). Other materials such as ceramics and carbon nanotubes require post processing after electrospinning. Therefore, it is important to have a basic understanding of the different types of materials to choose appropriate electrospinnable materials for specific applications [91, 101].

The type of the materials influences *the solution properties*, which play a significant role in the electrospinning process and fibre diameter and morphology as they are responsible for *the surface tension, viscosity and charge density of the solution*.

The viscosity of the solution affects the morphology of the obtained nanofibres. When the viscosity of the polymer solution is high, the beads become bigger and the spherical beads change to a spindle-like morphology, where the average distance between the beads are longer and the fibre diameter larger. Two polymers, namely, PEO dissolved in ethanol-to water solution and cellulose acetate (CA) dissolved in 2:1 acetone/DMAc

(dimethylacetamide), showed different viscosity ranges for producing smooth nanofibres without beads. For PEO in an ethanol-water solution the viscosity range was between 1–20 poises, and droplets were formed when the viscosity level was below 1 poise, where the viscosity range is too low. Above 20 poises, electrospinning was not possible because of flow instability caused by the high cohesiveness of the solution [102]. As for electrospun CA dissolved in acetone/DMAc, the acceptable viscosity range was between 1.2 and 10.2 poises. Similarly, below 1.2 poises, droplets were formed because of the low viscosity; the fluid jet broke up into droplets [103]. The lower the molecular weight of the polymer, the higher the solubility of the polymer; however, viscosity, flexibility and the degree of molecular chain entanglement increases with the increase of molecular weight. Therefore, a minimum concentration of the polymer is required to have the highest possible percentage of polymer while still having low viscosity to allow jet formation. Below this critical value a different process called electro spraying is taking place, instead of electrospinning or beaded fibres being formed [104].

The morphology of the fibres can be changed by changing *the surface tension* of the solution too. For example, changing the surface tension of the PEO solution by adjusting the ethanol-to-water ratio in the solvent system changes the fibre morphology from beaded to smooth nanofibres. The surface tension coefficient was between 35 and 55 dyne/cm, and above 55 dyne/cm beaded fibres were formed [89]. Similarly, experiments with cellulose acetate showed that the smooth fibre forming surface tension coefficient was 26–27 dyne/cm. A higher surface tension, namely 30 dyne/cm, produces beaded nanofibres [103]. Doshi and Reneker [105] also highlighted that fibres without beads could be obtained by reducing surface tension. However, this approach should be applied with caution, because it is not necessarily the case that a lower surface tension of a solvent will always facilitate smooth fibre formation. For example, Liu and Hsieh [103], in their work with CA dissolved in acetone, DMAc and a mixture of both solvents, demonstrated that no fibres but only beads were obtained for a sample dissolved only in DMAc and short fibres with diameter of around 1 μm and beads on the string morphology were obtained for a sample dissolved only in acetone, although their surface tension coefficient was 32.4 dyne/cm and 23.7 dyne/cm respectively. However, they could yield CA nanofibres without beads when they used the mixture of two solvents with a ratio of 2:1 acetone:DMAc; here the surface tension was 26–27 dyne/cm. The

variation in polymer concentration from 15 wt. % to 25 wt. % does not change the fibre morphology and surface tension, confirming that the polymer concentration has no effect on surface tension. Very smooth and uniform diameters of around 700 nm were obtained with a solvent ratio of 10:1 acetone:DMAc and 15 wt. % of CA [89]. Conversely, the study of the effect of diameter of the needle recommends increasing the surface tension [104].

Net charge density depends on the applied electrostatic field and to a lesser extent is influenced by the conductivity of the solution. If we increase the net charge density, the beads become smaller, more spindle-like and the fibre diameter also decreases. For example, Zong et al. [106] found that adding 1 wt. % salt into biodegradable poly(D,L-lactic acid) PDLA polymer solution will result in a uniform fibre diameter ranging from 200 nm to 1000 nm, where a no beads-on-string structure was formed. They suggested that the addition of salts increases charge density on the surface of the erupted jet during electrospinning, bringing more electric charges that are carried by the spinning jet. With the increase of charges carried by the jet, the elongation forces imposed to the jet increase under the electrical field. This results in smaller beads and thinner fibre diameter. The conductivity of the solution can be improved by using organic acid as the solvent too. Huang et al. [107] used formic acid as the solvent and a small amount of pyridine to dissolve the nylon and could obtain ultrathin (3nm) nylon fibres.

Fong et al. [102] studied all three parameters on PEO fibre formation and reported that non-beads fibres were obtained with higher viscosity. A higher net charge density was responsible for not only non-beaded fibres but also the formation of thinner fibres. Higher surface tension favours the formation of beaded fibres, hence the reduced surface tension produces fibres without beads. The viscosity depends on the polymer concentration and molecular weight, while the surface tension depends on the polymer and the solvent types.

Choice of spinning parameters

A crucial element in the electrospinning process is *the applied voltage* to the solution. Fibre formations occur only after reaching the threshold voltage to induce the necessary charges on the solution with the electric field, which initiates the electrospinning process [91]. Deitzel et al. [108] studied the influence of electrical potential on an example of PEO nanofibres. They

represented that with the increase of the electrical charge the nanofibres became beaded and rougher (**Figure 1.14**). Whereas, Reneker and Chun [109] using the example of PEO demonstrated that there is not much impact of the electric field on fibre diameter. However, Zhang et al. [110] and Demir et al. [111] suggested that with the higher voltage there is more polymer ejection, which facilitates the formation of a larger fibre diameter. On the other hand, Larrondo and Manley [112-114] observed a decrease in fibre diameter by approximately half by doubling the applied electric field. Similarly, other authors have reported that an increase in the applied voltage increases the coulomb force in the fluid jet as well as the electric field and this favours the narrowing of fibre diameter and also the rapid evaporation of solvent from the fibre [91]. However, other researchers have reported that at higher voltage there is a greater probability of beads formation [108, 111, 115-122].

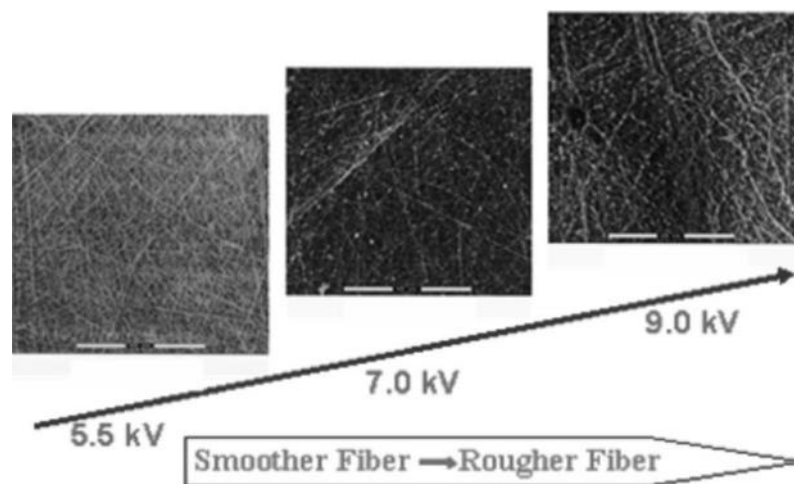


Figure 1.14. SEM images of PEO nanofibres electrospun at different electrical potentials. Adapted from [89].

The feeding rate of the polymer solution from the syringe is one of the important factors influencing the jet velocity and the material transfer rate. Low flow rates are more desirable as they allow enough time for evaporation. High feed rates result in beaded fibres because there is not enough time for solvent evaporation. Therefore, there should be a minimum flow rate of the electrospinning solution. On the example of polystyrene (PS) it has been observed that the fibre diameter and the pore diameter increases with an increase in the polymer flow rate [91]. Megelski et al. [116] and Zong et al. [106] investigated the relationship between the solution flow rate and fibre morphology and size. They showed a formation of beaded fibres

with a high flow rate due to the unavailability of a proper drying time before reaching the collector [91].

The distance between the tip of the needle and the collector has no significant impact on fibre morphology. This has been observed with the electrospinning of (polyvinyl alcohol) PVA [110], gelatine [123], and poly(vinylidene fluoride) (PVDF) [124]. However, there should be an optimum distance between the tip to the collector to allow enough time for the solvent to evaporate from the nanofibres [91]. Electrospinning of a silk-like polymer with fibronectin functionality resulted in a flatter fibre with a close distance and rounder fibres with an increase in distance [115]. The effect of the tip of the needle to collector distance was investigated by other researchers too and they found that distances that were either too close or too far fabricated beaded fibres [117, 123].

The diameter of the needle orifice also has an impact on fibre diameter. A larger needle diameter may cause clogging at the tip of the needle [118]. This is because of the surface tension, which can be increased by reducing the radius of the droplet by decreasing the diameter of the needle. Increasing the surface tension at the tip of the needle, while keeping the electrostatic field strength at a constant rate, serves to decrease the initial acceleration of the jet and the average velocity. This results in increasing the flight time from the tip of the needle to the collector. Thus, fibres with a smaller diameter and narrower size distribution can be fabricated with a smaller diameter of the needle. However, the droplet may be difficult to form if the diameter of the needle is too small, depending on the surface tension of the solution [104]. Yamashita et al. [125] demonstrated that there is no correlation between the nozzle diameter and the fibre diameter.

1.6.1 Emulsion and coaxial electrospinning

Emulsion electrospinning (EE) is similar to conventional electrospinning except the polymer solution contains an emulsion, either water-in-oil (w/o) or oil-in-water (o/w). EE enables the production of core-sheath nanofibres with desired functionalities, whereby two different APIs can be delivered at two different release rates. The mechanism of the formation of the core-sheath structure of emulsion is mainly due to de-emulsification. A number of researchers have suggested different mechanisms of the formation of the core tube: emulsion droplets

break up [126] and stretching and elongation [127, 128] induced by high voltage are examples reported in the literature. The oil phase is usually composed of amphiphilic polymers (poly(ethylene glycol)-poly(L-lactic acid) (PEG-PLA) diblock copolymer [127], poly(ethylene-co-vinyl acetate) [129], or any spinnable polymer dissolved in organic solvent immiscible with water phase such as chloroform, dimethylformamide, dichloromethane (DCM) or toluene and a water phase is comprised of hydrophilic polymers, with PEO and PVP being the most commonly used polymers [130, 131]. However, liquid oils were also incorporated in fibre by means of EE, but this fact is scarcely reported in the literature. For example, Angeles et al. [126] first reported successful electrospinning of oil-in-water (o/w) emulsion using 7 wt. % PEO, dissolved in water as a continuous phase, and mineral oil as a dispersed phase (2.5 wt. %), and Pluronic P105 (BASF) (0.5 wt %) as a surfactant. The optical microscope study showed that the produced fibres contain oil droplets within them and the diameter of the fibres was mostly less than 2 μm . Then, Kriegel et al. [132, 133] and Camerlo et al. [134] reported encapsulation of an antimicrobial essential oil, namely eugenol, and a highly volatile fragrance, namely (R)-(+)-limonene, in PVA nanofibres by means of EE. Moomand and Lim [135, 136] encapsulated fish oil (30 w/w %) in zein fibres using ethanol-isopropanol as a solvent (good oxidative stability for 14 days); however, the current production method of zein is costly which makes it an uneconomical material for food application [137]. Recently, García-moreno et al. [137, 138] encapsulated fish oil (1.5-5 w/w %) in nanofibres using EE. However, the first experiment, where they used PVA polymer as the continuous phase, was not successful, as although fish oil was encapsulated successfully in fibres as small droplets, the oxidative stability test showed the inability of the PVA fibres to protect the fish oil against oxidation. The authors concluded that PVA has trace metals, e.g. Fe, which catalysed lipid oxidation [137]. In the second experiment, when they used pullulan, the oxidative stability of the fish oil was superior for the sample prepared with emulsified neat oil compared to the sample prepared with emulsified fish oil [138].

Coaxial electrospinning is also another way of producing core-sheath structured nanofibres, although, unlike EE, it requires a special coaxial needle (**Figure 1.10**) and an extra solution pump. The configuration of the coaxial electrospinning setup is shown in **Figure 1.15**. As in conventional electrospinning, different types of collector can be utilized although here a rotating collector is illustrated.

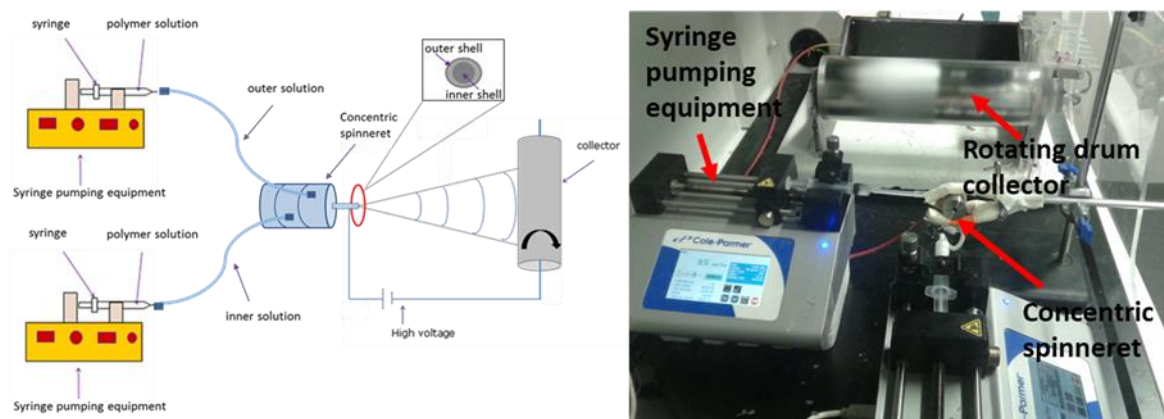


Figure 1.15. A schematic representation of coaxial electrospinning set-up with a rotating collector (left). The lab coaxial electrospinning set-up used in this study (right).

Coaxial electrospinning has some advantages over EE. In coaxial electrospinning, a material constituting the core solution does not need to be electrospinnable, as good spinnability of the outer solution is important [128, 131]. Two different polymer solutions are ejected through the concentric capillary spinneret; the core solution is enclosed in the outer solution producing core-sheath structured nanofibres. Based on the reasonable selection of the core-sheath constituent, biphasic drug release can be obtained where an immediate drug release is followed by a sustained release. Such systems have a wide application to deliver non-steroidal anti-inflammatory drugs (NSAIDs), antihypertensive, antihistaminic and anti-allergic agents [139].

1.7 Structured oil systems

Delivery systems for the encapsulation of micronutrients can be classified into four main groups according to the material used to formulate the delivery systems: protein-based delivery systems, lipid-based delivery systems, carbohydrate-based delivery systems, and mixed systems (**Figure 1.16**) [140].

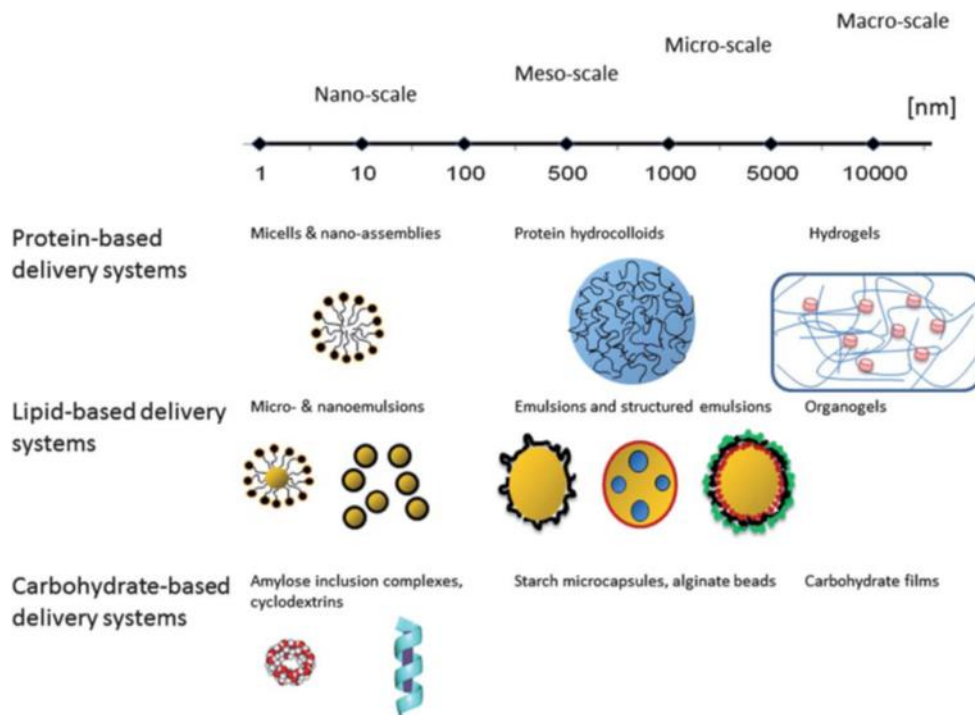


Figure 1.16. Commonly used food-grade delivery systems, as classified by Benshitrit et al. Adapted from [140].

Lipid-based delivery systems are the most efficient carrier system for the incorporation of lipophilic and hydrophilic ingredients and they constitute a considerable number of most food and pharmaceutical products. A lipid-based delivery system can be constructed as solid lipid nanoparticles, as self-micro-emulsifying systems and as micro- and nanoemulsion or structured emulsion systems. They provide good chemical protection for sensitive vitamins, better stability and controlled release with a wide range of materials and the most simple techniques are used to create them [140, 141].

Microemulsion or structured emulsion systems are defined as thermodynamically unfavourable systems; however, their kinetic stability can be improved by selecting the right emulsifiers and viscosity modifiers. Small molecule surfactants, polysaccharides, proteins, protein-polysaccharide complexes and amphiphilic biopolymers are emulsifiers which form an interfacial membrane, reducing interfacial tension by rapidly adsorbing at the oil-water interface [142]. Protein-polysaccharide complexes tend to form more stable emulsions, particularly o/w emulsions, in reaction to environmental stresses such as pH variation, thermal processing, freezing and dehydration. This property is widely used in the food and

pharmaceutical industries to produce a solid form of emulsions, which are the most preferable formulation, by freeze or thermal drying of stable emulsions. Proteins themselves are good emulsifiers; being surface active, they can adsorb at fluid interfaces by forming a thin and electrically charged layer. Thus, they prevent droplet aggregation by an electrostatic repulsion mechanism. Proteins have polar and non-polar amino acid residues. At the oil-water interface, non-polar residues orient in the hydrophobic phase and form a viscoelastic adsorbed layer. The extent of adsorption of proteins is related to the structural properties of the proteins, surface hydrophobicity and charge density. Mixing or deposition of polysaccharide on top of an adsorbed layer of proteins ensures better stability and resistance against environmental stresses [143, 144]. They can form covalent [145] and non-covalent interactions, mainly through hydrogen bonding, electrostatic interactions, steric exclusion, and hydrophobic interactions at the oil-water interface. Polysaccharides are the polymer of monosaccharides and have a large number of reactive groups. They can adsorb onto the surface of proteins by attractive electrostatic interaction, or compete with proteins to adsorb at the oil-water interface because of the repulsive interaction of two uncharged or similarly charged polymers [143, 144]. The strength of polymer interactions may switch from net attractive to net repulsive upon varying the pH and/or ionic strength. At $\text{pH} < \text{pI}$ of protein solution a strong attractive electrostatic complex forms with positively charged proteins and negatively charged polysaccharides. Weaker reversible complexes form when proteins $\text{pH} > \text{pI}$ and $\text{pH} \approx \text{pI}$, representing a net negative and nearly zero charge, respectively [144, 146].

In this study, we also created a soft solid structured oil system (SOS) made from protein and polysaccharide using a freeze drying technique. The obtained SOS can hold a large amount of oil and can be used as a carrier to deliver highly water-soluble, poorly water-soluble and oil-soluble drugs or nutrients.

The protein and polysaccharide that were used in this study to create an SOS were gelatine and xanthan gum (G/X). Being surface active, gelatine (G) adsorbs at the oil-water interface and xanthan gum (X) is non-surface active and forms an interfacial complex with gelatine through attractive electrostatic interactions and/or hydrogen bonding. They can be introduced to the oil continuous phase simultaneously (co-adsorption) or sequentially (layer-by-layer adsorption) forming a viscoelastic or tightly adsorbed layer stable against thermal

processing, freezing and dehydration [147]. However, Patel et al. in their research found no difference in the sequence of addition on product quality [147].

The drying technique used in this study was freeze drying. Freeze drying or lyophilisation is a widely used technique in the food and pharmaceutical industry to remove the water content of heat sensitive products. A freeze-dried formulation provides very low moisture content, therefore, improved long term stability and storage. In addition, automated processing with less human involvement, easy handling and shipping of the end product are advantageous elements of the freeze drying technique. However, the length of processing time, ranging from one day to one week, makes the technique relatively costly.

The freeze drying process consists of three stages: *freezing*, when water forms ice; *primary drying or ice sublimation*, when the chamber pressure goes down below the vapour pressure of ice and *secondary drying*, involving the complete removal of the rest of the ice from the solute, when the temperature is elevated and the pressure is very low. In mass production, the control of ice nucleation can significantly reduce the drying duration [148]. The impact and methods of control ice nucleation are discussed elsewhere [149]. We did not study the effect of ice nucleation and, therefore, it is not covered here.

1.8 Motivations and aims of the study

Despite tremendous progress in correcting nutritional deficiency in the global population over the last century, an estimated 3.5 million lives are lost each year due to undernutrition, more specifically, deficiency in essential nutrients, and most of the casualties are children and pregnant women (data from 2008) [150]. Over 100 million children are still vitamin A deficient [151], resulting in about 0.8 million annual deaths in total [152], while up to 4–5 billion people may suffer from iron deficiency [153] accounting for 841,000 deaths and 35 million disability-adjusted life years lost [154]. Meanwhile, 30 per cent of households are not consuming iodized salt, leaving 41 million newborns at risk of brain damage and impaired learning capability [151]. In addition, over 8 million children under five years of age die each year from illnesses, such as diarrhoea, malaria, HIV/AIDS (Acquired Immune Deficiency Syndrome), tuberculosis and pneumonia, due to the lack of medicines suitable for use by children, yet effective

treatments exist for most of these diseases. Even if the correct dosage forms do exist for children, there is a lack of access to them [155]. For comparison, cancer is the second leading cause of death globally, with 9.6 million deaths in 2018. However, while cancer involves many uncontrollable risk factors causing the cancer burden and encompasses one or more modalities to treat the disease, such as surgery, radiotherapy, and chemotherapy [156], nutrient deficiency can be prevented and/or corrected by simple nutrient intervention and over 8 million children's lives can be saved by simply improving the dosage form and making it accessible. One of the key challenges remaining today are the lack of cost-effective delivery mechanisms [151] to provide an adequate amount of essential nutrients and medicines for children and other vulnerable groups of population, especially for those living in developing countries. There is a scarcity of research regarding the paediatric dosage form. Therefore, the primary aim of this study was to address the needs of paediatric populations and make a contribution into the research area in the development of paediatric dosage forms, i.e. formulate oral delivery systems capable of delivering multiple micronutrients and which can be potentially adopted for delivering any other water-soluble and poorly water-soluble APIs.

Thus, the objective of this study are 1) to design an oral delivery system that can be used in two separate contexts: the delivery of drugs or the delivery of nutrients; 2) to investigate various processing parameters to improve the characteristics of delivery systems; 3) to ensure the development of safe, effective, cheap and easy administered dosage forms with sustainable mass-scale production technology. The following steps were undertaken to achieve them:

1. A fast-dissolving orodispersible film loaded with KIO_3 as an alternative solid form of iodine delivery was prepared using emerging electrospinning technology. All processing parameters were investigated in order to identify the effect of each processing parameter on the final product and to select the optimum processing parameters to obtain an effective delivery system for iodine. Characterization of the end product was performed to ensure the stability and effectiveness of the dosage form. The results are given in **Chapter 3**.
2. This study explored emulsion and coaxial electrospinning to produce core-sheath or oil-containing fibres for dual nutrient delivery, i.e. water-soluble nutrient, KIO_3 and fish

oil and a number of vegetable oils that have essential nutrients. The results are given in **Chapter 4**.

3. The study investigated a novel structured oil system capable of holding large amounts of oil prepared by means of a freeze drying technique. The research studied the effect of processing parameters on the formation of structured oil systems and characterized the end product using analytical techniques to understand the oil holding capacity and ensure the stability of the system. Dissolution testing was performed to assess the applicability of the system for delivery of highly water-soluble API. The results are given in **Chapter 5**.

2 Chapter 2. Materials and Experimental Methods

2.1 Introduction

This chapter provides detailed information regarding the physicochemical properties of the materials used in this study. Following this, the detailed sample preparation methods and characterization methods used throughout the project along with their working principles are discussed.

2.2 Materials

Table 2.1 represents information regarding the grades and suppliers of all chemicals and materials used in this study. All reagents and substances were employed without further purification.

Table 2.1. List of sources, chemicals and materials used in the study and their key physicochemical properties as highlighted by the manufacturer (taken from manufacturer data sheets).

Substance	Source	Description
Potassium iodide (KI)	Sigma-Aldrich, UK	ACS \geq 99%
Potassium iodate (KIO ₃)	Sigma-Aldrich, UK	ACS 99.5%
Sunflower oil	Sigma-Aldrich, UK	–
Flaxseed oil	Biona, UK	Virgin cold press
Olive oil	Sigma-Aldrich, UK	Ph.Eur.
Fish oil (liver oil from <i>Gadus morrhua</i>)	Sigma-Aldrich, UK	Ph.Eur.
Squalene oil	Sigma-Aldrich, UK	\geq 98%
Ketoconazole	Afine Chemicals Ltd., China	–
Metoprolol succinate	Colorcon Ltd., UK	–
Poly (ethylene oxide)	Sigma-Aldrich, UK	3×10^5 g/mol (PEO 300K)

(PEO)		6×10^5 g/mol (PEO 600K)
Polyvinyl pyrrolidone (PVP)	Sigma-Aldrich, UK	1×10^6 g/mol (PVP K90) [157]
TPGS (Kolliphor® TPGS)	BASF, Germany	–
Gelatine type B (bovine skin)	Sigma-Aldrich, UK	50,000 – 100,000 g/mol
Xanthan gum	Sigma-Aldrich, UK	4×10^6 – 12×10^6 g/mol
Hydroxypropyl methylcellulose (HPMC K4M – Methocel® K4M)	Colorcon Ltd., UK	95,000 g/mol [158] 86,000 g/mol [159]
Methylcellulose (MC)	Dow Chemical Co., UK	–
PEG-20 sorbitan monolaurate (Tween 20)	Sigma-Aldrich, UK	–
Sorbitan monooleate (Span 80)	Sigma-Aldrich, UK	–
Sodium chloride (NaCl)	Sigma-Aldrich, UK	ACS 99%
Sulphuric acid (H ₂ SO ₄)	Sigma-Aldrich, UK	ACS 95.0–98.0%
Coumarin 6	Sigma-Aldrich, UK	98%

2.2.1 Nutritional supplements (KI and KIO₃)

Potassium iodide (KI) is a chemical compound made up of 76% of the halogen iodine and 23% of the alkali metal potassium by weight [160]. It is considered to be a relatively unstable compound; on long exposure to air, light and moisture, potassium iodide becomes yellow due to the oxidation of iodide to iodine [161]. KI has many applications, including organic synthesis, photography and biomedical research [162]. In the pharmaceutical and food industries it is used as medication, a dietary supplement and as a source of iodine in salt iodization. As a medication, KI is used to treat dermatoses (300 mg 3 times daily followed by weekly increases as tolerated), thyrotoxicosis (250 mg 3 times daily as a Lugol's solution or saturated solution of KI) [163, 164], to protect against radiation (130 mg single dose) [165], as an expectorant (100 mg/5 ml 3–4 times daily) [166, 167] and as an antiseptic agent [168]. Reported uses for KI for inflammatory dermatoses and the related pharmacology, mechanism of action, contraindications and adverse effects of KI are reviewed by Sterling and Heymann [160]. As a supplement it is given on a daily basis to pregnant and lactating women, and to children less than 2-years old either alone or in combination with other minerals and vitamin

supplements so the total iodine intake meets the recommended nutrient intake of iodine per day [169]. In this study, KI was first selected as a source of iodine to be delivered by oral formulations for treating iodine deficiency in children (**Chapter 3**).

Potassium iodate (KIO_3) is a chemical compound made up of K^+ ions and IO_3^- ions in a 1:1 ratio. It undergoes five phase transitions as a result of temperature change at atmospheric pressure (**Appendix 4**). At room temperature phase III, it has a triclinic structure (P1) with a very pronounced pseudo-rhombohedral symmetry [170, 171]. KIO_3 has greater stability and a longer shelf life than KI and, therefore, is used as an alternative to KI for iodination of table salt in areas with severe climatic conditions [172]. Potassium iodate, according to the EU Member States legislation which was entered into force in July 2002, is a permitted source of iodine in iodine containing supplements [173]. It is also used in bread baking as a fast acting oxidant [174, 175] and in iodination of irrigation water [176, 177]. As medication, it is also used as in the case of KI for radiation protection (170 mg single dose) [165]. In this study, KIO_3 was subsequently selected as a more stable iodine source than KI (**Chapter 3**).

The physicochemical properties of KI and KIO_3 are presented in **Table 2.2**.

Table 2.2. Physicochemical properties of KI and KIO_3 , taken from [178, 179] and [180, 181], respectively.

Property	KI	KIO_3
IUPAC name	Potassium iodide	Potassium iodate
Chemical formula	KI	KIO_3
Molecular weight	166.00 g/mol	214.00 g/mol
Physical state	White crystalline solid	White crystalline powder
Odour	Odourless	Odourless
Specific density	3.1 g/cm ³	3.89 g/cm ³
Boiling point	1330 °C (sublimes)	–
pH	7–9 (saturated solution)	–
Solubility	–	Soluble in KI solution; insoluble in alcohol, liquid ammonia, nitric acid
Solubility in water	1280 mg/ml (0 °C) 1400 mg/ml (20 °C) 1760 mg/ml (60 °C) 2060 mg/ml (100 °C)	4.74 g/100 ml (0 °C) 9.16 g/100 ml (25 °C) 32.3 g/100 ml (100 °C)
Melting point	681 °C	560 °C (decomposes)

2.2.2 Oils

All the oils used in this study were selected due to their positive effect on human health.

Sunflower oil

Sunflower oil is a fatty oil obtained from the seeds of the sunflower. Sunflower oil's chemical structure is depicted in **Figure 2.1**. The viscosity is 47.4 cSt (at 20 °C ±2) [182].

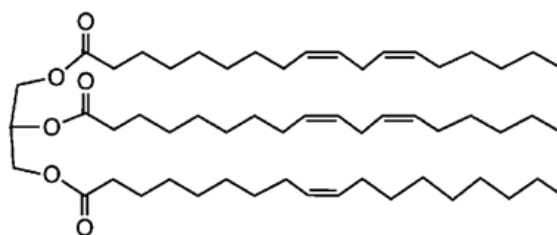


Figure 2.1. Chemical structure of sunflower oil.

Sunflower oil has various applications on a domestic and industrial level. In some countries, sunflower oil is a common edible oil, where it is used as a salad dressing and cooking oil. In industry, sunflower oil is used as a frying oil, a health food formulation [183] and in the manufacture of mayonnaise and oil-based dressings due to its comparatively high oxidative stability [184, 185]. In pharmaceutical formulations, it is used as a diluent, emollient, emulsifying agent, solvent and tablet binder. Therapeutically, sunflower oil is used for parenteral nutrition to provide energy and essential fatty acids, and in intramuscular injections because it does not induce tissue damage [157]. In this study, sunflower oil was used as a model oil for the oil phase in o/w emulsion to produce core-sheath nanofibres (**Chapter 4**) and within the SOS (**Chapter 5**).

Flaxseed oil (Linseed oil)

Flaxseed oil or *Linseed oil* is a fatty oil obtained by cold expression from the ripe seeds of flax [186]. The viscosity is 51.2 cSt (at 20 °C ±2) [182]. Flaxseed oil has a low level of saturated fatty acids (9%), a moderate level of monosaturated fatty acids (18%) and high levels of polyunsaturated fatty acids (PUFA) (73%) [187]. Oils rich in PUFAs have beneficial effects on human health [188] and a wound-healing action [189]. However, one of the concerns

associated with oils having a high content of PUFAs is their susceptibility to oxidation, resulting in the production of off-flavours and toxic peroxides on heating [190, 191].

Flaxseed oil is widely used in the pharmaceutical and food industry because it contains the richest vegetarian source of EFAs: linoleic acid (LA) ($\omega - 6$ fatty acid) and α -linolenic acid (ALA) ($\omega - 3$ fatty acid). It is used in pharmaceutical and food formulations in the form of neat oils, stable emulsions, microcapsules [192] and micro- and nano-encapsulated powders [188, 190, 191, 193, 194]. In this project, flaxseed oil was used as a functional food ingredient for the oil phase of o/w emulsion to produce core-sheath nanofibres (**Chapter 4**).

Olive oil

Olive oil is a fatty oil obtained from the ripe drupes of olive by cold expression or other suitable mechanical means. The viscosity is 84.0 cSt (at 20 °C ± 2) [182]. It is slightly soluble in ethanol (95%), miscible with ether, chloroform, light petroleum (50–70 °C), and carbon disulphide [157].

The major groups of compounds that are ascribed to have nutritional and healthy values are monounsaturated fatty acids (MUFAs) and PUFAs, squalene, phytosterols, triterpenic acids and dialcohols, pigments, tocopherols, and polyphenols [195, 196]. In pharmaceutical formulations, olive oil has been used in enemas, liniments, ointments, plasters, topically applied lipogels, as oral capsules and solutions, as a vehicle for oily injections and targeted delivery systems, emulsions for use in pre-term infants and ear drops [157]. In the food industry, it is widely used as a cooking oil and salad dressing. In this study, olive oil was selected as a functional food ingredient for the oil phase of o/w emulsion to produce core-sheath nanofibres (**Chapter 4**).

Fish oil

Fish oil is a purified fatty oil obtained from the fresh livers of farmed cod [186]. The major contents of cod liver oil are presented in **Table 2.3**. The viscosity is 42.0 cSt (at 20 °C ± 2) [182]. Unfortunately, the unpleasant odour of fish oil, its low solubility in most food systems and high susceptibility to oxidative degradation of $\omega - 3$ PUFA, limits their use in the food and

pharmaceutical industry. However, encapsulation technology is commonly carried out to overcome these drawbacks [138, 197].

Table 2.3. Cod liver oil contents. EPA – eicosapentaenoic acid, DHA – docosahexaenoic acid. Adapted from [186].

Content	Percentage (%) and mass (μg)
Sum of the contents of EPA and DHA (expressed as triglycerides)	10.0%–28.0%
Vitamin A	50 IU (15 μg) to 500 IU (150 μg) per gram
Vitamin D ₃	maximum 50 IU (1.3 μg) per gram

Fish oil has numerous beneficial effects on human health due to its high concentration of ω – 3 PUFAs, particularly docosahexaenoic acid (DHA) and eicosapentaenoic acid (EPA), which have been documented to prevent many diseases [57-60, 198]. It also has been used as a source of vitamins A and D in the pharmaceutical industry. In the food industry, fish oil is used as a functional food ingredient and can be encapsulated in emulsions [199], liposomes [200], solid lipid particles [201], micro- and nano-particles [197, 202, 203], and nanofibres [137]. In this project, fish oil was selected as a functional food ingredient for the oil phase of o/w emulsion to produce core-sheath nanofibres (**Chapter 4**).

Squalene oil

Squalene oil is a linear triterpene hydrocarbon consisting of six isoprene units (**Figure 2.2**) [204, 205]. Squalene and its hydrogenated form, squalane, are approved for human use, as they are non-toxic. It is widely present in nature and is synthesized in all types of cells. In humans, it is present in sebum at approximately 13%. However, the highest source of squalene is shark liver oil (60 w/w %), while substantial amounts are also found in olive oil and olive leaves [204, 206]. It is a highly hydrophobic compound due to the hydrocarbon composition of the molecules [204]. In addition, squalene is not very stable due to its chemical structure and high degree of unsaturation, and it is therefore easily oxidized [206]. The viscosity is 15.9 cSt (at 20 °C \pm 2) [182].

Squalene oil has many applications in the pharmaceutical and food industry. In the pharmaceutical industry, it is used for numerous vaccine [207] and drug delivery emulsions,

because squalene facilitate solubilization, modified release, and cell uptake of drugs and adjuvants [204, 208, 209]. In addition, it has stability-enhancing effects and is biocompatible. The biological and pharmacological activities of squalene are reviewed elsewhere [204, 206, 210, 211]. In this project, squalene oil was selected as a functional food ingredient for composing the oil phase of o/w emulsion to produce core-sheath nanofibres (**Chapter 4**).

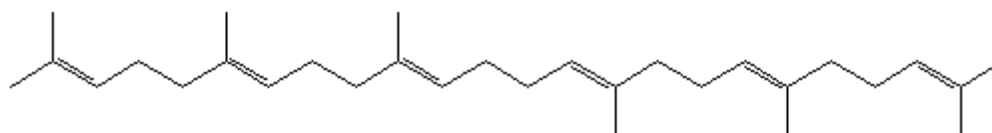


Figure 2.2. Chemical structure of squalene. Adapted from [204].

2.2.3 Model drugs

Ketoconazole

Ketoconazole is a broad-spectrum antifungal agent used primarily for the treatment of mucocutaneous fungal infections caused by the *Candida* species [212, 213]. The molecular weight is 531.431 g/mol [186]. The chemical formula is $C_{26}H_{28}Cl_2N_4O_4$ (**Figure 2.3**). It is an imidazole derivative and its structure presents two basic groups, a piperazine and an imidazole with pKa values of 2.94 and 6.51 respectively [212]. Thus, it readily dissolves in a solution with low pH rather than at higher pH [214]. Ketoconazole is rather lipid soluble, its octanol-water partitioning coefficient, log P, is 3.73 [215]. It is insoluble in water, soluble in methylene chloride and in methanol, and sparingly soluble in ethanol (96%) [186]. According to the BCS, ketoconazole is classified as a class II drug due to its high permeability and low aqueous solubility [216]. The melting point is between 148 °C and 152 °C [186].

Ketoconazole is administered topically (creams, shampoos, solutions). It has been reported to have a positive effect in the treatment of systemic blastomycosis, candidiasis, coccidioidomycosis, histoplasmosis, paracoccidioidomycosis, and tinea of skin and nails when given orally [216]. However, the drug was discontinued in Europe and Australia in 2013 due to the risk of serious hepatic side effects. In the US and Canada strict restrictions and cautionary advisements were added to the labelling of oral ketoconazole [217]. In this study,

ketoconazole was used as a model of a poorly soluble API incorporated in the oil phase of SOS (Chapter 5).

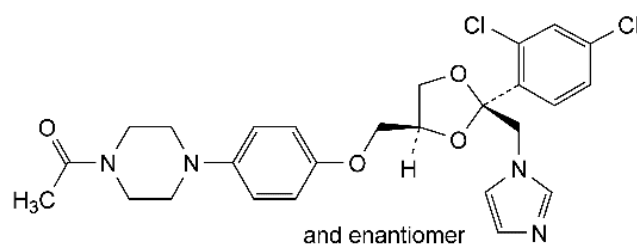


Figure 2.3. Chemical structure of ketoconazole. Adapted from [186].

Metoprolol succinate (MS)

Metoprolol succinate (MS) is a β_1 selective adrenoceptor antagonist used to treat high blood pressure, chronic heart failure [218], angina pectoris, arrhythmia [219] and reduce chest pain [220]. The chemical formula is $C_{34}H_{56}N_2O_{10}$ (Figure 2.4). The molecular weight is 652.826 g/mol. Metoprolol is a basic drug with a pKa of 9.6; however, the pH of 6 % w/v aqueous solution of its succinate drug is 7–7.6 [221]. The log P is 1.88. It is freely soluble in water (276 mg/ml at 37 °C [222]), soluble in methanol, slightly soluble in ethanol (96%), and practically insoluble in ethyl acetate [186]. The melting point is 135–137 °C [223–225].

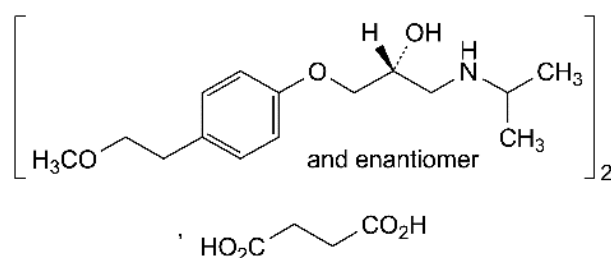


Figure 2.4. Chemical structure of metoprolol succinate. Adapted from [226].

MS is commonly formulated as an extended-release (ER) tablet [222–224, 227, 228] since it has a relatively short elimination half-life of 3–4 hours [219]. The ER tablet is dosed at 100 and 200 mg once daily [229]. MS is absorbed rapidly throughout most of the gastrointestinal tract when administered in the conventional dosage form [228, 230]; however, its absorption

mainly takes place in the duodenum and jejunum [231]. In this study, MS was used as a water-soluble model drug incorporated in the aqueous polymer phase of SOS (**Chapter 5**).

2.2.4 Excipients

Poly (ethylene oxide) (PEO K300 and K600)

PEO is a semi-crystalline, thermoplastic, hydrophilic and biocompatible polymer that is a non-ionic homopolymer of ethylene oxide [157, 232]. The structural formula is $[H(-OCH_2CH_2-)_nOH]$ (**Figure 2.5**) [157]. PEO has a range of molecular weights starting from 10^5 to 7×10^6 g/mol. The melting temperature (T_m) is 57–73 °C [233] and the T_g ranges from (-60 °C) to (-70 °C) [234]. It is freely soluble in water and organic solvents such as acetonitrile, chloroform, methylene chloride [157], ethanol and dimethylformamide [235], and insoluble in aliphatic hydrocarbons, ethylene glycol and most alcohols [157].

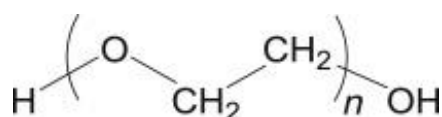


Figure 2.5. Chemical structure of PEO. Adapted from [236].

The main functional properties of PEO, as used in pharmaceutical and food technology, are its excellent mucoadhesive, lubricant and tablet binding properties. In addition, it can be used in coating and thickening agents, drug/nutrient delivery systems and as a food packing material for longer shelf life [237, 238]. Its E number is E1521 [239]. As a tablet binder, it can be used at concentrations of 5% to 85%. At low levels, it is an effective thickener. As a drug/nutrient delivery system, it can be used for immediate-, delayed-, or sustained-release matrix formulations because there is a good relationship between the swelling capacity and molecular weight of PEO, which is used as a guide to select the right molecular weight grades (**Figure 2.6**).

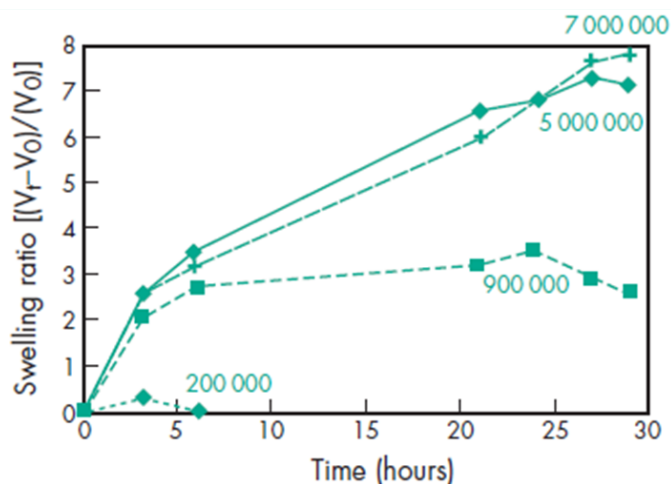


Figure 2.6. Swelling capacity of PEO tablets with d=28 mm in 300 ml water prepared with four different grades. Adapted from [157].

PEO was selected as a safe, inexpensive, water-soluble and good spinnable polymer to develop ultra-rapidly disintegrating orodispersible film in **Chapter 3** and in developing oil containing electrospun films in **Chapter 4**. The PEO used in this study has the molecular weight of 3×10^5 g/mol (PEO 300K) and 6×10^5 g/mol (PEO 600K) [157].

Polyvinyl pyrrolidone (PVP K90)

PVP is an amorphous synthetic polymer that has been regarded as essentially non-toxic and an official excipient in pharmacopoeia. One mono unit of PVP consists of 1-vinyl-2-pyrrolidone groups (**Figure 2.7**). It has been classified as an extremely hygroscopic substance (class IV) by Callahan et al. [240]. The hygroscopic nature of PVP is attributed to the electronegativity of the carbonyl group that can form hydrogen bonding with water [241]. There are different grades of PVP available in the market that are grouped according to their viscosity of 1% w/v aqueous solution, expressed as a K-value calculated via Fikentscher's equation. The higher the K-value, the higher the molecular weight and viscosity. PVP is soluble in water, acids, chloroform, ethanol (95%), ketones and methanol, and insoluble in ether, hydrocarbons and mineral oil. The melting temperature is 150 °C (softens) [157].

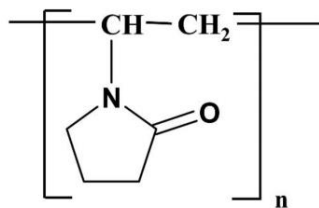


Figure 2.7. Chemical structure of PVP monomer unit. Adapted from [242].

PVP is one of the most frequently used polymers in the food and pharmaceutical industry. In the food industry, it is approved as a food stabilizer, E1201 [243]. In pharmaceutical technology, PVP is mainly used as a disintegrant, dissolution enhancer, suspending agent and tablet binder. In particular, PVP is widely used in a solid-dosage form due to its amorphous nature and high water solubility [157]. Recently, electrospinning has been introduced as one of the methods to produce PVP solid dispersion. However, only PVP K30 and K90 grades have been reported to be spinnable grades [244]. The typical concentration of PVP K30 and K90 required for fibre formation are 30–40 and 5–15% w/v solutions in ethanol, respectively [93, 245, 246]. In this study, PVP K90 was used in a blend with PEO to enhance the aqueous solubility of electrospun fibres as carriers for iodine delivery and for comparison purposes when the effect of polymer on the formation of inorganic nanocrystals was studied (**Chapter 3**).

D- α -tocopheryl polyethylene glycol 1000 succinate (TPGS)

TPGS is a water-soluble derivative of natural vitamin E that is formed by esterification of the acid group of crystalline D- α -tocopheryl acid succinate by polyethylene glycol 1000 [157]. As such its chemical structure comprises both a lipophilic alkyl tail (tocopherol succinate) and a hydrophilic polar head (polyethylene glycol) (**Figure 2.8**) exhibiting amphiphilic properties [247]. The hydrophile-lipophile balance (HLB) value is 13.2. TPGS, being one of the novel non-ionic surfactants, displays significant surface activity and can solubilize a variety of both water-soluble and water-insoluble compounds. It is completely miscible with water and also miscible with other surfactants, oils (soybean oil and medium-chain triglycerides), and cosolvents such as propylene and polyethylene glycols [48]. The physical form is a waxy solid at room temperature with a melting point of 37–41 °C [157] and a degradation temperature of 199.3 °C [248]. The molecular weight is 1513 g/mol [157].

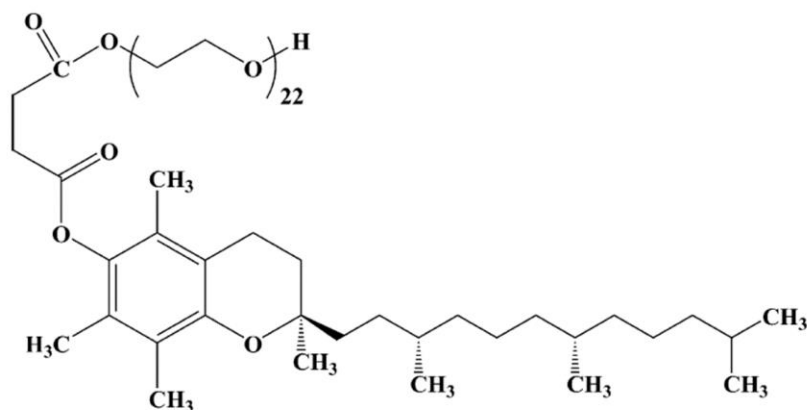


Figure 2.8. Chemical structure of TPGS. Adapted from [249].

TPGS is a GRAS (Generally Regarded As Safe) listed excipient [250] and an FDA approved pharmaceutically safe adjuvant [48]. It has many potential applications including as an absorption enhancer, antioxidant [249], emulsifying agent, granulation aid, ointment base, solubilizing agent, surfactant [250], suspending agent, tablet binder and as a water-soluble vitamin E nutritional supplement. It has been proven to have high drug encapsulation efficiency (up to 100%) [247], high cellular uptake *in vitro* and high therapeutic effects *in vivo* when used as an emulsifying agent for the synthesis of nanoparticles [49]. TPGS is readily absorbed in the GI tract and has an inhibitory effect on P-glycoprotein (P-gp). As a result, it enhances the cytotoxicity and oral bioavailability of anticancer agents such as doxorubicin, vinblastine and paclitaxel. Moreover, it can also act as an anticancer agent because it has the ability to induce apoptosis and develop a synergistic effect with other anticancer drugs [48]. TPGS could also enhance the absorption of vitamin D in chronic cholestatic liver disease of infancy and childhood, and provide a safe and effective form of vitamin E for preventing vitamin E deficiency during chronic childhood cholestasis and other forms of lipid malabsorption [248]. In this study, TPGS was used as an emulsifying agent and as a source of vitamin E nutritional supplement (**Chapter 4**).

Gelatine (Type B)

Gelatine is an inexpensive, non-irritating, biocompatible, and biodegradable protein [251] derived either by partial acid hydrolysis (Type A) or by partial alkaline hydrolysis (Type B) of animal collagen [157] with an average molecular weight of 65–300 g/mol [252]. Its chemical

liquid oil were formulated using gelatine and xanthan gum for bio- and non-bio-related applications [147]. Based on that research, gelatine type B with Bloom number 225-325 was used in this study as a surface active protein to prepare G/X SOS as a drug or a nutrient delivery system (**Chapter 5**). The reported T_m of gelatine type B with Bloom number 225-325 is 93.8 °C and its T_g is 35 °C [259].

Xanthan gum

Xanthan gum is a high molecular weight polysaccharide with branched chains and anionic characteristics produced industrially by a pure-culture aerobic fermentation of a carbohydrate using predominantly the Gram-negative bacterium *Xanthomonas campestris* [157, 260]. The molecular weight distribution ranges from 2×10^6 to 20×10^6 g/mol and depends on the variation of the fermentation conditions, and the association between chains, i.e. formation of aggregates [261]. The primary structure of xanthan gum consists of repeating units of five sugar residues: two glucose, two mannose and one glucuronic acid. The polymer backbone consists of four (1–4)-linked β -D-glucose units similar to a cellulose backbone; however, trisaccharide side chains attached to alternate glucose units in the main chain distinguish xanthan gum from cellulose (**Figure 2.10**) [157, 261]. Due to the presence of glucuronic and pyruvic acid groups in the side chain, xanthan gum has anionic characteristics [262]. It is insoluble in ethanol and ether, and soluble in cold or warm water. Xanthan gum has very high viscosity at low concentration (the dynamic viscosity is 1200–1600 mPa·s for a 1 % w/v aqueous solution at 25 °C) and stable rheological properties over a broad range of temperature (10–60 °C) and pH (pH 3–12) [157]. In addition, xanthan gum gels show pseudoplastic behaviour [263] and can form hydrogels by annealing the solution in sol state and subsequently cooling [264, 265]. Its melting point is 270 °C (chars) [157] and the reported T_g are 46.5 °C [266] and 143 °C [267].

Xanthan gum has a wide variety of industrial applications due to its pseudoplasticity, high viscosity and stability to acid, salt and temperature, non-toxicity, and compatibility with most other ingredients. It is commonly used as stabilizer, thickening (E415 [268]) and suspending agents in many foods [263]. In pharmaceutical technology, it is also widely used in oral and topical pharmaceutical formulations such as gelling, stabilizing, suspending, emulsifying, sustained-release and viscosity-increasing agents. Furthermore, it has shown the best release

profile for the colon-specific compression coated systems of 5-fluorouracil for the treatment of colorectal cancer when used with boswellia gum [269] and guar gum [270]. Xanthan gum has been used as a gelling agent for topical formulations of solid lipid nanoparticles containing vitamin A and for the microemulsion of ibuprofen [271]. It produces superior results when used as an excipient for spray-drying and freeze-drying processes [157]. In this project (**Chapter 5**), xanthan gum was selected as a non-surface active polysaccharide to prepare G/X SOS.

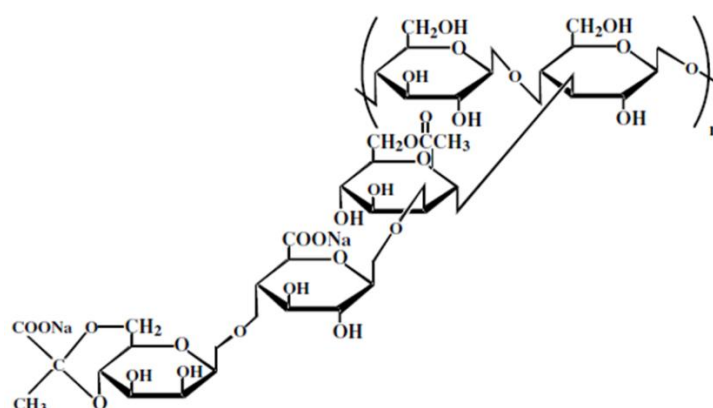


Figure 2.10. Chemical structure of xanthan gum. Adapted from [272].

Hydroxypropyl methylcellulose (HPMC K4M)

Hydroxypropyl methylcellulose (HPMC) is a semi-synthetic and non-ionic cellulose derivative. It belongs to the group of surface active polysaccharides due to the methyl substitutions that compose hydrophobic zones along the cellulose backbone and hydroxypropyl groups which are more hydrophilic (**Figure 2.11**) [273]. The physicochemical properties depend on: 1) the methoxy group content; 2) the hydroxypropoxy group content; and 3) the molecular weight. Therefore, the T_g values of HPMC range from 154 to 184 °C; however, values of 57 °C [274] and 186 °C [159] were also reported. In addition, different methods used to measure the T_g often lead to different values [274]. It is a cold water-soluble compound and has been classified as a moderately hygroscopic substance (class III) by Callahan et al. [240].

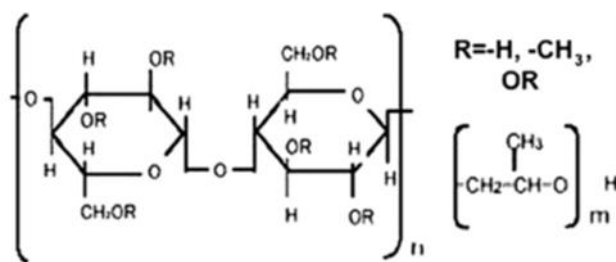


Figure 2.11. Chemical structure of HPMC. Adapted from [275].

Its capacity to form thermo-reversible gels that melt on cooling, alongside its good solubility in water and tastelessness, have resulted in wide usage in the food and pharmaceutical industries [276]. In the food industry, HPMC (E464) is used as a stabilizer and binder, as a barrier to oil and in moisture retention. In pharmaceutical formulations, HPMC is used in numerous oral, ophthalmic and topical nasal drug product preparations as a dispersing and thickening agent [277]. It is also an excellent carrier material due to its non-toxicity, GRAS status, ease of handling, ease of compressing, high drug load capacity and relatively simple tablet manufacturing technology [278, 279]. However, it is mainly used in the formulation of controlled release dosage forms as a swellable and hydrophilic polymer [277]. The mechanism of drug release is believed to be drug diffusion through the hydrated HPMC gel layer for soluble drugs and hydrated HPMC gel layer erosion for poorly water-soluble drugs or a combination of the two mechanisms above with one of them being dominant [280-282].

A number of studies have reported on the use of HPMC in oil-in-water emulsions due to its ability to reduce the surface tension and increase the viscosity of the water phase [273, 283]. It has also been used as an admixture to proteins, mainly to enhance the stability of dispersed systems [284], and as a replacement for fat and as a non-caloric bulking agent [277]. For example, structuring edible oils (oleogels) were evaluated using HPMC to replace fat-based building blocks [285]. Based on those studies, HPMC K4M was used as a surface active polysaccharide to prepare HPMC/X SOS (**Chapter 5**). The K letter indicates the HPMC chemistry, where R group is $-\text{OCH}_3$ (**Figure 2.11**). The number 4 identifies the viscosity of the 2% w/v aqueous solution at 20 °C [280], which is 3,000–5,000 mPa·s. The Tg of HPMC 4KM is 186 °C [159].

Methylcellulose

Methylcellulose (MC) is a water-soluble and long-chain cellulose polysaccharide derivative in which about 27–32% of the hydroxyl groups are substituted by methoxyl groups (CH₃O) (**Figure 2.12**). The molecular weights are in the range 10,000–220,000 g/mol. The physicochemical properties of MC depend on the degree of substitution (DS) (1.64–1.92), which is defined as the average number of methoxyl groups attached to each of the anhydroglucose units along the chain. At 190–200 °C MC begins to brown and at 225–230 °C it begins to char. The viscosity depends on the concentration and the temperature. The higher the concentration, the higher the viscosity will be. Increasing the temperature reduces the viscosity of the solutions until gel formation occurs at 50–60 °C. However, the process is thermo-reversible, as a viscous solution can be reformed on cooling. MC is practically insoluble in acetone, methanol, chloroform, ethanol (95%), ether, saturated salt solutions, toluene and hot water. It is soluble in glacial acetic acid and a mixture of equal volumes of ethanol and chloroform. In cold water, MC forms a clear to opalescent, viscous, colloidal dispersion by slow swelling and dispersion [157].

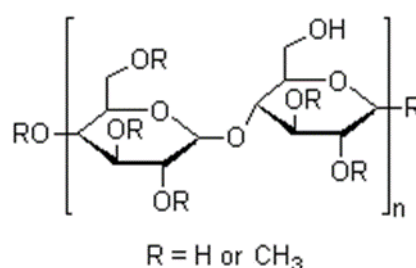


Figure 2.12. Chemical structure of MC.

The functional categories of MC include its application as coating, emulsifying and suspending agents, and as a tablet and capsule disintegrant, tablet binder and viscosity-increasing agent. In the pharmaceutical industry, MC is widely used in oral, injectable and topical formulations. Low or medium grades of MC are used in tablet formulations as a binding agent or to emulsify olive, peanut and mineral oils, whereas high viscosity grades are used as a disintegrant in tablet formulations or as a thickening agent for topically applied products such as creams and gels. Tablet cores may also be spray-coated to mask an unpleasant taste and to modify the

release or to produce sustained release of a drug. MC is a GRAS listed compound and is accepted as a food additive, i.e. as emulsifier, stabilizer, thickener and gelling agents [157] under the E number E461 [239]. For example, edible oleogels (containing >97 wt.% of sunflower oil) as shortening alternatives were developed using MC and xanthan gum [286]. Based on that study, methylcellulose polymer were used as a surface active polysaccharide to prepare MC/X SOS (**Chapter 5**).

Carboxymethyl cellulose (CMC)

Carboxymethyl cellulose (CMC) is a high molecular, amphiphilic [287], anionic linear polysaccharide and semi-synthetic derivative of cellulose which is manufactured by the partial substitution of the 2, 3, and 6 hydroxyl groups of cellulose by carboxymethyl groups ($-\text{CH}_2\text{COOH}$) (**Figure 2.13**) [288]. Since the reaction occurs in an alkaline medium, the product is normally sold in the form of either sodium or as calcium salts of carboxylic acid ($\text{R-O-CH}_2\text{COONa}$ or Ca) [142, 289]. The physicochemical characteristics of CMC depend on the molecular weight and DS. Commercial products usually have DS values ranging from 0.7 to 1.5 [290] and the molecular weight ranges from 21,000 to 500,000 g/mol. Depending on the degree of esterification, the viscosity of 1% w/v aqueous solution of CMC varies from 5 to 2,000 mPa·s. Its solutions are stable in the pH range 2–10 and precipitate below pH 2, and the viscosity decreases rapidly above pH 10. CMC is soluble in either cold or hot water but insoluble in organic solvents [289]. The reported T_g values of CMC with $M_w = 250,000$ g/mol are about 55 °C [287] and 75 °C [291]. Thermal degradations are described in one source at 172–327 °C while in another source they are given at 100–300 °C and 300–800 °C in a two-step process [292].

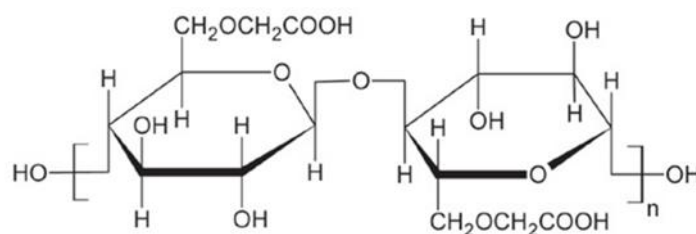


Figure 2.13. Chemical structure of CMC.

CMC has many desirable qualities, which include being non-toxic and non-allergenic, as well as its capacity for filming, thickening, emulsification, suspension, water binding and maintaining, combined with the low cost of the material [142, 291]. In the pharmaceutical industry, CMC has been successfully used for drug delivery and tissue engineering purposes. Applications include, for example, gastroretentive DDS [293], colon-targeted oral drug delivery [294] and nasal drug delivery [295]. It has been used in preparation of hydrogels with superabsorbent properties [296] and in bio-nanocomposite hydrogel beads as an anticancer drug carrier agent [297]. CMC (E466 [298]) is also commonly used in food, such as beverages, desserts, dressings and bakery products, to inhibit the gravitational separation of colloidal particles and to produce desirable textural attributes and mouthfeel [142]. In this study, CMC was used as a negatively charged polysaccharide, as an alternative to replace xanthan gum, to prepare G/CMC SOS (**Chapter 5**).

Tween 20 and Span 80

Tween 20 is hydrophilic and *Span 80* is lipophilic. They are both non-ionic surfactants that are used as emulsifying, solubilizing and wetting agents in concentrations from 1–15% w/v, 1–15% w/v and 0.1–3% w/v, respectively. They are also dispersing and suspending agents. The acceptable daily intake of Tween 20 and Span 80, as estimated by WHO, is up to 25 mg/kg body weight calculated as total polysorbate esters and as total sorbitan esters, respectively [157]. Their chemical structures are illustrated in **Figure 2.14**. The detailed physicochemical properties of Tween 20 and Span 80 are presented in **Table 2.4**.

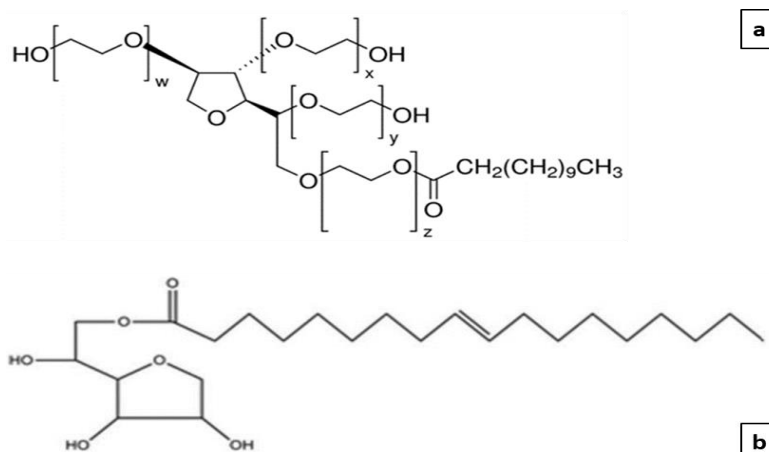


Figure 2.14. Chemical structure of Tween 20 (a) and Span 80 (b), adapted from [299] and [300], respectively.

Table 2.4. Physicochemical properties of Tween 20 and Span 80, taken from [157].

Physicochemical properties	Tween 20	Span 80
Chemical/common name	Tween 20/Polysorbate 20/PEG-20 sorbitan monolaurate	Span 80/Sorbitan monooleate
Empirical formula	C ₅₈ H ₁₁₄ O ₂₆	C ₂₄ H ₄₄ O ₆
Molecular weight (g/mol)	1128	429
Physical state at 25 °C	Yellow oily liquid	Yellow viscous liquid
Odour	Characteristic odour	Bland fatty odour
Specific density (g/cm ³)	1.1	1.01
Solubility	Soluble in water and ethanol, insoluble in mineral and vegetable oils	Soluble or dispersible in oils and most organic solvents, insoluble in water
Incompatibilities	With phenol, tannins, tars and tarlike materials	–
Pour point (°C)	–	-12
Flash point (°C)	149	>149
HLB value	16.7	4.3
CMC _n (10 ⁻⁵ mol/L)	8.04 [301]	1.7–1.9 depending on the oil phases, which are given elsewhere [302]
Surface tension of 1% aqueous solution (mN/m)	–	30
Viscosity at 25 °C (mPa·s)	400	970-1080

In pharmaceutical formulations, Tween 20 and Span 80 are used as emulsifying agents in the preparation of stable o/w emulsions and w/o emulsions, respectively. In addition, Tween 20 has been used as a solubilizing agent for essential oils and oil-soluble vitamins and as a wetting agent in the formulation of oral and parenteral suspensions. Whereas, Span 80 has been used in combination with varying proportions of a polysorbate to produce w/o or o/w emulsions or creams, as well as in self-emulsifying DDS for poorly soluble drugs and in Span 80 vesicular DDS for actively targeting specific cancer cells [303]. In the food industry, Tween 20 and Span 80 have the E numbers E432 and E494, respectively [239]. In this study, Tween 20 and Span 80 were used as emulsifiers to prepare core-sheath nanofibres (**Chapter 4**) and Tween 20 was additionally used as a surface active surfactant to prepare Tween 20/X SOS (**Chapter 5**).

2.3 General introduction to preparation techniques

2.3.1 Electrospinning general set up

Conventional electrospinning and coaxial electrospinning were performed using a solution pump (Cole-Parmer, UK) and high voltage power supply (Gamma High Voltage Research, Inc., Ormond Beach, FL, USA). In all experiments, the electrospun fibres were collected using the custom-made stationary collector, except when the effect of the drum collector was studied, when a custom-made drum collector was used, which is indicated with a given rpm in electrospinning processing parameters (EPPs). For the conventional electrospinning, a 5 ml plastic syringe (BD Plastipak™, Fisher Scientific), with an open end fitted with a blunt needle (Terumo, Tokyo, Japan), was used as a solution reservoir from which a polymer solution or a polymer solution containing an active ingredient were fed by means of a solution pump operating at a controlled rate. The size of the needle used in all the experiments was 18G (G-gauge), except when the effect of the needle gauge was studied, when 18G, 20G, 21G and 23G needles were employed (**Chapter 3**). In the case of the coaxial electrospinning, a single spinneret sealed coaxial needle (Linari Engineering S.r.l., Pisa, Italy) was used as a dual solution supplier. The needle was connected with two 5 ml plastic syringes (BD Plastipak™, Fisher Scientific), containing two different solution compositions, through two pieces of PVC

tubing ($d \approx 0.5$ mm, $\text{wall} \approx 1$ mm, $L \approx 150\text{--}200$ mm). The solutions in the syringes were fed by means of two solution pumps (Cole-Parmer, UK) at a controlled rate.

In terms of the EPP, the direct current (DC) voltage is given as a range from minimum to maximum. The reasoning for this is because, depending on the solution concentration and content, the applied DC voltage can be varied and therefore was adjusted accordingly during the processing until a stable jet was observed. All samples for electrospinning were prepared under room temperature at 26–35 % relative humidity (RH).

2.3.2 Homogenizing instruments

2.3.2.1 High-performance dispersing instrument (HPDI)

Basic principle

High-performance dispersing instruments (HPDI) are used for a variety of applications in pharmaceutical and food research for homogenization, emulsification, dispersions, particle reduction, and reaction enhancements. It uses the rotor-stator principle. The system consists of an outer stationary tube (stator) and an inner turning shaft (rotor) that is connected to a motor. The instrument works at a range of speeds from 8,000 to 30,000 rpm. The bottom of the rotor and the stator contain slots. When running at a high speed, samples pressed into the slots of the rotor-stator arrangement are subjected to high circumferential speed and extremely strong shear forces, due to the high speed and minimal gap between the rotor and the stator which results in better dispersion (**Figure 2.15**) [304, 305].

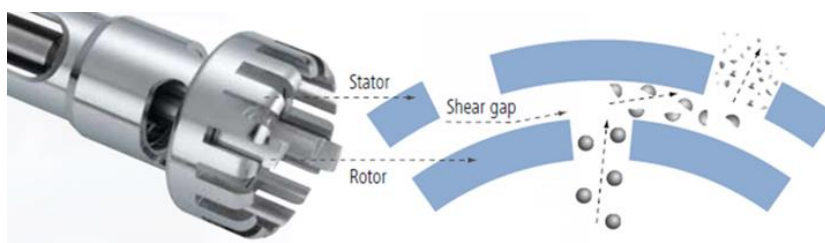


Figure 2.15. Schematic representation of the principle of dispersing the sample using a high performance dispersing instrument. Adapted from [305].

Technical characteristics

Emulsion was homogenized with an Ultra Turrax dispersing instrument (IKA T10 basic S2 from IKA Werke GmbH and Co., Germany). The rotation speed can retard slightly depending on the viscosity of solution, but the variance is insignificant.

2.3.2.2 High pressure homogenizer (HPH)

Basic principle

A *high pressure homogenizer (HPH)* is a continuously operated emulsifying device that is used in the food and pharmaceutical industries to create submicron emulsions in materials of low and intermediate viscosity. The HPH is a purely mechanical device that uses intense disruptive forces that mechanically break-up the larger droplets into tiny droplets. It consists of a high-pressure piston pump that pulls the crude emulsion into a chamber on its backstroke, and then forces it through a narrow valve at the end of the chamber on its forward stroke (**Figure 2.16**). As the crude emulsion passes through the valve, it experiences a combination of extremely high turbulence, shear and cavitation that causes the grinding of the droplets [142].

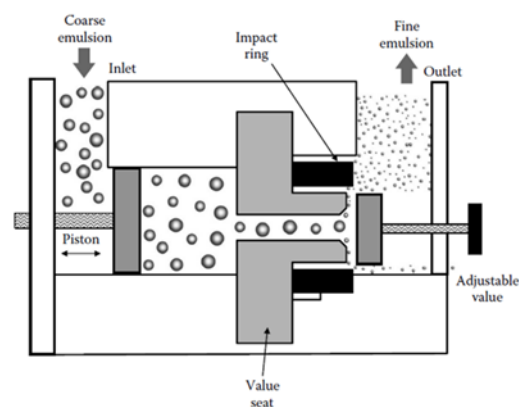


Figure 2.16. Schematic representation of the principle of operation of a high pressure homogenizer. Adapted from [142].

Technical characteristics

Emulsions were prepared using an EmulsiFlex-C5 High Pressure Homogenizer from Avestin, Ottawa, ON, Canada. The maximum homogenizing pressure is 30,000 psi. The maximum sample batch size is 5,000 ml and the minimum sample volume is 10 ml (the data is taken from the manufacturer's manual).

2.3.3 Freeze drying

Basic principle

Freeze drying, also known as lyophilization, is a widely used process for dehydration and improving the stability of various food and pharmaceutical products. It is based on the dehydration by sublimation of frozen products and consists of three process steps: freezing, primary drying and secondary drying. During freezing, an aqueous solution is frozen and then, during the primary drying phase, water is removed by sublimation under vacuum. In the final secondary drying stage, non-frozen water is removed by diffusion and desorption [149, 306].

Technical characteristics

The SOSs were lyophilized by using a VirTis AdVantage 2.0 freeze dryer (SP Scientific, Gardiner, NY, U.S.A). The lowest shelf temperature is -57 °C and the lowest condenser temperature is -67 °C. The defrost type is hot gas, the condenser type is internal and the refrigerator type is CFC free (taken from the manufacturer's manual).

2.4 General introduction to characterization techniques

2.4.1 Imaging techniques

One of the imaging techniques often used in science is the microscope. There are broad ranges of different types of microscope available in the market, which are grouped according to the way the instrument interacts with a sample to create images. **Figure 2.17** represents

the schematic illustration of the working principle of two categories of microscope used in this project. The featured characteristics of each type of microscope are described below. Another category of imaging technique used in this project is X-ray micro computed tomography (X μ CT). This imaging technique functions using a different principle than microscopes and is also described in this section.

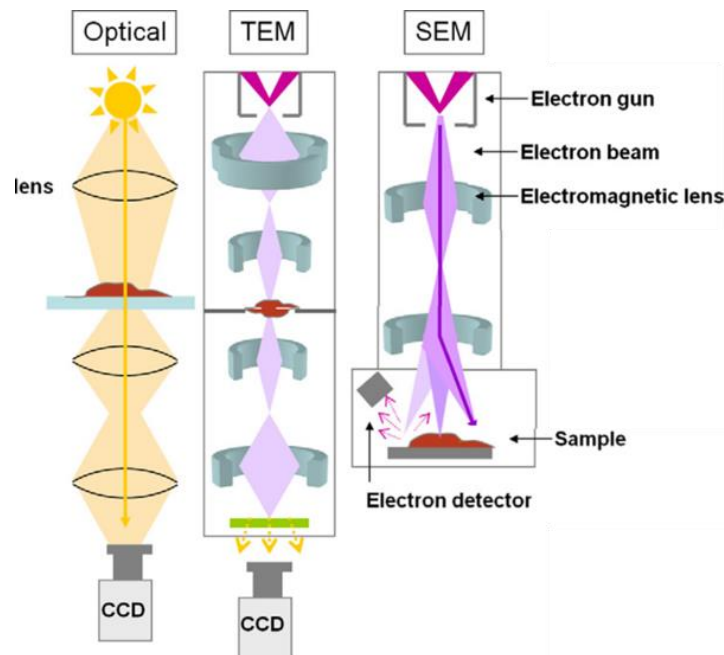


Figure 2.17. Schematic representation of principles of imaging using optical microscope compared with electron microscope techniques, transmission electron microscope (TEM) and scanning electron microscope (SEM). Adapted from [307].

2.4.1.1 Optical microscopes

Optical or light microscopes (LM) are a type of microscope using a visible light and lenses to produce a magnified image of the specimen. In the LM, the light passes through the condenser and then through the specimen. The underlying principle of LM relies on there being different optical densities for different parts of the sample. The dark sections have high optical density whereas the light sections do not and the light passes through them. As a result, the pattern of light and dark areas produces what we recognize as an image of the specimen. The eye lens of the eyepiece further magnifies the image and finally projects it on to a camera [308]. The main components of LM are the base, light source or illumination,

condenser, stage, the objectives, eyepiece and the fine and course adjustment knobs [309]. In addition, most of the modern microscopes are equipped with a fluorescent camera. The maximum magnification of LM is around 1300x and the resolution is around 200 nm [310]. It has tremendous applications in all areas of research.

LMs are available in two orientations, upright or inverted microscopes, and two designs, simple or compound microscopes. Besides, there are various modified optical microscopes equipped with an additional light path to improve the image, such as light polarized microscope (LPM), confocal laser scanning microscopes (CLSM) and stereoscopic microscopes. The distinguishing features of each type of optical microscope used in this project are described below.

2.4.1.1.1 Upright microscope

Basic principle

The *upright microscope* is the type of optical microscope that is designed so that the objective lens is pointing down onto the coverslip surface and the specimen is placed at the bottom with the light source and condenser. Other than the orientation of the specimen, the principle is the same as an optical microscope [311].

Operating conditions

An upright microscope was used to analyse the morphology and nature of emulsion, i.e. o/w or w/o emulsions (**Chapter 5**). Samples were imaged on a Zeiss AxioPlan 2ie microscope. Brightfield and fluorescent images were captured using a 10x Plan-Neofluar objective (0.3 NA), a 20x Plan-Apochromat objective (0.6 NA), or a 40x Plan-Neofluar objective using an oil-immersion objective lens (1.3 NA), alongside a Zeiss AxioCam HRm charge-coupled device (CCD) camera and AxioVision software (Carl Zeiss, Cambridge, UK). Fluorescence was excited at 300–400 nm and emission collected at 410–475 nm. All samples examined under fluorescence microscope were loaded with the fluorescence marker coumarin-6 in the oil phase, at a quantity of about 1 mg.

2.4.1.1.2 Stereomicroscope

Basic principle

The *stereomicroscope* is a type of optical microscope in which the light runs from two separate optical paths due to two objectives and two eyepieces that provide the opportunity of viewing the specimen from two slightly different angles. Thus, the image produced by a stereomicroscope is perceived by the human mind as three-dimensional. Modern stereomicroscopes provide both incident light and transmitted light. It has low magnification, at a little more than 300x, but a longer working distance; therefore, it allows inspection of large specimens [312].

Operating conditions

A stereomicroscope was used to visualize the dispersion of oil inside G/X SOS (**Chapter 5**). Brightfield and fluorescent images were acquired using a Zeiss M2 Bio Quad SV11 stereomicroscope. The samples were illuminated either using a halogen lamp (brightfield) or a 100W Hg arc lamp (fluorescent), and the reflected-light images were captured with a Zeiss AxioCam HRc CCD camera and AxioVision software (Carl Zeiss, Cambridge, UK). Fluorescence was excited with light passed through a 470 nm filter (40 nm bandpass) and the emission collected through a 525 nm filter (50 nm bandpass). All samples examined under stereomicroscope using fluorescent light were loaded with the fluorescence marker coumarin-6 in the oil phase.

2.4.1.1.3 Confocal laser scanning microscope (CLSM)

Basic principle

A *confocal laser scanning microscope (CLSM)* is a type of optical microscope that provides a fundamental improvement in imaging, in terms of high resolution and contrast, compared to a normal LM [313]. This is because of a pinhole aperture located in the image plane before the objective which blocks out-of-focus light (**Figure 2.18**) and point by point illumination of the specimen that minimizes aberrant rays of scattered light [314]. In addition, it is capable of distinguishing particular components within a complex matrix via the use of various fluorescent dyes and can directly create digital three-dimensional (3D) images by combining

a series of thin sections of specimen without needing to physically dissect the item. This is achieved due to a laser scanning function performed along the vertical axis of the specimen [315].

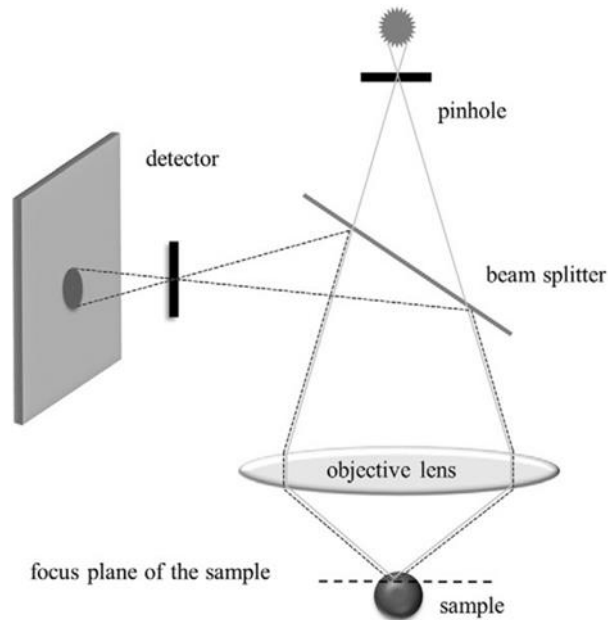


Figure 2.18. Schematic illustration of principle of imaging by CLSM. Adapted from [316].

Operating conditions

In this study, CLSM was used to analyse emulsion for comparison purposes, as it provides higher resolution and better contrast than the other microscopes (**Chapter 5**). Samples were imaged using a Zeiss LSM 510 META confocal microscope. The samples were loaded with the fluorescence marker coumarin-6 in the oil phase and fluorescent images were captured using a 40x Plan-Neofluar, an oil-immersion objective lens (1.3 NA) and LSM software. Fluorescence was excited with the 488 nm laser-line of an Argon ion laser and emission was collected at 505–550 nm.

2.4.1.2 Electron microscopes

The electron microscope (EM) is a type of microscope that uses a beam of accelerated electrons as a source of illumination instead of visible light and offers extremely high magnification with a maximum at or below 1 nm. There are different types of EM, which are

grouped according to the way the instrument interacts with the specimen to create images. The detailed features of the different types of EM used in this project are discussed below.

2.4.1.2.1 Scanning electron microscope (SEM)

Basic principle

A *Scanning Electron Microscope (SEM)* is a high-resolution electronic microscope that is employed to determine the surface properties and spatial relationships of the materials [307]. A low-energy electron beam (with a maximum accelerating voltage of 30 kV [307]) is produced by an electron gun focused into the sample and the surface of the probe is scanned in a raster fashion [317]. Various signals are generated as a result of the interactions between the incident electron beam and the atoms in the sample which are collected by various detectors in the specimen chamber to provide an image of the surface topography (**Figure 2.17**) [318]. The electron sources used in the SEM are a tungsten hairpin filament, or a lanthanum hexaboride LaB₆ or Schottky emitter, or a field emission gun [317, 319]. Magnification in a SEM can be achieved up to 1,000,000x with a maximum resolution of 1 nm [319]. The samples are normally pre-coated with conductive material, e.g. gold, and examined at ambient temperature within a high vacuum chamber [320].

SEM is a powerful tool to image at high magnification a large area of the surface or cross-section of pharmaceutical formulations and compounds as well as engineered nanomaterials in food matrices [307]. It is commonly used to study the orientation, diameter and the morphology of electrospun fibres, as well as crystalline materials and the recrystallization of APIs in solid dispersion formulations [93].

Operating conditions

In this project, SEM was utilized to investigate the morphology of the electrospun nanofibres (**Chapter 3**) and core-sheath nanofibres (**Chapter 4**) which were visualized using a JSM5900 LV SEM (JEOL Ltd., Japan) equipped with a tungsten hairpin filament and operating at an acceleration voltage of 5–20 kV. The samples were fixed on aluminium stubs using double-sided adhesive carbon tape and then Au coated using a Polaron High Resolution SC7640 gold coater (Quorum Technologies, Newhaven).

2.4.1.2.2 Cryo-scanning electron microscope (Cryo-SEM)

Basic principle

Cryo-scanning electron microscope (Cryo-SEM) is a modification of SEM, i.e. it is an SEM with a cryo-chamber attached to it. It was developed with the aim of preserving the microstructure of hydrated biological specimens in amorphous ice. However, it has been finding increasing application in many other fields, including pharmaceutical [321] and food [307] sciences when the preservation of the structural integrity of a porous structure or of hydrated, liquid and semi-liquid systems is required. In Cryo-SEM, the specimens are first rapidly frozen and then fractured. The fractured surfaces of the frozen specimens are deposited with conducting metal to avoid charging and are then viewed in an SEM which is equipped with a cryo-stage [322]. Typically, Cryo-SEM samples are frozen by plunging into a nitrogen slush (-210 °C); however, other coolants such as liquid propane and ethane can also be utilized [307]. Sample preparation and microscope operation are carried out between -180 and -60 °C depending on the purpose of the study and sample properties [320].

Operating conditions

In this project, a Cryo-SEM instrument was used to investigate the internal structure of semi-solid G/X SOS (**Chapter 5**). The microscope that was used in this study was a Zeiss SEM fitted with a Gatan cryosystem. Samples were attached to the sample holder and immediately plunged into liquid nitrogen slush at approximately -210 °C to cryo-preserve the material. This material was transferred onto the cryo-stage of an ALTO 2500 cryo-transfer system (Gatan, Oxford, England) and attached to a Zeiss Supra 55VP FEG scanning electron microscope (Zeiss SMT, Germany). The samples were fractured at -100 °C before sputter coating with platinum for 90 seconds at 10mA, at a temperature colder than -110°C. After sputter coating, the sample was moved onto the cryo-stage in the main chamber of the microscope and held at approximately -130°C. The sample was imaged at 3kV and digital TIFF files were stored.

2.4.1.2.3 Transmission electron microscope (TEM)

Basic principle

Transmission electron microscope (TEM) is another type of electron microscope which allows the examination of the morphology and the internal structure of nanosized objects [307]. The resolution of TEM is about 0.07 nm. In TEM, a high-energy electron beam (100-300 kV [317]) is transmitted through a thin layer of the specimen while some of the electrons are scattered [307]. The transmitted electrons bombard a fluorescent (phosphor) screen, which converts the electron images to a visible form (**Figure 2.17**) [317]. Alternatively, a high-resolution phosphor screen may be coupled to the sensor of a charge-coupled device (CCD) camera which allows the capture of digital images [321]. The contrast in TEM images is based on the detection of interactions of the electron beam with the sample and therefore, more dense materials create more intense shade [307]. As in the case of an SEM, the TEM also uses an electron gun (thermoionic or field emission sources) to generate the electron beam and focuses it on the specimen by using electrostatic and electromagnetic lenses [321].

TEM is an essential tool in pharmaceutical and food engineering for the exact characterization of novel vehicles, which are constantly decreasing in size range to provide efficient delivery and to decrease side effects [307, 321]. Different nanoparticles within composite matrices [323, 324], which cannot be seen by SEM, as well as semi-liquid [325, 326] and liquid systems were characterized by means of TEM. Beside, TEM analysis provided information about the physical stability of the different nanoemulsions [327].

Operating conditions

In this study, the TEM instrument was used in two separate chapters:

1. To visualize inorganic nanocrystals (KIO_3 and NaCl) within polymer nanofibres (PEO and PVP) (**Chapter 3**). Samples were electrospun directly onto TEM grid support films of holey carbon on 300 mesh Cu. The TEM instrument used was a Philips CM30 operating at 300 kV.
2. To investigate the internal structure of semi-liquid G/X SOS (**Chapter 5**). The freeze-dried SOS was cut into approximately 1 mm^3 cubes. The cubes were fixed

in 2.5% glutaraldehyde/0.1 M PIPES buffer (pH 7.4) for 2 hours at room temperature and then transferred to fresh fixative overnight at 4 °C. After 3 washes in the 0.1M PIPES buffer, the cubes were placed in 2% aqueous osmium tetroxide for 48 hours, washed 3 times with distilled water, then dehydrated through an ethanol series (10, 20, 30, 40, 50, 60, 70, 80, 90%). After 3 washes in 100% ethanol, the last wash was replaced with a 1:1 mix of LR White medium grade resin (London Resin Company Ltd) to 100% ethanol for 1 hour. This was followed by a 2:1 and a 3:1 mix of LR White resin to 100% ethanol and finally 100% resin, with at least 1 hour between each change. The resin was changed twice more with fresh 100% resin, after periods of at least 6 hours between changes. Five blocks from each sample were each put into BEEM capsules with fresh resin and polymerised overnight at 60 °C. Sections approximately 90nm thick were cut using an ultramicrotome (Ultracut E, Reichert-Jung) with a glass knife, collected on Formvar/carbon coated copper grids, and stained sequentially with 2% uranyl acetate and 0.5% lead citrate. Sections were examined and imaged in a FEI Tecnai G2 20 Twin transmission electron microscope at 200kV.

2.4.1.3 X-ray micro computed tomography ($X\mu$ CT)

Basic principle

X-ray micro computed tomography ($X\mu$ CT) is a non-destructive tomographic technique that uses X-rays to detect the internal defects of different materials and is classified as a 3D imaging technique with a high resolution to several microns [328]. The principle of visualizing material properties is premised on the material's electron density difference, which absorb X-rays differently. When analysing the object with $X\mu$ CT, the specimen is placed on a rotating stage and rotated stepwise about its axis with a defined angular step. At the same time, a conical beam from a microfocus X-ray source illuminates the specimen (**Figure 2.19**) [329]. Some X-ray photons are attenuated, whereas others will transmit through the sample and reflect in the shadow images produced on the detector. Then, $X\mu$ CT can assemble the accumulated data of 2-D cross-sectional images or slices into a volumetric dataset and can form a virtual 3-D image through mathematical operation (reconstruction) with accompanying software [330]. In addition, due to the pseudo-colouring function of the

software being linked to the density of the material, different phases can be distinguished. Therefore, $X\mu$ CT has been widely used in pharmaceutical science to control the quality of tablets, study the presence of various material sub-components and their local distribution, and examine the presence of cracks, voids, and the shape and size of the enclosure [329].

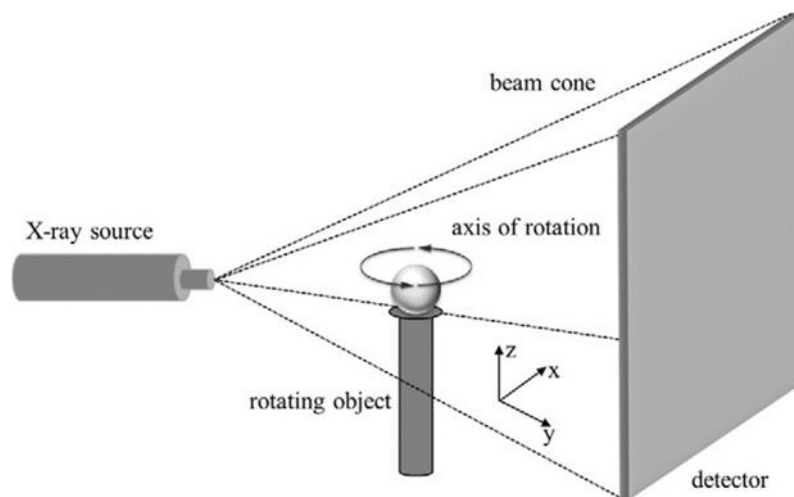


Figure 2.19. Schematic illustration of principle of imaging by $X\mu$ CT. Adapted from [316].

Operating conditions

$X\mu$ CT imaging was used to observe the inner structure of G/X SOS without dissecting it (**Chapter 5**). The samples were scanned using a SkyScan1172 high-resolution X-ray micro computed tomography scanner (Bruker microCT, Kontich, Antwerp, Belgium). The total scan time was 25 minutes. The samples were fixed on the rotation stage using a plastic tube and the samples were rotated over 360° in steps of 0.5° .

2.4.2 Energy-dispersive x-ray spectroscopy (EDS)

Basic principle

Energy-dispersive x-ray spectroscopy (EDS) is the most popular non-destructive analytical technique used in conjunction with SEM or TEM and is employed to quickly determine the elemental composition in solid materials with an atomic number greater than 5 [331]. The principle of this technique is premised on the detection of radiation. Characteristic radiation is emitted by atoms of the sample when excited by a high-energy beam of photons, electrons

or X-rays. During the bombardment of a sample with an incident beam, electrons are ejected from the inner-energy shell creating an empty hole, and these ejected electrons are replaced by electrons from the higher-energy shell. As a result, characteristic X-rays are emitted in order to compensate for the energy differences between electrons during this transition. The emitted X-rays are analysed by the EDS detector and the elemental composition of the sample is determined [312]. However, the data obtained from this technique is generally indicative and only the relative atomic proportions are estimated. Nevertheless, EDS can show the spatial distribution of elements and can help to determine the phases present in a sample, i.e. producing an element map, by progressively rastering the electron beam point by point across the surface of a sample [331].

Operating conditions

In this project, the distribution of inorganic salt KIO_3 within PEO nanofibres was determined using EDS (INCA Energy manufactured by Oxford Instruments) in conjunction with SEM (**Chapter 3**). The instrument is capable of detecting chemical elements using a spot mode manually chosen in the SEM scanned area. Resolution: 131 eV (Mn $K\alpha$). Acquisition time: 30–60 s. At least 5–10 spots at different locations were examined for each sample.

2.4.3 Powder x-ray diffraction (PXRD)

Basic principle

Powder x-ray diffraction (PXRD) is a non-destructive and rapid analytical technique used to identify chemical composition and the structure of all crystalline compounds.

In 1913, Bragg devised a theory to explain the relationship between diffraction data and crystal structure, based on the evidence that atoms in crystals are arranged periodically as parallel plates and separated by a definite distance. When X-rays strike the surface of a crystal, they are scattered by parallel planes of atoms and each plane of atoms acts as a half-silvered mirror, reflecting the incident radiation. In order for an X-ray to diffract, the distance between the atom planes must be comparable to the wavelength of the radiation. X-rays are electromagnetic waves with the wavelength of the order of $1 \text{ \AA} = 1 \times 10^{-10} \text{ m}$, which is similar to the distance between atoms, a suitable radiation to be diffracted [332]. Diffracted radiation

is produced by constructive and destructive interferences and its intensity has strong angular dependence. When waves interfere constructively, the diffraction pattern shows a peak, whereas destructive interference produces a low intensity [333]. This is explained by Bragg's Law:

$$n\lambda = 2d \sin \theta \dots\dots\dots (2.1)$$

Where λ is the wavelength of the radiation, n is an integer number of the diffracted beam, θ is the angle between the lattice planes and the incident beam and d is the distance between the lattice planes [334].

Since a highly regular structure is needed for diffraction to occur, crystalline materials produce sharp intense peaks. The position of each peak determines the crystal structure and symmetry of the contributing phase, which can be used to elucidate different chemical compounds including the polymorphs of crystalline pharmaceuticals [335]. In contrast, randomly oriented powders of small crystals and nanocrystals cause a broadening of diffraction peaks due to the absence of total constructive and destructive interferences of X-rays in a finite-sized lattice [336]. Amorphous materials show a halo pattern and do not produce a diffraction pattern at all because they do not have a periodic array with long-range order. Therefore, PXRD can also characterize the mixture of amorphous and crystalline materials; for example, semi-crystalline polymers will produce sharp peaks and a halo. For these reasons, PXRD is the key technique in all stages of drug development as it can elucidate different forms of drug moiety and drug delivery systems, which in turn have a great impact on quality, bioavailability and drug stability [337].

Operating conditions

In this study PXRD was utilized to study the physical form of KIO_3 with the increase of the loading into a PEO polymer chain, as well as the impact of KIO_3 on the degree of crystallinity of a semi-crystalline PEO polymer (**Chapter 3**). Also, new crystal modification of PEO was identified with the help of PXRD (**Appendix 4**). Diffraction peaks were measured with a Thermo ARL X'TRA Diffractometer (Thermo Scientific, UK) with a step size of 0.01° , 0.5 second time per step, from 3° to $60^\circ 2\theta$. The wavelength was 1.54 \AA , and the X-ray source was Cu $\text{K}\alpha_1$

with a power of 45 kV and a current of 40 mA. Samples were accurately folded and placed onto the sample holder with zero background and incorporated onto a spinner stage.

2.4.4 Attenuated total reflectance Fourier transform infrared spectroscopy (ATR-FT IR)

Basic principle

IR spectroscopy studies the interaction of infrared light with matter. When the IR beam radiates the sample, the absorbance of infrared light by molecules excites vibrations such as stretching, bending and rocking at specific frequencies and creates characteristic absorption bands for each functional group. The intensity of these bands is determined by the change in the dipole moment of the bond and the number of the specific bonds present. Thus, an infrared spectrometer gives you information about which molecules are present in a sample and at what concentration they appear. Many molecules have strong absorbance in the mid-infrared region ($4,000$ to 400 cm^{-1}) and, therefore, most of the samples are measured in this region. However, molecules with heavy atoms, such as inorganics, absorb far-infrared light (400 to 10 cm^{-1}) and near-infrared light ($14,000$ to $4,000\text{ cm}^{-1}$) and IR spectroscopy is frequently used to measure sample properties in difficult environments. IR spectra are plotted in terms of the % transmittance or absorbance intensities on the y-axis against wavenumber (cm^{-1}) on the x-axis.

The Attenuated total reflectance Fourier transform infrared spectroscopy (ATR-FT IR) is a specific type of infrared spectrometer that uses the technological advances of Fourier transformation and ATR. At the heart of all FT IR is an optical device called an *interferometer* that optically transforms the spectrum of the infrared beam into an *interference pattern* (the interferogram), which in turn is converted into a spectrum by using the Fourier transformation (a mathematical process). The main advantage of FT IR is the ability to scan the sample in a shorter time with a higher signal-to-noise ratio and wavenumber precision. The use of ATR, a sample preparation technique, makes the sample analysis fast and easy. This is attributed to the fact that the ATR crystal (internal reflection element) is used to take the spectrum of nearly any sample without the need for complicated sample preparation [338].

ATR-FT IR has gained wide application in pharmaceutical science as it is capable of identifying polymorphic contents in pharmaceutical materials [339], oxidation of oils [340] and drug-carrier [242] and carrier-carrier interactions [341, 342], such as hydrogen bonding and complexation.

Operating conditions

In this project, ATR-FT IR spectroscopy was used to study the structural confirmation and degree of crystallinity of PEO and the physical form of KIO₃ in the formulation (**Chapter 3**). Also, FT IR has been applied extensively to examine organic compounds and therefore was used to identify any interactions between protein and polysaccharide on the surface of oil/water interfaces (**Chapter 5**). Infrared absorption peaks were measured with an IFS 66/S FT IR spectrometer (Bruker Optics Ltd., Coventry, UK), fitted with a Golden Gate ATR accessory with a heated top plate equipped with a diamond internal reflection element. The spectral resolution was 2 cm⁻¹ with 64 scans taken for each measurement. Triplicate measurements for each sample were performed.

2.4.5 Differential scanning calorimetry (DSC)

Basic principle

Differential scanning calorimeter (DSC) is a type of thermoanalytical technique that is used to identify thermal transition, such as melting, crystallization, glass transition, and the thermal degradation of analysed material by measuring the small heat changes between a specimen and an inert reference as a function of temperature. As both specimen and reference are subjected to thermal treatment, heating, cooling or an isothermal process at an identical and controlled rate, the specimen undergoes a thermal event, which results in heat either being absorbed or released. This creates the temperature and energy differences between the specimen and reference. The DSC instrument examines these differences and a peak is produced.

In pharmaceutical product development, DSC has been mostly used to study the melting responses of the sample to the heating. However, many studies have also been carried out

on the crystallization, glass transitions, kinetic reactions and differentiation between polymorphs [343, 344].

Operating conditions

In this project, DSC analysis was performed to analyse the physical properties of G/X SOS and G/X SOS with and without loading of APIs (**Chapter 5**). DSC measurements were conducted on a TA Instruments DSC Q2000 (New Castle, DE, USA), equipped with an RSC 90 cooling unit which had been calibrated with indium, tin, and N-octadecane. The sample weights were between 2–3 mg with a heating rate of 10 °C/min over the temperature range 0–250 °C (**Chapter 5**). Triplicate measurements for each sample were performed.

2.4.6 Thermal gravimetric analysis (TGA)

Basic principle

Thermal gravimetric analysis (TGA) is another type of thermoanalytical technique that is used to evaluate the thermal performance of a material by accurately measuring the material weight loss over time as the temperature changes, under a controlled atmosphere. When the sample is subjected to a heating or isotherm at a certain temperature, the chemical and physical processes occur, e.g. decomposition, oxidation or sublimation. These processes are accompanied by mass loss. These mass changes are constantly measured by thermobalance, consisting of an electronic microbalance, a furnace and appropriate temperature controller, and is plotted as temperature/% mass or time/% mass on x- and y-axes.

TGA methods have been employed successfully in pharmaceutical studies to obtain information regarding thermal and oxidative stability, life expectancy, decomposition profile, moisture and volatiles content and partial chemical analyses that occur at a temperature characteristic for producing a particular reaction [343, 345].

Operating conditions

Thermal stability and moisture uptake of raw material, physical mixture and processed samples (5–7mg) (**Chapter 5**) were studied using a TGA Q5000 (TA Instruments, New Castle, DE, USA). The experiments were carried out at atmospheric pressure, under a nitrogen

atmosphere, with a flow rate of 60 ml/min, at linear heating rates of 10°C/min, in the range 0–400 °C. All experiments were performed in triplicate (n=3).

2.4.7 Texture analyser

Basic principle

A *texture analyser* provides a versatile technique and it is commonly used in industry to study the mechanical response of the materials that are linked to the surface or the internal structure of materials. The testing is performed by physically deforming the analysed sample in a controlled manner and measuring its response [346]. The following mechanical parameters can be described:

1. deformability (force required to achieve certain deformation);
2. adhesiveness (the work required to overcome the attractive forces that exist between the surfaces of the sample by the probe);
3. compressibility (the flow of the sample in response to compression) [347].

These parameters can give an indication of the sensory properties and provide an evaluation of the textural behaviour of the product [348]. Therefore, it is very useful in drug and food product development, quality control and manufacturing. In addition, it has been used to analyse the texture of a wide range of protein gels, including gelatine [349].

Operating conditions

The textural properties of SOS subjected to compression were measured using a TA-XT2 Plus Texture analyser (Stable Micro Systems Ltd, UK). A compression test mode was conducted with the following test sequence: zero force, remember position in memory location 1, move to force of 1 gram at 0.5mm/sec, move force to 30,000 grams at 0.5mm/sec, wait for 30 seconds, move to position stored in memory location 1 at 1 mm/sec. The load cell is 30 kg with a 25mm diameter aluminium cylinder. All experiments were performed in triplicate (n=3).

2.4.8 Particle size analysis

2.4.8.1 Dynamic light scattering (DLS)

Basic principle

Dynamic light scattering (DLS), which is also known as photon correlation spectroscopy or quasi-elastic light scattering, is a particle size distribution characterization technique commonly used to measure nanoparticulate colloidal systems, such as emulsions, micelles, liposomes and nanosuspensions. The technique particle sizing can be as low as 2 nm. However, larger particles (>3 μm) may cause misrepresentation of the measurements and, therefore, additional corroboration with laser diffraction (LD) or a laser scattering technique is recommended. The operation principle is that DLS calculates the diffusion coefficients of particles undergoing Brownian motion. When a laser beam is passed through a colloidal solution, the light is scattered off the particle and its intensity experience fluctuates [350]. The important characteristic of larger particles is that they have slower Brownian motion and the light propagates slowly, whereas small particles have faster Brownian motion and fluctuate quickly [351]. The DLS measures this fluctuation rate at a given scatter angle as a function of time and generates an exponentially decaying autocorrelation function [350]. This function is then analysed to determine the diffusion coefficient (D_t), which in turn can be used to measure the hydrodynamic diameter (D_H) of spherical particles using the Stokes-Einstein equation:

$$D_H = \frac{k_B T}{3\pi\eta D_t} \dots \dots \dots (2.2)$$

Where D_H is the hydrodynamic diameter, D_t is the translational diffusion coefficient, k_B is Boltzmann's constant, T is temperature and η is dynamic viscosity. For rod-like particles, the equation for D_t is given elsewhere [351]. Thus, DLS calculates the hydrodynamic size and, therefore, the particle diameter measured in DLS is inferred as being the particle size or hydrodynamic diameter.

Operating conditions

First, emulsions were characterized using a DLS technique using a Zetasizer Nano ZS instrument (Malvern Instruments Ltd., Worcestershire, UK) with the assumption that they have smaller particle size distribution (**Chapter 4**). A prepared O/W emulsion was divided into two parts, one part to be stored at room temperature and the other part at fridge temperature. The particle size distribution was measured immediately after emulsification and again after 7 days. All samples were highly diluted in Milli-Q water and measured in Milli-Q water. The results of DLS analysis were reported as the average of 3 measurements.

2.4.8.2 Laser diffraction (LD)

Basic principle

Laser diffraction (LD) is the most popular particle size distribution characterization technique in the pharmaceutical industry due to its ease of use, high precision, reproducibility and short analytical time [350]. Its range of applicability includes powders, suspensions and emulsions with a particle size distribution ranging from 0.1 μm to 3000 μm [352]. The basic principle is based on the evidence that particles of a given size diffract light through a given angle that increases logarithmically with decreasing size and vice versa [353]. The interaction of light with matter is calculated based on the algorithm of the Mie scattering theory, with its assumption that all particles have spherical morphology. The algorithm, at its core, consists of an optical system for Fourier transformation of the diffracted light onto a position-sensitive detector [350]. Additionally, users need to provide the refractive index of particles and dispersing medium. The instruments used mainly consist of a standard He-Ne laser high intensity light source, a sample handling system and an array of high quality photodiodes that record the angle and intensity of scattered light. The main drawbacks relate to particles having small sizes ($<1 \mu\text{m}$), non-spherical morphology and a low refractive index [354].

Operating conditions

Emulsions were analysed in a laser diffraction Helos/Rodos 1636 (Sympatec GmbH, Germany), as from the DLS results we concluded that emulsions have larger particle size distribution (**Chapter 4, 5**). All emulsions were highly diluted in an aqueous phase before analysing. All

experiments were performed in triplicate (n=3). The obtained data was evaluated using volume distribution as diameter (d) values of 10%, 50% and 90%. The diameter values show the percentage of particles that have a diameter equal to or lower than the given value.

2.4.9 In vitro dissolution testing

Basic principle

Dissolution testing is an important aspect in the development and quality control of pharmaceutical products, and it is employed to measure the dissolution rate of an API from a dosage formulation according to standardized conditions reported in official pharmacopoeia. It is an *in vitro* method used as a predictive tool for the *in vivo* performance of the drug and consequently its bioavailability. The dissolution testing of solid oral dosage forms is generally performed using USP-approved apparatuses and different dissolution media, listed in **Table 2.5**. The principle of dissolution testing is that the dosage unit is placed within the medium that simulates gastric and intestinal fluids, and the dissolution apparatus keeps the temperature of the medium at $37\text{ }^{\circ}\text{C}\pm 1$ and provides hydrodynamics (a fixed speed of agitation). As a result, the delivery system starts to solubilize in a given solvent and releases the drug. Then, a small amount of aliquot is withdrawn from the dissolution media within the specified time interval and is analysed by high-pressure liquid chromatography (HPLC) or UV-Vis spectroscopy to estimate the amount of drug released per unit time.

Table 2.5. USP-approved apparatuses for dissolution testing and different dissolution media used in experiments provided by British Pharmacopoeia (BP).

Dissolution testing apparatus	Dissolution media
Basket apparatus (USP 1)	Water
Paddle apparatus (USP 2)	Buffers
Reciprocating Cylinder apparatus (USP 3)	HCl solution
Flow through cell (USP 4)	Simulated gastric fluid
Paddle-over-disk (USP 5)	Simulated intestinal fluid
Cylinder (USP 6)	Surfactant solution
Reciprocating holders (USP 7)	

In this study, the USP apparatus 2 and UV-Vis spectroscopy were used to perform dissolution testing of G/X SOS in **Chapter 5**. USP apparatus 2 is the most commonly employed dissolution method to characterize oral solid-dosage forms of immediate-, modified-, and extended releases along with the basket method (USP1) [355], due to their simplicity, robustness and flexibility, and the fact they are well standardized and used worldwide [356]. It is the assembly from apparatus 1, i.e. it consists of a vessel, a motor and water bath, and in addition to that it uses a paddle formed from a blade and a shaft as the agitating element. The dosage unit can be sunk using a small piece of nonreactive wire helix or alternative sinker to prevent the unit from floating [357].

All drug concentrations of the dissolution testing samples were analysed using an *ultraviolet-visible (UV-Vis) spectroscopy*. UV-Vis spectroscopy measures the absorbance of ultra violet (UV – 190–400 nm) or visible light (Vis – 400–800 nm) of a sample and can provide both quantitative and qualitative information. The UV-Vis spectroscopy either performs a scan over a range in the spectrum or at a single wavelength. When light passes through the sample, some of the light is absorbed and some of the light is transmitted. Absorption of UV and Vis radiation induces electron transition from a ground state to an excited state. The UV-Vis spectroscopy process identifies which wavelengths were absorbed by the sample and to what extent the absorption occurred. It presents the results as a diagram with maximum absorption peak at specified wavelength and transmitted troughs.

UV-Vis spectroscopy can provide quantitative information according to the Beer-Lambert law, which states that the absorbance is proportional to the concentration of the substance in solution, as follows:

$$A = \varepsilon cl. \dots\dots\dots (2.3)$$

Where A is absorbance, ε is molar extinction, which is constant for a particular substance at a particular wavelength ($\text{dm}^3 \text{mol}^{-1} \text{cm}^{-1}$), c is concentration of solution (mol dm^{-3}) and l is optical path length, i.e. the dimension of the cell or cuvette (cm) [358].

Operating conditions

The *in vitro* dissolution testing of MS was performed using the BP paddle method using dissolution apparatus No. 2. The dissolution runs were carried out at $37\text{ }^{\circ}\text{C}\pm 1$ and an agitation speed of 100 rpm. The dissolution medium was 500 ml of pH 1.2 to simulate gastric juice prepared according to BP. The concentration of the drug in the dissolution media was 0.18 mg/ml. A basket sinker was used to prevent a dosage form from floating. A 5 ml aliquot of filtered medium was withdrawn at specific time points (3, 6, 9, 12, 15, 20, 30, 45, 60 and 90 minutes), and the drawn volume was replaced with a blank dissolution medium. An aliquot was filtered using a $0.22\text{ }\mu\text{m}$ Polyethersulfone membrane (EMD Millipore™, Fisher Scientific) and the absorbance of the filtrate was measured by UV-Vis spectroscopy (Perkin-Elmer 35 UV-Vis double-beam spectrometer) in a quartz cuvette (Hellma™ Suprasil™, Fisher Scientific, with a path length of 10 mm) over the range 240–350 nm. The λ_{max} of the drug was at 263–274 nm. The λ_{max} of MS given in the literature are 274 nm [228] and 222 nm [222]. The amount of released MS was calculated in a calibration curve. The calibration curve for MS was obtained by measuring the series of a standard solution with concentration from 0.00625 to 0.2 mg/ml with UV-Vis spectroscopy and a plot was made from the absorbance as a function of their concentration. The R^2 values for the calibration curve were 0.999.

3 Chapter 3. Development of an orodispersible film for delivering hydrophilic nutritional supplements

3.1 Introduction

As with pharmaceutical active ingredients, nutritional supplemental compounds can be loosely categorised by their solubility in aqueous media. The development of a novel delivery method for hydrophilic compounds with good aqueous solubility is the focus of this chapter. Iodine is used as the targeted nutritional compound.

As discussed in **Chapter 1**, iodine deficiency is still a major health problem in many developing countries and in some developed countries [25-30]. Therefore, in particular for developing countries, there is an increasing demand for new cost-effective iodine medicaments/supplements, especially to meet the needs of the paediatric population. This study reports the development of ultra-rapidly dissolving orodispersible films as an alternative solid form of iodine delivery, which can meet this urgent need for tackling paediatric iodine deficiency.

In this chapter, we propose and demonstrate the use of orodispersible films that are made with an overlapping iodine loaded nanofibre network to provide ultra-rapid disintegration and dissolution once wetted. Additional water, as is commonly used when taking conventional tablets and capsules and for the swallowing of bulky solids, is not required for the administration of this orodispersible film. The child only needs to put the film on the tongue, the formulation will dissolve rapidly in saliva, and the iodine can be largely absorbed by a conventional gastrointestinal route. It is anticipated that a small proportion of the saliva-dissolved iodine may also be absorbed via the buccal mucosa within the oral cavity, which has the advantage of both rapid uptake and the bypassing of the hepatic metabolism [72, 82]. This delivery concept can also benefit other unfulfilled therapeutic needs, such as providing emergency medications for patients who are unable to swallow conventional tablets and capsules, such as geriatric patients with dysphagia and unconscious patients who are in seizure.

The nanofibre-based orodispersible films were produced using electrospinning, which has recently attracted increased interest in the pharmaceutical, biomedical, food, and tissue engineering fields [89, 91, 359-362] (a detailed description of the electrospinning technology can be found in **Chapter 1, section 1.6**). The main advantages of nanofibres as a delivery system are their high surface to volume ratio, enhanced drug loading capacity, and relative cost effectiveness [234, 363, 364]. However, the characterization of the nanofibres can be challenging as a result of their submicrometre dimensions, but this characterization is crucial for understanding and thereby controlling the in vitro and in vivo performance, and the stability of the formulations. In this study, KIO_3 , which is the most stable form of iodine source under stressed conditions [365], was used as the active ingredient. In order to maximize the stability of KIO_3 and be able to form films that can be easily handled in practice and with a uniform distribution of a low dose of KIO_3 , PEO was used to form a solid dispersion with KIO_3 . PEO is easily processed by electrospinning and is water soluble [102, 235], which makes it a good carrier material for KIO_3 .

Despite a rich literature base that has provided insight into solid dispersion-based formulations, there is a lack of information regarding their use in the delivery of inorganic molecules. This study provides a thorough investigation into the behaviour of such a system. The results reveal the formation of nanocrystals of KIO_3 within the nanofibres at relatively lower loading concentrations than is the case with many organic, low molecular weight drugs [366]. The results of this chapter have demonstrated two significant outcomes: (1) the development of a prototype form of a novel solid oral paediatric iodine formulation which requires no water and swallowing for administration and (2) a considerable contribution to improving the understanding of solid dispersions containing inorganic molecules and the production of inorganic nanocrystals using a quick, simple, and organic solvent-free electrospinning method.

3.2 Materials and methods

3.2.1 Materials

The materials used in this Chapter are KI, KIO₃, PEO 300K, PEO 600K, PVP 90K, NaCl, H₂SO₄ and methylene blue dye. Their physicochemical properties are described in **Chapter 2 sections 2.2, 2.2.1 and 2.2.4.**

3.2.2 Methodology

3.2.2.1 Electrospinning

The electrospinning setup is given in **Chapter 2, section 2.3.1.**

PEO placebo nanofibres preparation

PEO 600K and PEO 300K were dissolved in aqueous media in 5 and 7 w/v % concentrations. The EPPs were as follows: the distance between the tip of the needle and the collector was 250mm, the flow rate was 0.1 ml/h, 0.5 ml/h and the applied DC voltage was from 12 to 15 kV (250 mm – 0.1 ml/h, 0.5 ml/h – 12–15 kV).

PEO/KI nanofibres preparation

We studied two grades of PEO with an average Mw of 6×10^5 g/mol and 3×10^5 g/mol, and two total solution concentrations of 5 and 7 w/v %. This is because their solutions have different viscosities which could affect the obtained fibres produced using electrospinning. The solution of PEO and KI was prepared by dissolving them in aqueous media in different w/w %, namely 99.86/0.14, 98/2, 90/10 w/w % (**Table 3.1**). Also, PEO and KI were dissolved in the ethanol/water (Eth/w) media, where the Eth/w concentrations were 30/70, 70/30, 40/60, 60/40 v/v % and the PEO/KI concentrations were 70/30, 85/15, 95/5 w/w %. The EPPs were as follows: 150, 250 mm – 0.1 ml/h, 0.5 ml/h – 12–15 kV.

Table 3.1. The polymer and KI salt concentration in the aqueous solution.

Total solution concentration (w/v %)	PEO/KI (w/w %)	Sample N
PEO 300K		
5	90/10	3.1.1
PEO 600K		
5	90/10	3.1.2
7	90/10	3.1.3
5	98/2	3.1.4
7	98/2	3.1.5
7	99.86/0.14	3.1.6

PEO/KIO₃ and PEO/NaCl nanofibres preparation

PEO and KIO₃ were dissolved in water in different concentrations. The concentration of KIO₃ in the solution was calculated in molar concentration and then the mass of KIO₃ was converted to wt. % with regard to PEO wt. % (**Table 3.2**), simply to make the numbers more convenient for a reader. Overall, the solid content concentrations of the electrospinning solutions were 3, 5 and 7 w/v %. The EPPs were as follows: 150 mm, 200 mm, 250 mm – 0.2 ml/h, 0.5 ml/h, 0.75 ml/h, 1 ml/h – 12–25 kV.

Table 3.2. Molar concentration of KIO₃ in the solution and its wt. % with regard to PEO wt. %.

Sample N	KIO ₃ molar concentration (M)	PEO/KIO ₃ w/w %
3.1	0.001	99.6/0.4
3.2	0.002	99.1/0.9
3.3	0.003	98.7/1.3
3.4	0.005	98/2
3.5	0.007	97/3
3.6	0.01	96/4
3.7	0.02	91/9
3.8	0.03	87/13
3.9	0.05	79/21
3.10	0.07	70/30
3.11	0.1	57/43
3.12	0.15	36/64
3.13	0.2	14/86

PEO and NaCl were dissolved in water in different w/w % concentrations, namely 87/13, 79/21, 57/43 w/w %. The total solid content concentration of the electrospinning solution was 5 w/v %. The EPPs were as follows: 150 mm, 200 mm, 250 mm – 0.2 ml/h, 0.5 ml/h, 0.75 ml/h, 1 ml/h – 12–25 kV. When the rotating drum was used the EPPs: 1,000 rpm – 150 mm – 0.5 ml/h – 22–30 kV.

PEO/PVP/KIO₃ nanofibres preparation

A PEO 600K/PVP 90K blend was prepared as follows: the total aqueous solution concentration was 5 w/v % and the PEO to PVP w/w % were 30/70 and 70/30. The KIO₃ concentrations in the formulation were 0.4, 2, 4, 5, 21, 43 w/w %. The EPPs were as follows: 150 mm – 0.5 ml/h – 13–19 kV.

PVP/KIO₃ and PVP/NaCl nanofibres preparation

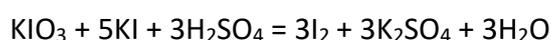
PVP/KIO₃ solutions were electrospun to compare with the PEO/KIO₃ formulation. The total solution concentration was 10 w/v and the PVP/KIO₃ wt. % were 87/13 and 36/64. The EPPs were as follows: 150 mm – 0.5 ml/h – until 26 kV.

The electrospun PVP fibres containing lower KIO₃ or NaCl concentrations were prepared to investigate the effect of polymer type on the formation of inorganic nanocrystals. PVP and crystalline salts were dissolved in aqueous solution, where the total solution concentration was 10 and 15 w/v % and the solid salt concentrations ranged from 4 to 14 w/w %. The EPPs were as follows: 150 mm – 0.5 ml/h – until 30 kV.

3.2.2.2 Wetting and dissolution testing

The wettability of the films was tested using a moist filter paper method described previously in the literature [93]. In summary, a piece of cellulose filter paper (Sigma-Aldrich, Gillingham, Dorset, UK) was wetted and saturated with distilled water. The filter paper was then placed in a Petri dish, and a piece of the electrospun film was placed on top of the wetted filter paper. The time taken for the film to transform from a dry and opaque colour to invisible (indicating complete wetting) was recorded. The tests were repeated at least three times. The dissolution tests of the ultra-rapidly dissolving orodispersible films were performed simply because the dissolution process was rapid. Placebo and KIO₃-loaded films were dissolved in water by

gentle stirring in a Petri dish, and the time taken for the film to dissolve was recorded. In order to see the release of KIO_3 , an iodometric reaction was used. An excess amount of KI and a small drop of methylene blue dye were added to water. A 1M H_2SO_4 solution was added after placing the fibre film in water to see the immediate release of iodine to confirm the fast release of the active ingredient from the carrier material. Methylene blue dye was used as a colourant indicator to allow the identification of the release of active ingredient. This is because the fibre films were white and became transparent and difficult to see in water. KIO_3 is a good oxidizing agent which oxidizes iodide to iodine in acidic media and indicates the colour change via the reaction:



3.2.3 Characterization techniques

The films were characterized with a range of analytical techniques described in **Chapter 2**. The morphology of the nanofibres and the physical form of the active ingredient were identified by means of microscopes such as SEM and TEM. The spatial distribution of KIO_3 nanocrystals in the fibrous mat was confirmed with the SEM-EDS instrument. The effect of KIO_3 loading on the solid-state physicochemical properties of the nanofibres was explored using PXRD and ATR-FT IR. The KIO_3 loaded fibres demonstrated ultra-fast disintegration and dissolution behaviour on conducting a wetting test using a moist filter paper method. The detailed methodologies of the characterization can be found in the relevant sections in **Chapter 2**.

3.3 Results and discussions

3.3.1 Impact of KI and KIO₃ incorporation on fibre formation

3.3.1.1 PEO loaded with KI

The morphology of the electrospun PEO/KI solutions was evaluated using the surface characterizing SEM technique. **Figure 1** represents the SEM images of PEO loaded with KI. As can be seen, all samples failed to form fibres, except PEO 600K loaded with 0.14 w/w % of KI. As discussed in **Chapter 1**, the production rate of electrospinning can be improved by adding some salts into the solution [99]. However, this study shows that not all salts facilitate better fibre formation. Although salts can improve the fibre diameter, they do not necessarily prevent the break-up of the jet. KI could favour fibre formation only at 0.14 w/w % concentration. All other samples with 10 and 2 w/w % concentration failed to form fibres, irrespective of the polymer molecular weight and concentration; instead, large crystals of KI were seen on the SEM images (**Figure 3.1**).

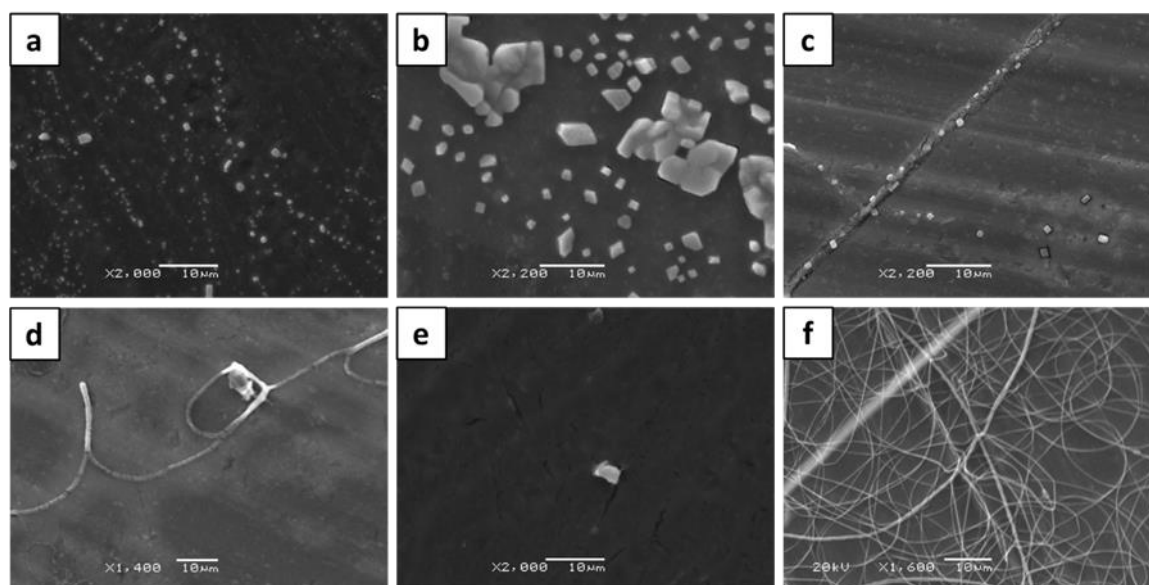


Figure 3.1. SEM images of PEO loaded with KI: a) sample N3.1.1; b) sample N 3.1.2; c) sample N3.1.3; d) sample N3.1.4; e) sample N3.1.5; f) sample N3.1.6 (**Table 3.2**). The EPPs: 150 mm, 0.5 ml/h, 12–21 kV.

3.3.1.1.1 Effect of the solvent

Fong et al. [102] reported that the addition of ethanol to the aqueous solution decreases the surface tension and increases the viscosity of the solution, because ethanol makes the solvent evaporate easier and thus increases the viscosity of the liquid jet. These two factors, the decreased surface tension and increased viscosity, makes the fibres smooth and non-beaded. Therefore, we changed the solvent to change the surface tension of the solution by varying the ethanol ratio. However, it was found that this does not improve fibre formation: the ethanol to water ratio has no effect on the fibre formation for this formulation. Fibres were obtained only with a sample with low KI content (**Figures 3.2 and 3.3**). In the first sample, when the Eth/w concentration was 30/70 v/v % and the PEO/KI concentration was 70/30 w/w %, fibres were not formed at all, whereas decreasing the KI content in the formulation by 15 w/w % could form fused fibres (**Figures 3.2a and 3.2b**). In comparison, the same concentration of PEO/KI, i.e. 85/15 w/w %, but with the ethanol concentration increased to 70 v/v % could yield smooth fibres (**Figure 3.2d**). However, when the KI concentration was high, as in the first sample, i.e. at 30 w/w %, the increased ethanol concentration to 70 v/v % does not improve fibre formation at all (**Figure 3.2c**). The same observation was performed for samples with 40/60 and 60/40 v/v % of Eth/w (**Figure 3.3**). Samples with a high ethanol content, namely 60 v/v %, and a low KI content, namely below 15 w/w %, yielded smooth nanofibres (**Figures 3.3e and 3.3f**). Smooth nanofibres were fabricated with a sample where the ethanol content was low, i.e. 40 v/v %; however, as in the previous experiment, the KI content was much lower, namely 5 w/w % (**Figure 3.3c**). Therefore, we concluded that ethanol decreases the surface tension and increases the viscosity so the fibres were formed; however when the KI content is high, the high ethanol concentration could not facilitate the fibre formation. These results suggest that KI has a greater impact on fibre formation. We anticipate that KI forms larger crystals in the jet, which can be seen in the figures above (**Figures 3.1a-c**), and thus break-up the jet. In addition, although, the SEM images showed that fibres could be yielded with a low KI content, the obtained nanofibre mat showed a yellowish colour, indicating the oxidation of iodide (the picture could not show the yellowish colour and therefore it is not given).

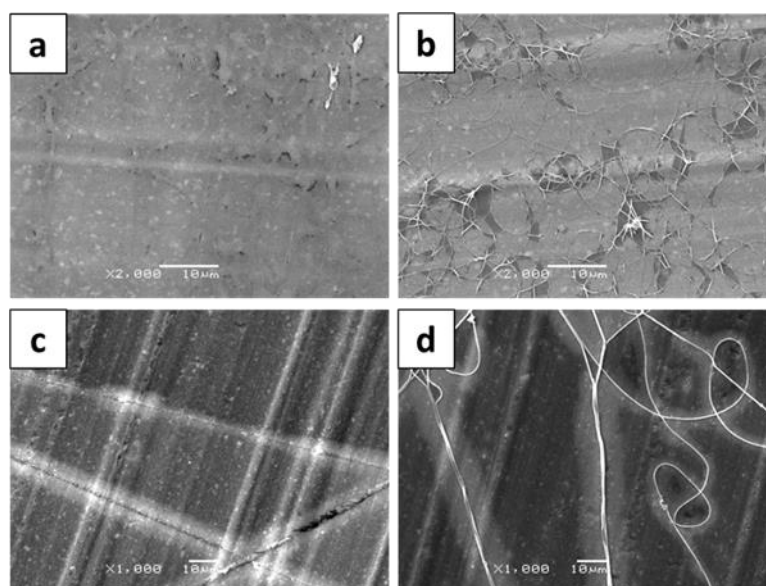


Figure 3.2. SEM images of PEO loaded with KI and the solution is Ethanol-Water: a) Eth/w-30/70 v/v %, PEO/KI-70/30 w/w %; b) Eth/w-30/70 v/v %, PEO/KI-85/15 w/w %; c) Eth/water-70/30 v/v %, PEO/KI-70/30 w/w %; d) Eth/w-70/30 v/v %, PEO/KI-85/15 w/w %. The total solution concentration was 5 w/v %. The EPPs were held at a constant for all samples: 250 mm – 0.1 ml/h – 12 kV.

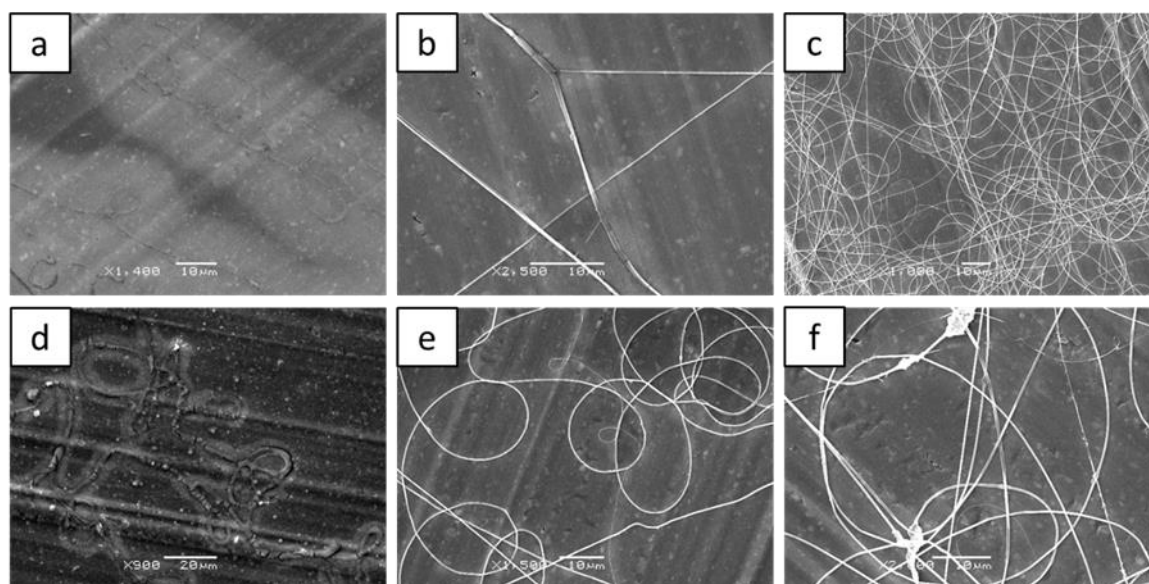


Figure 3.3. SEM images of PEO loaded KI and the solution is Ethanol-Water: a) Eth/w-40/60 v/v %, PEO/KI-70/30 w/w %; b) Eth/w-40/60 v/v %, PEO/KI-85/15 w/w %; c) Eth/w-40/60 v/v %, PEO/KI-95/5 w/w %; d) Eth/w-60/40 v/v %, PEO/KI-70/30 w/w %; e) Eth/w-60/40 v/v %, PEO/KI-85/15 w/w %; f) Eth/w-60/40 v/v %, PEO/KI-95/5 w/w %. The total solution

concentration was 5 w/v %. The EPPs were held at a constant for all samples: 250 mm – 0.1 ml/h – 12 kV.

3.3.1.2 PEO loaded with KIO_3

As PEO/KI formulations failed to form good fibres by electrospinning, an alternative iodine salt, KIO_3 was used. From the SEM images (**Figure 3.4**), it can be seen that the beaded fibres can be obtained if PEO is loaded with KIO_3 , even at high concentration, namely 43 w/w % (N3.11). Although it was beaded, the formulation was electrospinnable. The literature says that actually, K^+ ions form complexes with the ether oxygen of PEO and thus assist in separating the polymer chains and act as a plasticizer [367-370]. This increases the ionic conductivity of the solution and consequently should increase the production rate of fibres. However, this was the case with the sample with KIO_3 but not with KI. As discussed earlier, the reason might be due to the fast crystallization rate of KI and larger crystal sizes of KI in the jet.

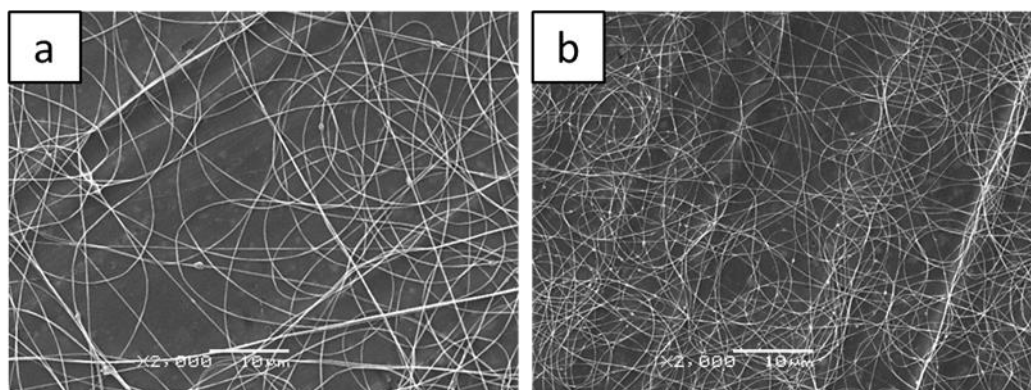


Figure 3.4. PEO loaded with KIO_3 : a) PEO 600K/ KIO_3 -96/4 w/w % (N3.6); b) PEO 600K/ KIO_3 -57/43 w/w % (N3.11). The total solution concentration was 5 w/v %. The EPPs: 250 mm – 0.1 ml/h – 12–15 kV.

3.3.1.2.1 Effect of the solvent

PEO/ KIO_3 was also dissolved in ethanol/water to study the effect of solvent on fibre morphology. The results showed no significant effect on fibre morphology, indicating that the solution concentration is more important than the solvent properties for that formulation

(Figure 3.5). Therefore, it was decided to use only water for further formulations to avoid the use of a hazardous organic solvent.

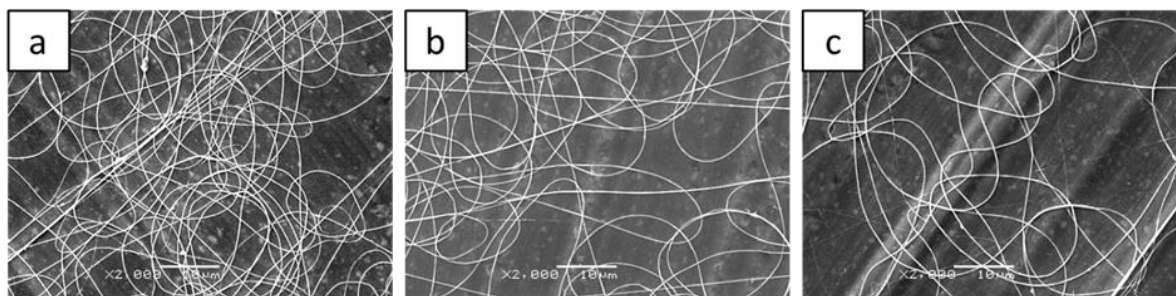


Figure 3.5. PEO 600K loaded with KIO_3 and the solution is Ethanol-Water, volume ratio 40/60 v/v: a) PEO/ KIO_3 -70/30 w/w %; b) PEO/ KIO_3 -85/15 w/w %; c) PEO/ KIO_3 -95/5 w/w %. The total solution concentration was 5 w/v %. The EPPs: 250 mm – 0.1 ml/h – 12 kV.

3.3.2 Formulation optimization

3.3.2.1 Effect of polymer concentration

In order to study the optimum polymer concentration to produce smooth nanofibres, the SEM technique was used to characterize the dimensions and surface morphologies of the nanofibre. PEO with a Mw. of 600K yielded smooth placebo nanofibres with a uniform diameter range between 50 nm and 1.2 μm (measured using ImageJ analysis software), as seen in the images (**Figures 3.6b and 3.6d**). Beaded nanofibres were obtained with the sample prepared using PEO with Mw. 300K (**Figures 3.6a and 3.6c**). The solution concentration with the same Mw. produced insignificant variations, which resulted in the same form.

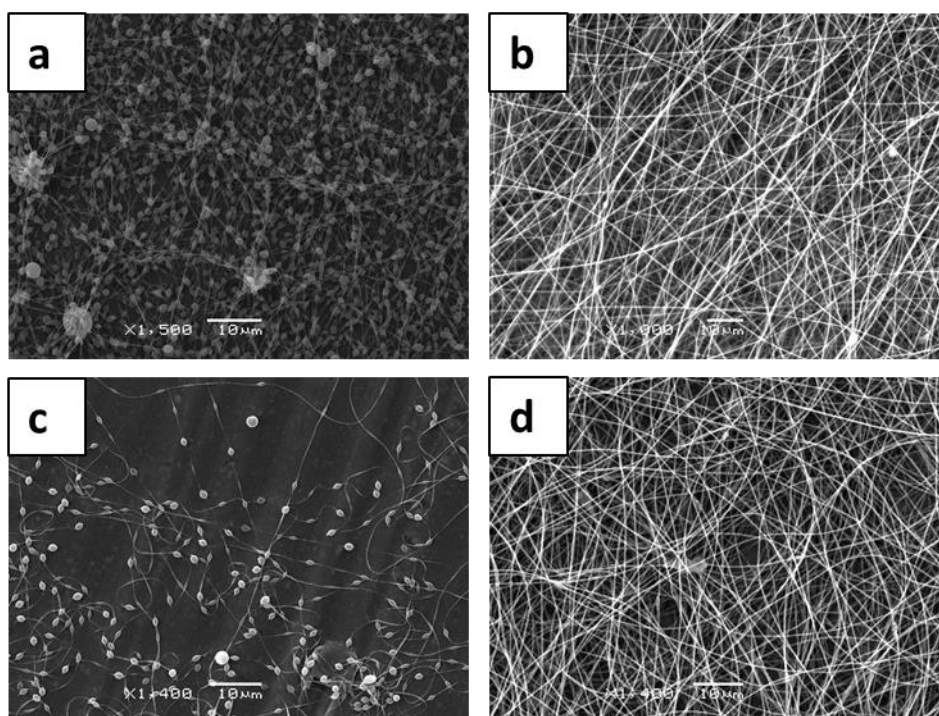


Figure 3.6. SEM images of placebo PEO nanofibres with different concentrations: a) 5 w/v % solution concentration, PEO 300K; b) 5 w/v % solution concentration, PEO 600K; c) 7 w/v % solution concentration, PEO 300K; d) 7 w/v % solution concentration, PEO 600K. The EPPs: 150 mm – 0.5 ml/h – 10kV–12kV.

3.3.2.2 Probing maximum loading of KIO_3

The addition of KIO_3 up to 21 w/w % (N3.9) led to a slightly reduced fibre diameter but no change in the fibre morphology (**Figures 3.7a to 3.7e**). Using the formation of nanofibre films, which can be easily peeled off from the collector surface as the key measure, a maximum loading of KIO_3 was also studied. The optimal loading range to result in an elastic and easy-to-peel fibre film with smooth and uniform fibre was up to 21 w/w % (N3.9) of KIO_3 loading with a 0.2 mL/h feeding rate. Further increases in KIO_3 content to above 43 w/w % (N3.11) led to the formation of beaded (formation of small beads on the fibres) nanofibres and brittle films (**Figure 3.7f**).

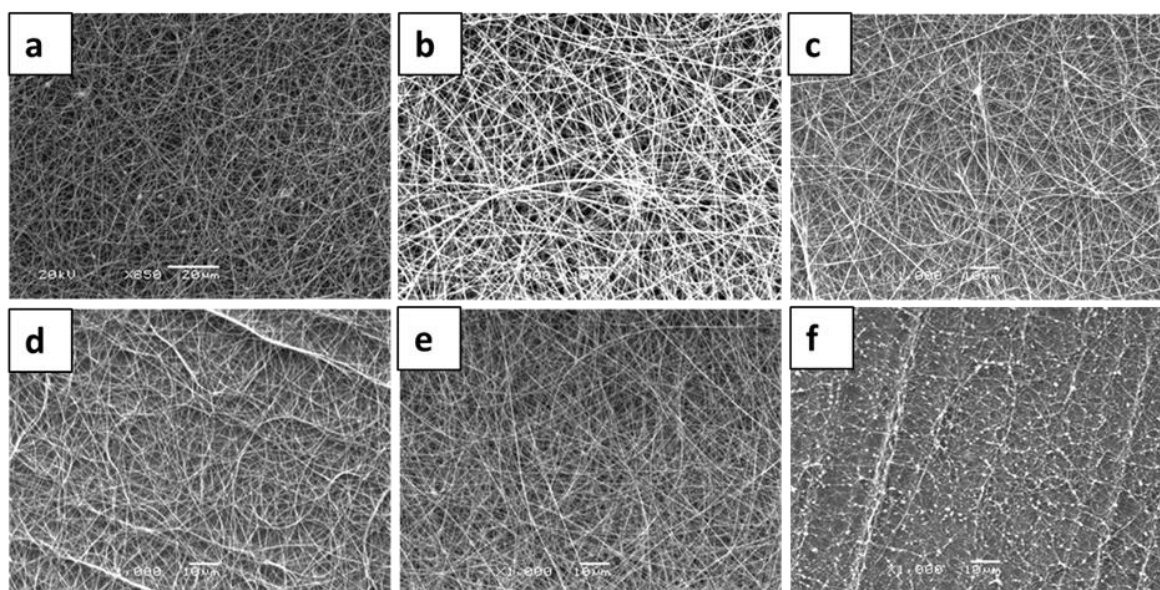


Figure 3.7. SEM images of PEO 600K nanofibres loaded with KIO_3 : a) 0.4 w/w % (N3.1); b) 2 w/w % (N3.4); c) 4 w/w % (N3.6); d) 13 w/w % (N3.8); e) 21 w/w % (N3.9); f) 43 w/w % (N3.11). The total solution concentration is 5 w/v %. The EPPs: 250 mm – 0.2 ml/h – 20–24 kV.

Nonetheless, it is possible to load up to 86 w/w % of KIO_3 (N3.13) into the fibre film, but the morphology of the fibres would be beaded and more particulate. As seen in **Figure 3.8**, beaded fibres form with a diameter of 2 μm , although the amount of KIO_3 loading was very high, 86 w/w %, potassium iodate crystals cannot be seen. Therefore, TEM analysis was performed and the results are in the sample characterization **section 3.3.5.2**.

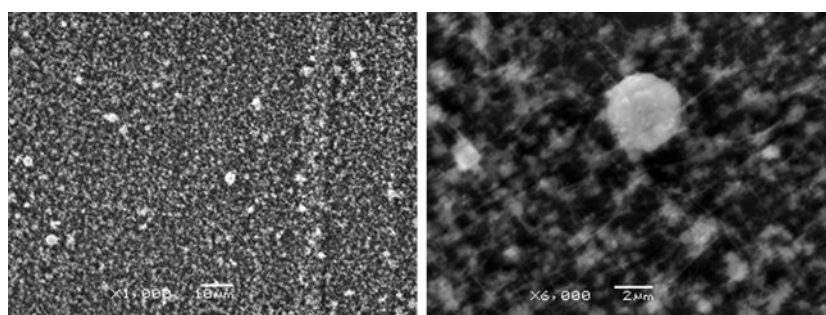


Figure 3.8. SEM images showing the film with the maximum 86 w/w % of KIO_3 (N3.13) concentration. The left and the right images are the lower and the higher magnifications, respectively. Total solution concentration was 5 w/v. The EPPs: 150 mm – 0.5 ml/h – 20 kV.

We checked the solution conductivity with the increase of KIO_3 to put on record the impact of KIO_3 on solution conductivity. As shown in **Table 3.3**, the solution conductivity increased proportionally to the content of KIO_3 .

Table 3.3. Solution conductivity of pure PEO polymer solution and PEO loaded with KIO_3 .

Solution (at 20 ± 2 °C)	Conductivity ($\mu\text{S}/\text{m}$)
Milli-Q water	1.2
5 w/v % of pure PEO 600K	61.9
5% w/v (PEO/ KIO_3 – 99/0.9 w/w %)	198.2
5% w/v (PEO/ KIO_3 – 98/2 w/w %)	464.0
5% w/v (PEO/ KIO_3 – 96/4 w/w %)	998.0
5% w/v (PEO/ KIO_3 – 87/13 w/w %)	3300.0

The amount of KIO_3 loading has a significant impact on fibre diameters. As seen in **Figure 3.9**, the fibre diameter size decreases with the increase of the KIO_3 concentration. The diameter sizes of the placebo nanofibres are from 100 nm to 700 nm, whereas the diameter size of the nanofibres loaded with 21 w/w % of KIO_3 (N3.9) are from 50 nm to 500 nm.

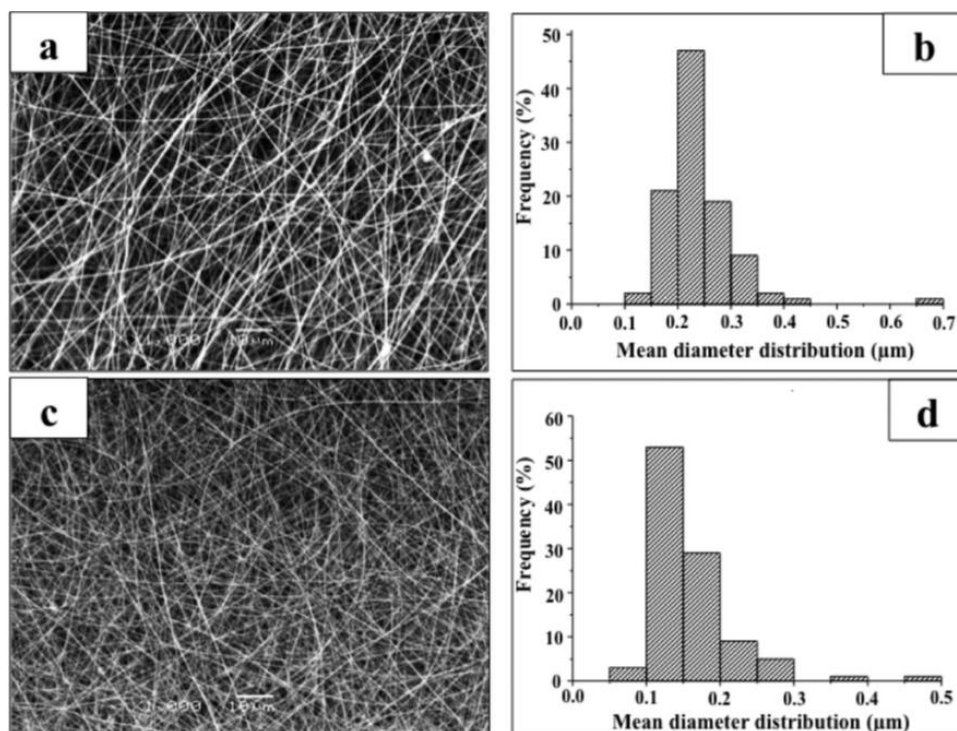


Figure 3.9. SEM images of the (a) morphology and (b) diameter size distribution of placebo nanofibres, respectively, (c) morphology and (d) diameter size distribution of PEO nanofibres.

nanofibres loaded with 21 w/w % of KIO_3 , (N3.9) respectively. The diameters of the nanofibres were measured using ImageJ analysis software.

3.3.3 PVP and PVP/PEO polymer blend loaded with KIO_3

We conducted a feasibility study with PVP/PEO blend because PVP is highly water-soluble and adding PVP into a PEO solution could improve the dissolution rate of the fibre mat. The SEM images showed significant differences in fibre morphology depending on the PVP to PEO ratio. Smooth and uniform nanofibres were obtained with samples containing 30/70 w/w % of PVP to PEO ratio and KIO_3 content from 0.4 to 21 w/w % (N3.1-3.9) (**Figure 3.10**). As was observed with pure PEO, beaded fibres formed when the KIO_3 content reached 43 w/w % (N3.11) (**Figure 3.10f**). On the other hand, samples with 70/30 w/w % of PVP/PEO ratio showed beaded fibres irrespective of the KIO_3 content (**Figure 3.11**). Spindle-like beads converted to rounded beads at 43 w/w of KIO_3 content (**Figure 3.11f**).

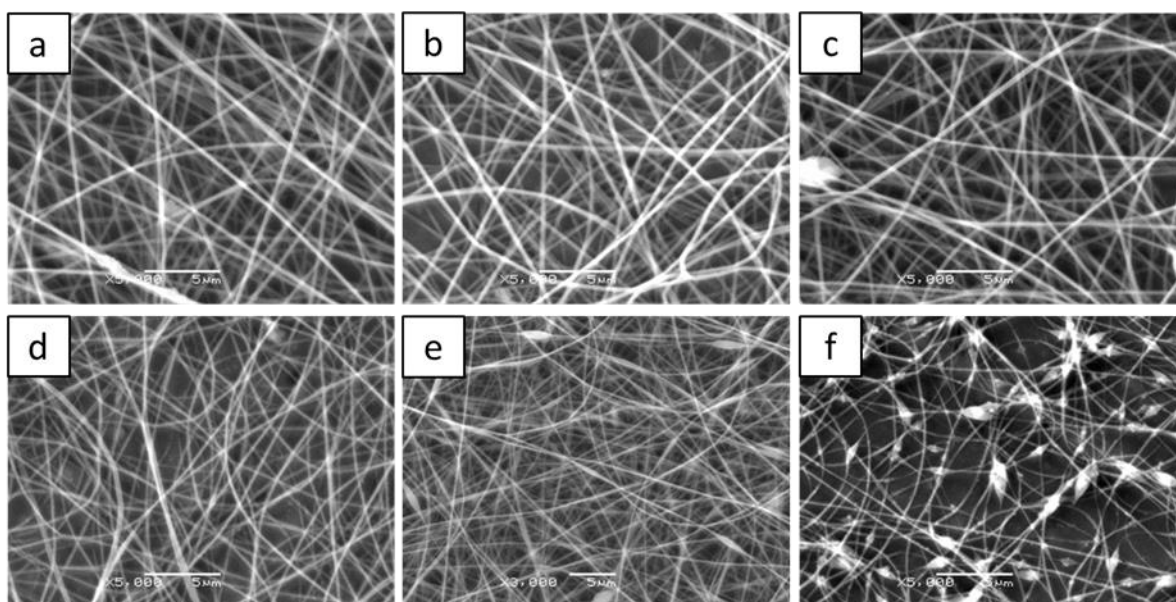


Figure 3.10. SEM images of PVP/PEO 600K 30/70 w/w % blend with different KIO_3 concentrations: a) with 0.4 w/w KIO_3 , 14kV; b) with 2 w/w % KIO_3 , 17kV; c) with 4 w/w % KIO_3 , 17kV; d) with 5 w/w % KIO_3 , 16kV; e) with 21 w/w % KIO_3 , 19kV; f) with 43 w/w % KIO_3 , 19kV. The total solution concentration was 5 w/w %. The EPPs: 0.5 ml/h – 150 mm.

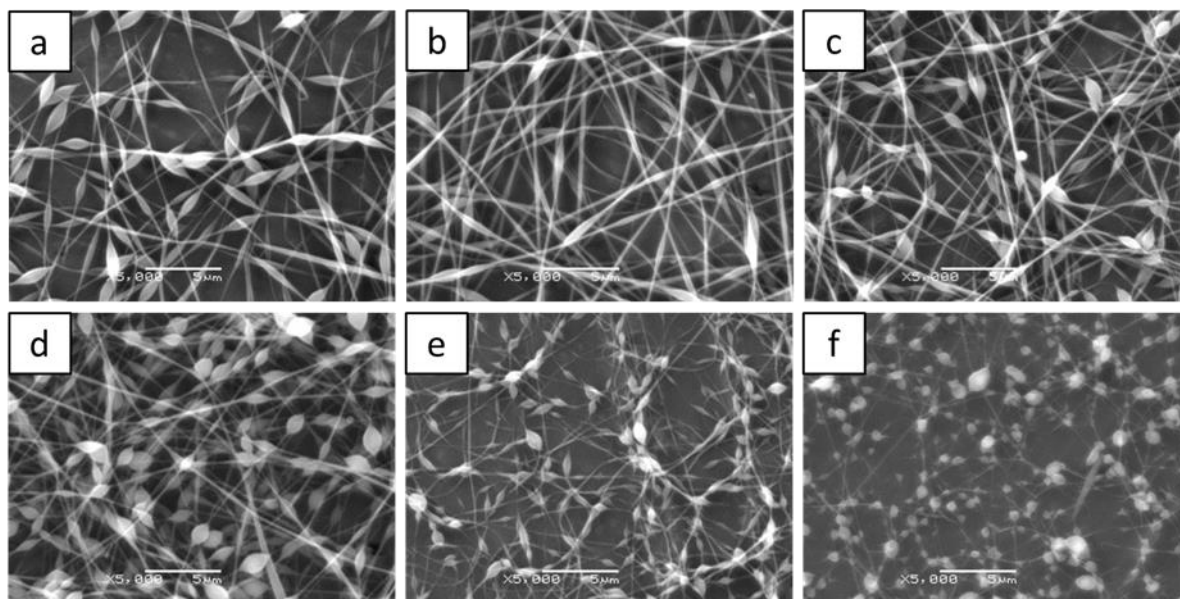


Figure 3.11. SEM images of PVP/PEO 600K 70/30 w/w % blend with different KIO_3 concentrations: a) with 0.4 w/w % of KIO_3 , 13kV; b) with 2 w/w % of KIO_3 , 15kV; c) with 4 w/w % of KIO_3 , 15kV; d) with 5 w/w % of KIO_3 , 13kV; e) with 21 w/w % of KIO_3 , 18kV; f) with 43 w/w % of KIO_3 , 18kV. The total solution concentration was 5 w/w %. The EPPs: 0.5 ml/h – 150 mm.

Pure PVP loaded with 13 w/w % KIO_3 showed rounded beads and no fibres with 64 w/w % KIO_3 (**Figure 3.12**). The results show that electrospinning of KIO_3 with PVP is feasible only with a low concentration of KIO_3 and, if the polymer concentration is decreased, it is possible to obtain polymer nanoparticles with smooth morphology by means of electrospinning. In order to obtain smooth nanofibres, probably a much higher PVP concentration is needed, for example 15-35 w/v %. However, in this study we did not investigate the PVP polymer solution concentration because it was a trial experiment. We wanted only to see if it is possible to obtain smooth nanofibres with PVP to increase the dissolution rate in aqueous media in the future.

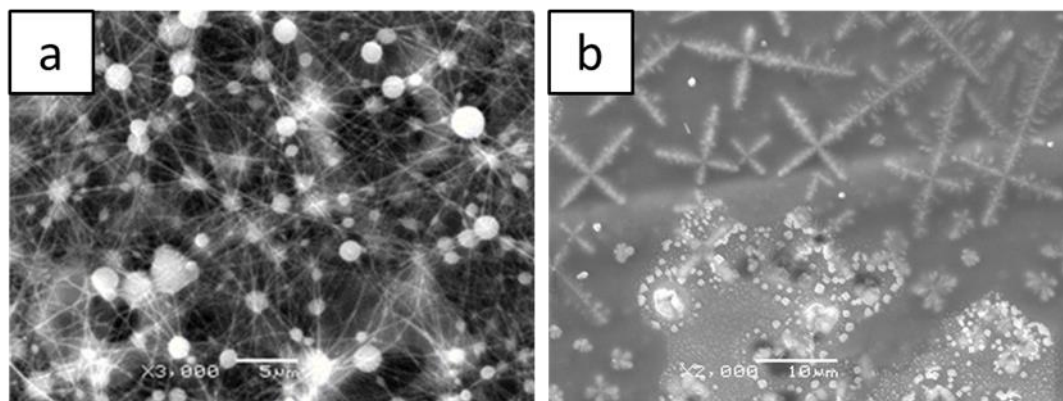


Figure 3.12. SEM images of PVP loaded with KIO_3 : a) with 13 w/w % of KIO_3 ; b) with 64 w/w % of KIO_3 . The total solution concentration was 10 w/v %. The EPPs: 150 mm – 0.5 ml/h – 26 kV.

3.3.4 Processing parameters optimization

Once an electrospinnable formulation is established, the processing parameters need to be optimized in order to obtain fibres with desirable physical properties, including the required morphology, fibre diameters and uniformity of fibre size. There are 5 main factors investigated in this chapter, namely the distance between the collector and the needle, the diameter of the needle, the applied DC voltage, the feeding rate and the type of collector.

3.3.4.1 Distance between the needle and collector

A number of researchers have studied the effect of the distance between the tip of the needle and collector and found that if the distance is too close or too far then beaded fibres are fabricated [117, 123]. In our study we found no difference when the distance was varied from 150 mm to 250 mm (**Figure 3.13**). This is in accordance with the studies undertaken with PVA [110] and PVDF [124]. Three different distances, namely 150 mm, 200 mm and 250 mm, yielded smooth and uniform nanofibres. However, with the increase of the distance between the collector and the needle, the production of nanofibres per square centimetre decreases. This is due to the widening of the diameter of the cone, which is formed during electrospinning, at a higher distance. Therefore, we concluded that the optimum distance between the needle and collector is 150 mm for this formulation. This distance was enough

for water evaporation and the fabrication of a higher amount of nanofibres per square centimetre in contrast to the 200 mm and 250 mm distances.

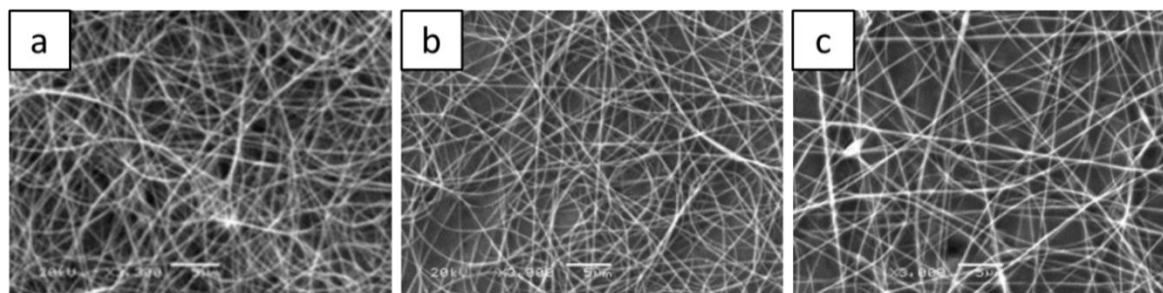


Figure 3.13. SEM images of PEO loaded with 13 w/w % of KIO_3 . Solution concentration was 5 w/v %. The feeding rate and applied DC voltage was held at a constant, namely 0.5 ml/h and 25 kV, respectively. The changing parameter is the distance between the collector and the needle: a) 150 mm; b) 200 mm; c) 250 mm.

3.3.4.2 Diameter of the needle

The variations in the diameter of the needle were 18G, 20G, 21G and 23G. There were slight differences observed in terms of fibre morphology, namely with the uniformity of the fibres affected by the 20G, 21G and 23G needle diameters. However, the applied voltage requires slightly less for the needle with the lower diameter size, i.e. 21G and 23G, due to the polymer amount at the exit (**Figure 3.14**). Nevertheless, the diameter of the needle of 18G was recommended as the optimum diameter for use in electrospinning for PEO/ KIO_3 solution because it yielded a relatively uniform fibre diameter distribution.

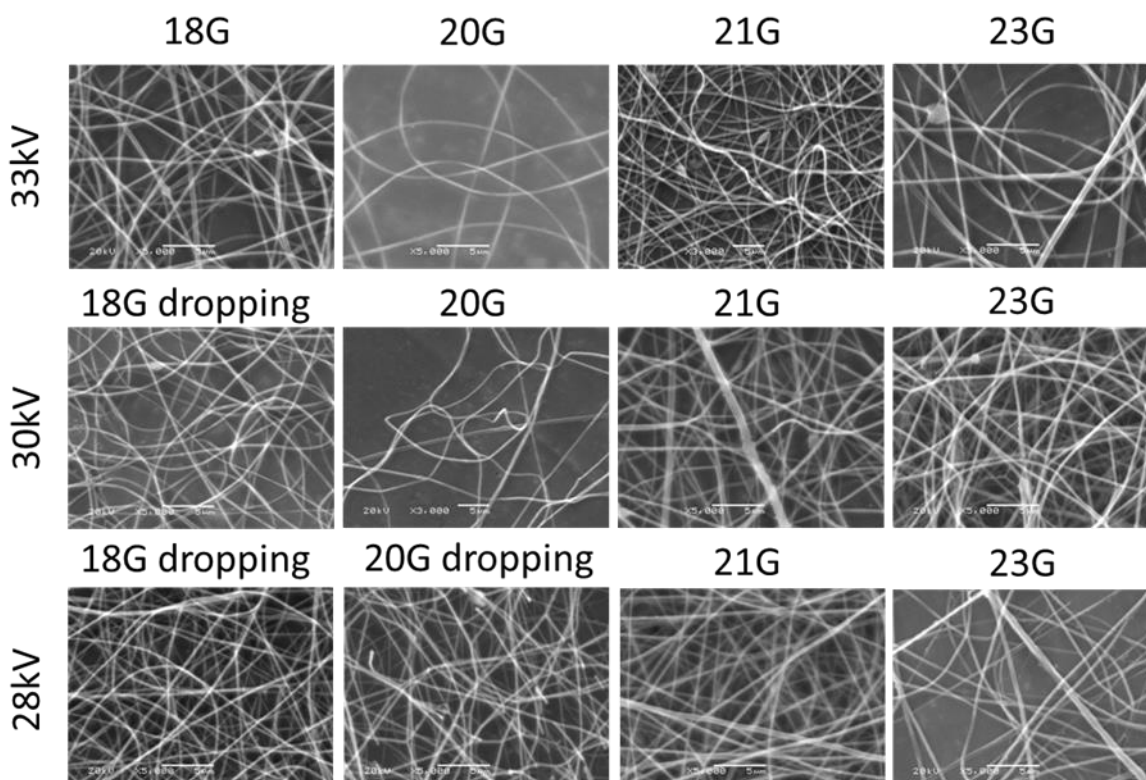


Figure 3.14. Effect of the diameter of the needle for the sample with 7 w/v % total solution concentration and PEO 600K/KIO₃ ratio of 91/9 w/w %. The EPPs: 150 mm – 0.5 ml/h.

3.3.4.3 Applied DC voltage

Generally, low voltage does not form a Taylor cone and high voltage forms beaded nanofibres. However, if the solution concentration is right enough to form nanofibres, the applied DC voltage has little effect, which is seen clearly in a sample with 3 w/v % of PEO 600K and 5 w/v % of PEO 600K concentration (**Figures 3.15 and 3.16**). The sample with 3 w/v % concentration forms beaded nanofibres, with the amount of beaded nanofibres increasing with the increase of applied DC voltage. This is not observed for the sample with 5 w/v % concentration, which does not form beaded fibres at all and the applied DC voltage has no effect. Therefore, as long as the Taylor cone is formed and the jet is ejected from the tip of the needle at certain applied DC voltages, then this voltage level is sufficient to produce nanofibres. There is no need to increase the voltage further to improve the fibre morphology or production rate for that formulation.

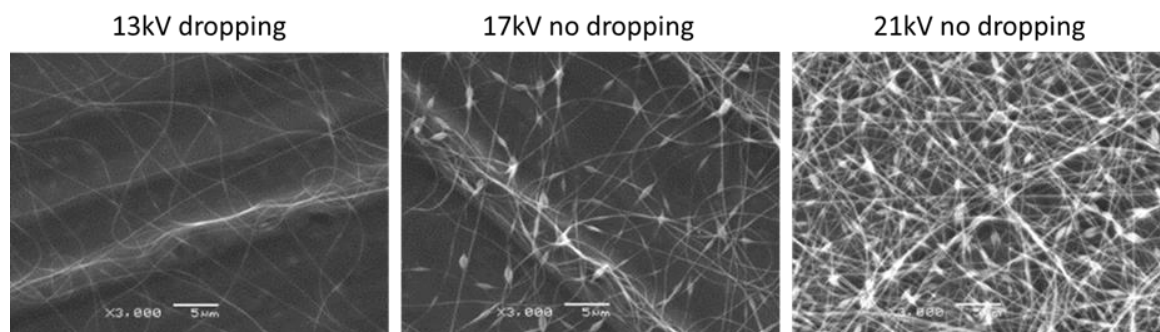


Figure 3.15. Effect of applied DC voltage for the sample with 3 w/v % of total solution concentration and PEO 600K/KIO₃-87/13 w/w %. The EPPs: 0.5 ml/h – 150 mm.

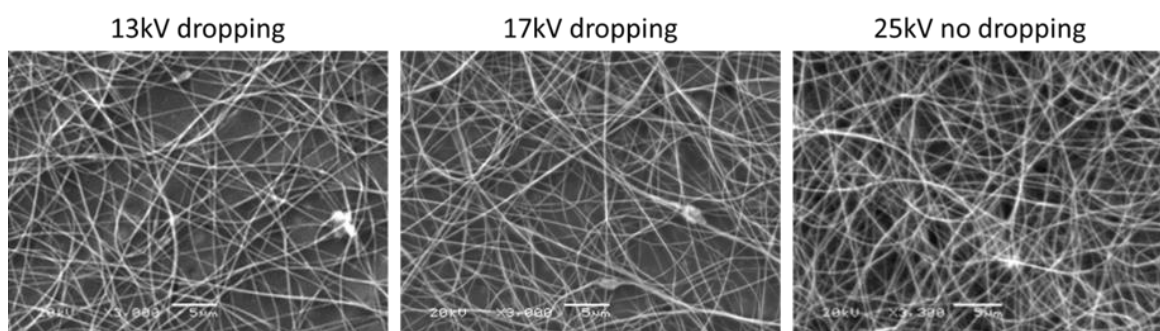


Figure 3.16. Effect of applied DC voltage for the sample with 5 w/v % of total solution concentration and PEO 600K/KIO₃-87/13 w/w %. The EPPs: 0.5 ml/h – 150 mm.

3.3.4.4 Feeding rate

The variation of feeding rate was 0.5ml/h, 0.75ml/h and 1ml/h. The results show no difference in the three samples electrospun at three different feeding rates (**Figure 3.17**). Generally, a low feeding rate yields poor collection and a high feeding rate affects fibre morphology because there is not enough time for solvent evaporation. Therefore, it is recommended to use 0.5 ml/h feeding rate to make sure that the solvent has enough time for evaporation for that formulation.

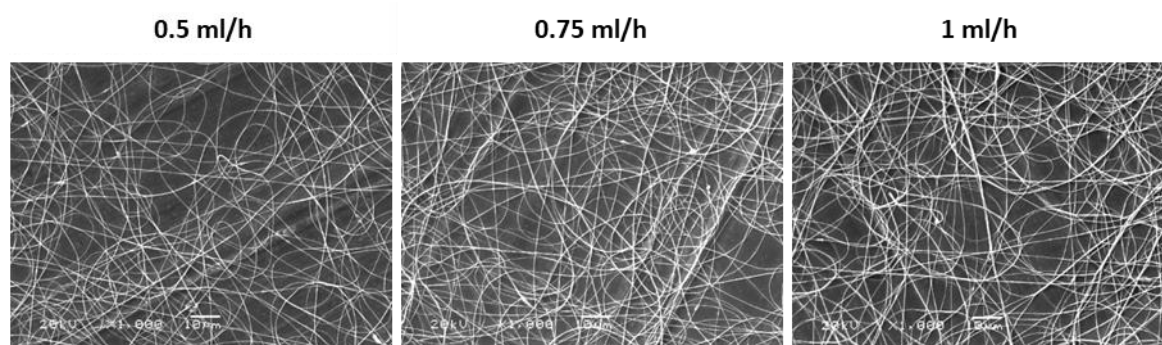


Figure 3.17. Effect of feeding rate for the sample with 5 w/v % of total solution concentration and PEO 600K/KIO₃-96/4 w/w %. The EPPs: 250 mm – 21-23 kV.

3.3.4.5 Type of collector

It is desirable to develop an aligned fibrous mat in many applications because it improves mechanical and electrical properties, and cell adhesion and proliferation [371]. Therefore, we decided to study the effect of a rotating collector, which is reported to be used to fabricate mats with aligned fibres that depend on the rotating speed of the drum. We studied only one rotating speed, namely 1,000 rpm, which was given in the literature as the optimum speed to fabricate aligned nanofibres [372] and used different polymers with different salts and concentration, namely pure PEO loaded with KIO₃ and pure PEO loaded with NaCl, and pure PVP loaded with KIO₃ and pure PVP loaded with NaCl. NaCl was used for comparison purposes. Pure PEO loaded with KIO₃ produces beaded fibres irrespective of the PEO to KIO₃ weight ratios, i.e. 99.6/0.4, 96/4, 87/13, 57/43, 36/64 w/w % (**Figure 3.18**). However, PEO loaded with NaCl generated aligned nanofibres without beads but the fibres were broken (**Figures 3.20a-c**). Some degree of fibre direction alignment with some spherical beads was generated with PVP polymer solutions with both salts, KIO₃ (**Figure 3.19**) and NaCl (**Figures 3.20d-f**), except when the NaCl loading was high, namely 57/43 w/w %, where fused nanofibres were obtained. In comparison, PVP loaded with KIO₃ showed more aligned fibre direction even at a high KIO₃ loading, namely 64 w/w %. Interestingly, here we increased the total solid concentration by 15 w/v %, because in **section 3.3.3** we determined that 10 w/v % concentration was not enough to fabricate fibres with a high loading of KIO₃, and with this concentration we were able to yield PVP nanofibres with a high loading of 64 w/w % of KIO₃. The principle of producing aligned fibres direction using a drum collector is that during the

rotation of the drum collector, the fibres are taken up on the surface of the drum and if the surface speed of the rotating drum matches that of the evaporated jet depositions, the fibres are taken up tightly in a circumferential manner and the fibres are fairly aligned. If the surface speed of the drum collector is slower than the fibre deposition speed, the fibres will be deposited randomly [89]. In addition, the deposition of randomly oriented fibres on a rotating drum can be due to the residual charge accumulation on the deposited fibres, interfering (repelling) with the alignment of the incoming fibres [90]. These two factors or one of them alone are possible reasons for some random deposition of the PVP/NaCl and PVP/KIO₃ formulations. However, if the surface speed of the drum collector is faster than the fibre deposition speed, the fibres will be broken [89], as happened in the case of the PEO/NaCl formulation. The faster speed of the drum collector compared to the fibre deposition speed will break the fibre jet and continuous fibres cannot be collected [89]. The formation of beaded fibres in PEO/KIO₃ is possibly also associated with droplet break up during electrospinning, causing reduced chain entanglement. In addition, later we found that Kessick et al. [373] reported that PEO nanofibres exhibited a higher degree of fibre alignment on the drum collector when the AC potential was applied instead of DC potential. The alternating polarity of the AC applied potential reduces the charge net on the fibres, resulting in the reduction of electrostatic forces that cause the fibre instability. However, it was observed that the fibre mat contained more residual solvent.

The rotating drum was good for the PVP sample but not for the PEO sample. As the stationary collector worked well in yielding smooth uniform PEO nanofibres, it was decided to exclude the rotating drum collector when electrospinning PEO/KIO₃ formulation.

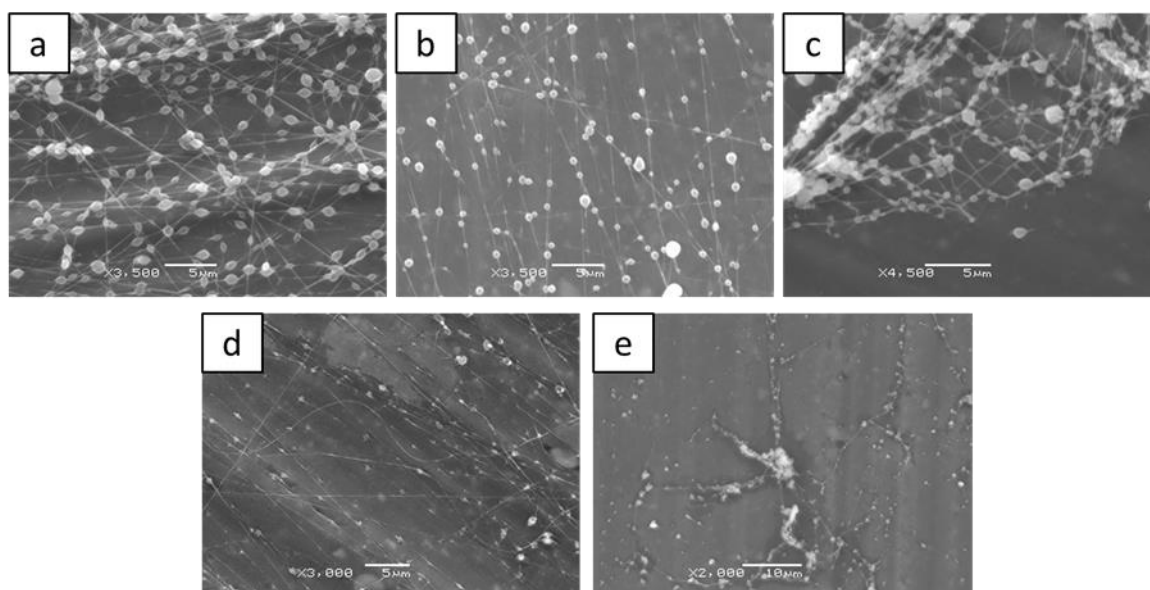


Figure 3.18. SEM images of fibres obtained using the rotating collector for PEO/KIO₃ formulations: a) with PEO/KIO₃ 99.6/0.4 w/w %; b) with PEO/KIO₃ 96/4 w/w %; c) with PEO/KIO₃-87/13 w/w %; d) with PEO/KIO₃ 57/43 w/w %; e) with PEO/KIO₃ 36/64 w/w %. The total solution concentration was 5 w/v %. The EPPs: 1,000 rpm – 150mm – 0.5ml/h – 12–14kV.

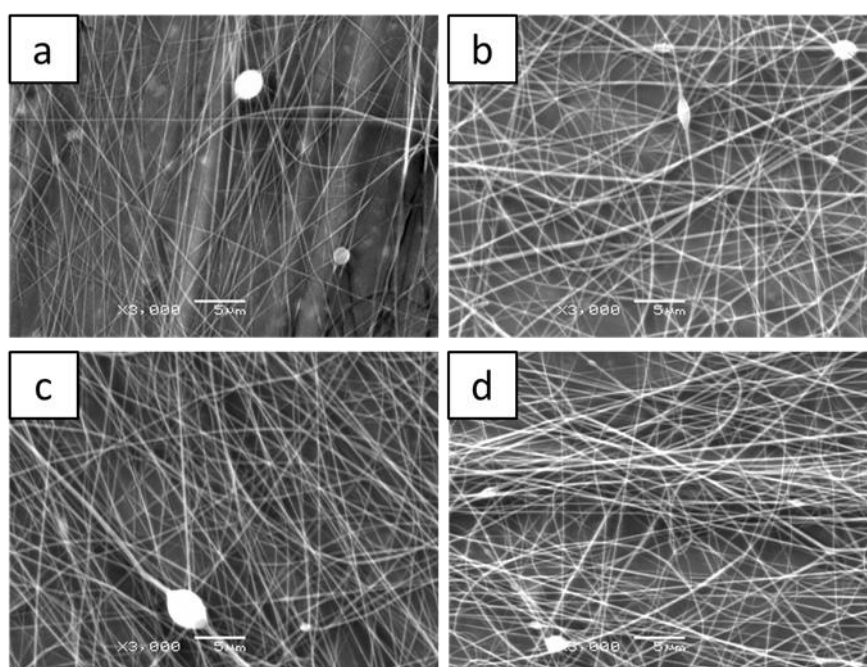


Figure 3.19. SEM images of fibre morphology obtained using the rotating collector for the PVP/KIO₃ formulations: a) with PVP/KIO₃ 87/13 w/w %; b) with PVP/KIO₃ 79/21 w/w %; c) with

PVP/KIO₃ 57/43 w/w %; d) with PVP/KIO₃-36/64 w/w %. The total solution concentration was 15 w/v %. The EPPs: 1,000 rpm – 150 mm – 0.5 ml/h – 30kV.

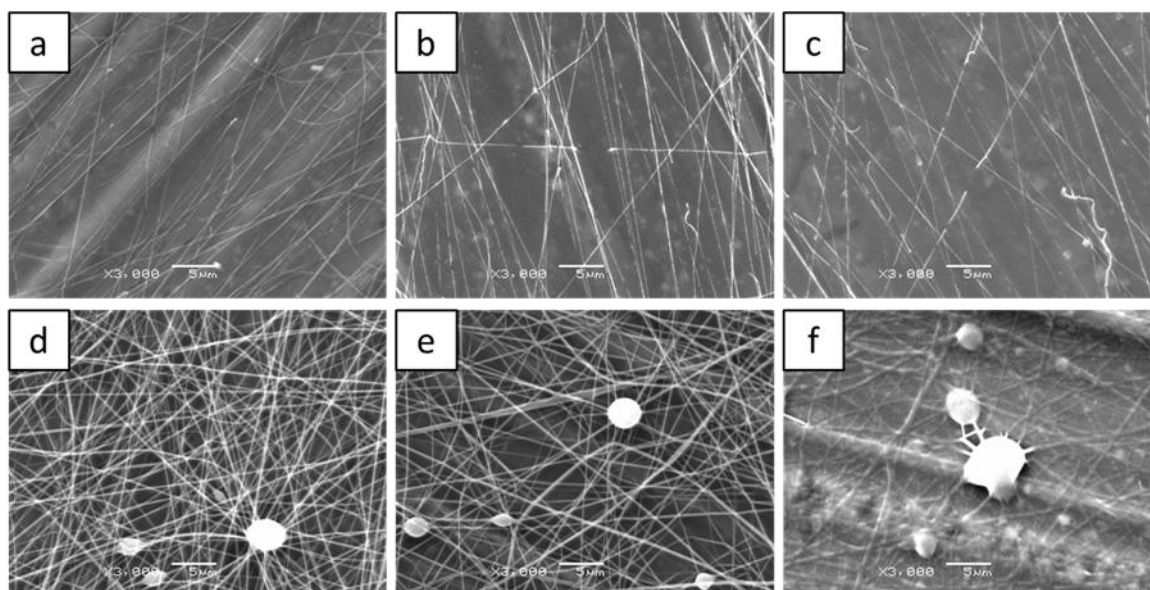


Figure 3.20. SEM images of fibres obtained using the rotating collector for the samples loaded with NaCl: a) PEO/NaCl 87/13 w/w %; b) PEO/NaCl-79/21 w/w %; c) PEO/NaCl-57/43 w/w %; d) PVP/NaCl-87/13 w/w %; e) PVP/NaCl-79/21 w/w %; f) PVP/NaCl-57/43 w/w %. The total solution concentrations were 15 and 5 w/v % when PVP 90K and PEO 600K were used, respectively. The EPPs: 1,000 rpm – 150 mm – 0.5 ml/h – 22–30 kV.

3.3.5 Characterization of PEO nanofibres loaded with KIO₃

3.3.5.1 Validation of the distribution of KIO₃ in the PEO fibres

The EDS is able to detect elements with an atomic number greater than 5. In combination with SEM, it can be used to gain elemental distribution information [331, 374, 375]. As seen in **Figure 3.21**, the results revealed that the KIO₃-loaded fibre films consist of K, I, O, C, and Au. The presence of Au is due to pre-treatment of the SEM sample, C and O are polymer constituents, and K, I, and O are constituents of KIO₃. As the electrospun films were highly porous, the quantitative elemental composition assignment of the EDS results would have limited reliability. Nevertheless, the atomic ratios between C, O, K, and I largely align with the molar ratios of these atoms within the formulations examined. The high similarity of the K

and I peak intensities in different areas of the sample using the spot mode indicates the homogeneity of the distribution of KIO_3 in the nanofibre films. Peak intensity is related to the amount of substance in the formulation. As seen in **Figure 3.22**, the higher KIO_3 loading shows a stronger intensity. Overall, the results confirmed that electrospinning is a suitable method for producing easy-to-use orodispersible films for the delivery of iodine.

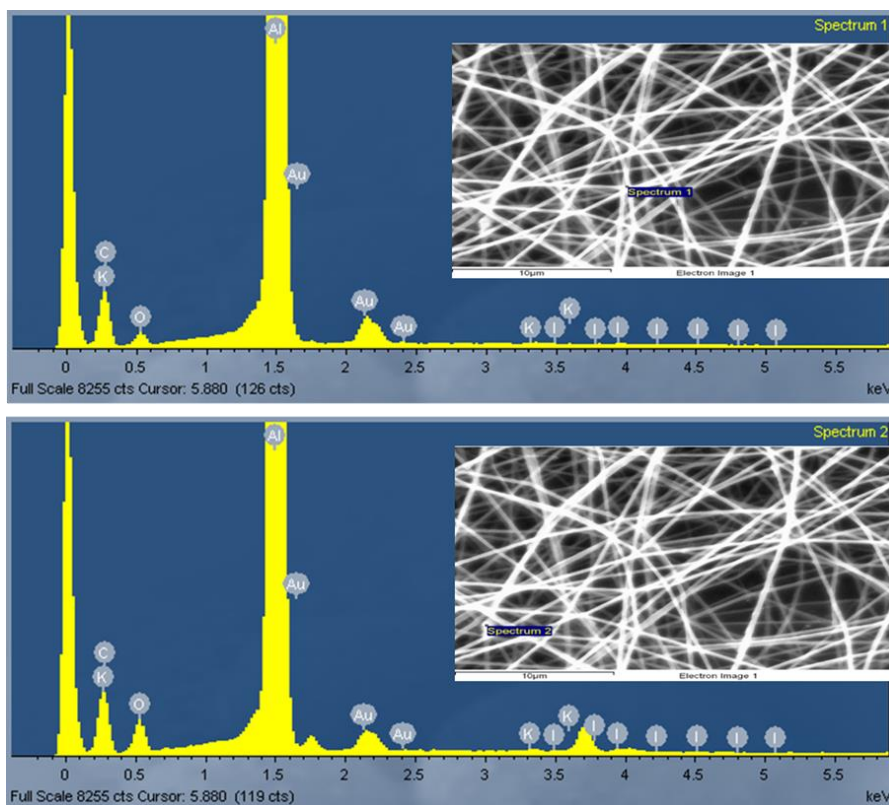


Figure 3.21. Representative EDS results of PEO nanofibres loaded with 4 w/w % KIO_3 showing the detection of K, O, and I elements on the fibres.

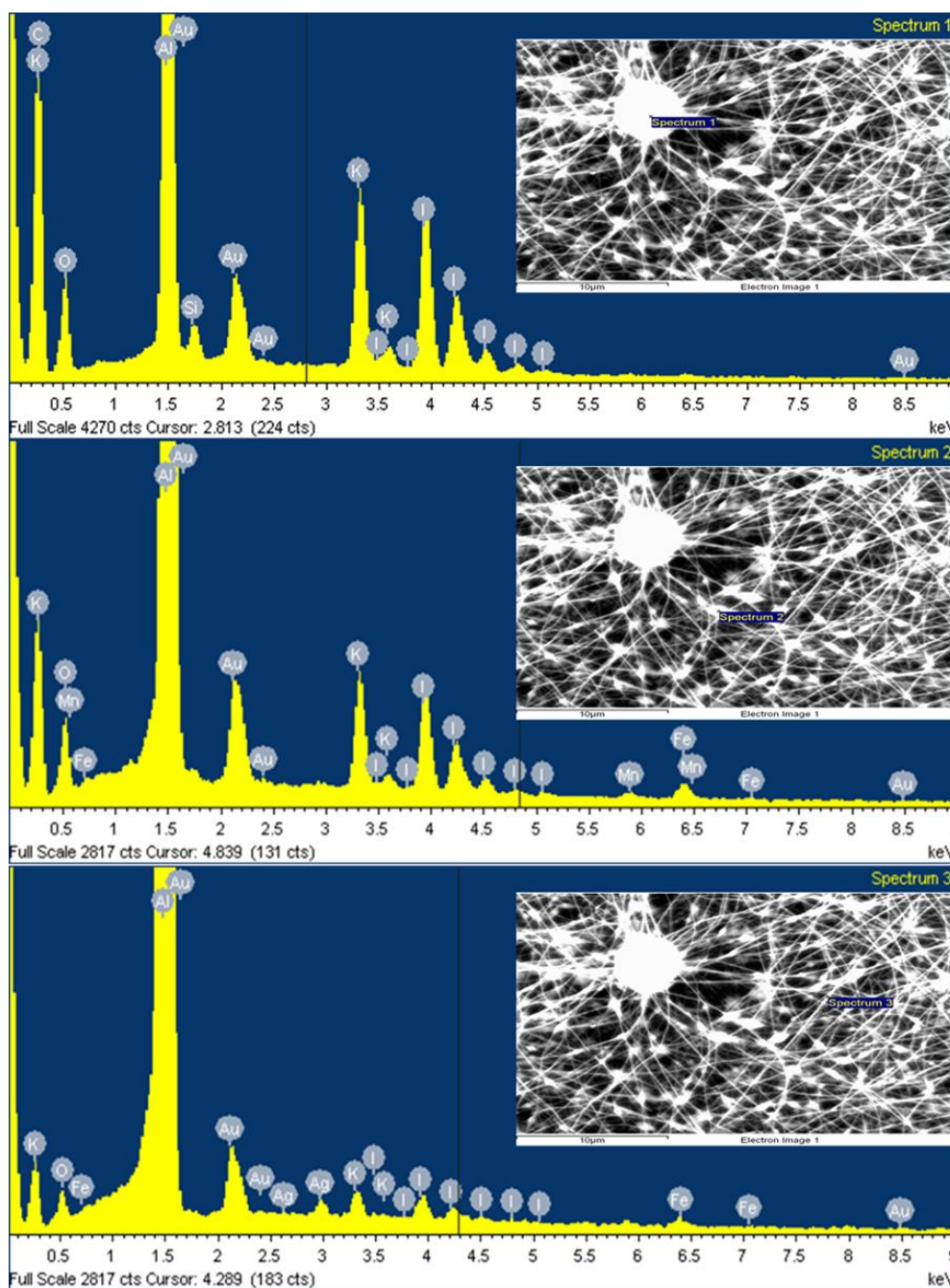


Figure 3.22. Representative EDS results of PEO nanofibres loaded with 43 w/w % KIO_3 showing the detection of K, O, and I elements on the fibres.

3.3.5.2 Formation of KIO_3 nanocrystals in PEO nanofibres

As discussed earlier, the increases in KIO_3 loading affected the mechanical properties of the formed fibre films by converting the smooth fibres to beaded fibres, as well as reducing the PEO content which is responsible for the elasticity of the film. It was also suspected that the

physical form of KIO_3 might be altered with increasing loading. This assumption was made on the basis of the existing literature on polymer-based solid dispersions for delivering organic molecules, in which a crystalline drug is expected if the loading significantly exceeds the solubility limit of the organic drug in the polymer [366]. The generation of significant quantities of crystalline KIO_3 could also reduce the mechanical strength of the fibres and result in weak and brittle fibre films. This hypothesis was tested using PXRD.

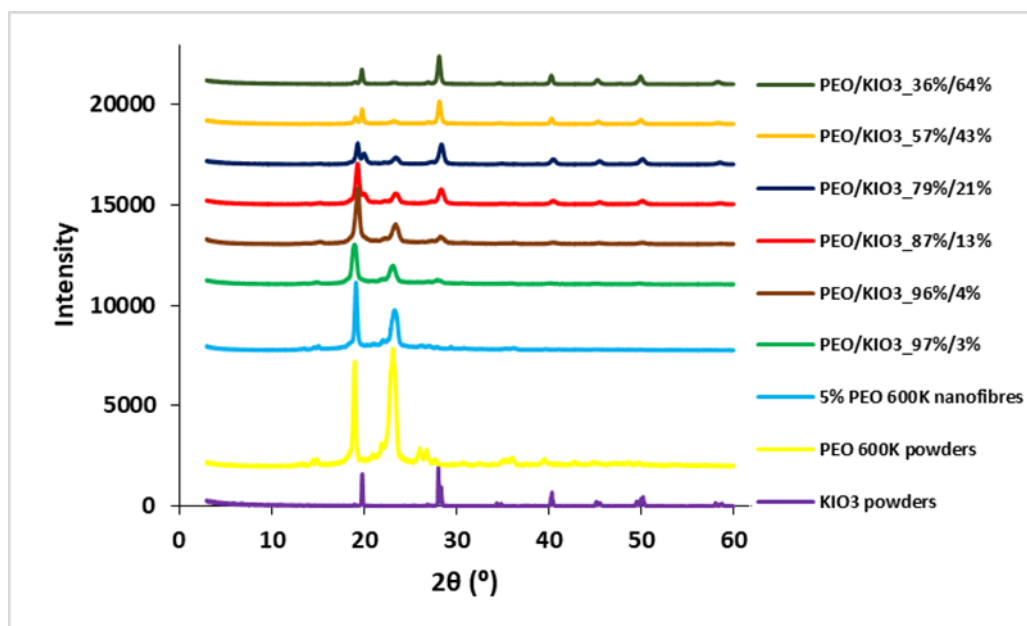


Figure 3.23. PXRD diffraction patterns of the starting materials and electrospun nanofibres.

The PXRD results confirm the crystalline and semi-crystalline nature of KIO_3 and PEO, respectively. All of the characteristic diffraction peaks match those reported in the literature. As seen in **Figure 3.23**, it is evident that with increasing KIO_3 loading, crystalline KIO_3 was formed with low loadings at and above 3 w/w %. The PXRD data of each sample can be found in **Appendix 4, Figure A4.7**, where crystal formation can be seen even at lower concentration than that, namely at and above 1.3 w/w %. This indicates that an inorganic salt such as KIO_3 has low solubility in solid PEO, and instead of the formation of a solid solution or amorphous solid dispersion KIO_3 is likely to form crystalline solid dispersions with PEO after electrospinning. However, no crystal or particulate feature was observed using SEM, which is an imaging technique that examines the surface of the fibres. Therefore, TEM was applied to further investigate KIO_3 crystal formation in the PEO fibres.

As seen in **Figure 3.24**, darker, nano-size particles can be clearly seen in the TEM images of the fibre films. These high density nanoparticles are highly likely to be the KIO_3 crystals. It is interesting that these nanocrystals are distributed relatively evenly within the core of the fibres. This confirms the earlier EDS result, which suggested a uniform distribution of KIO_3 through the fibres. There appears to be no surface accumulation of the nanocrystals. This finding is in contrast to the surface and bulk crystallization behaviour of other inorganic salts in electrospun fibres reported in the literature.

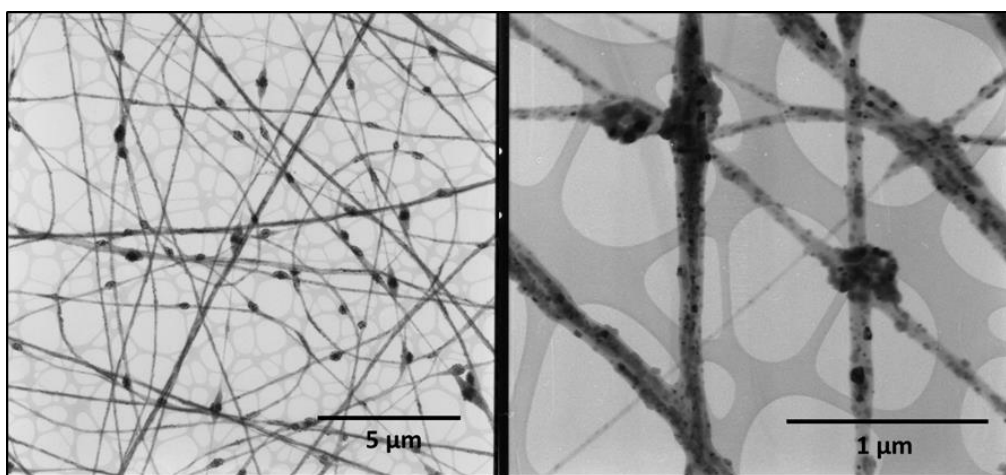


Figure 3.24. Representative TEM image of PEO nanofibres loaded with 43 w/w % KIO_3 . KIO_3 nanocrystals can be seen as black dots in the fibres.

Inorganic salts are employed in the electrospinning of polymers, mainly, to increase the surface charge density and conductivity of the solution to improve fibre morphology, i.e. to obtain smoother and thinner fibres. However, studies of the physical characteristics of inorganic salts within electrospun polymers have not been reported. All of the previous studies have focused on the effect of using inorganic salts on fibre morphology and fibre physicochemical characteristics [102, 106, 376-382]. There are a number of examples when salts appear on the surface of the fibres, starting from 0.2 w/w % concentration [110, 383, 384], and only in those cases was it reported that crystals formed, albeit, that crystals can be entrapped within the fibres too and therefore cannot be seen in the SEM images. This salt crystal entrapping phenomena might be due to the salt, polymer or solvent physicochemical properties as well as processing parameters [384, 385]. In our case, we clearly see that KIO_3 crystals were entrapped, even with high loadings such as 43 w/w %. Nanocrystals can be seen

with a 3 w/w loading (**Figures 3.25a and 3.25a'**). The pictures taken for the PEO nanofibres with 13 w/w % KIO_3 loading (**Figures 3.25b and 3.25b'**) show some aggregated but mostly well defined nanocrystals of different geometric shapes within the fibre core. Whereas, further increasing the KIO_3 loading, up to 43 w/w %, forms nano-clusters with a rough width of 30 nm (**Figures 3.25c and 3.25c'**).

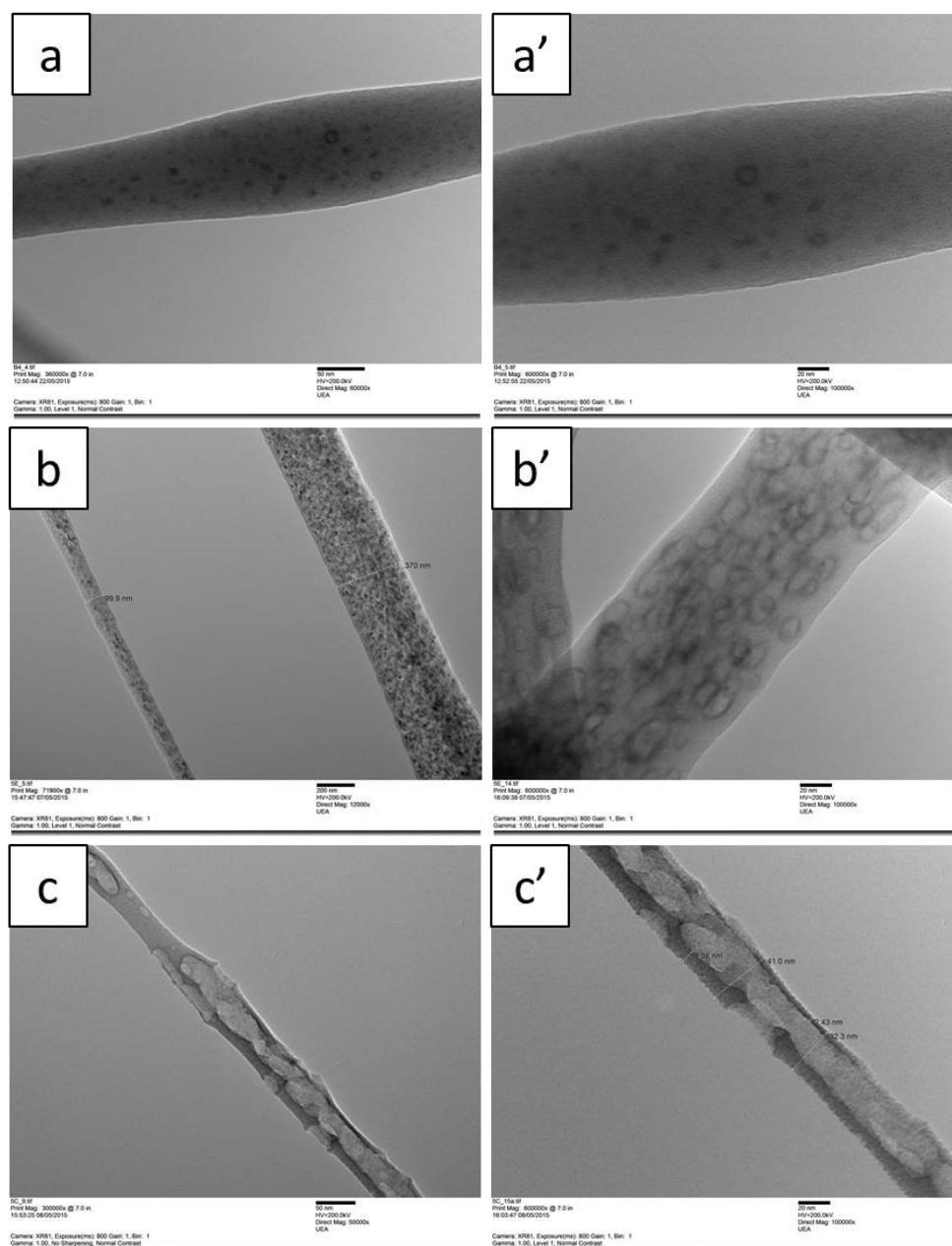


Figure 3.25. TEM images show the presence of nanocrystals of KIO_3 in the PEO nanofibres with loadings ranging from 3–43 w/w %. With the increasing of the KIO_3 loading, the crystal

size and density increase: a) 3 w/w % of KIO_3 (a' higher magnification); b) 13 w/w % of KIO_3 (b' higher magnification); c) 43 w/w % of KIO_3 (c' higher magnification).

To support our interpretation that inorganic salts can form a crystalline solid dispersion with polymers during electrospinning, and that electrospinning is a means to yield nanocrystals of inorganic salts, we studied another commonly used inorganic salt, NaCl, within the polymer PVP. This interior-specific crystallization behaviour in hydrophilic polymeric fibres was also observed in electrospun PVP, a widely used pharmaceutical hydrophilic and hygroscopic polymer. Small crystals in the nano-size range were obtained from low loadings (**Figure 3.26**), as was observed with KIO_3 (**Figure 3.25**). In addition, we checked whether nanocrystal formations occur because of electrospinning or the presence of a polymer. Therefore, we electrospayed KIO_3 without a polymer (**Figure 3.27**) and electrospun with another polymer, PVP (**Figure 3.26b**), and PEO was electrospun with another salt, NaCl (**Figure 3.26c**). The results showed that electrospayed KIO_3 appears in its crystal state and in the range of nanometres to micrometres (**Figure 3.27**). Thus, we have assumed that the polymer matrix acts as a solid dispersing agent to keep the crystals separate and produces nano-size crystals.

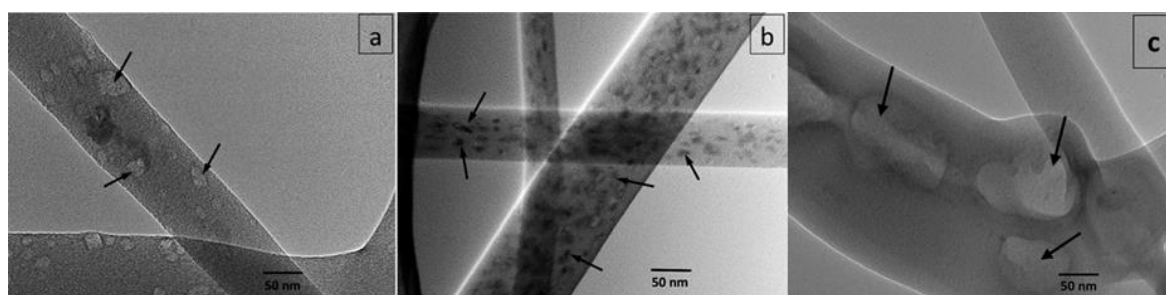


Figure 3.26. Representative TEM image of PVP nanofibres loaded with (a) 4 w/w % of NaCl, (b) 14 w/w % of KIO_3 and (c) PEO/NaCl-57/43 w/w %. Nanocrystals of NaCl and KIO_3 (examples highlighted by arrows in the images) can be observed in the core of the fibres with the surfaces of the fibres being largely crystal free.

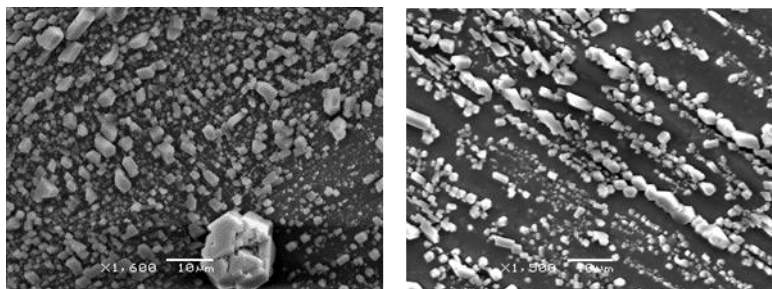


Figure 3.27. Aqueous solution of KIO_3 was electrospayed. Yield crystals are in the range of nanometres to micrometres. The right and the left images are different areas in the sample.

In the PVP/ KIO_3 mixture, KIO_3 was also incorporated in a PVP polymer in the same way as observed with the PEO polymer in the nano-size range (**Figure 3.26b**). This indicates that the phenomenon of inorganic salt crystallization in the bulk of electrospun fibres is not PEO- KIO_3 system specific. Although the mechanism of this crystallization behaviour is unclear and further investigation is required, it is noted that both PEO and PVP are hydrophilic polymers which exhibit some hygroscopic behaviour. The large surface area and hygroscopic nature of the polymer fibres may lead to a higher moisture content at the surface layer of the fibres, and this may be sufficient to solubilize the surface salts. The interior core of the fibres is likely to be drier than the surface, with the low solubility of the salts in the dry polymer interior driving the crystallization. With increasing iodate loading, beading of the fibres can be seen and agglomeration of KIO_3 nanocrystals at the beading sites is clearly evident (**Figure 3.24**). This indicates that there are significantly higher KIO_3 local concentrations at the beading sites. It is worth mentioning that as the formation of the nanocrystals occurs at very low loading, it is reasonable to suggest that the presence of the nanocrystals per se is not the key factor responsible for the mechanical weakness of the fibre films. The formation of highly concentrated KIO_3 nanocrystal beads at higher iodine loadings, in combination with a low PEO content, is more likely to be the underlying reason for the poor mechanical properties of those fibres with high KIO_3 loadings.

3.3.5.3 Effect of processing and KIO_3 loading on the crystallization behaviour of PEO

PEO is a semi-crystalline polymer, and the crystallinity of the polymer can be affected by the electrospinning process and the incorporation of KIO_3 . These factors could potentially lead to

stability concerns in the finished product. Therefore, the structural conformation and crystallinity of the processed PEO in the fibres were studied in depth. ATR FT-IR spectroscopy was used in the first instance to reveal the co-existence of helical (H) and trans (T) structure conformations of PEO. As seen in **Figure 3.28**, IR peaks at 1358, 1278, 1235, 1060, 947, and 842 cm^{-1} have been specified as indicators for the thermodynamically stable helical structure (H) and 1341, 1240, and 961 cm^{-1} for the trans planar (T) conformation. Any changes in these peaks would indicate a change in T or H conformation [323]. All absorption peaks are due to the PEO polymer remaining unchanged in comparison to the placebo and are independent of KIO_3 loading. This implies no significant change in the overall PEO chain conformation occurred after the incorporation of KIO_3 . With 43 w/w % of KIO_3 loading, the absorption peak at 745 cm^{-1} was split into two bands at 756 and 738 cm^{-1} . The band splitting at 745 cm^{-1} indicates a change of symmetry in the crystal structure. However, according to the literature, PXRD is unable to detect such subtle changes in KIO_3 crystal symmetry; thus, this change was not observed in the PXRD results. Nevertheless, for the purpose of this study, such subtle changes in KIO_3 nanocrystal are not anticipated to impact the dissolution behaviour of the formulation because of the high solubility of KIO_3 . Detailed assignments of all detectable FT-IR peaks of the PEO and KIO_3 samples can be found in **Table 3.4** and **Table 3.5**.

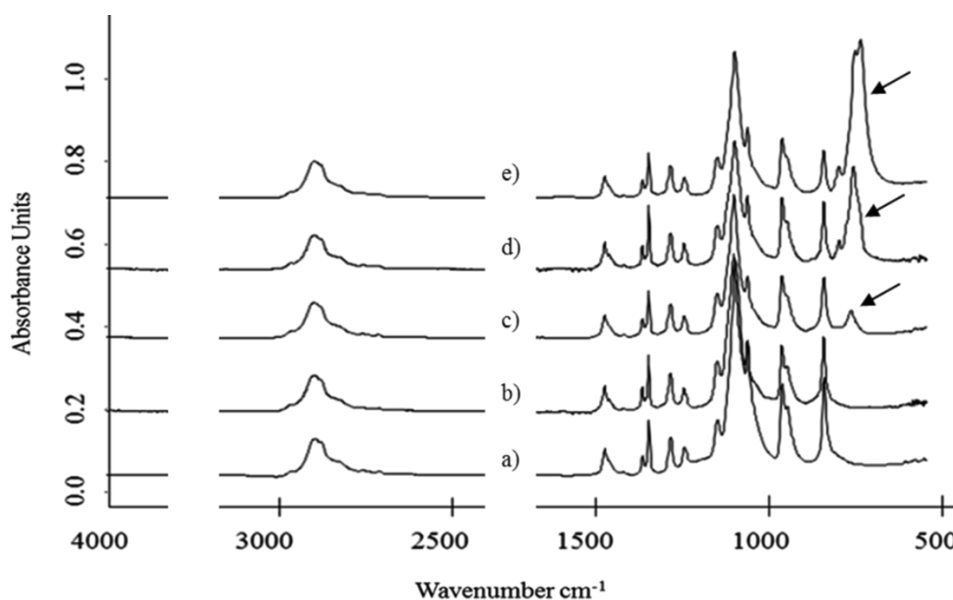


Figure 3.28. ATR FT-IR spectra of (a) pure PEO powder and (b) electrospun placebo PEO nanofibres and PEO nanofibres loaded with (c) 4 w/w, (d) 21 w/w %, and (e) 43 w/w % KIO_3 . Arrows indicate the position of the KIO_3 signature absorbance peak.

Table 3.4. Detailed assignments of all detectable ATR FT-IR peaks of the PEO 600K, electrospun PEO and KIO₃ loaded PEO fibres.

PEO reported by Yoshihara [386]	PEO powder	PEO Electro spun	PEO/KIO ₃ 96/4 w/w %	PEO/KIO ₃ 79/21 w/w %	PEO/KIO ₃ 57/43 w/w %	Assignment [323, 367, 387-390]
1466 ⊥ m	1466.47	1466.68	1466.76	1466.85	1466.85	CH ₂ bending
1453 m	1454.25	1454.91	1454.91	1455.08	1455.06	CH ₂ bending
1358 ⊥ m	1359.44	1359.59	1359.64	1359.71	1359.73	CH ₂ wagging CC stretching (H)
1342 s	1341.42	1341.68	1341.64	1341.67	1341.66	CH ₂ wagging (T)
1278 ⊥ m	1278.97	1279.38	1279.66	1279.75	1279.79	CH ₂ twisting (H)
1240 s	1240.86	1241.38	1241.34	1241.38	1241.40	CH ₂ twisting (T)
1147 ⊥ s	1144.53	1145.12	1147.39	1147.57	1147.92	CC stretching COC stretching
1103 vs	1094.65	1097.08	1098.25	1098.62	1098.72	COC stretching
1060 ⊥ m	1059.14	1060.15	1060.64	1060.75	1060.78	CH ₂ rocking (H) COC stretching
958 s	960.76	961.53	961.61	961.74	961.78	CH ₂ rocking (T)
947 ⊥ m	946.53	946.97	947.66	947.72	947.91	CH ₂ rocking (H)
844 ⊥ s	841.09	841.48	841.91	842.10	842.30	CH ₂ rocking (H)

Table 3.5. Detailed assignments of all detectable ATR FT-IR peaks of the KIO₃ and KIO₃ loaded fibres.

KIO ₃ reported by Nakamoto [391]	KIO ₃ reported by Miller and Wilkins [392]	PEO/KIO ₃ 96/4 w/w %	PEO/KIO ₃ 79/21 w/w %	PEO/KIO ₃ 57/43 w/w %
796 (A₁)	800 (w)	799.43	798.35	798.27
745 (E)	755 (s) 738 (vs)	763.57	760.87	756.43 738.88

3.3.5.4 Ultra-rapid wetting and dissolution of PEO nanofibres loaded with KIO₃

With the intention of providing rapid dissolution of these electrospun films on the tongue after administration, these films should first demonstrate the ability to be wetted rapidly. The

wetted filter paper method reported in the literature was adopted for simulating the moist surface of the tongue. As seen in **Figure 3.29**, the electrospun film wetted rapidly and transformed from an opaque dry film to being invisible in less than 20 seconds. As indicated by the disappearance of the opaque films, the KIO_3 -loaded films showed ultra-rapid dissolution in the media within less than a minute.

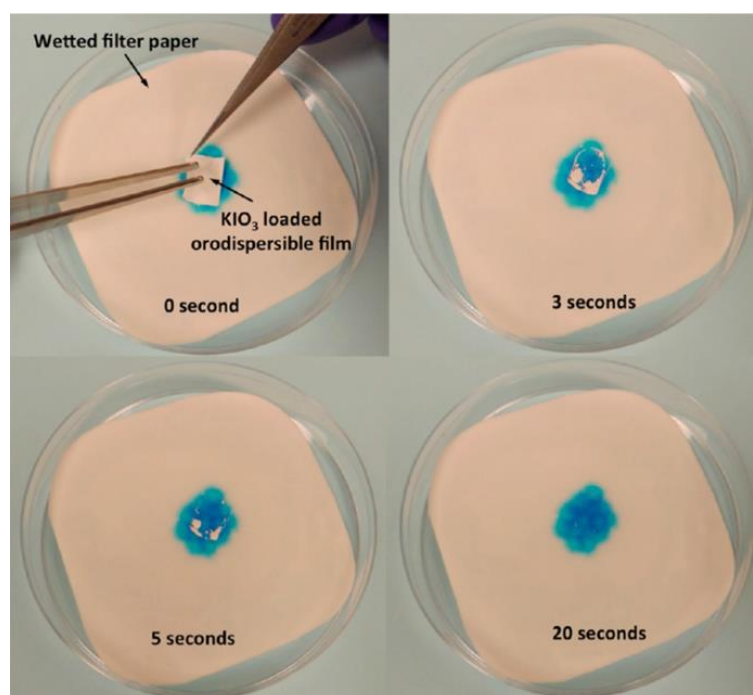


Figure 3.29. Demonstration of the rapid wetting of a piece of KIO_3 -loaded PEO nanofibre orodispersible film. The blue area was used to provide the colour contrast to allow easy observation of the opaque film.

For the fibre films with 13 w/w % of KIO_3 loading, delivering 0.5 and 1.1 mg of a piece of film with dimensions of approximately 1×1 and $1 \times 2 \text{ cm}^2$ is required, respectively, which meet the WHO recommended daily dose of $90 \mu\text{g}/\text{day}$ for children aged 0–5 years and $200 \mu\text{g}/\text{day}$ for pregnant and lactating women, respectively. This low mass may be difficult to handle but, with a reduction in the drug loading, the weight of oral film administered can be easily increased into an easily manageable size. An alternative delivery method is to put the film on top of an edible bulky item, such as conventional children's snacks, which may also improve patient adherence as they are appealing to the paediatric population.

In order to see the dissolution rate and release of KIO_3 , an iodometric reaction was used. As seen in **Figure 3.30**, the dark brown colour of the media after adding sulphuric acid indicates the liberation of I_2 , which appeared immediately after the fast disintegration and dissolution of the nanofibre film. The total dissolution was within less than 30 seconds.

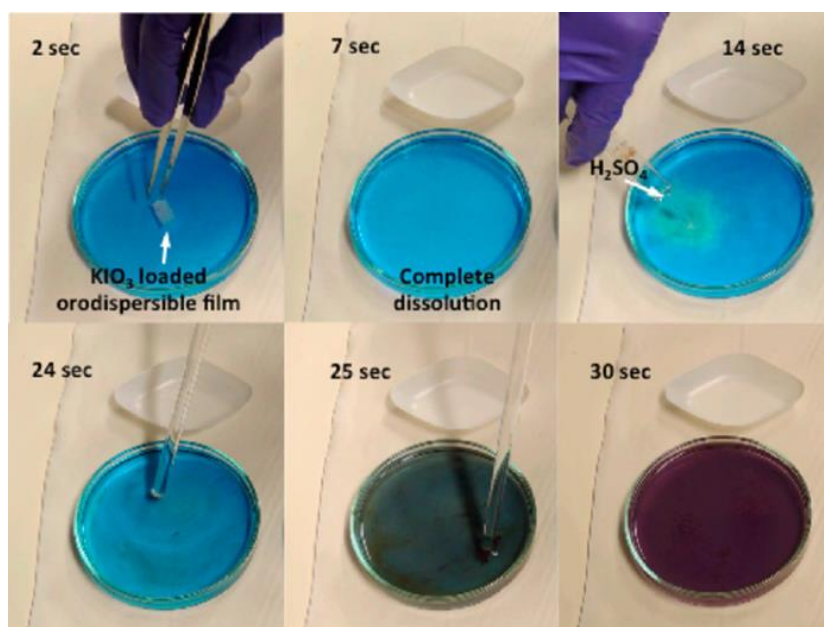


Figure 3.30. Ultra-rapid dissolution of KIO_3 -loaded PEO nanofibre mats. Complete release of KIO_3 is demonstrated by the colour change of the dissolution medium containing the molecular indicator, methylene blue, after adding a small amount of H_2SO_4 solution.

3.4 Conclusion

This study was conducted with a clear aim of finding an alternative low-cost and easy-to-use oral iodine supplement formulation for the paediatric population, who often have swallowing and adherence difficulties. The formulation developed should fulfill the essential criteria of not requiring the swallowing of large solids and has the potential to be easy and fun for children to take. The solution proposed in this study is to use electrospinning to produce thin orodispersible films which can instantly dissolve on the tongue for easy administration of nutritional supplements to children. The key outcome reported for this proof-of-concept study is that this is achievable with low requirements for operational optimization and little effect on the structural conformation of PEO. The formation of KIO_3 nanocrystals in nearly all

loaded fibre films indicates the low miscibility of PEO with KIO_3 . This provides new insights into the research area of using polymeric-based solid dispersions for inorganic material delivery which is still significantly lacking. The fact that KIO_3 forms nanocrystals in the PEO fibres and the PEO remains in its original stable conformation is likely to ensure the physical stability of the finished product.

Additionally this research has also demonstrated a novel and easy method for producing and harvesting nanocrystals of inorganic salts that can be potentially adopted for other relevant fields.

4 Chapter 4. Feasibility study of using emulsion electrospinning for the co-delivery of multi-nutrients

4.1 Introduction

As discussed in **Chapter 1**, multiple micronutrient deficiency is more common than single nutrient deficiency. Therefore, the development of novel delivery systems and methods that are capable of delivering several nutrients simultaneously is needed. This would be similar to pharmaceutical products which have multi-drug combinations in a single unit dose, in which different drugs can be incorporated into one formulation, but are released at different rates [393-395]. If the nutrients that need to be co-delivered in a single supplement product have different aqueous solubility levels, then the delivery system must be able to incorporate both water-soluble and oil-soluble compounds. Lipid-based formulations have been proven to be one of the efficient carrier systems for the incorporation of poorly and highly water-soluble drugs and nutrients. Numerous techniques are well documented in the literature for manufacturing lipid-based formulations. In this chapter, we explore the use of EE technology for producing lipid formulation, which allows the production of a lipid-based core which can solubilize oil-soluble compounds and a shell made of water-soluble polymers that can host water-soluble compounds. This core-sheath structure can provide good protection for sensitive oil-soluble vitamins and can potentially be used for the co-delivery of drugs. The materials used in EE are usually hydrophilic polymers in the water phase and amphiphilic polymers or any spinnable polymers dissolved in organic solvent as the oil phase. However, recently, liquid fish oil has been encapsulated in nanofibres by EE [137, 138].

In this chapter, we used PEO and PVP polymers in the water phase, due to their good water-soluble and electrospinnability, as they could carry water-soluble nutrients such as KIO_3 (as demonstrated in **Chapter 3**). Oil-soluble nutrients such as vitamin A, where it has been reported that deficiency can be connected with hypothyroidism [396], and vitamin E, which has also been reported to have a positive effect on this clinical state [43], can both be delivered in the oil core of the EE fibres. This allows a synergistic effect to tackle the iodine

deficiency. The solution of EE is an emulsion composed of the water phase and the oil phase (dispersed phase). In this chapter, we investigate the use of a range of oils, namely sunflower, fish, flaxseed, squalene and olive oils, as the dispersed phase carrier oil and their effects on the EE process. These oils were selected as they are widely used in food and pharmaceutical formulations as functional ingredients and carriers for poorly water soluble active ingredients. TPGS was selected as a source of vitamin E and an emulsifying agent. Span 80 is often used in EE and was selected to adjust the emulsifier HLB value in a mixture with TPGS, as it has a low HLB value of 4.3 [397]. Tween 20 was selected as it is often used in the preparation of o/w emulsions.

EE can be performed by either single spinneret or coaxial electrospinning (a detailed description and comparison can be found in **Chapter 1, section 1.5**). We investigated both methods to assess their feasibility for producing emulsion based core-shell fibres or fibres incorporating oil drop phases.

The main purpose of this chapter is to establish the feasibility of EE as a potential method for creating formulations for the co-delivery of multi-nutrients. A range of factors that could affect the EE process was studied, as listed below:

1. Study the impact of oil, polymer, emulsifier types and their concentration on stability of emulsion and production of nanofibres (SEM and photographic study)
2. Assess the impact of the type of electrospinning technique used to produce EE nanofibres (SEM)
3. Assess droplet size and size distribution of emulsions (DLS and LD)

4.2 Materials and methods

4.2.1 Materials

The materials used in this chapter are PEO 600K, PVP 90K, KIO₃, TPGS, Tween 20, Span 80, sunflower, fish, flaxseed, squalene and olive oils. Their physicochemical properties are described in **Chapter 2, sections 2.2, 2.2.1, 2.2.2, 2.2.4**.

4.2.2 Methodology

4.2.2.1 Emulsion preparation technique

Emulsions were homogenized using HPDI, the technical characteristics of which are described in **Chapter 2, section 2.3.2.1**.

4.2.2.2 Conventional emulsion electrospinning

4.2.2.2.1 Emulsions prepared using Tween 20 and TPGS

Emulsions were prepared using two types of continuous phases, namely PEO and PEO/PVP polymer solutions as a continuous phase, and three types of emulsifier compositions, namely Tween 20/TPGS, Tween 20 and TPGS. The oil phase was constituted only of sunflower oil.

The description of the preparation is as follows: first, the emulsifiers and the polymer solution already studied in the previous chapter were dissolved in aqueous media to form a continuous phase for an o/w emulsion. Second, the dispersed phase constituted of sunflower oil was accurately measured and poured into a 50 ml vial. Then the continuous phase was poured into the oil phase and homogenized by means of HPDI at 11,400 rpm for 3 minutes, and immediately electrospun. The total concentrations of all excipients are given in **Table 4.1**.

Two types of collectors, stationary and rotating (1,000 rpm), were used for EE. The EPPs are as follow: 200 mm – 0.2 ml/h – 20–30 kV.

Table 4.1. Concentration of emulsions.

Polymer solution type	Emulsifier type	Emulsifiers concentr.	Continuous phase v/v %	Dispersed phase v/v %	Sample N
5 and 7 w/v % of PEO 600K	Tween 20	3 v/v %	62	30	4.1
	TPGS	5 w/v %			
	Tween 20	5 v/v %	65	30	4.2
	TPGS	3 w/v %	67	30	4.3
5 w/v % (PEO 600K/PVP 90K-70/30 w/w %)	Tween 20	3 v/v %	62	30	4.4
	TPGS	5 w/v %			
	Tween 20	5 v/v %	65	30	4.5
	TPGS	3 w/v %	67	30	4.6

4.2.2.2.2 Emulsions prepared using Span 80 and TPGS

The polymer solution already studied in the previous chapter, i.e. 5 w/v % of PEO 600K solution, was prepared in aqueous media. This forms a continuous phase for o/w emulsion, which constitutes 75 v/v %. The dispersed phase is constituted of 20 v/v % of oils. Sunflower, fish, flaxseed, squalene and olive oils were used. Span 80 and TPGS were used as emulsifiers with the concentrations presented in **Table 4.2**. Span 80 was dissolved in an appropriate oil phase while TPGS was dissolved in cold water. Oil phase was added into the TPGS/PEO aqueous solution and homogenized by means of HPDI at 11,400 rpm for 3 minutes. The emulsions obtained were divided into three parts: one to be stored at fridge temperature, the other at room temperature for one week to check the stability of emulsions over time and a small quantity of the third part was analysed by DLS and LD immediately, with the remainder being electrospun immediately. The EPPs are as follow: 150 mm – 0.1 ml/h – 12–20 kV.

The HLB values for blended emulsifiers were calculated as follows:

$$\text{The wt. \% of first emulsifier in the formulation} \cdot \text{HLB value of first emulsifier} = X_1$$

$$\text{The wt. \% of second emulsifier in the formulation} \cdot \text{HLB value of second emulsifier} = X_2$$

$$\text{HLB of blend} = X_1 + X_2 \text{ [398]}$$

Table 4.2. Emulsifier concentrations in the formulation and their calculated HLB values.

Sample No.	Emulsifiers blend		Calculated HLB value
	Span 80 v/v	TPGS w/v	
4.7	100 %	—	4.3
4.8	87 %	13 %	5.5
4.9	68 %	32 %	7.1
4.10	48 %	52 %	8.9
4.11	28 %	72 %	10.7
4.12	6 %	94 %	12.7
4.13	—	100 %	13.2

4.2.2.3 Coaxial emulsion electrospinning

4.2.2.3.1 Emulsions prepared using Tween 20/TPGS emulsifiers and PEO/KIO₃ polymer solution

For coaxial electrospinning, two types of solution were prepared. One is for the inner phase and the other for the outer phase. For the inner phase, o/w emulsion was prepared as described in **section 4.2.2.2.1** for sample N4.1 in **Table 4.1**. The outer phase is composed of PEO 600K/KIO₃ polymer solution with 5 w/v % total solution concentration and 98/2 w/w % of PEO/KIO₃ concentration prepared in aqueous media. The EPPs for coaxial EE are as follows: 200 mm – 0.1 ml/h (inner phase) and 0.2 ml/h (outer phase) – 20–30 kV. Two types of collectors were used: stationary and rotating (1,000 rpm).

4.2.3 Characterization techniques

The morphology of the emulsion electrospun films were visualized by means of SEM. Photographic study using a digital camera was carried out to assess the impact of oil, emulsifier types, storage conditions and HLB value on the stability of emulsions. DLS and LD analysis were used to determine the droplet size and size distribution of the emulsions.

4.3 Results and discussion

4.3.1 Feasibility study of emulsion electrospinning

When we started the experiments, there was not any literature available on producing nanofibres by means of EE using liquid edible oils. Therefore, we did not know whether it was feasible or not, as the principle of electrospinning, including EE, is that the spinning solution must be conductive. However, there was only one report from Angeles et al. [126], and the authors electrospun o/w emulsion containing mineral oil and reported that emulsion drops deform and break up during electrospinning; thus even drop size in the order of tens of microns was electrospun, where the drop phase was incorporated into fibre. Thus, we anticipated that if mineral oil containing emulsion can be electrospun, we can also encapsulate edible oil into a conductive spinnable polymer solution, which will cover the oil

drops with a thin layer and will be capable of carrying oil droplets towards the collector if the oil drops are small enough to be light. In order to validate our assumption, a series of experiments was carried out, as described above in the methodology. The SEM images of all the EE samples carried out as the first step of the feasibility experiments are given in **Figure 4.1**.

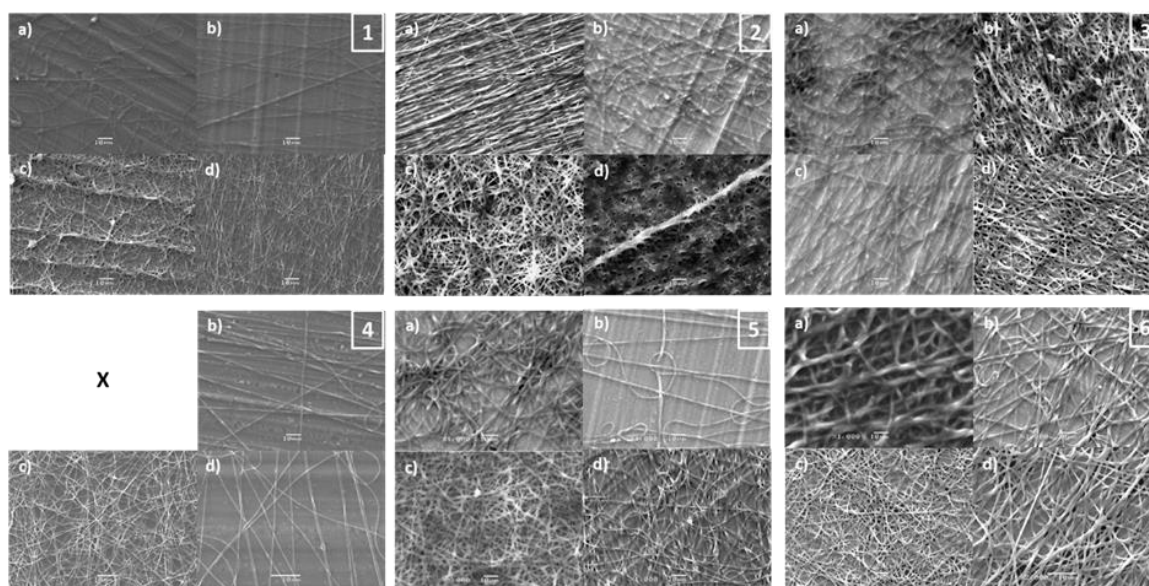


Figure 4.1. The SEM images of emulsion electrospun films: the top three tetrads, i.e. (1–3) are made with 5 w/v % of PEO-600K polymer concentration, and the bottom three tetrads, i.e. (4–6) are made with 7 w/v % PEO-600K. Both sets emulsified as follows: with Tween 20 (1) and (4): a) conventional electrospinning – standing collector (the image of 4a is absent because the oil comes out for that sample and the SEM technique was unable to capture an image); b) conventional electrospinning – rotating collector; c) coaxial electrospinning – standing collector; d) coaxial electrospinning – rotating collector. (2) and (5) were emulsified with TPGS and the type of the electrospinning and the collector were used in the same order as listed above. (3) and (6) were emulsified with a mix of Tween 20 and TPGS and the type of the electrospinning and the collector were used in the same order as listed above.

4.3.1.1 The effect of PEO and PEO/PVP continuous phase composition on fibre formation

The preliminary experiment results show an unstable emulsion formation, as the oil started to separate during electrospinning. Even so, the o/w emulsions were electrospun, and we were able to obtain a number of samples with a dry fibre mat, which releases oil when squeezed. From visual observation, all the firm, dry samples were created with emulsions prepared using PEO polymer solution as continuous phase. However, from the SEM images of the electrospun films, there were no apparent differences in fibre morphology of the samples prepared with 5 and 7 w/w % of PEO concentration (**Figure 4.1**). Whereas, all PEO/PVP polymer solutions used as continuous phase failed to encapsulate oil phase, as the oil comes out on the surface of the film and we could not take SEM images.

The inspection of the electrospun films by the naked eye immediately after preparation did not reveal any apparent differences between the films prepared with 5 and 7 w/v % of PEO concentration. All the samples were dry and non-greasy. However, after 8 months it was seen that the majority of the samples prepared with 7 w/v % of PEO concentration were dry and without oil on the surface, almost twice the number of the dry samples that was with 5 w/v % concentration. The oil comes out for most of the electrospun films prepared using 5 w/v % of PEO concentration. These results suggested that the solution viscosity can affect the stability of the end product and the encapsulation of the oil phase.

The preliminary experiments showed promising results and thus validate the feasibility of electrospinning o/w emulsions prepared using vegetable oil without hazardous organic solvents. However, many improvements were needed to achieve continuous production and core-sheath structured nanofibres. Therefore, the following changes in formulation were implemented in the next step. In spite of the fact that the 7 w/v % of PEO concentration had better stability, it requires a high DC voltage during electrospinning, more than 30kV to overcome the surface tension, which is an unsafe condition as our laboratory equipment is not suitable for conducting such experiments. Therefore, it was decided to decrease the oil content, i.e. by 20 v/v %, and use a polymer solution with a safe 5 w/v % PEO concentration which does not require high DC voltage. The results are described below in **section 4.3.2**.

4.3.1.2 The effect of emulsifier type on fibre formation: Tween 20 and TPGS

The effect of emulsifiers at this stage was not clear, as the electrospun samples with Tween 20 by itself, TPGS by itself and a mix of them both were dry and few of them became oily. This is due to the instability of o/w emulsions, as the oil in the syringe separated during electrospinning and thus the oil content was inconstant. Nevertheless, from the SEM images, the morphology of the mats of the samples containing Tween 20 shows sparse and thin fibres, whereas the morphology of the samples prepared using TPGS show a dense fibre-like net. The samples prepared with a mixture of both emulsifiers were somewhere in between, comprised of a fibre-like net and thin film (**Figure 4.1**).

The results suggest that an improved methodology needs to be developed to obtain stable emulsion to see the emulsifiers' effect and to produce reproducible core-sheath structured nanofibres. This was achieved by changing the emulsifier type, which is described in **section 4.3.2**.

4.3.1.3 The effect of conventional and coaxial emulsion electrospinning on fibre formation

The SEM images show that the coaxial electrospun o/w emulsions show comparatively better fibre morphology than conventional electrospun emulsions (**Figure 4.1**). This might be due to the PEO/KIO₃ solution from the outer needle that provides an extra layer to entrap the oil phase and facilitate fibre formation. However, in the next step in **section 4.3.2**, electrospinning was performed using conventional EE from the beginning to work out the best solution concentration and component ratio relative to each other. Later, if it is necessary, coaxial electrospinning can be utilized.

4.3.1.4 The effect of the type of collectors: stationary and rotating drum

The effect of the type of the collector was also inaccurate due to the process of oiling off of emulsions (the phase separation of oil from the emulsion) during electrospinning. Therefore, it was hard to interpret the results. In the next step, to minimize this complication, and during the feasibility studies carried out in this chapter, only the stationary collector was used.

4.3.2 Emulsion electrospinning using emulsions prepared using Span 80 and TPGS

From the feasibility experiments with the emulsions prepared using Tween 20/TPGS, we could see that it was possible to electrospin emulsions; however, the stability issue led to the necessity to formulate emulsions using different emulsifiers. Emulsion stability, of duration longer than the Tween 20/TPGS formulation, was achieved by changing the emulsifier type, i.e. by replacing Tween 20 with Span 80 and reducing the amount of oil by 20 v/v %. Span 80 has a low HLB value that can be used to obtain emulsions with a range of HLB values in a mixture with emulsifier that has a high HLB value and thus can select the most stable emulsion from the range of formulations. In addition, following our aim to formulate a delivery system suitable for the delivery of different poorly and highly water-soluble active ingredients, in addition to sunflower oil a number of other widely used oils were employed, such as flaxseed, fish, olive and squalene oils. Span 80 helps to achieve the desired HLB value required for each oil type. TPGS was retained as it shows better fibre forming capability than Tween 20. In addition, using two emulsifiers always promotes better emulsion stability than when one is used alone [142]. The sections below discuss the stability of emulsions, prepared using Span 80 and TPGS emulsifiers, assessed by photographic study and parameters affecting their stability.

4.3.2.1 Stability test of emulsions analysed by photographic study

Of the variety of analytical instruments available to characterize the composition, microstructure and physicochemical properties of emulsions, photographic study is one of the most straightforward, simple, cheap and quick approaches to provide information about the overall appearance of emulsions [142] and the experimental determination of gravitational separation. The principle of this method is to take photographs of an emulsion placed in a transparent test-tube over time using a digital camera. The images can be used as a record of the stability of the emulsion and/or can be used for further analysis using image analysis software by measuring the change in height of any boundaries formed between different layers [399, 400].

Thus, a photographic study was carried out to study the stability of emulsions prepared with different emulsifier concentrations and stored at room and fridge temperature for one week to correlate emulsion stability with fibre formation. We measured the height of phase separated boundaries to estimate the stability of emulsions (**Table 4.3**) and revealed the impact of the emulsifier type and storage conditions, and the effect of the HLB value of emulsifiers in the formulation and oil type (**Figures 4.2-4.6**).

Table 4.3. The height of boundaries of separated phases (measured using ImageJ software), which have occurred in samples N4.7, N4.12 and N4.13. Abbreviations: o-oil, w-water.

Type of oil	The height of boundaries of separated phases (mm)					
	Sample N4.7		Sample N4.12		Sample N4.13	
	Room T	Fridge T	Room T	Fridge T	Room T	Fridge T
Sunflower oil	4±0.23	5±0.53	13±0.21	10±0.27	46±0.43	6±0.39
Flaxseed oil	3±0.28	3±0.56	7±0.26	8±0.16	28±0.59	7±0.28
Olive oil	5±0.11 (o) 3±0.08 (w)	8±0.28 (o) 2±0.39 (w)	6±0.42	2±0.24	28±0.34	0
Fish oil	3±0.21	3±0.35	5±0.54	3±0.08	22±0.45	4±0.23
Squalene oil	20±0.46 (o)	0	32±0.33	20±0.44	59±0.24	35±0.5



Figure 4.2. Photographic study of emulsions prepared using different oils after one week: a) sunflower; b) flaxseed; c) olive; d) fish; e) squalene oils. The left picture is of the emulsions stored at room T and the right at fridge T. The numbers on the top of each sample are the numbers of the samples, which were prepared with different types of emulsifier concentrations (Table 4.2).

4.3.2.1.1 The impact of oil type

Figure 4.2 shows the photography of emulsions prepared with different types of oils stored at room and fridge temperatures. Here, we will compare emulsions stored at room temperature. As can be seen, the type of oil used to prepare emulsions has an impact on the stability of o/w emulsions in only two samples. Thus, if we compare the emulsions of samples N4.8, N4.9, N4.10 and N4.11 that have the same emulsifier concentration but are differentiated by oil type, then we cannot see any apparent differences. However, sample N4.7 shows an apparent impact of oil type on the stability of emulsions. In the case of N4.7, squalene and olive oils have oiling off, whereas other samples with the same emulsifier concentration but with other types of oil show stability of emulsions. We anticipated that this might be due to oil viscosity, which has been reported to have an impact on droplet size distribution, and consequently on the stability of emulsions. For example, Wooster et al. [401] reported that the droplet size of nanoemulsions was affected by the viscosity of oil. High viscosity oil such as peanut oil has a larger $D = 120$ nm than nanoemulsions prepared with low viscosity oils such as hexadecane, with a $D = 80$ nm. Conversely, Bouchemal et al. [402] reported that they obtained the smallest droplet size with oils that have high viscosity (3,000-4,500 mPa s at 20 °C) and low viscosity (4.5-7.5 mPa s at 20 °C), namely α -tocopherol ($171 \text{ nm} \pm 2$) and hexyl laurate ($310 \text{ nm} \pm 14$), respectively. Pal et al. [403] also revealed that with the increase of emulsion viscosity, the droplet size decreases. Therefore, in order to understand the effect of oil viscosity on emulsion stability, we compare the viscosities of oils (**Table 4.4**) and their stability using a photographic study (**Table 4.3, Figure 4.2**). However, we did not conduct LD analysis for squalene and olive oils, and we cannot say with certainty how the viscosity affects the droplet size of these emulsions. Nevertheless, if we consider the work of Wooster et al. [401], K. Bouchemal et al. [402] and Pal et al. [403], from the photographic study we can assume that squalene and olive oils, which have the lowest and the highest viscosities of the oils presented in this study, respectively, may probably have larger droplet sizes in sample N4.7, which favours oil droplets coalescence faster compared to emulsions with smaller droplet sizes.

Table 4.4. The viscosities of oils, taken from [182].

Oil type	Sunflower	Flaxseed	Olive	Fish	Squalene
Viscosity in cSt (at 20° C±2)	47.4	51.2	84.0	42.0	15.9

Samples N4.12 and N4.13 show a creaming, aqueous phase was separated at the bottom of the tube, irrespective of the oil type used in the formulation; however, there were differences in the creaming rate depending on oil type (**Figures 4.2, Table 2**). Therefore, we speculated that oil type has a small effect on the stability of emulsions prepared in this study. Additional analysis needs to be carried out to confirm the possible influence of oil type on emulsion stability for a given formulation, such as droplet size distribution by means of LD and longer storage for at least one month, to reveal the differences in stability in samples N4.8, N4.9, N4.10 and N4.11.

4.3.2.1.2 The impact of emulsifier type

The effect of emulsifier type is significant with samples N4.12 and N4.13 because creaming has occurred in those samples irrespective of oil type, as already discussed in the previous subsection. This suggests that in sample N4.13, possibly the TPGS emulsifier alone cannot provide stability of emulsions with the given emulsion composition in this study and/or with the given concentration. If the concentration of the emulsifier is not sufficient enough, oil droplets may not be fully covered by the emulsifier during droplet break up and therefore emulsifier depletion will occur in the oil-water phase causing droplet creaming [142]. Sample N4.12 shows a slower creaming rate, assessed from the height of the aqueous phase, compared to the pure TPGS emulsion (**Table 4.2, Figures 4.2**). This may be due to the Span 80, which could have completed to some extent the emulsifier depleted surface and thus formed a more stable emulsion. Similarly, in samples prepared using squalene and olive oils, oiling off has occurred with the emulsion prepared with Span 80 alone. However, other samples with the same amount of emulsifier concentration but with different oils show stability of emulsions. Therefore, we anticipated that this issue might be due to oil viscosity, as mentioned in **section 4.3.2.1.1**.

Generally, emulsions prepared with a combination of emulsifiers possess better stability than emulsions prepared with only one type of emulsifier [142]. This is probably why samples N4.8,

N4.9, N4.10 and N4.11 demonstrated better stability in all types of oil used to prepare emulsions, compared to emulsions prepared with only one type of emulsifier.

4.3.2.1.3 The impact of the HLB value of emulsifiers in the formulation

Stable emulsions are formed when the HLB values of emulsifiers or the combination of emulsifiers are close to the required HLB value of the oil phase [404]. Therefore, we compared the stability of emulsions and the emulsifiers' HLB values in the formulation (**Table 4.2**) with the required HLB value of the oils.

Sunflower and olive oil require a similar HLB value of 7 ± 1 ; however, the stability assessment shows some differences in the stability of emulsions. Thus both samples, according to the literature [404], should have stable emulsions in samples in which the emulsifiers' HLB values are close to 7, i.e. from 5 to 9. This is supported by the case of the emulsion containing olive oil, in which oiling off and creaming has occurred with samples that have low and high HLB values, i.e. 4.3 (N4.7) and 12.7–13.2 (N4.11-4.13), respectively. However, in emulsion containing sunflower oil, creaming has occurred only for samples that have high HLB values as in the samples N4.12 and N4.13, but the sample with a low emulsifiers' HLB value showed good stability and no phase separation. As for flaxseed oil, which has a low HLB value requirement of oil (3.23 ± 1), good stability should be demonstrated by samples that have low emulsifiers' HLB value. However, no distinguishing changes in stability were observed. As in the case with sunflower and olive oils, it shows poor stability with samples that have a high emulsifiers' HLB value, i.e. N4.12 and N4.13, but others were stable. The required HLB values of fish and squalene oil were not found in the literature, and determining these values was not within the scope of this study. Nevertheless, we can report that emulsions prepared using fish and squalene oils also have creaming with samples N4.12 and N4.13. However, Yuan et al. [405] have shown that high HLB value emulsifiers facilitate stability of o/w emulsions because of their emulsifier type, i.e. their HLB value affects the particle sizes of the emulsion. According to Yuan et al.'s results, emulsion prepared using Tween 20 has the smallest particle size ($173\text{ nm}\pm 2.07$) and emulsion prepared using Tween 40 has the largest particle size ($184\text{ nm}\pm 4.9$). The study explained that emulsifiers with a greater hydrophilicity could stabilize the particles in o/w emulsion more efficiently and therefore produce smaller particles. Tween 20 has a higher HLB value (16.7) than Tween 40 (HLB = 16.5). In this study, the most stable

emulsions of all five type of oils used in the emulsion preparation were for samples N4.8, N4.9, N4.10, N4.11 that have moderate HLB values ranging from 5.5 to 10.7. These results suggest that the emulsifiers or the combination of emulsifiers' HLB values that are close to the required HLB value of the oil phase have little impact on emulsion stability for these formulations. This conclusion is based on the example of olive and sunflower oils, which have instable and stable emulsions at low emulsifier HLB values respectively. As discussed above in **section 4.3.2.1.1**, other parameters such as oil viscosity may also play a role.

4.3.2.1.4 The impact of storage conditions

The storage conditions have an impact on emulsion stability depending on the composition formulation. Emulsions prepared using sunflower, flaxseed, olive, fish and squalene oils resulted in aqueous phase separation in samples N4.12 and N4.13 after one week of storage at room temperature. However, this phase separation was not significant for emulsions stored at fridge temperature (**Figures 4.2, Table 4.2**). In addition, the apparent impact of storage conditions was seen for the sample prepared using squalene oil, sample N4.7. The oil phase separation was clearly seen for the sample stored at room temperature, while the sample stored at fridge temperature had a more stable appearance. Conversely, for emulsions prepared using olive oil, the phase separation of oil phase was observed also for sample N4.7; however, separation was seen with the samples stored at both room and fridge temperatures. Other than that, the stability results for squalene and olive oils were the same as for sunflower, flaxseed and fish oils.

4.3.2.2 Particle size analysis

4.3.2.2.1 Particle size analysis of emulsions using DLS

The DLS technique was used in order to determine particle size distribution in the emulsion and the physical stability of emulsions, because we expected to have particle sizes below 10 μm . The physical stability of emulsions was estimated by measuring emulsion droplet size as a function of time. Three formulation parameters and two storage conditions were studied to see the impact on particle size distribution and the stability of the finished product. These parameters were oil and emulsifier type, room and fridge temperature storage for 1 week, and the HLB value of emulsifiers. However, the results were not informative, as the particle

size distribution of o/w emulsions show random size distribution for all samples, namely from 0.1 μm to 9 μm (**Table 4.5**), thus it was difficult to assess the impact of the parameters listed above on droplet size distribution. This is due to the DLS technique droplet size measurement limitations, namely up to 10 μm , and it was reported that particles larger than 3 μm may distort the measurements and therefore, additional corroboration with laser diffraction (LD) or a laser scattering technique is recommended [350]. Thus, we conducted particle size analysis using the LD technique, in the next section, to check whether there are larger droplets.

Table 4.5. Approximate droplet size distribution of emulsion prepared using different type of oils and emulsifiers measured immediately after preparation and after one week, stored at room and fridge temperatures. N=3.

Oil type	Storage conditions	Particle size distribution (μm)-Span 80 v/v % – TPGS w/v %						
		100	87–13	68–32	48–52	28–72	6–94	100
Sunflower oil	1 st day	>1<10 unimodal	-	$\geq 1 < 10$ unimodal	>1<10 unimodal	>1<10 unimodal	>1<10 unimodal	>1<10 bimodal
	After 7 days- room T	$\geq 1 < 10$ bimodal	>0.1<10 bimodal	>0.1<10 bimodal	>0.1<10 bimodal	>0.1<10 bimodal	>1<10 unimodal	>1<10 unimodal
	After 7 days- fridge T	>1<10 unimodal	>0.1<10 bimodal	$\geq 0.1 < 10$ bimodal	>0.1<10 bimodal	>1<10 unimodal	>0.1 \leq 1<10 bimodal	>1<10 bimodal
Flaxseed oil	1 st day	>1<10 unimodal	>1<10 unimodal	>1<10 unimodal	>1<10 unimodal	$\geq 1 < 10$ bimodal	>1<10 bimodal	>1<10 bimodal
	After 7 days- room T	>1<10 unimodal	>0.1<10 bimodal	>0.1<10 bimodal	>1<10 unimodal	>1<10 unimodal	>1<10 unimodal	>1<10 unimodal
	After 7 days- fridge T	>1<10 unimodal	$\geq 0.1 < 10$ bimodal	$\geq 0.1 < 10$ bimodal	>1<10 unimodal	$\geq 1 < 10$ unimodal	>1<10 unimodal	>1<10 unimodal
Olive oil	1 st day	>1<10 bimodal	>0.1<10 bimodal	$\geq 0.1 < 10$ bimodal	>0.1<10 unimodal	>1<10 unimodal	$\geq 0.1 < 10$ trimodal	$\geq 0.1 < 10$ trimodal
	After 7 days- room T	>1<10 unimodal	>1<10 unimodal	>0.1<10 bimodal	>1<10 unimodal	>0.1<10 bimodal	>1<10 unimodal	>1<10 unimodal
	After 7 days- fridge T	-	$\geq 0.1 < 10$ bimodal	>1<10 unimodal	$\geq 0.1 < 10$ bimodal	$\geq 0.1 < 1 < 10$ trimodal	$\geq 0.1 \leq 1 < 10$ trimodal	-

(Continuous)

Oil type	Storage conditions	Particle size distribution (μm)-Span 80 v/v % – TPGS w/v %						
		100	87–13	68–32	48–52	28–72	6–94	100
Fish oil	1 st day	>1<10 unimodal	>1<10 unimodal	>0.1<1<10 bimodal	\geq 0.1<10 bimodal	>1<10 unimodal	\geq 0.1<10 bimodal	>0.1<1<10 unimodal
	After 7 days- room T	>1<10 unimodal	\geq 1<10 unimodal	\geq 0.1<10 bimodal	\geq 0.1<10 bimodal	>1<10 unimodal	>1<10 unimodal	>0.1<1<10 bimodal
	After 7 days- fridge T	>1<10 unimodal	>1<10 unimodal	>1<10 unimodal	>1<10 unimodal	>1<10 unimodal	>1<10 unimodal	>1<10 bimodal
Squalene oil	1 st day	>1<10 unimodal	-	\geq 0.1=1<10 trimodal	\leq 0.1<1<10 bimodal	>1<10 bimodal	\geq 1<10 bimodal	\geq 1<10 bimodal
	After 7 days- room T	-	-	\geq 0.1<10 trimodal	\geq 0.1<10 bimodal	-	>1<10 unimodal	>1<10 unimodal
	After 7 days- fridge T	-	-	-	-	-	-	>1<10 unimodal

4.3.2.2.2 Particle size analysis of emulsions prepared using sunflower oil by LD

LD analysis was conducted only for emulsions prepared using sunflower oil. **Figure 4.3** shows the results of the volume density distribution of emulsions as bimodal size distribution. As we assumed, the result of LD analysis shows that the emulsions have a droplet size larger than 10 μm (**Table 4.6**). However, there was no correlation between the droplet size distribution and the emulsifiers' HLB values. The droplet size distribution of all emulsions prepared using two types of emulsifiers show random results, i.e. the result was not correlated to the HLB value. The emulsions with the lowest HLB value of 4.3 and a high HLB value of 12.7 resulted in comparatively small particle size distribution. At the same time, emulsions that have a comparatively lower HLB value of 5.5 and the highest HLB value of 13.2 resulted in comparatively large droplet size distribution. The emulsions having moderate HLB values (7.1, 8.9 and 10.7) have comparatively moderate particle size distribution. Whereas the photographic study shows that emulsions with low and moderate particle size distribution have good stability in comparison with high HLB values. In addition, bimodal size distribution is attributed to the dominance of coalescence instability of emulsion droplets [145, 406].

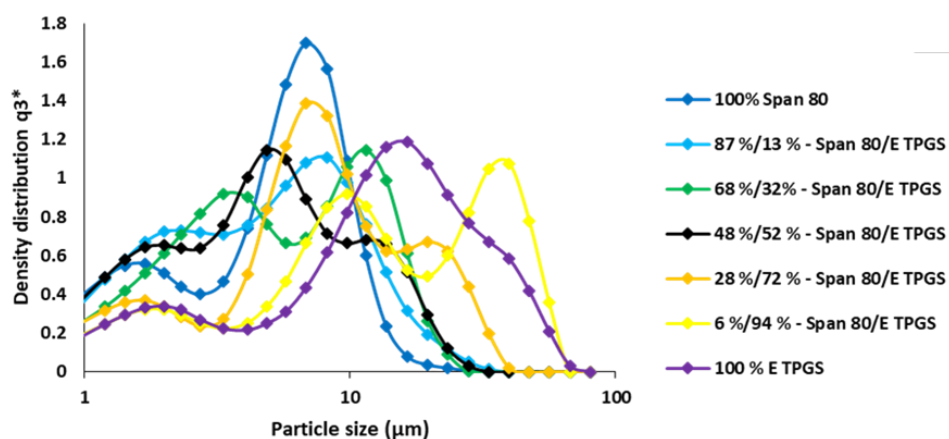


Figure 4.3. Volume density distribution of emulsion particle size prepared with HPDI. X-axis is plotted on log scale. q_3^* – density distribution by volume.

Table 4.6. Droplet size distribution of emulsion prepared using sunflower oil immediately after preparation. Emulsifier ratio and their calculated HLB values. N=3.

Sample No.	Emulsifier blend		D10 (μm)	D50 (μm)	D90 (μm)	Calculated HLB values
	Span 80 v/v %	TPGS w/v %				
4.7	100	—	1.17 \pm 0	5.42 \pm 0	10 \pm 0.026	4.3
4.8	87	13	1.82 \pm 0.02	12.24 \pm 0.29	42.2 \pm 0.6	5.5
4.9	68	32	1.43 \pm 0.018	7.31 \pm 0.21	21.47 \pm 1.02	7.1
4.10	48	52	1.25 \pm 0	4.59 \pm 0.02	13.8 \pm 0.19	8.9
4.11	28	72	1.44 \pm 0.005	5.02 \pm 0.036	14.23 \pm 0.07	10.7
4.12	6	94	1.28 \pm 0	4.75 \pm 0.015	12.28 \pm 0.09	12.7
4.13	—	100	1.85 \pm 0.025	13.66 \pm 0.425	35.85 \pm 2.35	13.2

4.3.2.3 Morphology of the emulsion electrospun films

When Span 80 was used, the effects of emulsifiers on fibre formation were distinguishable. Thus, from the SEM images (**Figures 4.4-4.8**), it is evident how the morphology of films changed, insensible to the human eye, from the thin film to a more fibrous composite in direct proportion to TPGS content. When electrospun films were examined by the naked eye, the samples emulsified with 100 v/v % of Span 80 were producing subtle and fine films, whereas film electrospun from emulsion prepared using 100 w/v % of TPGS showed a firm, fibre-net texture. In addition, from the SEM images, better fibre morphology appeared for samples with 94 and 72 w/v % of TPGS, i.e. where there was a higher content of TPGS. This confirms the advantage of TPGS in producing nanofibres. As for oil type, fibres from emulsions prepared using squalene oil produced separate and uniform fibres (**Figure 4.8**); however, the emulsion's stability was poorer than in emulsions containing sunflower and fish oils (**Figure 4.2, Table 2**). Flaxseed oil containing emulsion failed to produce fibres, as the oil comes out on the surface of the film, although these emulsions had shown good stability. Therefore, we could obtain SEM images of only two samples (**Figure 4.5**). The samples with fish, sunflower, and olive oils showed dry and firm films, yet the fibre morphology from the SEM images are not as nice as the fibres from squalene emulsions. However, olive oil containing emulsions show poorer stability than sunflower and fish oils containing emulsions. Samples N4.8, N4.9, N4.10 and N4.11 demonstrate better emulsion stability compared to samples N4.7, N4.12 and N4.13. However, from the SEM images and from inspection of the electrospun films by the naked eye, the better morphology appears in samples N4.11, N4.12, N4.13. The results show

that the stability of emulsions is not the key parameter that determines the spinnability of emulsions. However, the stability of emulsion is crucial for quality control of a delivery system during manufacturing. The type of oil and emulsifier demonstrated an impact on fibre formation; however, we cannot indicate what physicochemical properties of oil affect the fibre formation as there is no correlation with the viscosity of the oil. Flaxseed oil has moderate viscosity, as do sunflower and fish oils; however, it failed to form dry and firm films.

It would be very interesting to study the parameters that affect fibre formation and design a more stable emulsion. However, we discontinued this project because we discussed the results and came to the conclusion that emulsion electrospinning is a fascinating method to prepare ultrathin fibres capable of delivering both poorly and highly water-soluble active ingredients. Nevertheless, emulsion electrospun fibres encapsulate a low amount of oil, and are therefore an insufficient method to encapsulate large doses of oil-soluble vitamins and poorly water-soluble drugs. Therefore, we decided to focus our attention towards SOS, which was described by Patel et al. [147] as a system capable of holding enormously large amounts of oil. The results are described in the next chapter.

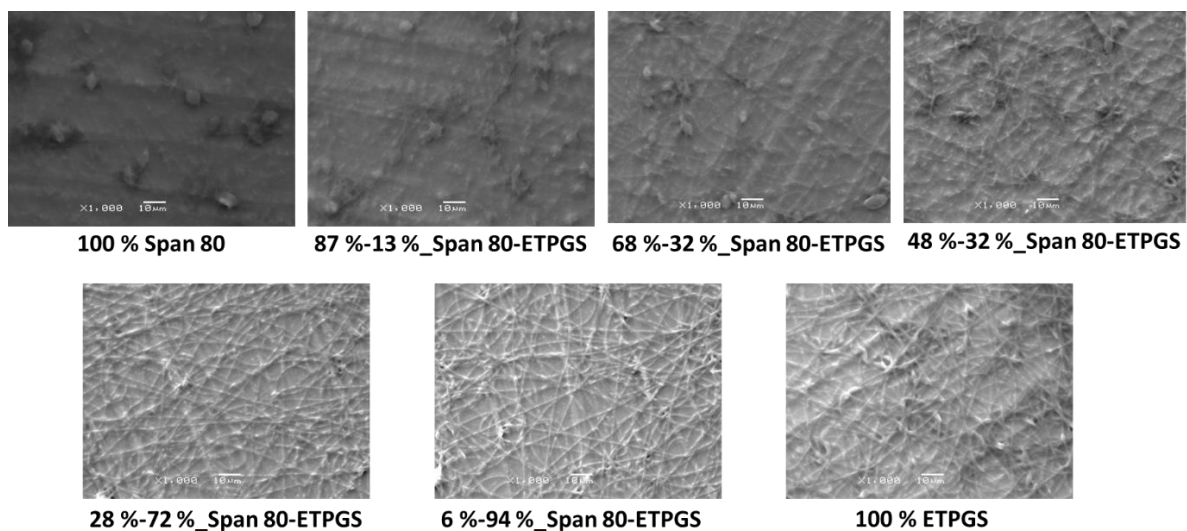


Figure 4.4. SEM images of o/w emulsion electrospun films with sunflower oil.

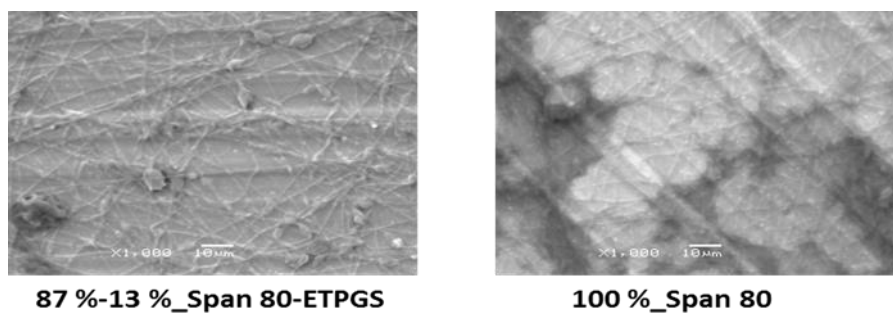


Figure 4.5. SEM images of o/w emulsion electrospun films with flaxseed oil.

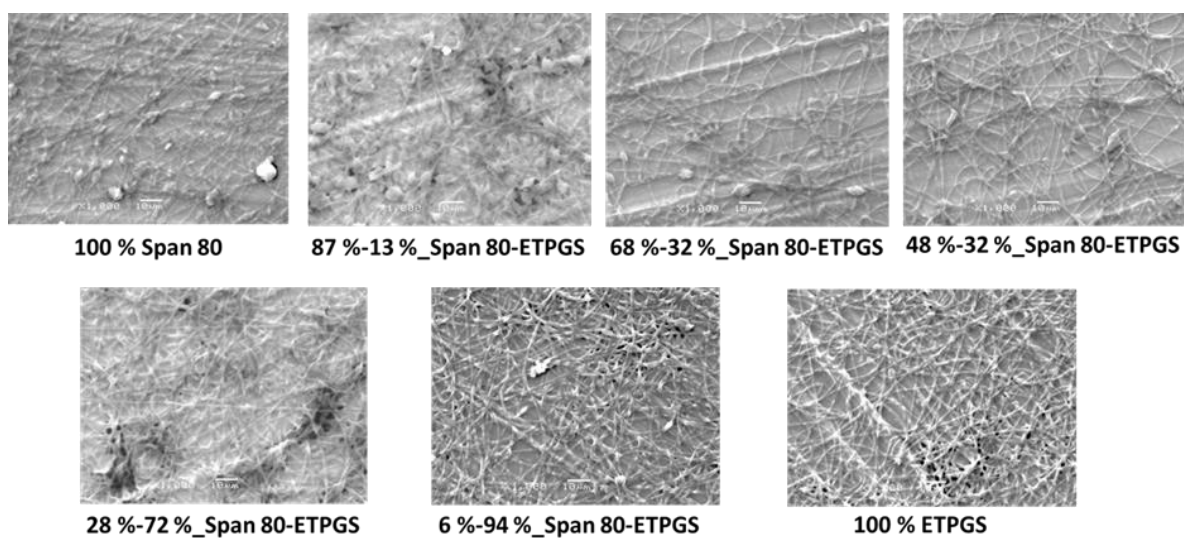


Figure 4.6. SEM images of o/w emulsion electrospun films with olive oil.

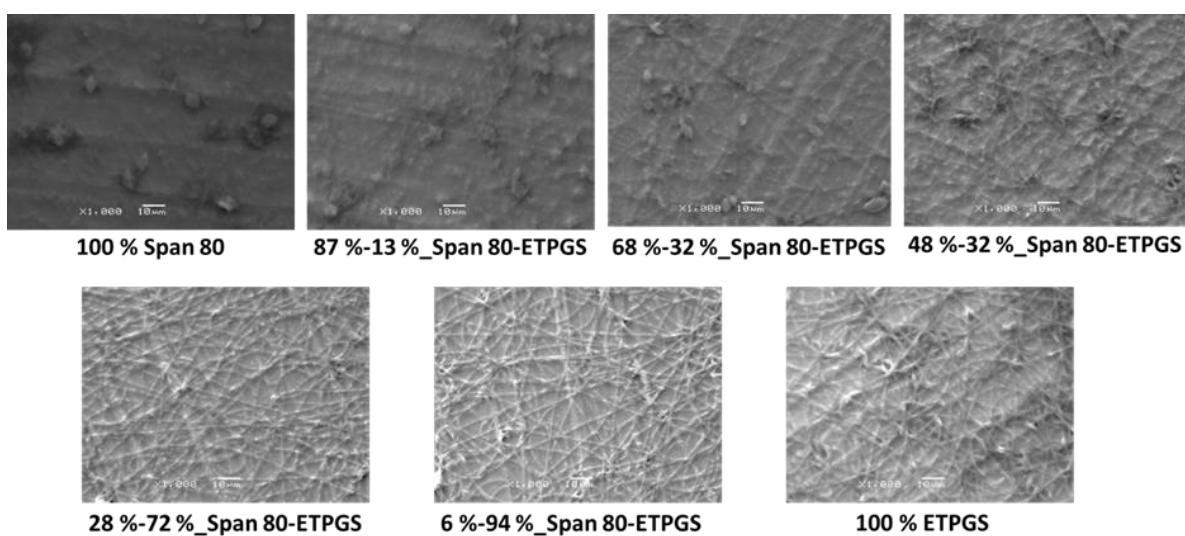


Figure 4.7. SEM images of o/w emulsion electrospun films with fish oil.

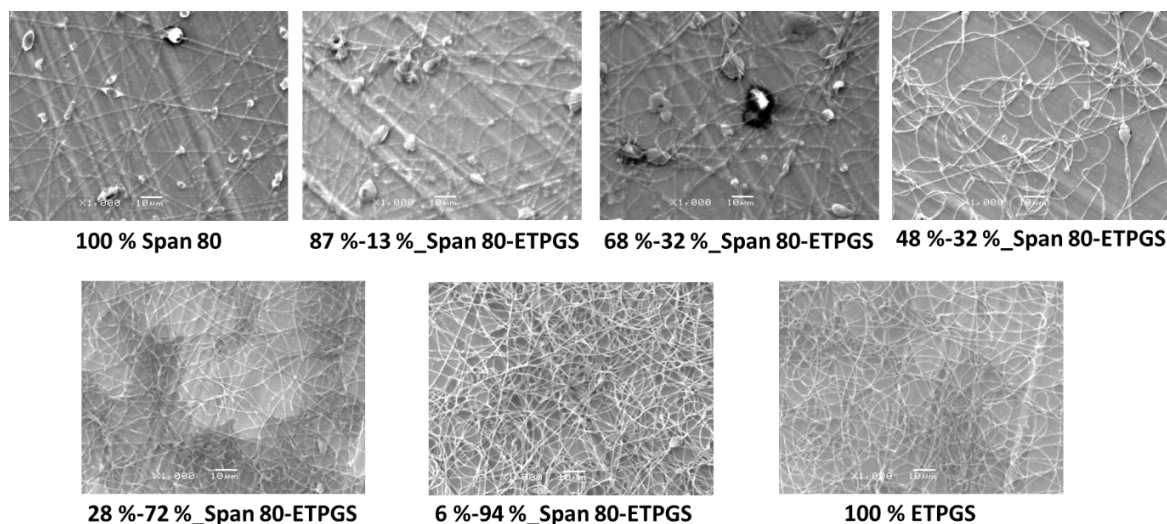


Figure 4.8. SEM images of o/w emulsion electrospun films with squalene oil.

4.4 Conclusion

A potential delivery system for poorly and highly water-soluble active ingredients has been developed by means of conventional EE. O/W emulsions were successfully electrospun without the use of organic solvents. Four different functional components can be encapsulated in this formulation: Iodine, Vitamin E, vegetable oils and fish oil. TPGS was proven as a good emulsifier for protecting the oil phase from leaking, which could often result in the greasiness of the film. In addition, TPGS can be used as a source of vitamin E and an enhancer of the bioavailability of many drugs and nutrients [48-50]. Thin films, possibly core-sheath structured nanofibres or oil drops incorporated in fibres, were opaque and matted, free of oil on the surface for up to 8 months and demonstrating a good encapsulation of liquid oil. However, the drawback of this delivery system is that it can only encapsulate a very limited amount of liquid oil, which is often insufficient for the doses required. Therefore, in the next chapter we investigate the development of another delivery system, the structured oil system (SOS), which can hold a significantly larger amount of oil.

5 Chapter 5. Structured oil as a platform for the delivery of water-soluble and oil-soluble drugs

5.1 Introduction

In conventional nutritional and medical products, soft capsule gels are most often used to deliver large doses of oil. However, the stability of the soft gel capsules is often a concern. The most effective way to maintain the stability of the capsule shells is to individually pack the capsules in blister packs using highly impermeable packaging materials (used for medical products). However such packaging is more costly and most of the soft gel capsule nutrient supplements are often packed in plastic bottles. Tackiness of the shell due to the absorption of moisture is one of the most common issues with such products. In this project, we are aiming to develop a new type of formulation to deliver a high dose of oil in a solid form. A solid structured oil system, which can hold a large amount of oil, has been designed to use as a carrier to deliver water-soluble (solubilized and contained in a polymeric scaffold) and oil-soluble drugs or nutrients (solubilized in the liquid oil and immobilised by a polymeric scaffold). As discussed in detail in **Chapter 1**, structured oils, also known as oleogels, are formed by removing the water from a dense emulsion which is often stabilised by a blend of polymers/surfactants. In this chapter, we utilized the combination of protein and polysaccharide that has been used widely in the food and pharmaceutical industry to form the stable emulsions. The emulsions were then dehydrated by using either a thermal or freeze drying process. Similar structured oil formulations have been developed by food scientists and are primarily used as a shortening agent [147, 285, 286]. These works inspired us to adopt such structures and apply them in the pharmaceutical area for drug and nutrient delivery. In this chapter we also investigated the impact of the formulation and processing parameters on the formation, stability and properties of SOSs, the oil holding capacities of the formulations and their drug release behaviour using a model drug.

Gelatine (G) and xanthan gum (X) were utilized in this study to create the SOS because they are GRAS and biodegradable excipients. They have been widely used as emulsifying agents

and viscosity modifiers in pharmaceutical and food products. Gelatine, being surface active, adsorbs at the oil-water interface and Xanthan gum is non-surface active and forms an interfacial complex with gelatine. Sunflower oil was used as the model oil phase. In addition, HPMC, MC, Tween 20 and CMC were also used to replace either gelatine or Xanthan to explore other mechanisms of the formation of SOSs. Metoprolol succinate, used for treating high blood pressure, was used as a model of a highly water-soluble drug, and ketoconazole and coumarin were used as the oil-soluble model compounds to evaluate the drug encapsulation and dissolution behaviour of SOS formulations.

5.2 Materials and methods

5.2.1 Materials

Gelatine, xanthan gum, HPMC, MC, CMC, Tween 20, sunflower oil, ketoconazole, metoprolol succinate and coumarin 6. The physicochemical properties of the materials used are described in **sections 2.2, 2.2.2, 2.2.3, 2.2.4**.

5.2.2 Methodology

5.2.2.1 Emulsions prepared using HPDI

Emulsion prepared using pure G. G in 1.6 w/v % concentration was dissolved in a warm aqueous solution and was then mixed with the oil phase with the help of HPDI at $\approx 11,400$ rpm for 5 minutes. The oil ratio to aqueous phase was 30/70 v/v %.

Emulsion prepared using pure X. Emulsion containing pure X as an emulsifier was prepared as described above for G, except, X was dissolved in cold water.

Emulsion prepared using G and X. G and X were separately dissolved in water to make G and X aqueous solutions. The concentration of G and X in all analysis was 1.6 and 0.6 w/v %, respectively, except, when the effect of protein to polysaccharide ratio on SOS formation was studied where three concentration variations were employed (**Table 5.1**). The two solutions were mixed in a 50/50 v/v % concentration and were used as the aqueous phase of the emulsion formulations. For the emulsions, the aqueous and oil phases were mixed in a 70/30

v/v % concentration. When the effect of oil volume fraction was studied, emulsions were prepared with an oil phase comprising 20, 30, 40 and 60 v/v % of the system. Sunflower oil, which was used as an oil phase, was dispersed in the aqueous polymer solution and mixed vigorously using HPDI at $\approx 11,400$ rpm for 5 minutes, except when the effect of HPDI processing parameters were being studied, when the following parameters were used: 11,400 and 14,000 rpm, 5 and 9 minute durations.

Table 5.1. Concentration of G and X used in the preparation of emulsions when the effect of protein-polysaccharide concentration on SOS formation was studied.

Gelatine w/v %	Xanthan gum w/v %
1.2	0.6
2.3	0.9
0.6	1.2

Emulsion prepared using different emulsifiers. Emulsions were prepared as described in **section 5.2.2.1** for the emulsion prepared using G and X. The following emulsifier compositions were used: HPMC and X, MC and X, Tween 20 and X, G and CMC. The concentration of the compositions was the same as for G and X. When G was replaced with another emulsifier, that emulsifier would be used in the same concentration as G, i.e. 1.6 w/v %, and when X was replaced with another emulsifier, that emulsifier would be used in the same concentration as X, i.e. 0.6 w/v %.

Freeze-dried G/X mixture without oil. Freeze-dried G/X mixture without oil was prepared to compare with G/X SOS containing oil. G and X with a concentration of 1.6 w/v % and 0.6 w/v % was prepared in aqueous media and homogenized using HPDI at $\approx 11,400$ rpm for 5 minutes, then immediately freeze dried.

All experiments were performed in triplicate (n=3).

5.2.2.2 Emulsions prepared using HPH

Emulsion was prepared as described in **section 5.2.2.1**, and the G and X concentrations were 1.6 and 0.6 w/v %, respectively. After homogenization using HPDI, the primary emulsion obtained was subjected to HPH homogenization to obtain a secondary emulsion. The inlet

pressure of the HPH homogenizer was oscillating from 6,000 to 12,000 psi and for analysis we used samples that pass only once, except, when the effect of cycling duration of HPH on emulsion stability was studied, when the duration of cycling was for 3, 5 and 7 minutes. All experiments were performed in triplicate (n=3).

5.2.2.3 Producing structured oil systems

5.2.2.3.1 Freeze drying

All emulsions prepared in **sections 5.2.2.1 and 5.2.2.2** were subjected to lyophilization by means of a freeze dryer. The emulsions were first frozen at -23 °C overnight and then freeze dried under vacuum for 24 hours to obtain solid SOS at -20 °C.

5.2.2.3.2 Oven drying

Emulsion prepared using G and X with concentrations of 1.6 and 0.6 w/v % was subjected to lyophilization by means of an oven. The experiments were conducted at 70–80 °C for 24 hours using a Carbolite Natural Convection Laboratory Oven – PN 60, with a temperature range of 30–300 °C. The experiments were performed in triplicate (n=3).

5.2.2.4 Oil holding capacity under compression

The measurements were carried out using the compression test mode of a texture analyser. The sample was placed on a flat aluminium stage and compressed by a 30,000 gram load disk with d 25mm. The movement speed was 0.5mm/sec. The stiffness of 5 samples was high enough for that given load, therefore the samples were then kept at a maximum compressed point for 30 seconds to observe the resistance of the specimen to the force. Cellulose filter paper was placed on the flat aluminium stage of the texture analyser under the SOS. The amount of oil released during compression was assessed quantitatively from the weight difference between the oil soaked filter paper and the dry filter paper, by weighing the cellulose filter paper before compression of the SOS and after compression of the SOS when the filter paper is soaked with the released oil.

5.2.3 Characterization techniques

In this chapter, SOS for the delivery of water-soluble and oil-soluble drugs or nutrients were characterized using a range of techniques. An upright fluorescence microscope was mainly used to image the o/w emulsions. Brightfield images were substituted in some instances where the quality of the fluorescent images was poor and where validation of the o/w emulsion nature was not needed. CLSM images were also taken as the CLSM has higher resolution and better contrast [407]. Emulsions' particle size and stability were determined by means of an LD technique. The internal structure of the SOS and distribution of oil within the SOS were examined under fluorescence stereo microscopes, Cryo-SEM, TEM and X μ CT. ATR FT-IR was used to identify any protein-polysaccharide interaction in the sample of G/X SOS. The thermal degradations of raw materials and placebo G/X, HPMC/X, MC/X, G/CMC SOSs prepared using HPDI and stored at room, 40 °C and 75% RH were analysed by TGA. DSC estimates the thermal transitions of raw materials, freeze-dried G/X mixture without oil, placebo G/X SOS and G/X SOS loaded with APIs (ketoconazole and metoprolol succinate). A texture analyser was utilized to assess the mechanical properties of G/X, HPMC/X, MC/X, G/CMC SOS and their oil holding capacity under compression. Dissolution testing was conducted to study the dissolution profile of water-soluble API from G/X SOS prepared using two different homogenizing instruments: HPDI and HPH.

5.3 Results and discussion

5.3.1 Emulsion formation development

A number of studies have shown that protein-polysaccharide complexes have better emulsifying properties than when they are used by themselves. Selecting the right protein-polysaccharide ratio is important to produce a small emulsion droplet size with good stability to environmental changes. Normally, proteins tend to form smaller emulsion droplets at lower concentration than polysaccharides, and polysaccharides are better at producing emulsions with higher stability in a range of environmental conditions such as temperature, pH, and ionic strength [142]. However, Sun et al. [408] found that when increasing the protein concentration, smaller droplet sizes were produced. Similarly, Patel et al. [147] showed that

a variation in xanthan concentration does not change the droplet size of emulsions significantly; however, the droplet sizes were reduced when gelatine concentration is increased. In addition, emulsions prepared with a higher gelatine concentration show an increase in the values of elastic modules, G' and yield force (hardness) of emulsions, suggesting a stronger polymer network formation at the oil-water interface. It was found that 1.6 and 0.6 w/v % of G and X concentration was the best concentration to produce the strongest gel hardness. Therefore, all emulsion characterizations were conducted for samples prepared in 1.6 w/v % of G and 0.6 w/v % of X, except when the effect of protein to polysaccharide ratio on SOS formation was studied, where three concentration variations were employed (**Table 1**).

5.3.1.1 The effect of processing parameters: HPDI and HPH

The preparation processing parameters of emulsions may affect emulsion formation, and the nature of emulsions, i.e. o/w emulsion or w/o emulsion and droplet size. The fluorescent images of emulsions prepared using G/X as emulsifiers show the formation of o/w emulsions (**Figure 5.1**). The morphology of the obtained o/w emulsions shows discrete oil droplets with a heterogeneous size distribution. However, on inspection of fluorescent images using the naked eye, the impact of duration and speed of homogenizing of HPDI on emulsion droplet size were indiscernible. As shown in **Figures 5.1a and 5.1b**, the variation in duration of dispersing of emulsion resulted in nearly the same size distribution and increase in the speed of homogenizing, while keeping the duration constant (**Figure 5.1c**) does not change the droplet size dramatically. However, when droplet size measurements were conducted using ImageJ analysis software, the impact of the processing parameters was significant. The results show a decrease in the particle size distribution substantially with the increase of the duration and the speed of homogenization (**Figure 5.2**). The largest droplet size of an emulsion prepared using HPDI at 11,400 rpm for 5 minutes ranged from 120 μm to 130 μm , whereas for emulsion prepared using HPDI at 11,400 rpm for 9 minutes and emulsion prepared using HPDI at 14,000 rpm for 5 minutes ranged from 60 μm to 70 μm . In addition, emulsion prepared using HPDI at 14,000 rpm for 5 minutes has a higher frequency of small droplets below 10 μm compared to an emulsion prepared using HPDI at 11,400 rpm for 9 minutes.

These results confirm the well-known fact that a higher energy input or longer homogenization time results in a smaller droplet size [142].

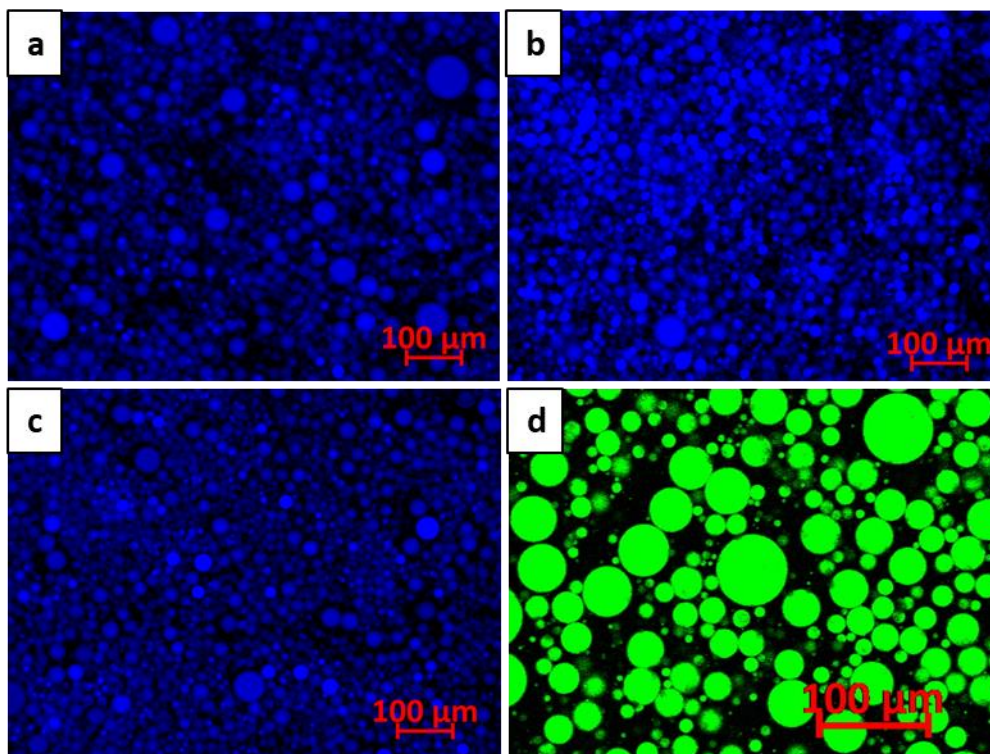


Figure 5.1. Fluorescent images taken with an upright microscope of o/w emulsions prepared at two different durations and speeds of homogenizing using HPDI: a) duration is 5 minutes and the speed is 11,400 rpm; b) duration is 9 minutes and the speed is 11,400 rpm; c) duration is 5 minutes and the speed is 14,000 rpm; d) confocal image of emulsion prepared at 11,400 rpm for 5 minutes.

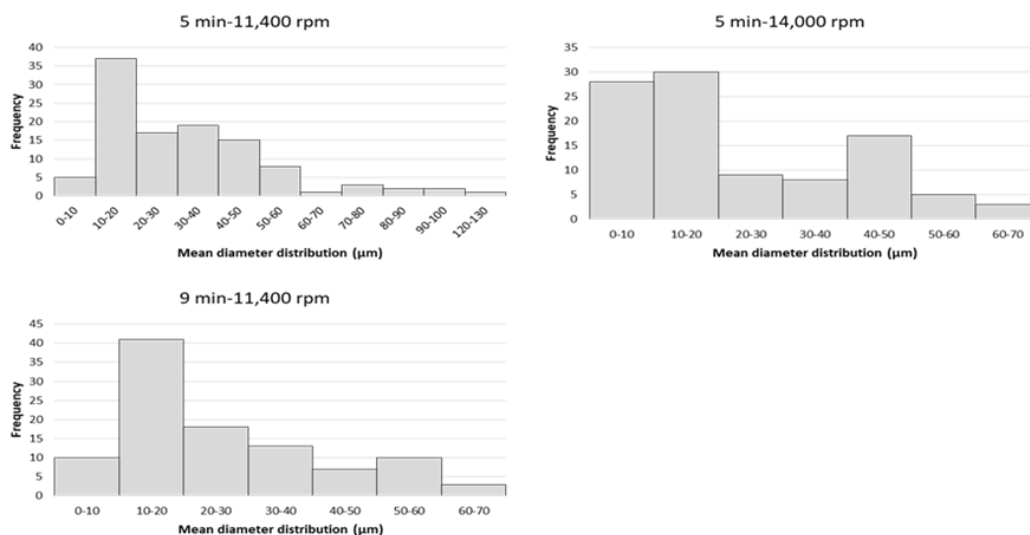


Figure 5.2. Particle size distribution of emulsion prepared using different processing parameters of HPDI measured by ImageJ software.

The size of droplets that emulsions contain determine the shelf life, appearance, texture, release characteristics, flavour profile and biological fate [142]. The processing operation of emulsification affects the emulsion droplet size and stability. Emulsion preparation can involve two steps of emulsification. The first is primary homogenization, which leads to the formation of emulsion from two immiscible phases mixing at high speed, and the second is secondary homogenization, which causes the further reduction of emulsion droplet size in an existing emulsion. Emulsions prepared with two steps of emulsification benefit from a substantial impact in terms of emulsion droplet size and stability. Therefore, an emulsion prepared in two steps of emulsification, where HPDI and HPH as a secondary homogenizer were used, was compared with an emulsion prepared in one step, where HPDI was used, in order to observe the impact on emulsion formation and droplet size, and to see the impact of two homogenizing instruments. As can be seen in **Figure 5.3**, emulsions prepared using HPDI have more big droplet sizes and are more homogeneous, while emulsions prepared using HPH have a heterogeneous distribution with many small droplets and some big droplets. Both samples show the o/w emulsion formation under fluorescence microscope.

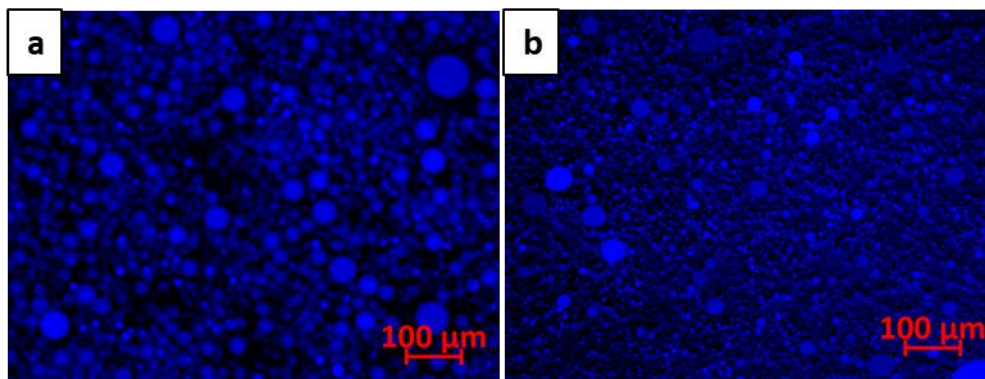


Figure 5.3. Fluorescent images taken with an upright microscope of o/w emulsions prepared with two different homogenizing instruments: a) HPDI and b) HPH (1 pass).

From the fluorescent images of emulsions prepared using different emulsification processing parameters, it can be seen that HPDI, in comparison with emulsions prepared using an HPH instrument, results in substantial changes in particle sizes. Therefore, in order to obtain a more precise estimation, an LD technique was used to determine the particle size distribution of emulsion prepared in one step using HPDI and compared with emulsion prepared in two steps where HPDI was used with HPH as a secondary homogenizer (**Figure 5.4**). The cumulative size distribution of emulsion prepared using HPDI and HPH is presented in **Table 5.2**. Emulsion prepared using HPH has a much smaller size distribution in comparison with emulsion prepared using HPDI.

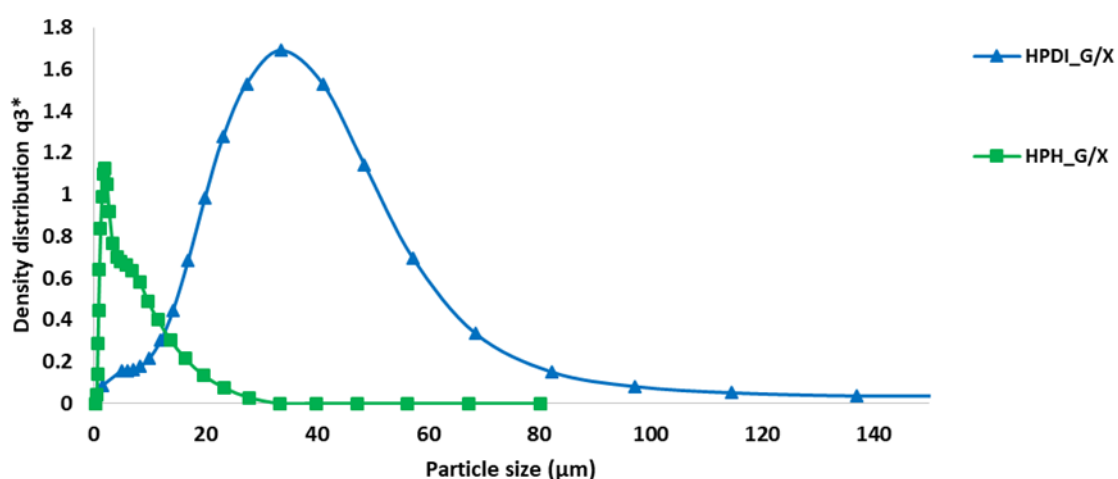


Figure 5.4. Volume density distribution of emulsion prepared with HPDI and HPH. $q3^*$ – density distribution by volume.

Table 5.2. Emulsion droplet size distribution and the span value of HPDI and HPH prepared placebo samples immediately after preparation. N = 3.

Placebo G/X emulsion	D10 (μm)	D50 (μm)	D90 (μm)	Span value
HPDI	6 \pm 1.25	27 \pm 2.54	49 \pm 6.23	1.6
HPH	1.02 \pm 0.02	2.6 \pm 0.05	10 \pm 0.47	3.5

The mean droplet size distribution was expressed as a span of distribution as described in the British Standards. A small span value (span index <0.7) indicates a narrow particle size distribution, whereas a big span value indicates a broad particle size distribution [409]. Both the emulsions prepared using HPDI and HPH show a broad particle size distribution, with span indexes of 1.6 and 3.5, respectively (**Table 5.2**). However, the width of the size distribution of the HPDI prepared emulsion was lower than the HPH prepared emulsion. The broad droplet size distribution of the emulsion prepared using HPH was possibly because the analysis was designed for the sample which has passed through HPH only once in order to save time. The number of homogenization cycles has a great impact on particle size distribution, as usually two or three passes gives narrower particle size distribution [409].

5.3.1.1.1 Stability of emulsions prepared using HPH

The stability test of emulsions prepared using HPH was performed using a photographic study. Different cycling durations, namely 3, 5 and 7 minutes of 10 ml emulsion, were studied after 5 days (**Figure 5.5**). The most stable emulsion was the emulsion prepared with 7 minute cycling, as after 5 days there was no sign of any phase separation or oiling off. In contrast, emulsions prepared with 5 and 3 minute cycling showed oiling off, and small droplets of oil and mould can be seen on the surface. This is one of the most common forms of instability in emulsions called gravitational separation. Oil droplets have a lower density than the surrounding liquid, so a net gravitational force acts upon them; therefore, low density oils have a tendency to move upward [142]. This stability test has a good correlation with the density distribution of the emulsions prepared with HPH, which has a bimodal size distribution. Normally, gravitational separation causes droplets to have a close contact with each other for extended periods, which leads to enhanced coalescence and at the end to oiling off [142].

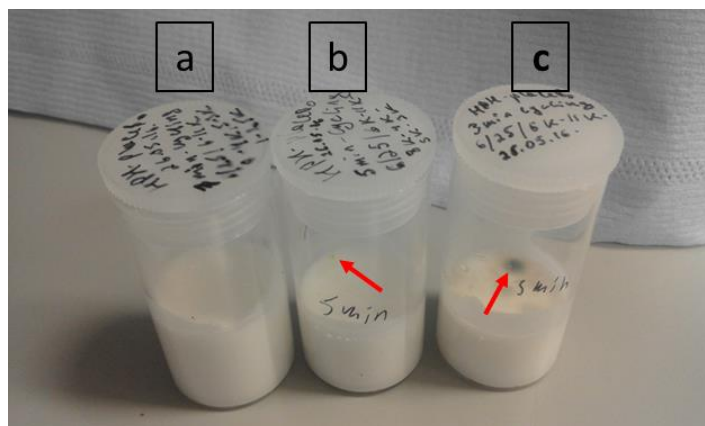


Figure 5.5. Stability test of emulsion prepared using HPH: a) 7 minute cycling; b) 5 minute cycling; c) 3 minute cycling after 5 days.

5.3.1.2 The effect of oil volume fraction

It is well known that emulsion formation and stability are also influenced by oil to water ratio, i.e. by the concentration of droplets in an emulsion [410]. This also determines the cost, appearance, texture, flavour, and nutritional attributes [142]. The same influence can extend to the formation of SOS too and this is discussed in **section 5.3.2.3**. Therefore, emulsions were prepared with a range of oil volume fractions, i.e. 10, 30, 40, and 60 v/v %, while keeping other composition concentrations constant. The obtained emulsions were freeze dried immediately and the quality of the obtained SOS were examined using the naked eye. The results show that the appearance of the SOS was altered with the sample containing 60 v/v % of oil (**Figure 5.16, section 5.3.2.3**). Therefore, we did not increase the oil volume fraction above 60 v/v % and here we present the characterization of o/w emulsions, prepared with up to 60 v/v % of oil phase, using upright fluorescence and brightfield microscopes.

As can be seen in **Figures 5.6a and 5.6g**, the emulsion droplet size with the sample containing 60 v/v % of oil has not changed notably in the microscope images, whereas the droplet density in the system increased appreciably compared to the sample containing 10 v/v % of oil content. However, the droplet size distribution, measured using ImageJ analysis, revealed significant changes (**Figures 5.6b, d, f, h**). The largest droplet size was from 90–100 μm to 30–40 μm for samples containing 10 and 60 v/v % of oil, respectively. The largest droplet size of samples containing 30 and 40 v/v % of oil were the same, namely 120–130 μm . However, the highest frequency of droplet size existing in the formulation shifted from 0–10 μm to 10–20

μm and to 20–30 μm as the oil content rises from 10 to 40 v/v % and again dropped down to 0–10 μm at 60 v/v % oil content. Normally, when the percentage of the dispersed phase is increased while other parameters are held at constant, the mean droplet diameter increases gradually because of the possible increase in emulsion viscosity and the limitation of surface active agents in the oil concentrated emulsion, which favours oil droplet coalescence and increases the mean droplet diameter [408, 411-414]. However, Schubert et al. [415] reported that there is no difference in particle size distribution when changing the dispersed phase volume fraction. In addition, at a sufficiently high dispersed phase volume fraction, emulsions are more stable to creaming, because the droplets are so closely packed together that they are prevented from moving [142]. Therefore, an emulsion with a 60/40 v/v % oil/water ratio does not increase its droplet size because increasing the oil phase volume fraction enhances emulsion droplet density, which in turn lowers the creaming rate. The creaming rate affects the droplet size; for instance, an oil droplet with a radius of 1 μm and ≈ 17 mm/day creaming rate will not have a long shelf life, while an oil droplet with a radius less than ≈ 0.15 μm and less than ≈ 0.5 mm/day creaming rate is considered to be stable towards creaming. The concentrated emulsion has less creaming rate of droplets than that of the diluted emulsions. When emulsion droplets move upwards because of gravity, an equal volume of continuous phase moves downwards to compensate; as a result, a net flow of continuous phase downward resists the upward movement of the droplets and decreases the creaming rate. In addition, in more concentrated emulsions, there are a number of other types of hydrodynamic interaction, which also reduce the creaming rate of the droplets. Possibly, 60/40 v/v % is a critical dispersed phase volume fraction at which the droplets are prevented from moving because they are so closely packed. Whereas, emulsion with 40/60 v/v % probably does not have a sufficiently high dispersed phase volume fraction to prevent droplets from movement, but still has a large number of droplets that move and collide with each other, come into close contact for extended periods of time and consequently the rate of creaming is increased. The same can apply to emulsion containing 10 % oil volume fraction, in which the droplet concentration is low and, therefore, the droplets are free to move, collide with each other and coalescence occurs if there is no deep secondary minimum, high-energy barrier or strong short-range repulsion. This type of coalescence occurs immediately after two or more droplets collide with each other during a collision and it is called coalescence immediately after collision [142].

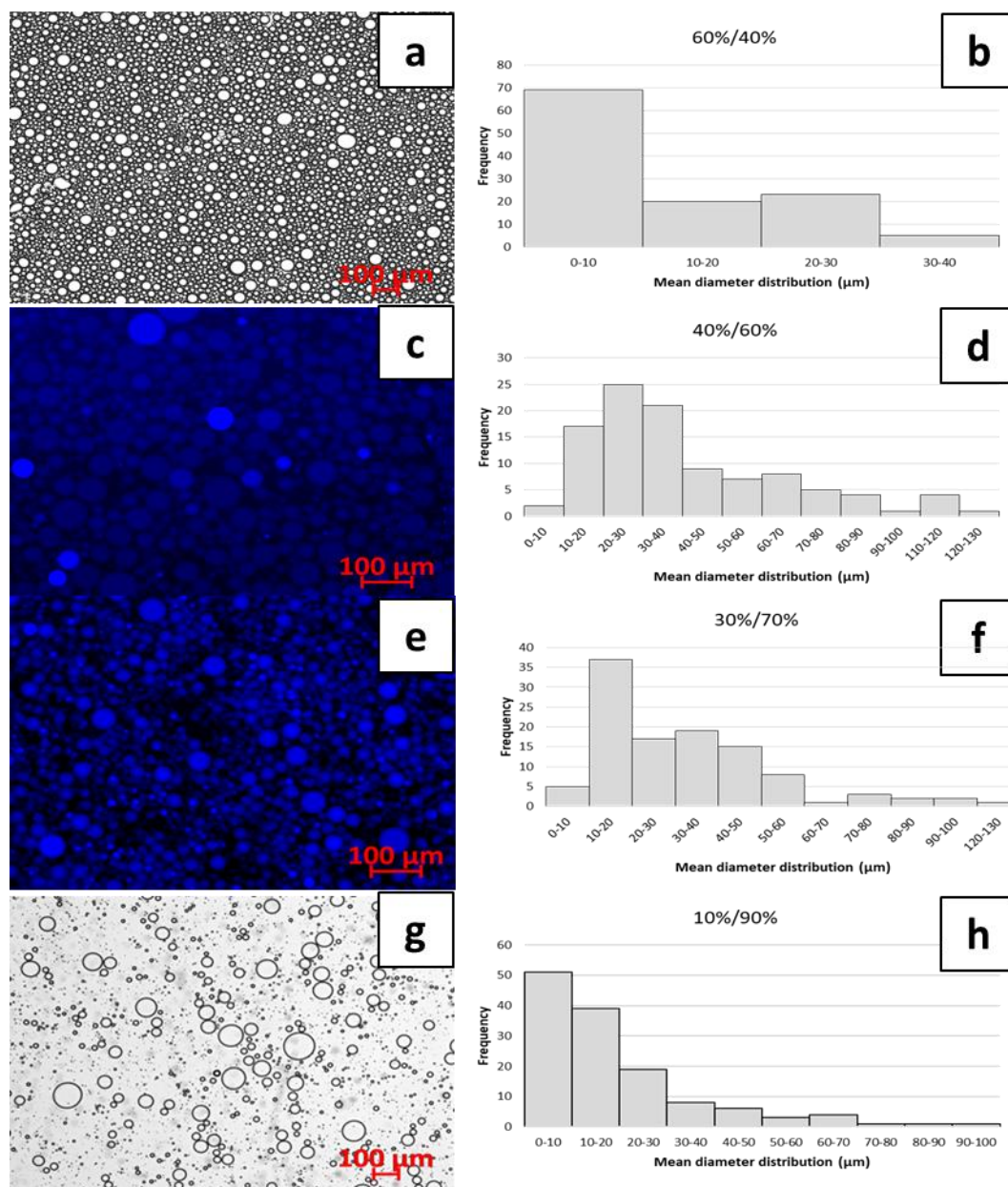


Figure 5.6. Fluorescent and brightfield images taken with an upright microscope of o/w emulsions prepared with various oil/aqueous phase ratios: a) 60/40 v/v %; b) 40/60 v/v %; c) 30/70 v/v %; d) 10/90 v/v %. Particle size distribution of emulsion prepared with various oil/aqueous phase ratios: b) 60/40 v/v %; d) 40/60 v/v %; f) 30/70 v/v %; h) 10/90 v/v %.

5.3.1.3 The effect of API: metoprolol succinate and ketoconazole

The effect of API on emulsion formation and droplet size was investigated using water-soluble MS in an aqueous phase and poorly water-soluble ketoconazole in an oil phase. MS and ketoconazole were added in quantities ranging from 1 mg/ml to 3mg/ml. As can be seen in

Figure 5.7, there was no difference at all. MS has no impact on emulsion formation and droplet size. Also there were no crystals seen on the surface of the droplets suggesting good solubility of API in the formulation. However, emulsions containing ketoconazole showed undissolved crystals, suggesting poor solubility of ketoconazole in sunflower oil (**Figure 5.8**), although ketoconazole's partitioning coefficient, $\log P$, is 3.73 and it showed good solubility in corn and cottonseed oils, at about 40 mg/ml [416].

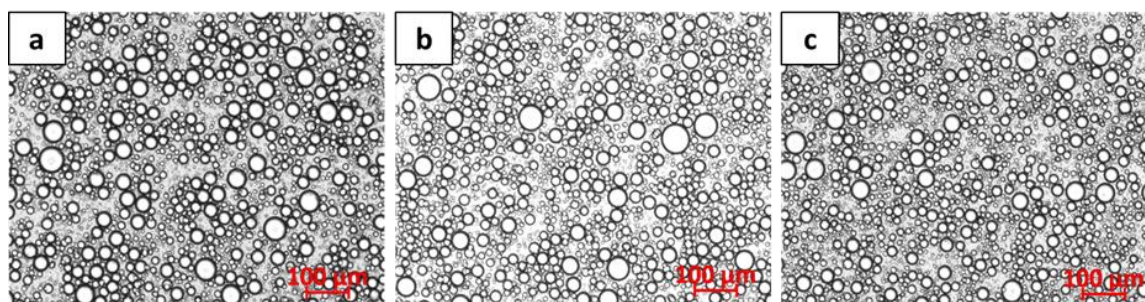


Figure 5.7. Brightfield images taken with an upright microscope of o/w emulsions prepared with various metoprolol succinate concentrations: a) 1 mg/ml; b) 2 mg/ml; c) 3 mg/ml.

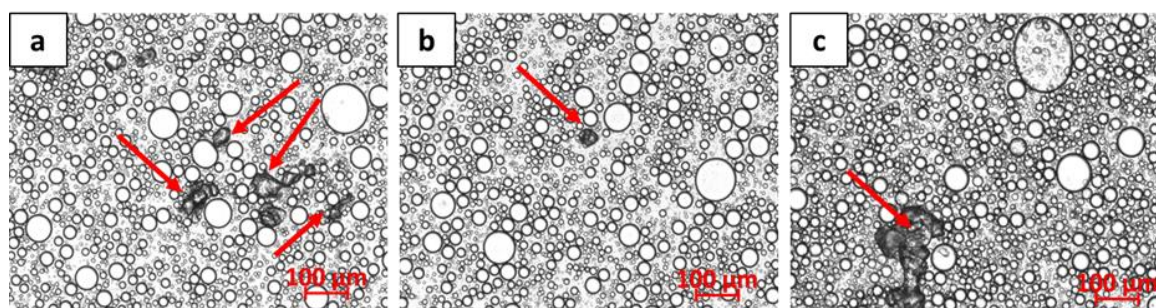


Figure 5.8. Brightfield images taken with an upright microscope of o/w emulsions prepared with various ketoconazole concentrations: a) 1 mg/ml; b) 2 mg/ml; c) 3 mg/ml.

The volume density distribution of emulsion with added water-soluble API (metoprolol succinate) shows minor changes for primary emulsion and no change for secondary emulsion (**Table 5.23**). The results are consistent with Yang et al. [417]. They studied the effect of bovine serum albumin (BSA) loading on the the size of microspheres, prepared from water-in-oil-in water (w/o/w) double emulsion, and found that API loading has no significant effect on the properties of microspheres. The stability test of placebo and drug loaded emulsions

shows an increase of particle size distribution after 7 days and bimodal size distribution (**Figure 5.9-5.10**). This may be attributed to the dominance of coalescence instability of emulsion droplets [142, 406].

The addition of MS slightly decreases the span distribution for both techniques used to prepare emulsions, being 1.5 and 3.4 for HPDI and HPH prepared emulsions, respectively (**Table 5.3**). This indicates slightly narrower particle size distribution. The same was true for samples stored for 7 days at ambient conditions. The span value calculated for placebo emulsions stored for 7 days were 1.7 for emulsion prepared using HPDI and 6.2 for emulsion prepared using HPH, whereas the span value of emulsions containing metoprolol succinate were 1.4 and 5.9 respectively. However, the span values of both placebo emulsion and API containing emulsion prepared using HPDI and HPH measured after 7 days were increased in comparison with freshly prepared emulsions, indicating coalescence instability when two or more droplets merge together and form a single large droplet [409, 418]. Moreover, the larger droplets tend to merge more rapidly than the smaller droplets causing more polydispersed particle size distribution [142]. The exception was for emulsion containing metoprolol succinate prepared using HPDI. The span value for this emulsion decreased from 1.5 to 1.4. This might be because the larger droplets move upward more rapidly than small droplets; however, during this movement they may collide with smaller droplets and aggregate. These aggregates will cream at a faster rate than the isolated droplets, thus small droplets disappear and the polydispersity becomes narrower [142].

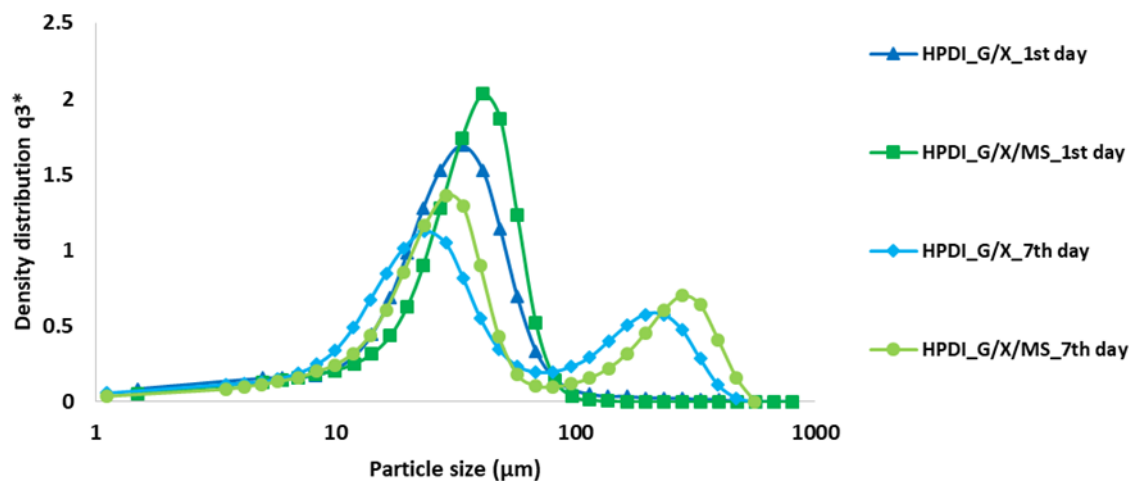


Figure 5.9. Volume density distribution of emulsion particle size prepared with HPDI: 1) placebo emulsion measured immediately after preparation; 2) placebo emulsion measured after 7 days; 3) MS loaded emulsion measured immediately after preparation; 4) MS loaded emulsion measured after 7 days. X-axis is plotted on log scale. q_3^* – density distribution by volume.

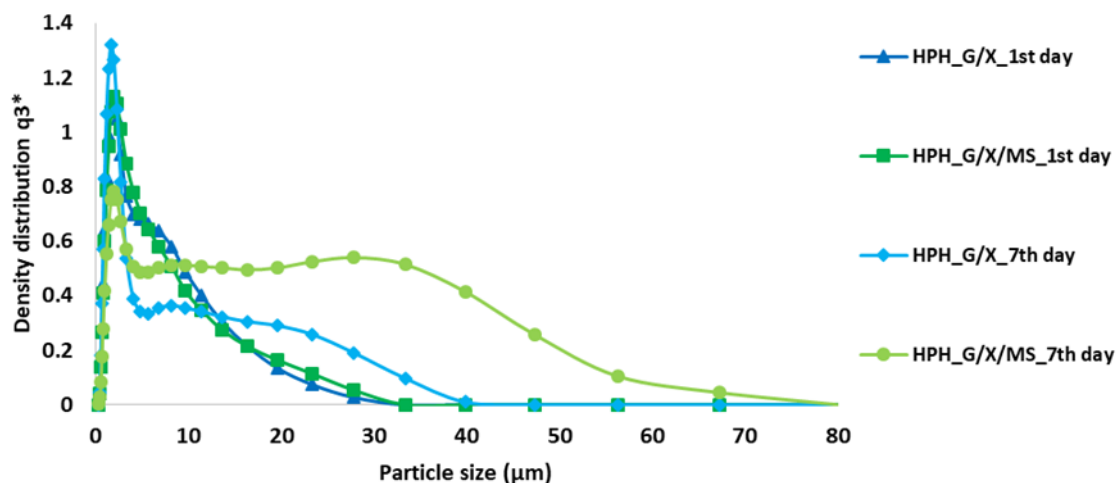


Figure 5.10. Volume density distribution of emulsion particle size prepared with HPH: 1) placebo emulsion measured immediately after preparation; 2) placebo emulsion measured after 7 days; 3) MS loaded emulsion measured immediately after preparation; 4) MS loaded emulsion measured after 7 days. q_3^* – density distribution by volume.

Table 5.3. Emulsion droplet size distribution and the span value of HPDI and HPH samples with and without drug loadings immediately after preparation and after one week. N = 3.

G/X emulsion – HPDI	D10 (μm)	D50 (μm)	D90 (μm)	Span value
Placebo after preparation	6 ±1.25	27 ±2.54	49 ±6.23	1.6
MS loaded after preparation	7 ±1.64	32 ±2.6	54 ±3.76	1.5
Placebo after one week	5 ±1.49	28 ±3.29	53 ±9.01	1.7
MS loaded after one week	10 ±3.04	35 ±2.64	58 ±2.94	1.4
G/X emulsion – HPH	D10 (μm)	D50 (μm)	D90 (μm)	Span value
Placebo after preparation	1.02 ±0.02	2.6 ±0.05	10 ±0.47	3.5
MS loaded after preparation	1.04 ±0.03	2.66 ±0.06	10 ±0.49	3.4
Placebo after one week	0.94 ±0.02	2.1 ±0.05	14 ±1.56	6.2
MS loaded after one week	1.2 ±0.04	5.1 ±0.68	31 ±5.58	5.9

5.3.1.4 The effect of emulsifiers type: G/X, HPMC/X, MC/X, Tween 20/X, G/CMC

In addition, the ability to form and stabilize emulsions depends on the molecular and physicochemical characteristics of the emulsifier [142, 405]. Therefore, to see the effect of different emulsifiers on emulsion formation, four different compositions were evaluated, namely HPMC/X, MC/X, Tween 20/X and G/CMC. All processing parameters, emulsifier concentrations and oil to water ratios were held at a constant. **Figure 5.11** shows fluorescent images of emulsions consisting of different emulsifiers. The fluorescent images show the o/w nature of the emulsions and there were no substantial changes in droplet size and morphology of obtained emulsions. The exception was with emulsions prepared using MC/X and G/CMC as emulsifiers, where the formation of flocs is seen clearly (**Figures 5.11c and 5.11e**). Whereas, emulsions prepared using G/X, HPMC/X and Tween 20/X show partial flocculation, as it looks as though there are some flocs but, at the same time, there are individual droplets too. The stability analysis of emulsions by means of LD provides supplementary information about the nature of instability, which is discussed below.

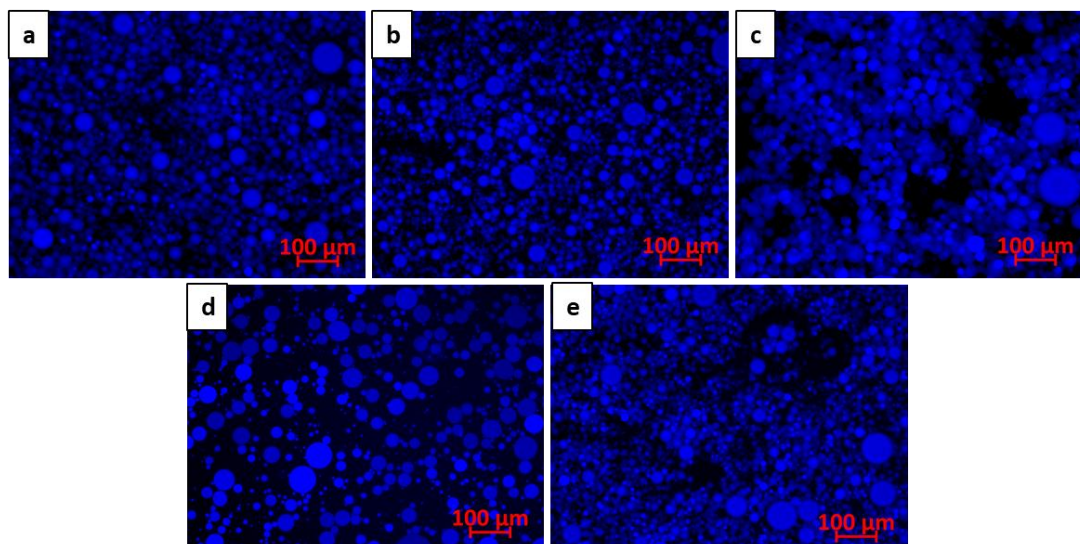


Figure 5.11. Fluorescent images taken with an upright microscope of o/w emulsions prepared with different emulsifiers while keeping all other parameters constant: a) G/X; b) HPMC/X; c) MC/X; d) Tween 20/X; e) G/CMC.

The density distribution of emulsion particle size prepared with HPDI with different emulsifiers immediately after preparation is presented in **Figure 5.12**. As can be seen on the graph, composition G/X and HPMC/X showed more homogeneous density distributions compared to the other three compositions. Compositions MC/X, Tween 20/X and G/CMC showed heterogeneous density distribution, having very small and very big particle sizes. The cumulative size distribution of primary emulsion is presented in **Table 5.4**. The stability test of placebo emulsions shows a slight increase of particle size distribution on the third day for emulsion prepared using a G/X composition and a decrease for the four other formulations (**Figure 5.13**). This may be attributable to the dominance of coalescence [142, 406] and flocculation instabilities of emulsion droplets, respectively. Before measuring the emulsions by droplet size analyser, samples were highly diluted in an aqueous phase and stirred. If there is an increase in droplet size after measurement it means a coalescence instability has occurred. However, if there is a decrease in droplet size after measurement it means that flocs were disrupted during stirring, and consequently the droplet size is decreased [142]. These results confirm the nature of instability seen with the fluorescence microscope.

In addition, the span values were calculated for those emulsions and are given in **Table 5.4**. The highest span value was for emulsion prepared using G/CMC emulsifiers, namely 14.9,

then for Tween 20/X and MC/X compositions having 7.5 and 6 span values, respectively. G/X and HPMC/X give relatively narrower particle size distribution, namely 1.6 and 1.4, respectively. However, the span value was decreased significantly after three days for the measurement of the emulsion prepared using Tween 20/X emulsifiers, namely 1.2. Then it was followed by emulsion prepared using MC/X emulsifiers, where the span value was 3 and an insignificant decrease was for G/CMC, 14. These are due to flocculation instability, where mixing the diluted samples causes disruption of the flocs and hence decreases the particle sizes. The span value of HPMC/X was increased after three days, namely 1.8, which indicates a dominance of coalescence instability [409, 418]. G/X did not change the span value after three days indicating the stability of the emulsion for three days.

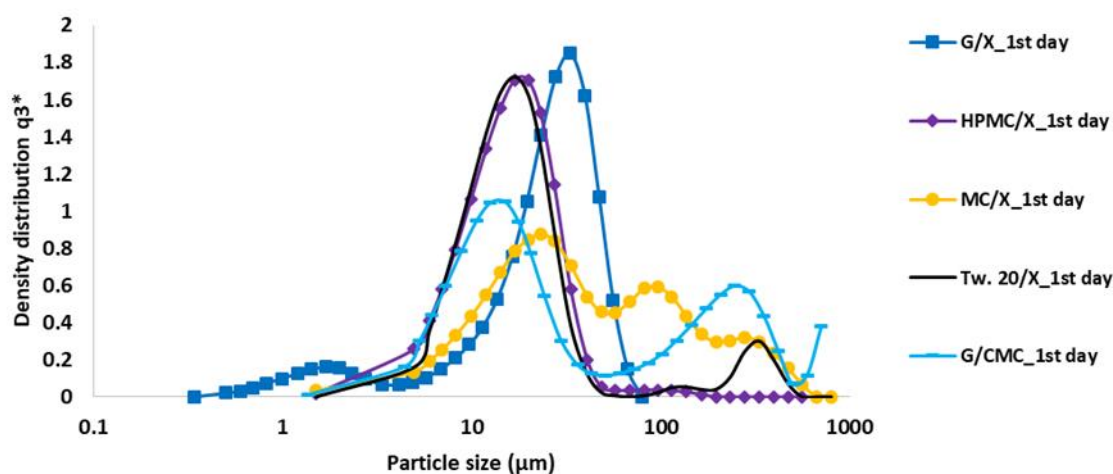


Figure 5.12. Volume density distribution of emulsion particle size prepared with different emulsifiers immediately after preparation: 1) G/X; 2) HPMC/X; 3) MC/X; 4) Tween 20/X; 5) G/CMC. X-axis is plotted on log scale. q_3^* – density distribution by volume.

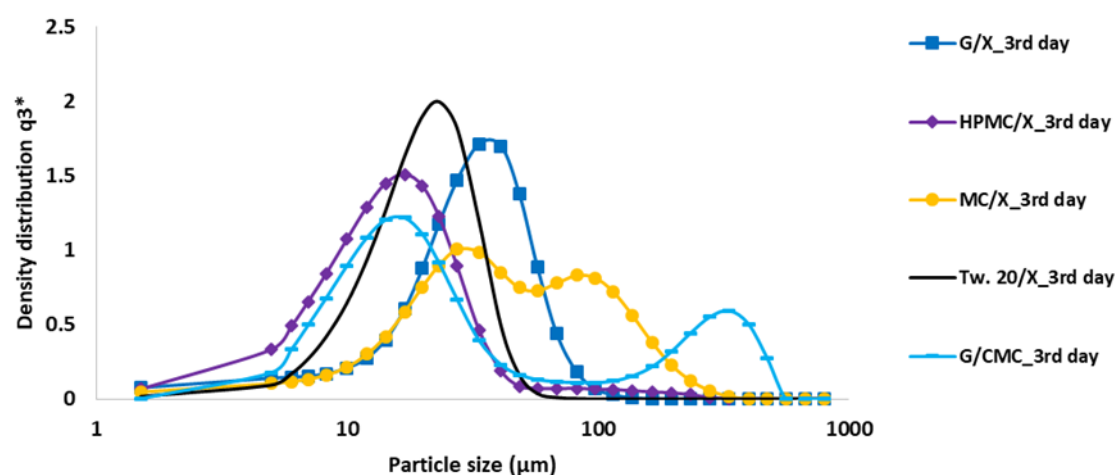


Figure 5.13. Volume density distribution of emulsion particle size prepared with different emulsifiers on third day: 1) G/X; 2) HPMC/X; 3) MC/X; 4) Tw. 20/X; 5) G/CMC. X-axis is plotted on log scale. q_3^* – density distribution by volume.

Table 5.4. Emulsion droplet size distribution and the span value of emulsions prepared with different emulsifiers immediately after preparation and on third day. \pm – standard deviation.

1 st day	D ₁₀ (μm)	D ₅₀ (μm)	D ₉₀ (μm)	Span value
G/X	6 ±1.25	27 ±2.54	49 ±6.23	1.6
HPMC/X	7 ±0.43	16 ±1.37	30 ±4.84	1.4
MC/X	10 ±2.15	33 ±10.64	208 ±132.85	6
Tween 20/X	8 ±0.54	17 ±1.87	132 ±172.78	7.5
G/CMC	7 ±2.17	20 ±3.4	305 ±243.65	14.9
3 rd day	D ₁₀ (μm)	D ₅₀ (μm)	D ₉₀ (μm)	Span value
G/X	7.26 ±1.09	31 ±2.98	56 ±2.83	1.6
HPMC/X	6 ± 0.67	14 ±1.1	31 ±5.52	1.8
MC/X	11 ±1.1	40 ±4.38	129 ±5	3
Tween 20/X	10 ±0.85	20 ±2.45	34 ±4.35	1.2
G/CMC	8 ±0.16	20 ±2.5	292 ±82	14

5.3.2 Producing structured oil systems

5.3.2.1 Impact of protein and polysaccharide ratio

Emulsions prepared with different G and X concentrations show good stability against freezing and an acceptable quality of SOS were obtained for all formulations, irrespective of

the protein and polysaccharide ratio. As can be seen in **Figure 5.14**, all samples have a similar morphology, i.e. a white, matted, dry, cottony, thick, densely packed sponge-like structure. This indicates that the G and X ratio was not the key factor influencing the formation of SOS. Thereby, the formulation with 1.6 % w/v of G and 0.6 % w/v of X were selected for further characterization based on the overall stability of the emulsion and the quality of the SOS.

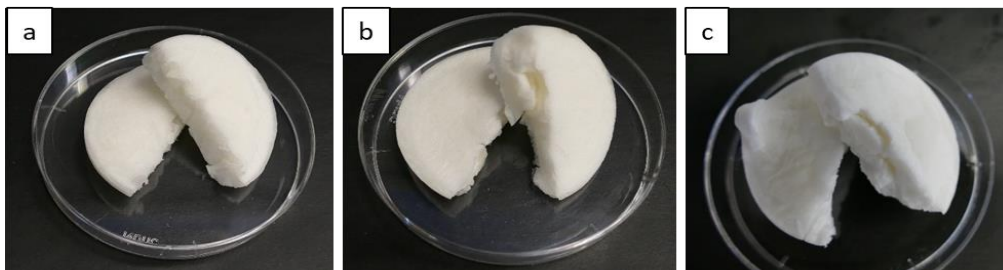


Figure 5.14. SOS prepared with different G and X concentrations using a freeze drier: a) G with 1.2 w/v % and X with 0.6 w/v %; b) G with 0.6 w/v % and X with 1.2 w/v %; c) G with 2.3 w/v % and X with 0.9 w/v %.

5.3.2.2 Impact of dehydration method

The method of drying was also checked, and the oven-dried samples were easy to crack and fracture, as they have a frangible structure. Nevertheless, oil was encapsulated successfully, indicating good stability against thermal processing too.

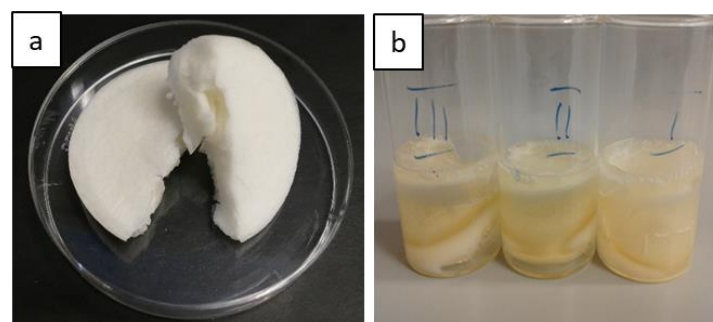


Figure 5.15. SOS prepared with different dehydration methods: a) freeze-dried G with 1.6 w/v % and X with 0.6 w/v %; b) oven-dried G with 1.6 w/v % and X with 0.6 w/v %.

5.3.2.3 Impact of oil volume fraction

The impact of oil content in the emulsion on the formation and morphology of SOS was studied. For this, emulsions were prepared with an oil phase comprising 10, 30, 40, and 60 v/v % of the system. As can be seen in **Figure 5.16**, there was no difference on SOS morphology with samples prepared with 10, 30 and 40 v/v. However, the morphology of SOS was changed when the oil content reached 60 v/v %. The matted appearance altered with a glassy like morphology appearing; however, it was still holding a large amount of oil. Nevertheless, the recommended maximum oil loading is 40 v/v %.

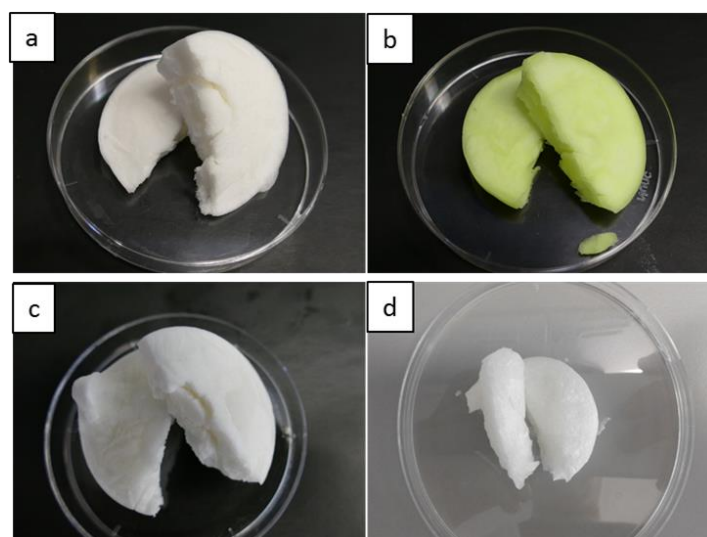


Figure 5.16. Study the impact of oil volume fraction on formation and morphology of SOS: a) 10 v/v %; b) 40/60 v/v % (with fluorescent dye); c) 30 v/v %; d) 60 v/v %.

5.3.2.4 Impact of processing parameters: HPDI and HPH

The morphology was changed too when emulsion was prepared using HPDI and HPH, as seen in **Figure 5.17**. The samples prepared with HPDI were rougher than the sample prepared with HPH. SOS prepared with HPH had a smoother surface, drier and airier texture and was whiter in colour, which could be attributed to the fact that the SOS prepared using HPH had a much smaller droplet size in the emulsion than the ones prepared using HPDI.

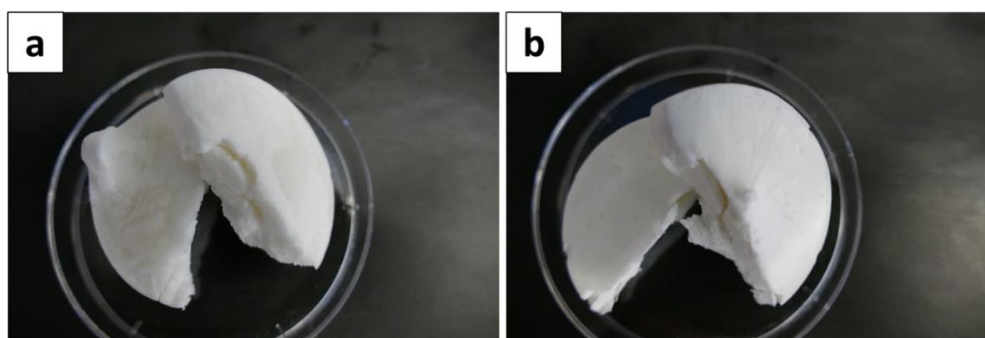


Figure 5.17. Placebo G/X SOS prepared with a) HPDI and b) HPH.

5.3.2.5 Impact of protein and polysaccharide: G and X

We studied the effect of G and X on the formation of SOS separately. **Figure 5.18** shows the appearance of SOS prepared with pure G and pure X. Interestingly, both G and X can form SOS independently. However, the textural properties are different. SOS prepared using X alone showed soft, cottony, marshmallow-like morphology while SOS prepared using G alone has a rigid, glassy and dry property as examined by naked eye. In addition, the literature suggested that X does not adsorb at oil interface [419]; however, in this study, X shows that it can hold liquid oil by forming a firm layer around the oil phase, i.e. encapsulating the oil phase, without leaking the oil and protecting against stress conditions, as examined by naked eye.

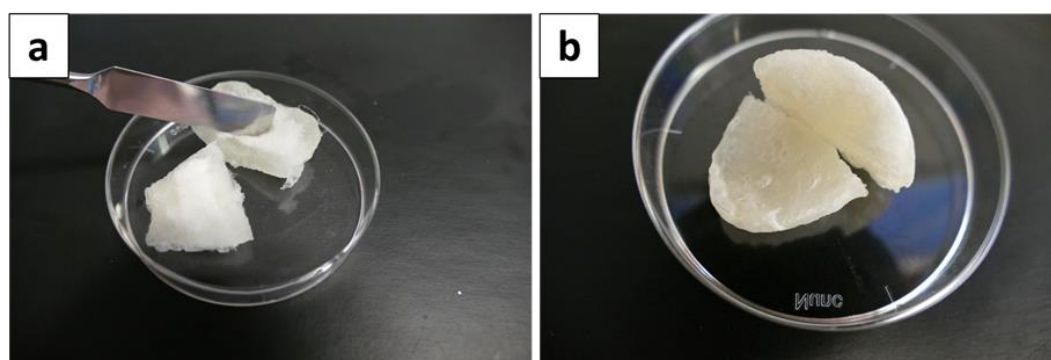


Figure 5.18. SOS prepared with pure: a) X; b) G.

5.3.2.6 Impact of emulsifiers

As the ability to form and stabilize emulsions depends on the molecular and physicochemical characteristics of the emulsifier [142, 405] we anticipated that the type of emulsifier can also

affect the formation of SOS. In addition, it would help to understand the underpinning principles of its oil holding capacity and nature. Therefore, in order to understand the nature and key parameters affecting the formation of SOS and for comparison purposes, four different compositions were evaluated, namely HPMC/X, MC/X, Tween 20/X and G/CMC. All processing parameters, emulsifier concentrations and oil to aqueous phase ratios were held at a constant. In addition, following our aim to develop delivery system for any water-soluble and oil-soluble drugs or nutrients, we would like to offer a range of materials that can be utilized for variety purposes.

The study shows that the type of emulsifier used in the emulsion formulation has great impact on the morphology of SOS. Depending on the emulsifier type, different SOSs were produced (**Figure 5.19**). Although all samples were prepared using HPDI, the G/CMC sample gave the best SOS in terms of appearance, as if it was prepared using HPH. As with the sample prepared using HPH, HPDI prepared G/CMC was smooth, and was the driest and most white, although the droplet size was much bigger than the sample prepared using HPH. This suggested that the droplet size of emulsions is not the key parameter to obtain SOS. HPMC/X and MC/X were soft, cottony and have a marshmallow-like appearance. The Tween 20/X sample failed to form SOS, although the emulsion was stable and the droplet size was approximately the same as the sample prepared using G/X as an emulsifier, suggesting that the formation of a stable emulsion and droplet size are not important factors affecting the formation of SOS. Moreover, Tween 20 is also as surface active as HPMC, MC and G, and potentially it should interact with the non-surface active X by forming a stable layer against stress conditions such as freezing. However, it failed to form SOS, suggesting that probably there is no strong interaction between Tween 20 and X or the polysaccharide-surfactant concentration was not optimal. It may also have failed because, generally, polysaccharide-surfactant interactions (electrostatic and hydrophobic) strongly depend on polysaccharide and surfactant characteristics such as the backbone, pendant groups, hydrophobic moieties, chain stiffness, and on their relative concentrations [420-422]. In addition, there could be a lack of surfactant at the interface or polysaccharide may retard the diffusion of the surfactant to the interface which may in turn affect the continuous phase viscosity and hence the mechanical properties and stability. Although there is abundant literature about surfactant and polysaccharide interaction [420-424], there are only two papers where a combination of Tween 20 and Xanthan were used as

an emulsion stabilizer [425] and encapsulation layer in the hybrid entrapment–encapsulation system [426]. However, these papers did not study whether there is an interaction between Tween 20 and X or not.

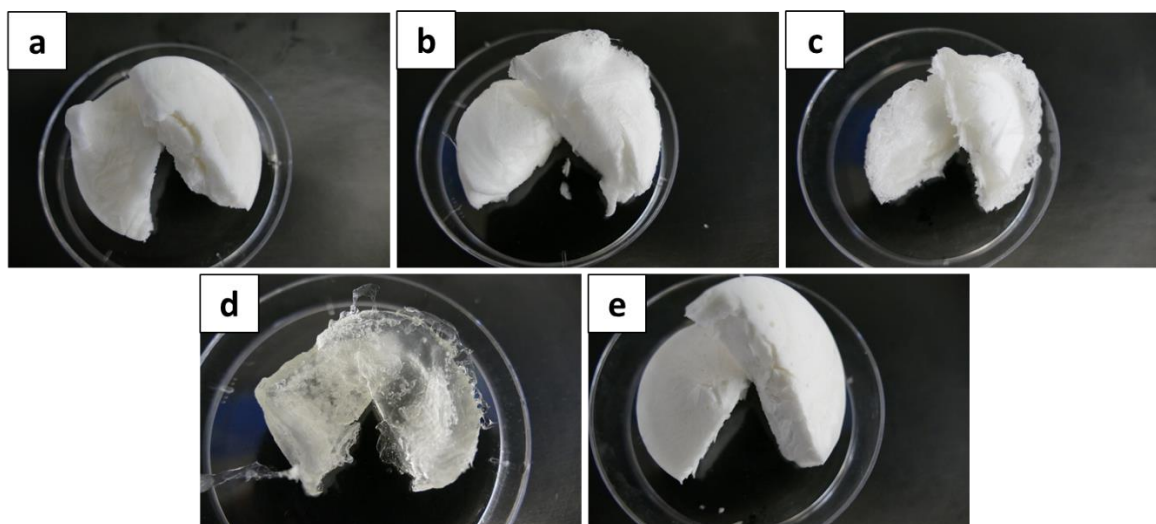


Figure 5.19. Study the impact of emulsifier type in emulsion on formation and morphology of SOS: a) G/X; b) HPMC/X; c) MC/X; d) Tw. 20/X; e) G/CMC.

5.3.3 Characterization of structured oil systems

5.3.3.1 Structured oil system under a fluorescence stereomicroscope

Macroscopically, SOSs look dry and matted and, therefore, in order to see the dispersion of oil in SOS a fluorescent image was taken using a stereo microscope. As can be seen in **Figures 5.20-5.21**, a piece of SOS, loaded with fluorescent marker coumarin-6 in an oil phase, was examined under a fluorescence microscope and clearly defined the presence of oil. In addition, the fluorescence microscope confirms the hollow structure of SOS, and the cavities are shown as a dark-green colour.

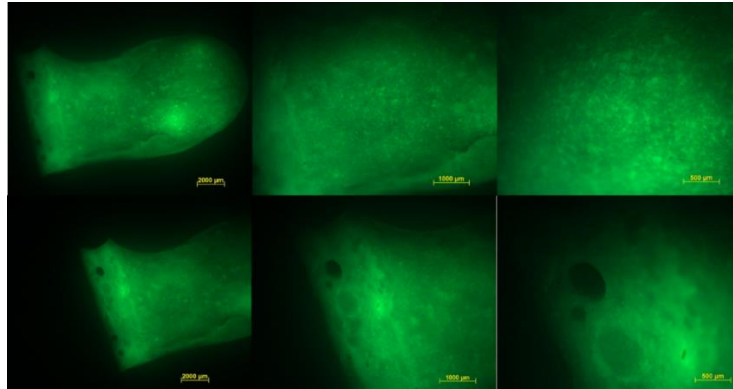


Figure 5.20. Surface and cross-section of a small piece of SOS (SOS was immersed in liquid nitrogen before examination).

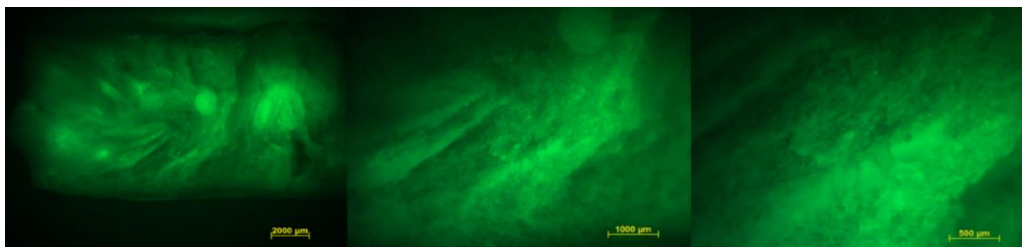


Figure 5.21. Higher magnification of cross-section of SOS.

5.3.3.2 X-ray micro computed tomography (X μ CT)

X μ CT imaging is a non-destructive technique that allows the visualization of the inner structure of an object. It relies on the different absorption of X-rays for different materials, i.e. when the beam passes through matter, the intensity of the X-rays decreases according to the density, thickness and attenuation coefficient of the different materials [427, 428]. The density difference of the different samples enables the presentation of the object in different colours that are linked to the density of the material. In food and pharmaceutical research, it has been used widely for the inspection of the presence of various material sub-components and their local distribution [329].

The density of the analysed materials is in the following order: X > water > oil > G, namely 1.5 g/cm^3 (20 °C) > 1 g/cm^3 [429] > 0.9188 g/cm^3 [430] > 0.68 g/cm^3 (20 °C), respectively. In **Figure 5.22**, G/X SOS is depicted in green, yellow and purple colours in the 2D reconstructed images. The scale band on the left side of **Figure 5.22** shows the density of the materials linked to

each colour. The low density materials start from the beginning of the scale as a black colour and move to the higher density materials at the other end as a white colour. The green, yellow and purple colours appear in a decremental order of density in the scale band. However, in this system the order of densities does not determine the way in which the system is formed. Densities would be important if the system was not mixed and the layers were formed due to gravity for example in a water and oil system without mixing the layers separate with the lower density material on top. Whereas, when water and oil are mixed together to form o/w or w/o emulsions, the density is not the determining factor in this case but the interfacial properties are. In the figure the oil is depicted in the green colour and it is surrounded by G/X, shown in the yellow colour. The purple coloured network is the back part of this structure and the black area represents air spaces. This suggests that the oil is entrapped in a polymer network.

Figure 5.23 illustrates X μ CT images of freeze-dried G/X solution without oil. As was expected, in comparison with SOS, it does not have oil in its content, i.e. there are not many greenish and yellowish colours. It has only a purple network and thin area of yellowish colour. From TGA analysis, it is known that the G/X placebo mixture contains water; therefore, we concluded that this yellowish colour indicates the presence of water and the purple colour represents G/X polymers. In addition, the structure of the freeze-dried G/X solution without oil has mild air pocket size with a well-defined mosaic grid of irregular shape; in contrast, the size of the air pockets of SOS has a population of small air pockets divided by large and mild size gaps. The small size of the air pockets of SOS is due to formation of emulsions, i.e. oil droplets that makes the structure of SOS denser and compact.

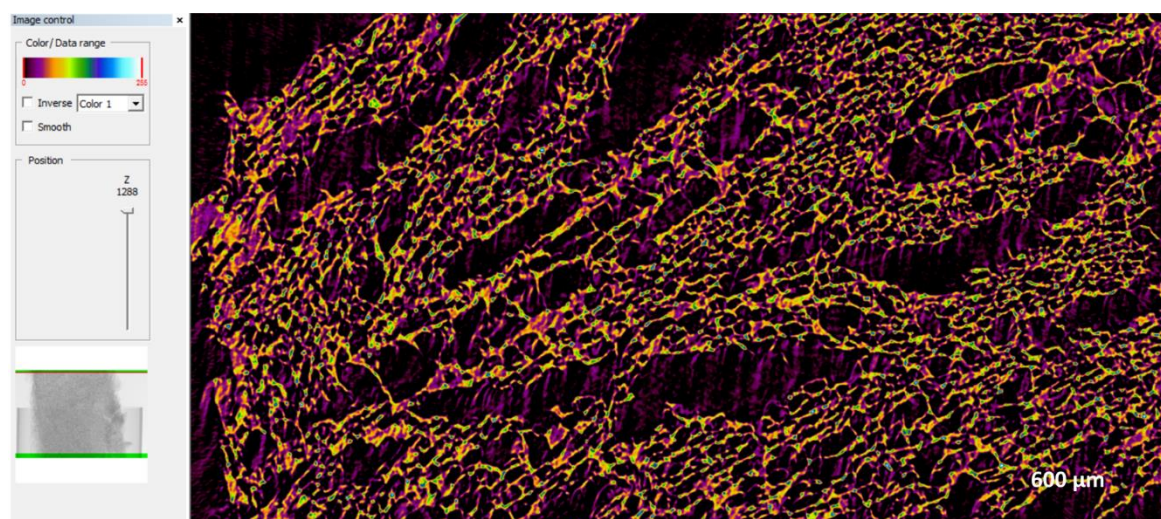


Figure 5.22. X μ CT images of G/X SOS prepared using HPDI.

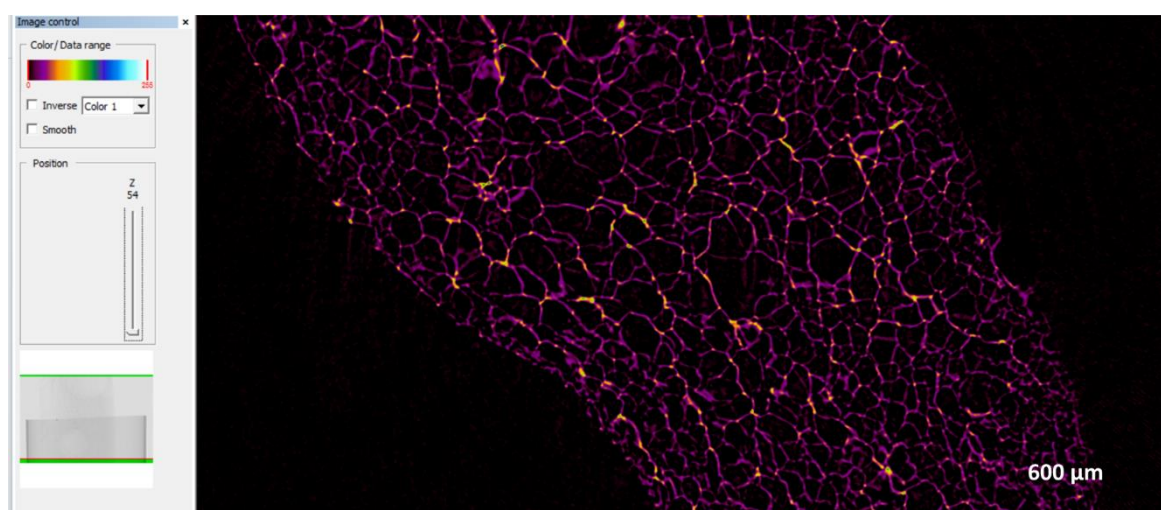


Figure 5.23. X μ CT images of G/X placebo mixture.

5.3.3.3 Cryo-SEM

Cryo-SEM is widely used to characterize the microstructure of liquid containing specimens through rapid freezing, which allows the immobilization of the original microstructure of the liquid containing specimen [322]. In our case, Cryo-SEM images allow direct visualization of the shape of the oil droplets and polymer layer surrounding the droplets. Therefore, in order to obtain more detailed information of the structural integrity of the oil droplets entrapped by the polymer network, selected formulations were analysed using Cryo-SEM. These formulations were a G/X SOS prepared using HPDI and a freeze-dried G/X mixture without oil

for comparison purposes. The G/X SOS sample was attached to the sample holder and immediately plunged into liquid nitrogen slush at approximately -210°C to cryo-preserve the material. This was transferred onto the cryo-stage, where the sample was fractured at -100°C and subjected to sputter coating with platinum for 90 seconds at 10mA. After sputter coating, the sample was moved onto the cryo-stage in the main chamber of the microscope, held at approximately -130°C and was imaged at 3kV. Digital TIFF files were stored.

Figures 5.24 and 5.25 represent Cryo-SEM images of G/X SOS prepared using HPDI and a freeze-dried G/X mixture without oil, respectively. As can be seen in **Figures 5.24a and 5.24a'**, G/X SOS shows a porous structure with sizes in the range of 10-200 μm . **Figures 5.24a'' and 5.24a'''** illustrate the higher magnification of the fractured area, where a shell-like layer of G/X polymers covering the oil are seen clearly. In contrast, Cryo-SEM images of the freeze-dried G/X mixture without oil shows hollow, flat, irregular form shells with widths of about 4-5 μm (**Figure 5.25**). These results also confirmed that the oil droplets were covered by a thin, shell-like layer of polymer and the width of the polymer layer may vary depending on the formulation components.

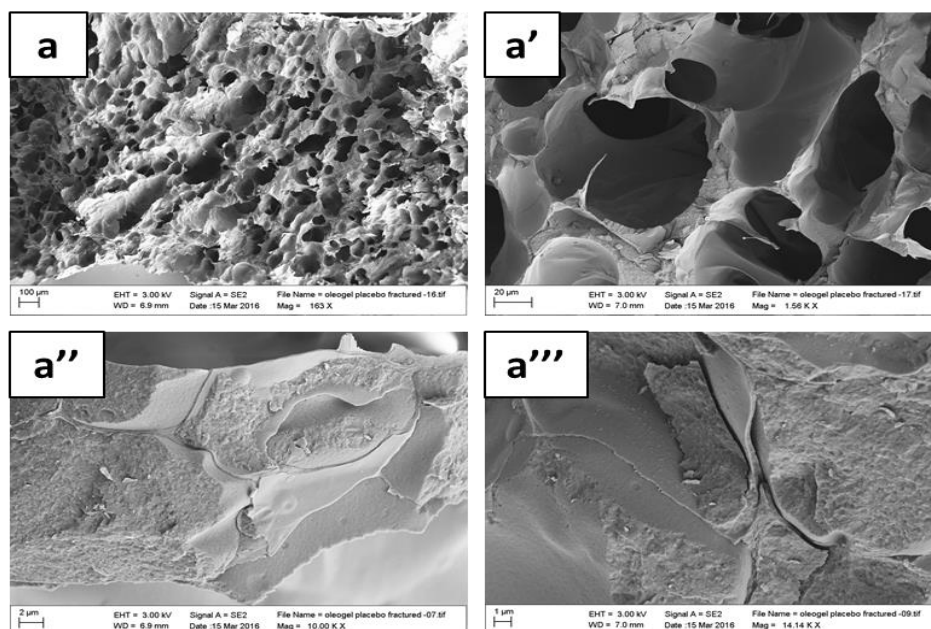


Figure 5.24. Cryo-SEM images of (a) G/X SOS prepared using HPDI. (a') (a'') and (a''') images are higher magnifications of (a).

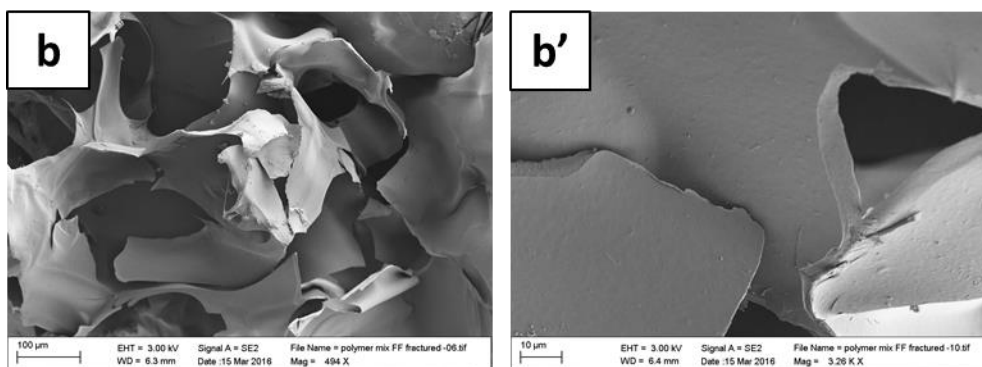


Figure 5.25. Cryo-SEM images of (a) G/X placebo mixture prepared using HPDI. (b') image is a higher magnification of (b).

5.3.3.4 TEM

TEM has much higher magnification abilities and a greater resolution than light microscope. Therefore, TEM analysis was conducted to observe the nano-structure of SOS prepared using HPDI and HPH. In order to obtain TEM images, SOS was subjected to a series of treatments and at the end it was put into BEEM capsules with fresh resin and polymerised overnight at 60 °C. This procedure was undertaken because the TEM instrument, as opposed to Cryo-SEM, cannot just freeze the sample, a process which enables the sample to be cut into stable pieces and images to be taken. SOS is a semi-solid component and the integrity of the sample can be destroyed if it is cut into pieces, which is necessary when you analyse with the TEM technique. Therefore, pre-treatment of the sample was conducted to preserve the integrity of the structure. The treatment procedure is described in detail in **section 2.4.1.2.3**. However, it is worth mentioning that the pre-treatment during the sample preparation of TEM may cause some level of swelling of the structured oil. Therefore, the dimensions of the polymer domains observed in the TEM may not fully correspond and be larger than the ones observed in the Cryo-SEM images.

Figure 5.26 illustrates TEM images of G/X SOS prepared using HPDI where at lower magnification it shows large oil areas with separated borders and at higher magnification it is clearly seen that the oil droplets are surrounded by thick polymer layers. In comparison, the TEM images of G/X SOS prepared using HPH showed big and small oil droplets in a polymer matrix (**Figure 5.27**). There were not clear borders, but well-defined oil droplets were seen clearly. These results are consistent with the fluorescence microscope results, where the

emulsion prepared using HPH has heterogeneous droplet size distribution compared to the emulsion prepared using HPDI. Thus, the SOS prepared using HPH has heterogeneous oil droplets and SOS prepared using HPDI has homogeneous large droplets after processing too.

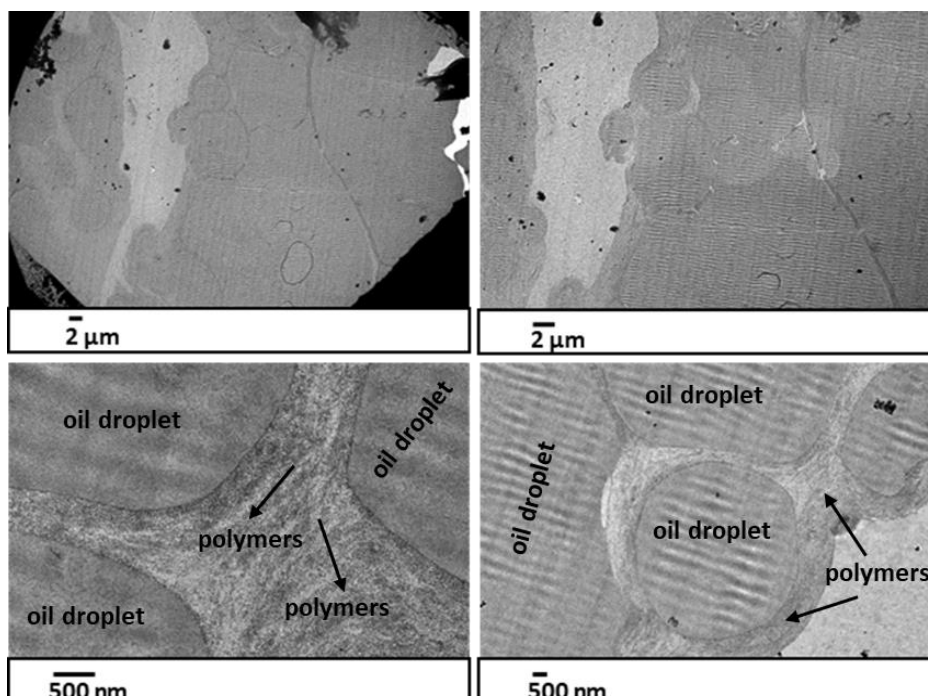


Figure 5.26. TEM images of G/X SOS prepared using HPDI.

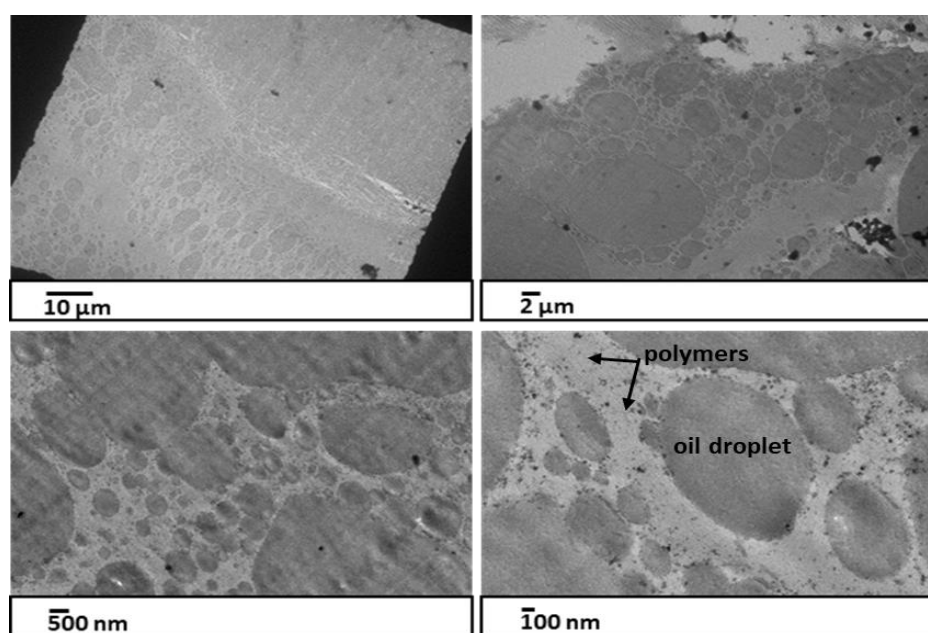


Figure 5.27. TEM images of G/X SOS prepared using HPH.

5.3.3.5 ATR-FT IR

Organic compounds can be determined qualitatively by infrared spectroscopy because each molecular group, influenced by the surrounding functional groups, have a characteristic vibrational mode, which causes the appearance of bands at a specific frequency in the infrared spectrum. It is possible to perform quantitative analyses too because, according to Beer-Lambert law, the intensity of the bands is dependent on the product of the extinction coefficient and the concentration [431]. In this study, infrared spectroscopy was used to see if there are any interactions between protein and polysaccharide, the sequence or nature of adsorptions of protein and polysaccharide on the surface of the oil interface and the presence of oil. The FT-IR analysis was carried out for pure G powder, X powder, pure sunflower oil, freeze-dried G/X mixture without oil, and G/X SOS prepared using HPDI or HPH (**Figure 5.28**). The infrared spectrum of xanthan gum and sunflower oil and their frequencies, functional groups and mode of vibrations are given in **Appendix 2**. Here we have presented the IR assignments of G only in **Table 5.5**.

The FT-IR spectrum of pure G powder shows vibration bands at 3274 cm^{-1} NH, OH stretching; 2939 cm^{-1} CH₂ asymmetrical stretching; 1628 cm^{-1} C=O, NH stretching (Amid I); 1522 cm^{-1} NH bending (Amide II), C–N, C–C stretching; 1445 cm^{-1} CH₂ bending; 1332 cm^{-1} CH₂ wagging; 1235 cm^{-1} C–N stretching, NH bending (Amid III) and a shoulder at approximately 1400 cm^{-1} COO⁻ stretching. Those bands were shifted to a higher frequency for the freeze-dried G/X mixture without oil, namely to 3290 , 2932 (exception), 1633 , 1546 , 1451 , 1337 and 1238 cm^{-1} respectively. The shifting of absorption peaks to a higher frequency suggests that there is some interaction between G and X. If there is an electrostatic interaction, changes in the Amide I and Amide II regions are expected [432]. In addition, G and X are believed to interact with each other via hydrogen bonding with the involvement of NH and OH groups [433]. Also, the shoulder band, at approximately 1400 cm^{-1} emerged in G powder, appeared as an intensive band at 1400 cm^{-1} for the freeze-dried G/X mixture without oil, which is concentration dependant. G/X SOS prepared using HPDI and HPH also shows some interesting changes in absorption peaks. Compared to the freeze-dried G/X mixture without oil, the frequencies of absorption peaks of SOS were shifted again to a higher frequency (**Table 5.5**). What is more, the SOS prepared using HPH have higher frequencies than the SOS prepared

using HPDI, namely the Amide A, Amide I, Amide II and CH₂ bending shifted from 3303 to 3330, 1636 to 1652, from 1547 to 1552 and from 1455 to 1457 cm⁻¹ respectively. However, the intensities of all HPH absorption peaks were lower than that of SOS prepared using HPDI. The decrease in the intensities can be explained, as SOS prepared using HPH has a small oil droplet size compare to SOS prepared using HPDI. This may facilitate the fine distribution of a protein-polysaccharide layer on the surface of the oil droplets of SOS prepared using HPH, in comparison with the bulky oil droplets of SOS prepared using HPDI. Consequently, SOS prepared using HPH has a lower concentration of protein-polysaccharide layer per square centimetre. In addition, the intensity of oil absorption peaks were higher for the HPH sample than for the HPDI sample, also confirming that a large quantity of small oil droplets resulted in a fine distribution of protein-polysaccharide layer.

As can be seen from **Figure 5.28**, the pure X powder IR spectrum showed one strong band at 1018 cm⁻¹ OH bending and two medium bands at 3266 cm⁻¹ axial deformation of the OH group [434] and 1601 cm⁻¹ –C=O of pyruvate [435]. The IR spectrum of the freeze-dried G/X mixture without oil demonstrated shifting to a higher frequency too, as it was for G, namely from 1018 cm⁻¹ to 1031 cm⁻¹ (**Appendix 2**). SOS prepared using HPDI showed shifting and splitting of 1018 cm⁻¹ into three strong bands, namely 1083, 1060, 1031 cm⁻¹. Shifting the absorption peak of the G/X placebo mixture and the splitting into three bands of SOS prepared using HPDI suggest that there is some interaction between G and X. However, all other absorption peaks and the absorption peaks of SOS prepared using HPH were overlapped by G and sunflower oil bands, due to the low concentration of X in the formulation. Therefore, it is hard to interpret any apparent peak shifts.

The FT-IR results confirmed the presence of oil in dry SOS as the main IR peaks of sunflower oil 3008, 2922, 2853, 1743, 1465, 1377, 1237, 1160, 1120, 1098, 1031, 913, 722 cm⁻¹ exist in both SOS prepared using HPDI and HPH (**Figure 5.28**) (**Appendix 2**). Only 1120, 1098 and 722 cm⁻¹ IR peaks in the HPDI sample were overlapped by X bands.

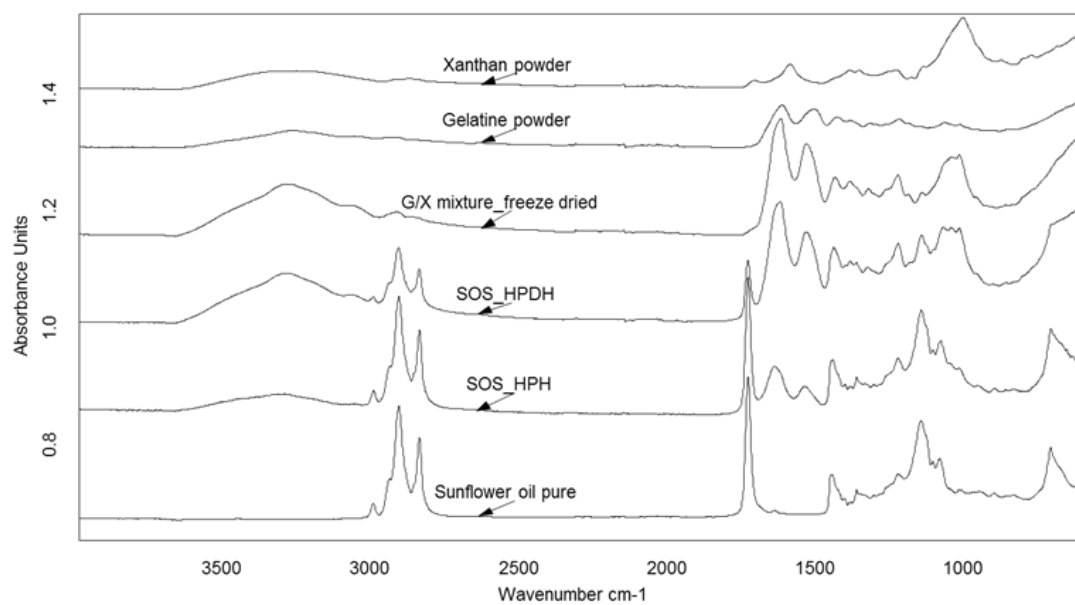


Figure 5.28. ATR FT-IR spectra of pure X and G powder, pure sunflower oil, freeze-dried G/X mixture without oil, G/X SOS prepared using HPDI and HPH.

Table 5.5. Frequencies (cm^{-1}) of bands of G mid-infrared spectra, together with the tentatively assigned functional group, the mode of vibration, and the approximate intensity. Abbreviation sh denotes shoulder, st – strong, m – medium, vw – very weak, SF – sunflower oil, X – xanthan gum.

Gelatine type B – IR peak assignments					
Frequency (cm^{-1}) raw material	Frequency (cm^{-1}) HPDI G/X mixture without oil	Frequency (cm^{-1}) HPDI G/X SOS	Frequency (cm^{-1}) HPH G/X SOS	Assignment & mode of vibration [342, 436]	Region
3274	3290	3303	3330	NH, OH stretching	Amide A
2939	2932	overlapped SF	overlapped SF	Asym. CH_2 -stretching, N-H stretching	Amide B
1628	1633	1636	1652	C=O stretching, N-H bending	Amide I
1522	1546	1547	1552	NH bending, C-N stretching, C-C stretching	Amide II
1445	1451	1455	1457	CH_2 bending	
sh	1400 s	1399 m	1399 sh	COO^- stretching	
1332	1337	1338	-	CH_2 wagging	
1235	1238	1238	1238	C-N stretching, NH bending	Amide III
1081	-	1083 overlapped X	-	Skeletal C-O stretching	

5.3.3.6 DSC

DSC analysis was conducted for pure metoprolol succinate powder, pure ketoconazole powder, pure G powder, pure X powder, freeze-dried G/X mixture without oil, G/X placebo SOS prepared using HPDI, G/X SOS containing 2 mg/ml water-soluble metoprolol, G/X SOS containing 1 mg/ml poorly water-soluble ketoconazole (**Figure 5.29**). Scans were performed from 0 to 250 °C at a controlled constant heating rate of 10 °C/min. We performed DSC analysis for X to detect T_g according to the method described in the literature [266]; however, we could not detect T_g. Therefore, we did not present DSC results for pure X powder.

The DSC thermographs of metoprolol succinate show two endothermic peaks: the first refers to the melting temperature of pure metoprolol succinate at 137.69 °C [225] and the second refers to the decomposition temperature starting from 161 °C. Enagbare [437] conducted TGA analysis and found that the decomposition of metoprolol succinate starts from 139 °C to 300 °C [438, 439]. As can be seen in **Figure 5.29**, the melting temperature of pure ketoconazole is at 149.16 °C. The result is consistent with the literature [212]. The DSC thermogram of pure G powder shows two endothermic peaks at about 92 °C (broad) and 225 °C (small). This broad peak can be attributed to water evaporation [440] which interfered with the ability to see the melting temperature of G. Li et al. [259] found that the melting temperature for pure G fibres was 93.8° C. The melting temperature at 225 °C can possibly be attributed to decomposition of G, because TGA analysis of G showed that it starts to decompose at 212 °C. The freeze-dried G/X mixture without oil also shows two melting transitions at 103 °C and 234.98 °C corresponding to water evaporation and possibly decomposition of G (which started at 218 °C), respectively. The DSC results of the G/X placebo SOS, the G/X SOS containing metoprolol succinate and the G/X SOS containing ketoconazole, all showed one small melting peak at about 125 °C, 125 °C and 129 °C, respectively. TGA analysis showed that SOS does not contain water, therefore, we were able to see one small transition peak at 125 °C and we assumed that this might be the melting temperature of G, which was shifted to a higher temperature. This may mean that there is some interaction between G and X which resulted in the formation of a G/X complex and the changing of the physical properties of gelatine [267]. G and X have electrostatic and/or hydrophobic interaction, so possibly these interactions take

place [441]. Neither metoprolol nor ketoconazole exhibit melting transition during DSC analysis, indicating non-crystalline form or low concentration of APIs [92].

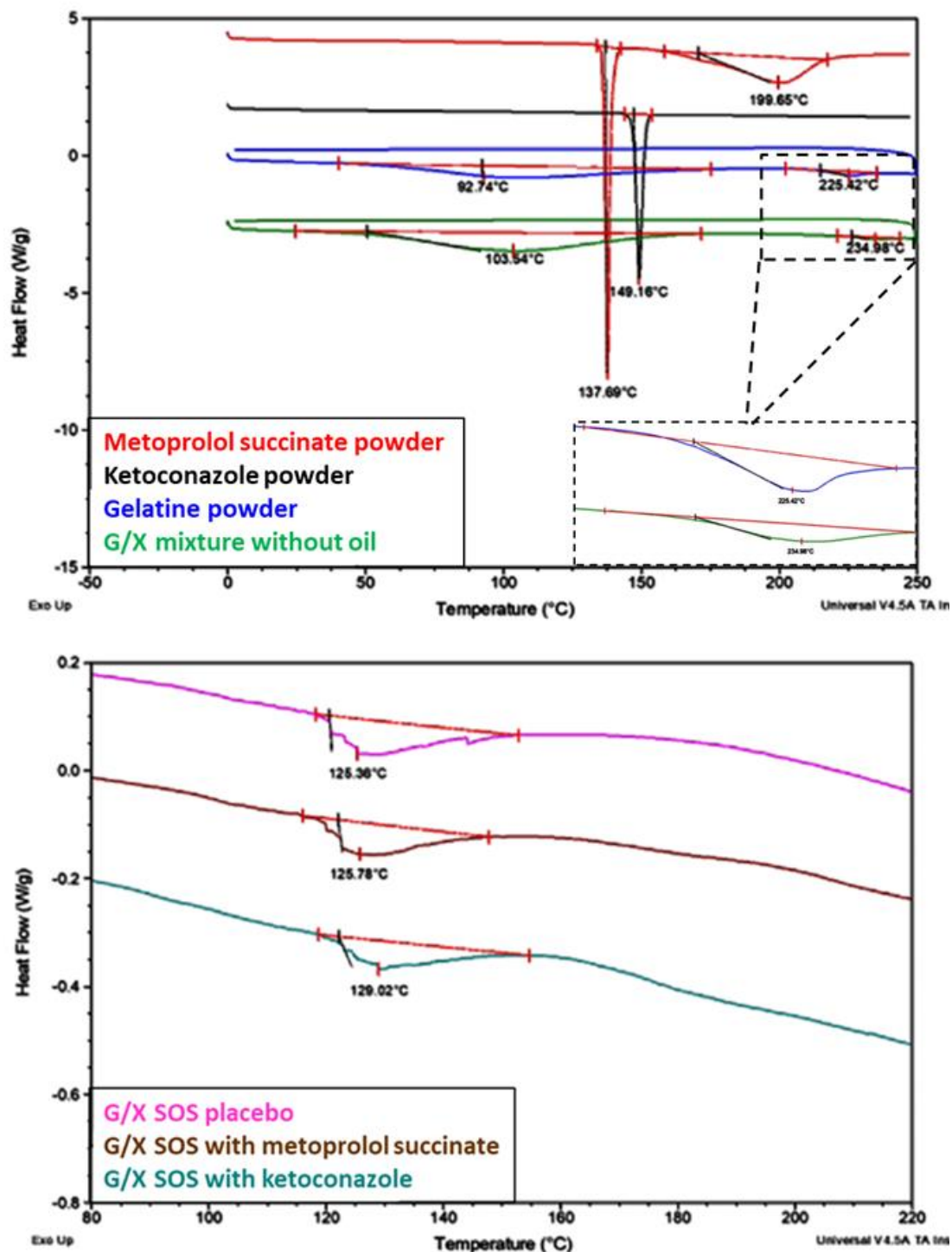


Figure 5.29. DSC thermographs of starting materials and freeze-dried G/X mixture without oil, placebo G/X SOS and G/X SOS loaded with APIs.

5.3.3.7 TGA

TGA experiments were performed for all the freeze-dried SOS and raw materials in order to estimate moisture content and thermal degradation of the fresh samples and after storage. **Figure 5.30** shows the TGA results of raw materials G and X, the freeze-dried G/X mixture without oil, and the SOS of G/X immediately after preparation, after 24 h and after 72 h (stored at ambient conditions). As can be seen on the graph, weight loss is observed for raw materials and the G/X freeze-dried mixture without oil, up until 100 °C for the freeze-dried G/X mixture without oil and up until 155 °C for G and X powder, which corresponds to water desorption in the samples. The thermal degradation, as can be seen, started at 212 °C and completed at 342 °C for X and at 400 °C for G and the freeze-dried G/X mixture without oil in a single step process. These results are in good agreement with the literature for X [442] and G [443]. However, water loss was not observed for the SOS of G/X measured immediately after preparation, after 24 h, after 72 h and after 1 month (stored at ambient conditions) (**Figure 5.30**), suggesting no moisture uptake by the samples. The decomposition for these samples started, as for the raw materials, at 212 °C and it was also a single step process. The absence of water was observed for G/CMC, HPMC/X, MC/X SOS stored at ambient temperature, at 40 °C and 75% RH (**Figures 5.30**), also indicating no significant moisture uptake, which favours better stability of the finished product. The thermal degradation started at 200 °C for samples stored at ambient temperature and at 75% RH, whereas for samples stored at 40 °C it started at 150 °C in a single step process, except for G/X SOS-HPDI which has a two step degradation process, the first at 128 °C and the second at 245 °C. Although in the literature, pure HPMC decomposes in two step processes, the first refers to evaporation of unbound water at 65.5 °C and the second decomposition refers to cellulose ether degradation, dehydration and demethoxylation at 300 °C (the weight loss is ~75%) with the maximal rate at 355–356 °C [444, 445]. From the literature, CMC decomposes in two-step processes, first due to water removal at 38–172 °C and with the second thermal event starting at 172 °C and finishing at 327 °C, which may correspond to the degradation of the side chain and loss of CO₂ [291]. In another source, CMC decomposes in a three step process. In the first step, from 25–100 °C (the weight loss is ~10%) which is due to loss of moisture and then from 100–300 °C (the weight loss is ~39%) the CMC starts to decompose due to loss

of CO₂ from the polysaccharide, and the third decomposition of the polysaccharide backbone in the CMC occurs in the range of 300–800 °C (the weight loss is ~22%) [292].

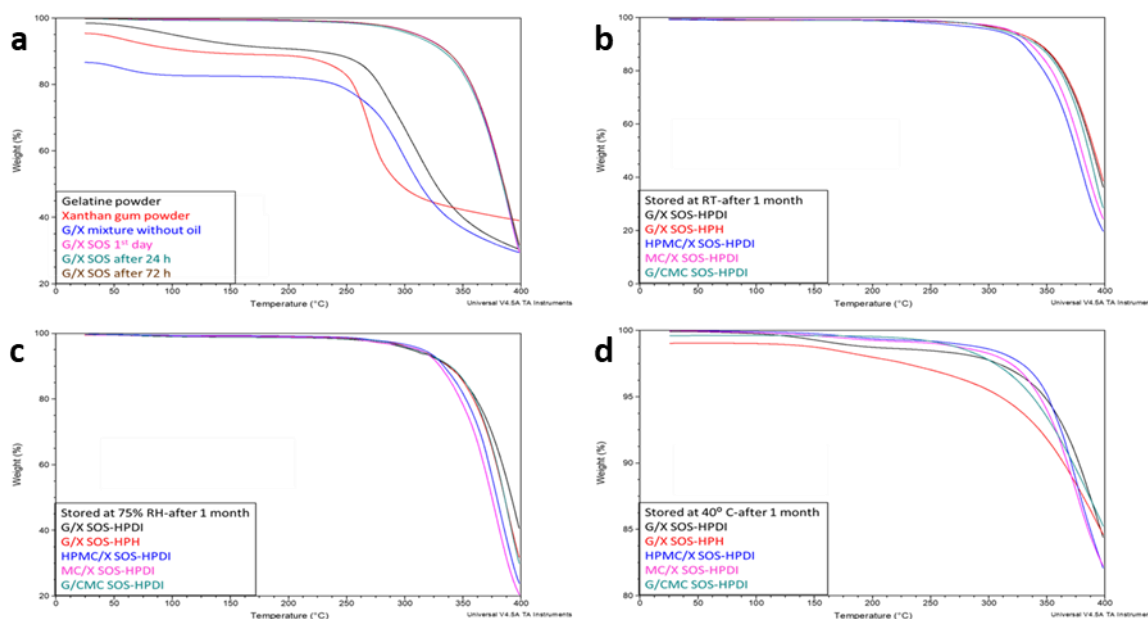


Figure 5.30. TGA thermogram of raw materials and processed samples immediately after preparation and after storage: a) at ambient temperature for 24 h and 72 h; b) G/X, HPMC/X, MC/X and G/CMC SOSs prepared using HPDI and HPH after storage at room (ambient) temperature (RT) for 1 month; c) G/X, HPMC/X, MC/X and G/CMC SOS prepared using HPDI and HPH after storage at 75% RH for 1 month; d) G/X, HPMC/X, MC/X and G/CMC SOS prepared using HPDI and HPH after storage at 40 °C for 1 month.

5.3.3.8 Mechanical properties and oil holding capacity under compression

The measurements were carried out using a compression test mode to examine the resistance of the specimen to force. As can be seen in **Figure 5.31**, G/CMC showed the highest rigidity than those SOS prepared with X mixture; namely it could resist the force for 30 seconds of a load of 20,000 grams. G/X prepared using HPDI and HPH showed medium stiffness, while HPMC/X and MC/X have the softest structural properties; they could resist the force for 30 seconds of 1,800 and 1,500-1,400 grams loads respectively. Blank paper was used for comparison purposes to show the behaviour of line for rigid material. The results showed that the SOSs prepared using G has higher rigidity than those prepared without it. The degree

of complexation is possibly different for those compositions, which affects the mechanical properties of these samples [446]. This should be checked with ATR FT IR. The amount of oil released during compression was assessed quantitatively by weighing the cellulose filter paper before and after soaking with oil and it was placed on a flat aluminium cylinder under the SOS. **Table 5.6** represents the summary in grams. The amount of oil released correlates well with the stiffness of the samples; the softest MC/X sample released the highest amount of oil, namely 1.73 grams, whereas the rigid G/CMC released 0.5 grams.

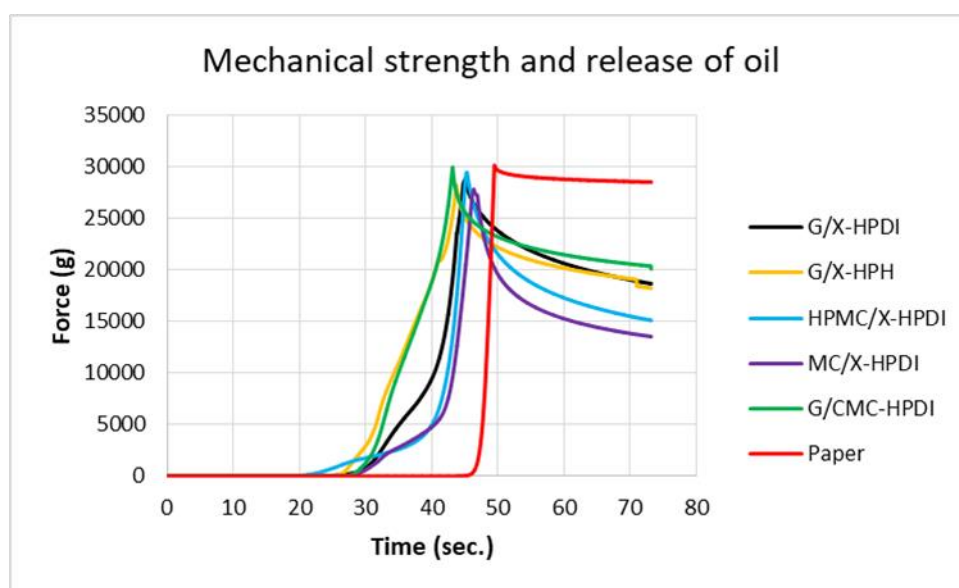


Figure 5.31. Mechanical strength of 5 different SOS under compression.

Table 5.6. Amount of oil released during compression.

Type of SOS	Amount of oil released in grams
G/X – HPDI	0.5698 ± 0.02
G/X – HPH	0.5533 ± 0.1
HPMC/X	0.7433 ± 0.03
MC/X	1.7309 ± 0.34
G/CMC	0.5077 ± 0.23

5.3.3.9 Water uptake ability

The drug release kinetics from SOS depends on the rate of water uptake and drug dissolution/diffusion rate, which in turn can also be affected by the preparation method [447].

Therefore, a water uptake study was performed for SOS prepared using HPDI and HPH as described in the literature [448]. The equilibrium water uptake ability of SOS was measured as follows: a pre-weighed dry sample was immersed in distilled water and at different time intervals was taken out to measure the weight of the wet sample. The water uptake ability was calculated according to the following equation:

$$\text{Water uptake ability} = (W_w - W_d)/W_d$$

where W_w represents the weight of the wet sample and W_d represents the weight of the dry sample.

Figures 5.32 and 5.33 illustrate the water uptake of G/X SOS prepared using HPDI and HPH, respectively. As can be seen in the images, the preparation method has a great impact on water uptake ability and disintegration in the aqueous phase. SOS prepared using HPDI showed a slow water uptake and disintegration in water. There was a burst uptake within 5 minutes, the weight was increased to almost twice of its weight, then it slowed down and almost no changes were observed after 45 minutes. During water uptake, swelling of the SOS was observed. If the initial length and width of the SOS pieces were 1.2 cm and 0.5 cm respectively, at the end, after 60 minutes, they were 1.6 cm and 0.7 cm. SOS prepared using HPH showed a burst of water uptake and disintegration within 5 minutes. The same swelling behaviour was observed for SOS prepared using HPH. The initial length and width were 1.1 cm and 0.4 cm respectively, after 5 minutes they were 1.2 cm and 0.6 cm. **Table 5.7** represents the water uptake ability which was determined from the weight difference between the wet state and dry state of SOS.

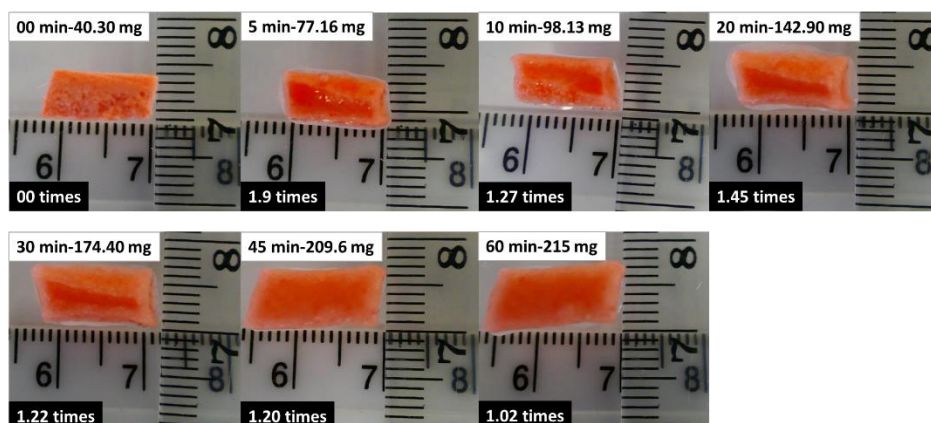


Figure 5.32. Water uptake of G/X SOS prepared using HPDI.



Figure 5.33. Water uptake of G/X SOS prepared using HPH.

Table 5.7. Water uptake ability of placebo G/X SOS prepared using HPDI and HPH.

Sample	Amount of water in mg					
	5 min	10 min	20 min	30 min	45 min	60 min
SOS HPDI	0.9146	1.4350	2.5459	3.3275	4.201	4.35
SOS HPH	1.2809 and then disintegrated					

5.3.3.10 Dissolution testing

In vitro drug release of SOS was conducted for G/X SOS prepared using HPDI and HPH. Metoprolol succinate was selected as a model of highly water soluble drug.

Figure 5.34 shows the dissolution testing results obtained for G/X SOS prepared using HPDI and HPH in acidic media. It can be seen that the release rate of metoprolol succinate was different for formulations prepared using HPH and HPDI. G/X SOS prepared using HPH showed faster drug dissolution compared to the G/X SOS prepared using HPDI. In the SOS

formulation prepared using HPH, over 60% of the drug releases in the first 3 minutes, whereas in the SOS formulation prepared using HPDI, the same amount of drug was released over 20 minutes and then sustained release was observed. These results showed that the preparation process has a great impact on the dissolution profile of API, indicating the dissolution enhancement effect of formulations prepared using HPH. This can be explained as the SOS prepared using HPH has greater air pockets in the bulk, so the water penetration is faster. In addition, a high pressure homogenized sample has smaller emulsion droplet size distribution, which has resulted in a higher surface to volume ratio thus faster polymer swelling and dissolution. SOS prepared using HPDI shows sustained drug release, which is consistent with the water uptake ability test. The release of the drug from both dosage forms was incomplete in this experiment because the selected time of 60 min and 90 min was not enough to completely dissolve the given amount of dosage form (this is due to miscalculation, which was based on water uptake study that lead to assumed that that time was enough to dissolve the dosage form. Unfortunately, we did not have time to repeat this experiment with lower dosage weight)

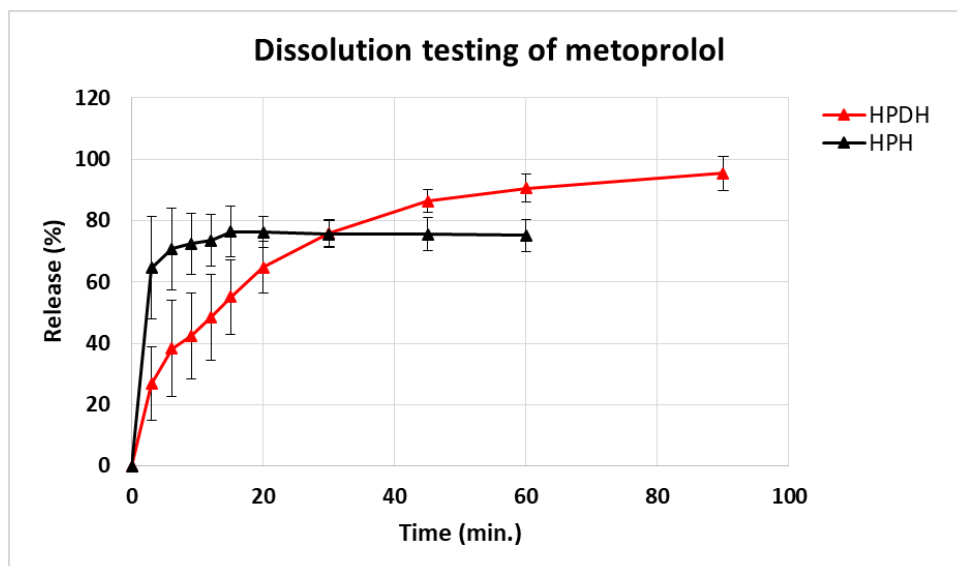


Figure 5.34. In vitro drug release of SOS prepared using HPDI and HPH.

5.4 Conclusion

A novel drug delivery system called SOS has been designed to use as a carrier to deliver water-soluble and oil-soluble drugs or nutrients. This structured oil system was prepared using an organic solvent-free method and a relatively inexpensive freeze drying technique which is preferential for heat sensitive agents. Electrostatic and/or hydrophobic interaction between protein and polysaccharide was utilized to produce emulsions stable against stress conditions. The materials used in preparation are inexpensive food and pharmaceutical grades.

In this chapter, the preparation and characterization of freeze-dried SOS prepared using HPDI and HPH was discussed. Two different model drugs, metoprolol succinate and ketoconazole, and five different compositions, namely G/X, HPMC/X, MC/X, Tween 20/X and G/CMC were used to prepare freeze-dried SOSs. First emulsion characterizations were performed using upright brightfield and fluorescence microscopes, a confocal microscope and an LD particle size analyser to investigate the impact of emulsion stability and particle size on the formation of SOS. Second, the morphology and inner structure of SOS was studied using a stereo fluorescence microscope, TEM, X μ CT and Cryo-SEM to confirm the entrapping of sunflower oil in the polymer network. DSC and ATR FT-IR analysis confirms electrostatic and/or hydrophobic interaction between G/X polymers. TGA analysis showed good stability of the prepared SOS against moisture. A texture analyser revealed the most resistant SOS against force, which was the SOS prepared using G/CMC polymers, and also determined oil holding capacity. Dissolution testing was conducted for only water-soluble API prepared using HPDI and HPH. The results revealed two different dissolution profiles depending on the preparation tool, namely burst and sustained release of metoprolol succinate for SOS prepared using HPH and HPDI, respectively. The dissolution testing results were consistent with the water uptake ability of SOS prepared using HPDI and HPH.

The oil holding capacity of SOSs directly depends on the ability of emulsifiers to resist stress conditions. The Tween 20/X system failed to form a structured oil system, confirming that the formation of stable emulsions and particle sizes are not key parameters ensuring the formation of SOS. The morphology of SOS can be affected by the preparation method as well as polymer type. G/X SOS prepared using HPH and G/CMC SOS prepared using HPDI showed the best morphology and appearance of the samples tested.

6 Chapter 6. Concluding remarks and future prospects

6.1 Reflection on the key findings

In **Chapter 3**, the preparation and characterization of an orodispersible film of iodine delivery was discussed. KIO_3 loaded nanofibres show excellent stability for at least four years and efficient release of iodine upon wetting. This novel formulation design by means of electrospinning allows easy administration of iodine for preventing childhood iodine deficiency. In addition, this orodispersible film potentially can be used as medication for radiation protection. It can be of benefit in this respect since the concept of taking KI and KIO_3 containing tablets during radiation is to quickly provide the body with a stable source of iodine in order to prevent accumulation of radioactive iodine, and the ultrarapid dissolution of orodispersible film in the oral cavity can ensure a rapid delivery of iodine into the body. In addition, the orodispersible film does not require water intake compared to conventional tablets, which is important in an emergency situation, when looking for water can be a bit stressful because of panic. Moreover, the stability of KIO_3 in extreme conditions and the long shelf life of the finished product allows for it to be stocked in quantities in places far away from towns and cities. Besides, this study has demonstrated: 1) that electrospinning technology has a great potential for use in the formulation of dosage forms for children; 2) that not all salts facilitate better fibre formation and can improve fibre morphology; 3) the importance of the characterization of electrospun nanofibres loaded with active ingredient using TEM along with SEM, showing that TEM is a simple and straight forward instrument to reveal and visualize the distribution of the crystalline active ingredient within nanofibres or confirm the absence of a crystalline form; 4) a novel and easy method for producing and harvesting nanocrystals of inorganic salts; 5) a contribution to the research area of polymeric-based solid dispersion for inorganic material delivery; 6) the importance of handling the electrospun nanofibres during sample examination. Even mild to moderate stretching of the fibres can lead to the change of molecular conformation of polymer and hence its physicochemical properties. Thus, we revealed the change in molecular conformation of PEO in the stretched state, previously not reported, examined using PXRD.

Chapter 4 is an extension of the work presented in **Chapter 3**, wherein EE was explored to produce lipid-based biphasic drug release delivery system for a water-soluble and oil-soluble drugs or nutrient. The key challenges of this project were (1) utilizing non-conducting edible oil, an uncommon approach in EE, as an oil phase in o/w emulsion that was designed for further electrospinning, (2) selecting only food grade substances and (3) organic solvent free formulation and processing. The results obtained from this study show the feasibility of EE for certain types of formulations, namely for formulations prepared using TPGS as the emulsifier, which prove to be effective in facilitating fibre formation based on the SEM images and ensure better encapsulation of liquid oil within an electrospun fibrous-like film as examined by the naked eye. These results open a wide area to explore different materials for the development of lipid-based solid dispersion using EE wherein liquid edible oils and fish oil can be encapsulated. However, the maximum oil volume fraction in the disperse phase of o/w emulsion that was achieved during the given period of time was 20 v/v %. That oil volume fraction was not sufficient for the purpose of the study and therefore this study was discontinued. However, these results were presented in this thesis because this delivery systems has a great potential to be evaluated for other nutrients and APIs that require small doses. This study, in addition, provides primary information about the formulation and processing parameters affecting fibre formation in EE. However, in order to establish the applicability of these formulations as delivery system for water-soluble and oil-soluble drugs or nutrients, additional investigations and improvements are needed, such as in relation to the stability of emulsions and end product, reproducibility, carrier-drug interactions, and drug dissolution tests of two types of drug or nutrient.

Despite the numerous lipid-based formulations that are available today, the majority of oral dosage forms that can carry large amounts of oil is limited by the soft or sealed hard gelatine capsules in use [449], which are limiting the possibilities to improve the dosage forms for children. SOS studied in **Chapter 5** contributed to the research area of large oil containing delivery systems. It presents a thorough investigation of a novel G/X structured oil system, capable of holding a large amount of oil, to be applied in the pharmaceutical area as a carrier of water-soluble and oil-soluble nutrients or drugs. The results, which are mainly based on the example of G/X SOS, show that emulsifier type (G/X, HPMC/X, MC/X, Tween 20/X, G/CMC), oil volume fraction (20–60 v/v %) and processing parameters (HPDI and HPDI/HPH)

affect the formation and properties of emulsions and hence SOSs. The oil holding capacity of SOSs directly depends on the ability of emulsifiers to resist stress conditions. The freeze-dried SOS comes out as white, matted, dry, and cottony with a sponge-like structure and looks heavy/ponderous/bulky/cumbrous if HPDI was used in the emulsion preparation and lightweight/gentle/delicate/fine if HPDI/HPH were used in the emulsion preparation or if G/CMC emulsifiers were used. The shape of SOS can take any form depending on the jar that was used during freeze drying. This property is advantageous as it allows direct production of a round disk dosage similar to tablets in continuous manufacturing as a future prospect. However, it needs thorough investigation to fully assess the applicability of this system as a carrier, particularly, in the first place, with a dissolution test for the oil-soluble active ingredient.

6.2 Future outlook

Building on the foundations established by this project, two ranges of supplement formulations that can be used and scaled up for nutrient delivery should be further refined and developed. To achieve this, first, the permeation of nutrients or drugs through the oral mucosa should be studied to ensure the efficacy of delivery of the nutrient or drug from both orodispersible films and SOS, as well as the palatability and safety of the dosage forms. Secondly, whereas the freeze-drying technique has established a routine procedure for large-scale production, the industrial scale up of the emerging electrospinning technique is still in its developing stages and, as discussed in **Chapter 1**, the main challenges associated with mass production of electrospun nanofibres could nullify the processing parameters used to produce nanofibres in the lab. Therefore, for the orodispersible films electrospun in the lab, it is important to re-check the processing parameters for large-scale production and validate the reproducibility of the final product.

One of the challenges in this research was estimating the amount of released oil from SOS. We had a fine accumulation of oil on the top of the dissolution media, which raised the question of sampling the released oil. There are no standard pharmacopoeial methods for testing lipid-based formulations. However, we came across the work of Onoue et al. [450], who carried out dissolution testing using a conventional dissolution test apparatus. They

were withdrawing the aliquot from the dissolution media, then centrifuging it at 15,000 rpm for 5 minutes, then supernatants were diluted with a 10-fold volume of methanol and they then measured the concentration. Thus, we used the same principle but with some changes. Sudan III was used as the oil-soluble substance, of which the concentration in oil can be correlated with the amount of oil released at a certain period of time. The test was carried out in a handmade set up because we used organic solvents, such as hexane, toluene and 1-octanol, which are harmful to dissolution vessels, and we did not sample, we took the whole medium, diluted it with solvent and then centrifuged the supernatant (**Figure 6.1**). However, centrifugation did not help to separate the oil phase from the dissolution media; conversely, it resulted in many air bubbles and re-emulsification. Then we decided to shake the sample gently by hand to ensure that the solvent extracts the oil (we do not have a shaking incubator in the lab) and leave it for 15 minutes to allow time for oil to accumulate on the top of the media. Thus, we were able to withdraw only a small amount of oil, which was then diluted with standard solution and analysed using UV-Vis spectroscopy at 259 – 265 nm. However, the release of dye was undulant. We anticipated that this might be due to human factors, because the dissolution media was shaken by hand, which cannot ensure the fixed speed of shaking. The second reason is that the solvents that we used were affecting the UV maximum, which was shifting every time. Therefore, the development of a proper methodology for testing the released oil from the dosage form is important both for conventional oral tablets and for oral disintegrating tablets.

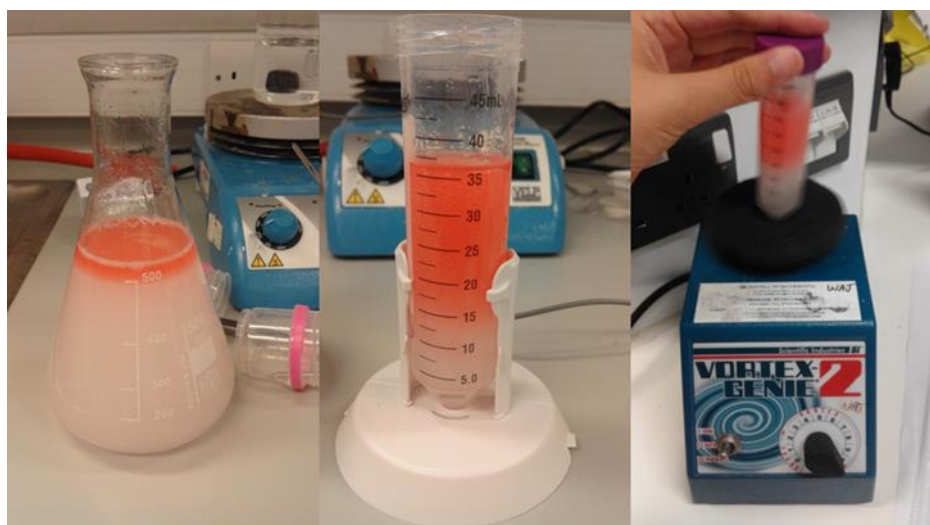


Figure 6.1. Testing the release oil from the dosage form using oil-soluble dye Sudan III.

When emulsifier type was studied, HPMC/X, MC/X and G/CMC show capability to serve as a structuring system for oil phase. Characterizing these systems, as it was done for G/X SOS, may provide new insights into protein-polysaccharide and polysaccharide-polysaccharide interactions, into their dissolution profile and mechanism, and understanding the oil holding ability of SOS. In addition, HPMC/X, MC/X and especially G/CMC show interesting morphology that is different from G/X SOS. It would be very interesting to conduct two-step emulsification to prepare emulsions for producing those SOS to see the impact of the HPH instrument on their properties. This would give a range of delivery systems capable of carrying oil phase and open up a wide range of possible combinations. Particularly, G/CMC SOS prepared by HPDI shows a fine and light morphology as with the G/X SOS prepared using HPDI and HPH in a two-step emulsification method. This means that if G/CMC SOS were prepared in a two-step emulsification method, the morphology of the end product most probably will be even finer and lighter, which in turn can increase the disintegrating and the dissolution rate, hence can also be used as a fast disintegrating tablet.

Another characteristic of protein and polysaccharide that is worthy of study is to determine how G/X, HPMC/X, MC/X and G/CMC were distributed on the oil-water interface. This information is useful for predicting the stability of emulsion droplets to flocculation or coalescence. A range of techniques, including AFM, scattering techniques and spectroscopy techniques, are used to analyse changes in interfacial thickness and structural organization that can give information about the distribution of protein and polysaccharide on the oil-water interface [142]. In addition, ATR-FTIR and PXRD analysis for HPMC/X, MC/X and G/CMC SOS formulations would give information on the type of interactions and of the crystalline and amorphous state of the materials after processing, respectively, which in turn may explain the mechanical properties of SOS discussed in **Chapter 5, section 5.3.3.8**.

Furthermore, this study opens two new research areas worthy of investigation. These aspects were not investigated here because it was not within the scope of this study.

- Investigate the properties of KIO_3 and NaCl nanocrystals in order to explore and find application areas where they can be of benefit. Determine the key processing parameters affecting the production of nanocrystals of inorganic salts and apply to other inorganic crystals to establish a routine production. Besides, in obtaining

nanocrystals of inorganic salts, we anticipated that different polymorphs can also be obtained during electrospinning processing. Generally, electrospinning and electro spraying technologies have been employed for the production of nano-range materials such as nanofibres and polymer nanoparticles; however, it was not reported to be used for the production of nanocrystals. We anticipate that this method can be used not only for the production of inorganic nanocrystals but also can be applied to any other chemical substances that can be dissolved or melted. In contrast with other methods of obtaining nanocrystals, electrospinning/electro spraying technology offers a simple three-step process: solution preparation, electrospinning or electro spraying, and collecting the nanocrystals. In the case of electrospinning, it is necessary to use special solvents that can dissolve fibres but will not dissolve the nanocrystals and to perform the procedure on a flat surface that immediately can wash down or adsorb the solvent, so the nanocrystals will not get in contact with each other; the dry nanocrystals can then be collected on the surface area and it is possible to sieve them. In the case of electro spraying, collect the crystals and simply sieve them through a nano-range orifice.

- Investigate the molecular conformation of PEO in its stretched state using other analytical tools, such as ATR-FT IR to validate the conformational changes and scanning tunnelling microscopy that can help to obtain visual evidence of conformational changes, as well as the tensile strength in order to determine the maximum applied force to rupture the film. In addition, the change in molecular conformation of PEO upon stretching the electrospun sample led us to make an assumption that other polymers that change their molecular conformation upon stretching may also exhibit new conformation upon stretching an electrospun sample. Thus, we found a number of polymers that change their conformation upon stretching and performed a literature search to find out whether these polymers are electrospinnable. We found that among them polypropylene, poly(vinylidene fluoride), polybutene and nylon 6 are electrospinnable. We anticipated that these polymers may also exhibit different conformation changes if stretched after electrospinning, because electrospinning gives a certain flexibility to electrospun polymers thus they may possess higher tensile strength and hence higher stretching is obtained, which resulted in stronger changes in the polymer conformation.

Investigation of the conformation of these polymers after stretching them following electrospinning will give scientists and manufacturers information on how to handle such samples, contribute to the area of polymer research and may open new arenas for application.

7 Appendices

7.1 Appendix 1. The effect of Tween 20 surfactant on fibre morphology

This experiment was carried out to see the effect of surfactant and oil on fibre formation when attempting to electrospin emulsion. Emulsion electrospinning failed to effectuate (**Chapter 4**). However, the results show significant improvement of fibre morphology from beaded fibres to smooth and uniform fibres with only a small amount of surfactant, namely 1 w/w % (**Figure A1.1**).

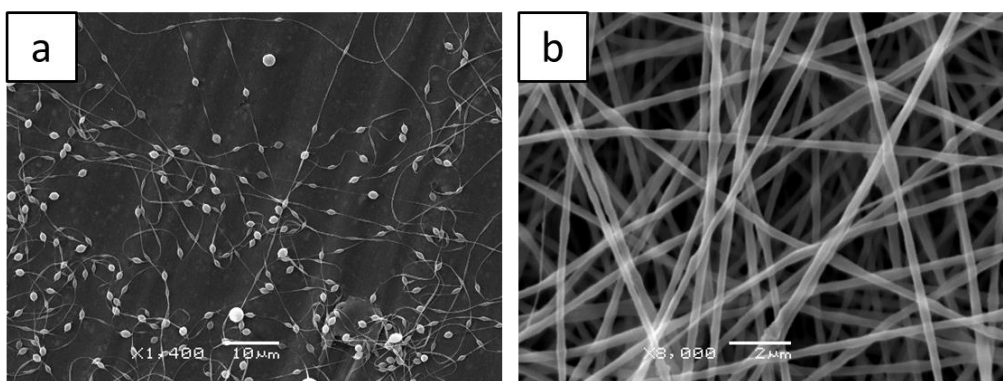


Figure A1.1. SEM images of a) pure PEO 300K with 7 w/v % solution concentration; b) PEO 300K mixed with 1 w/w % of Tween 80 with 7 w/v % solution concentration. The EPPs: 150 mm – 0.5 ml/h – 12 kV.

7.2 Appendix 2. ATR-FT IR analysis of G/X SOS

ATR FT-IR analysis was carried out for pure gelatine and xanthan gum powders, pure sunflower oil, a mixture of G/X solution without oil and subsequently freeze dried, G/X SOS prepared using HPDI and HPH (**Chapter 5**). The infrared spectrum of each of the samples is given in **Figures A2.1 – A2.6**. The frequency, functional groups and mode of vibration of xanthan gum powder and pure sunflower oil are given in **Tables A2.1 – A2.2**.

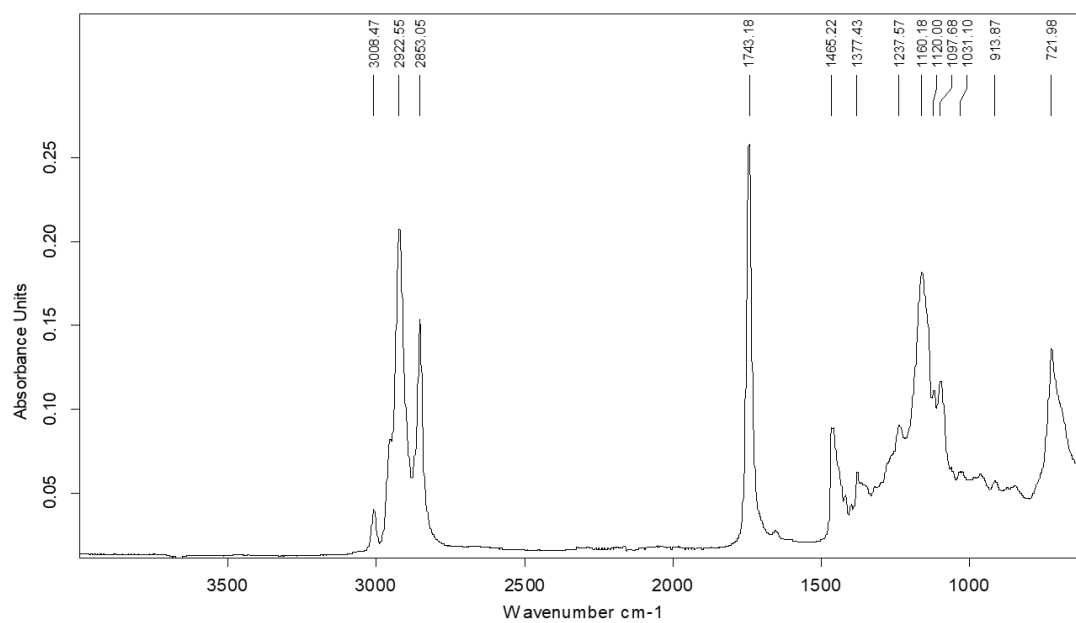


Figure A2.1. ATR-FTIR spectra of pure sunflower oil.

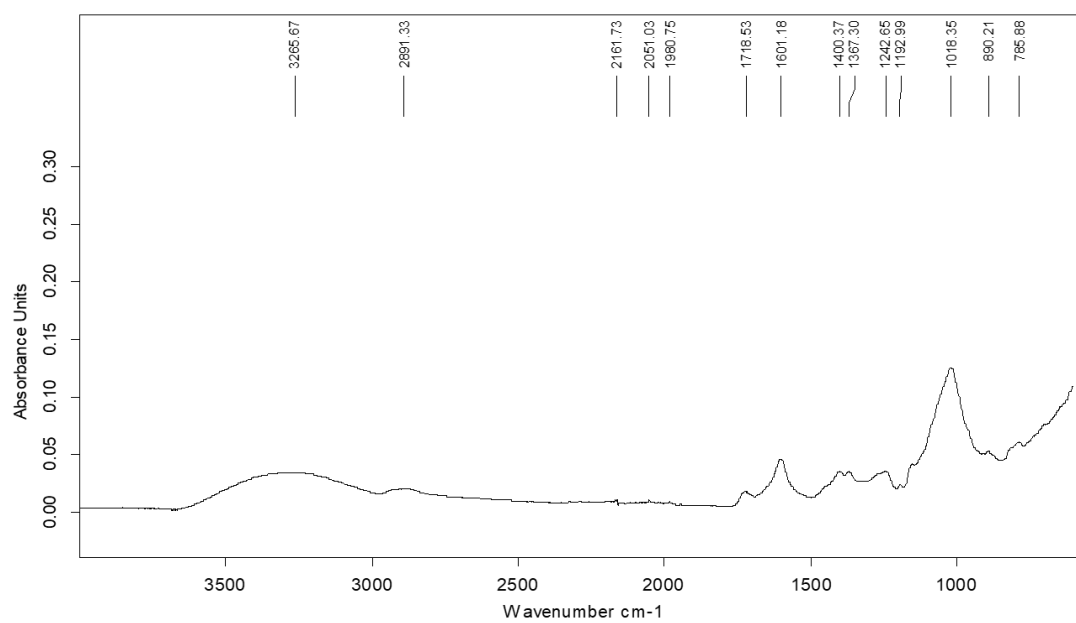


Figure A2.2. ATR-FTIR spectra of pure xanthan gum powder.

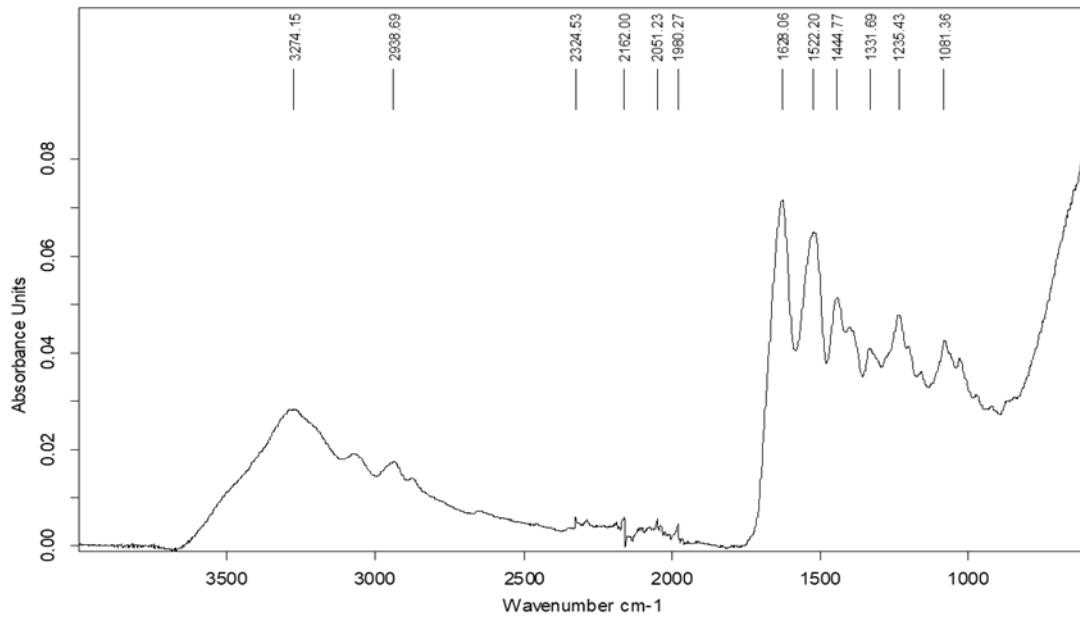


Figure A2.3. ATR-FTIR spectra of pure gelatine powder.

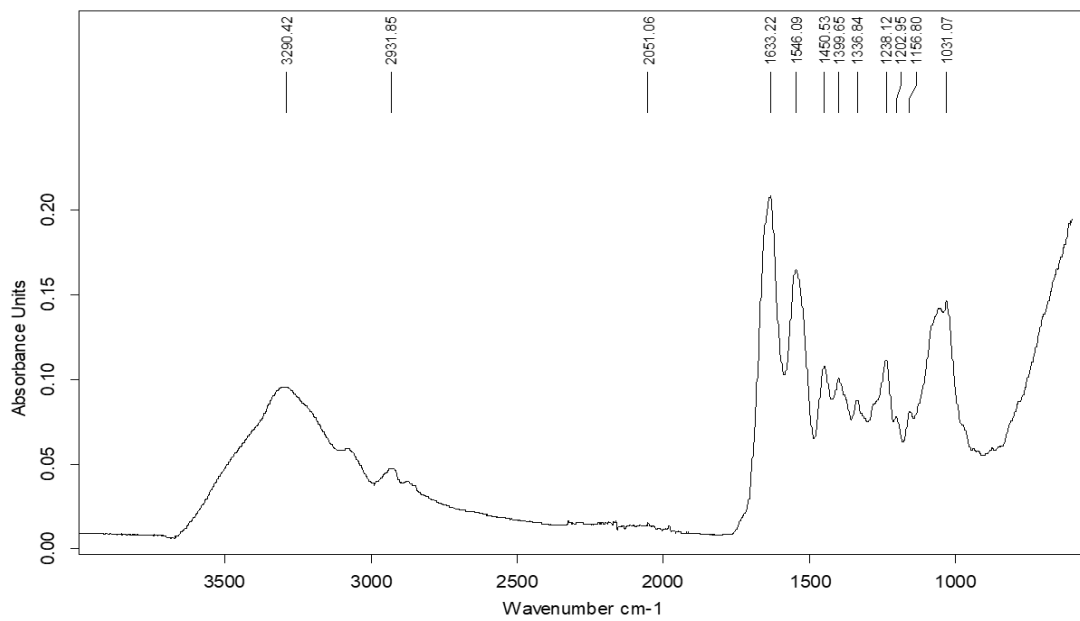


Figure A2.4. ATR-FTIR spectra of G/X mixture without oil and freeze dried.

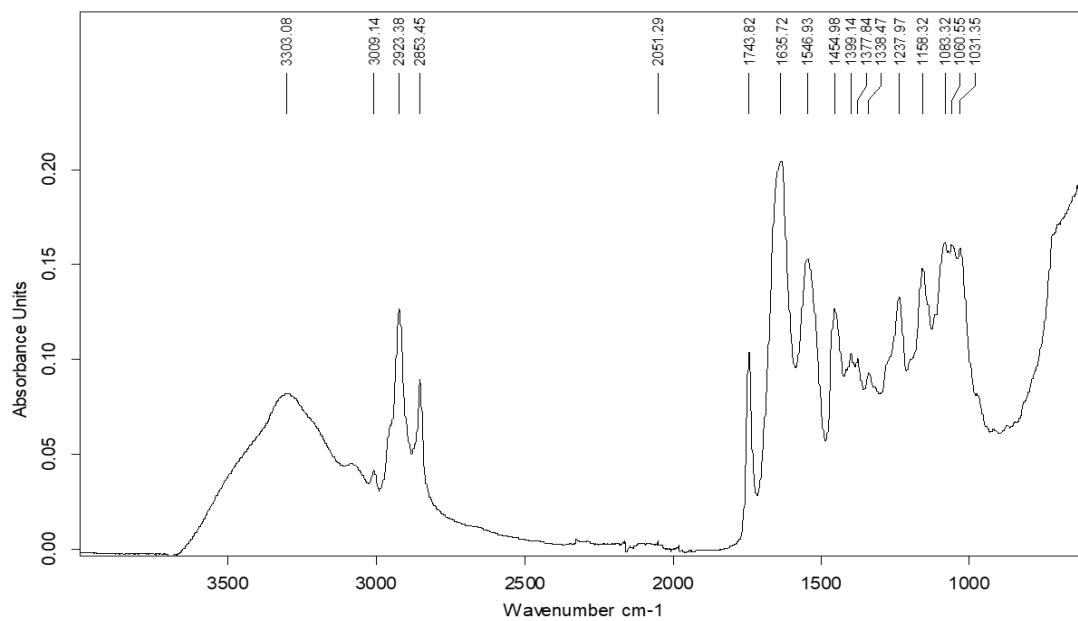


Figure A2.5. ATR-FTIR spectra of G/X SOS prepared using HPDI.

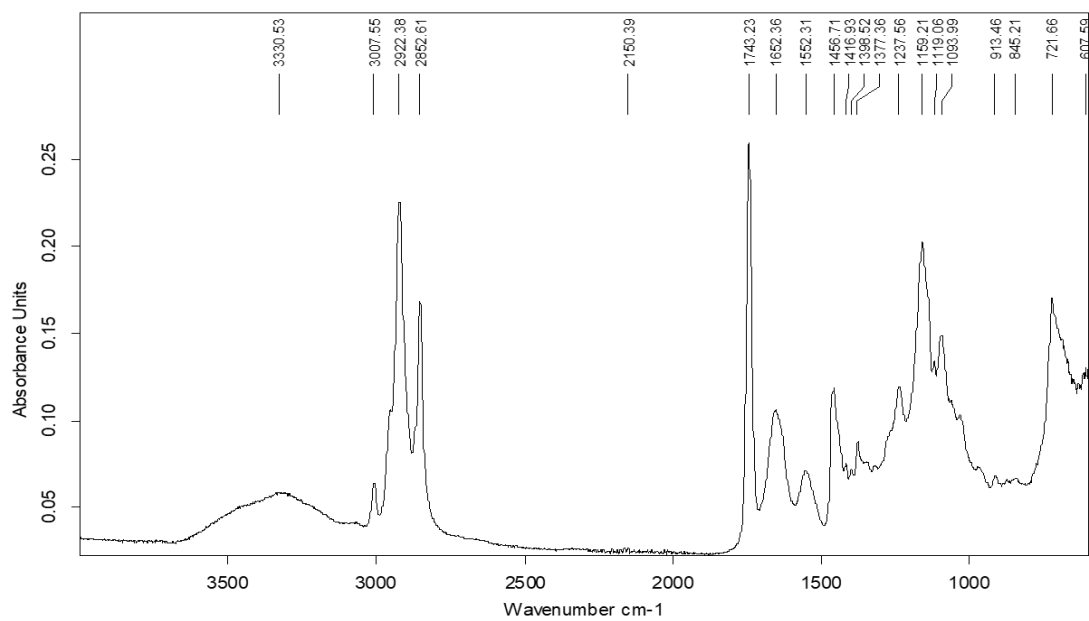


Figure A2.6. ATR-FTIR spectra of G/X SOS prepared using HPH.

Table A2.1. Frequencies (in cm^{-1}) of bands of sunflower oil mid-infrared spectra, their functional groups, the mode of vibration, and the approximate intensity. Adapted from [451]. Abbreviations: vst denotes very strong, st – strong, m – medium, vw – very weak.

Sunflower oil - IR peak assignments			
Frequency (cm^{-1})	Functional group	Mode of vibration	Intensity
3008	=C–H (cis)	stretching	m
2922	–C–H (CH_2)	stretching (asym)	vst
2853	–C–H (CH_2)	stretching (sym)	vst
1743	–C=O (ester)	stretching	vst
1465	–C–H (CH_2 , CH_3)	bending (scissoring)	m
1377	–C–H (CH_3)	bending (sym)	m
1237	–C–O, – CH_2 –	stretching, bending	m
1160	–C–O, – CH_2 –	stretching, bending	st
1120	–C–O	stretching	m
1097	–C–O	Stretching	m
1031	–C–O	Stretching	vw
913	–HC=CH– (cis)	bending out of plane	vw
721	–(CH_2) $_n$ –, –HC=CH– (cis)	rocking, bending out	m

Table A2.2. Frequencies (in cm^{-1}) of bands of X powder mid-infrared spectra, together with the tentatively assigned functional group, the mode of vibration, and the approximate intensity. Abbreviation: st denotes strong, m – medium, vw – very weak, G – gelatine.

Xanthan gum - IR peak assignments				
Frequency (cm^{-1}) row material and intensities	Frequency (cm^{-1}) HPDI G/X placebo mixture	Frequency (cm^{-1}) HPDI G/X SOS	Frequency (cm^{-1}) HPH G/X SOS	Assignment & mode of vibration [435, 452-454]
3266 m	overlapped G	overlapped G	overlapped G	–OH stretching
2891 vw	overlapped G	overlapped G	overlapped G	–CH ₂ stretching
1719 vw	overlapped G	overlapped G	overlapped G	–C=O stretching
1601 m	overlapped G	overlapped G	overlapped G	–C=O of pyruvate
1400 vw	overlapped G	overlapped G	overlapped G	CH bending
1367 vw	overlapped G	overlapped G	overlapped G	–C–H
1243 vw	overlapped G	overlapped G	overlapped G	–C–O–C–
1193 vw	overlapped G	overlapped G	overlapped G	–C–O–C–O–C– acetal
-	-	1083	-	axial deformation of C–O
-	-	1060	-	CO stretching of alcohol
1018 st	1031	1031	-	OH bending
890 vw	overlapped G	overlapped G	overlapped G	– C ₁ –H of β -pyranose

7.3 Appendix 3. PXRD analysis of xanthan gum

We conducted PXRD analysis to confirm the crystalline or amorphous form of xanthan gum used in this study because different sources stated different properties. Kumar et al. [453] and Yahoum et al. [455] reported that xanthan gum has an amorphous structure, whereas Izawa et al. [456] reported that xanthan gum has a higher-ordered structure in the gel and Su et al. [435] reported that xanthan gum has a higher degree of crystallinity. Guo et al. [433] reported that xanthan gum decreases crystallinity with the increase of the aldehyde content. Lad et al. [457] found that the intensity of the diffraction peak of xanthan gum gradually decreases with the increase of water content in the sample. From our PXRD results (**Figure A3.1**), the xanthan gum that we used in our experiments is amorphous. However, at the same time, two broad humps may indicate a low degree of ordering. A broad peak at $2\theta=20.21$ and a sharp peak at $2\theta=32.27$ corresponds, probably, to double-helix conformation of xanthan gum [456] and the presence of sodium sulphate crystals [457], respectively.

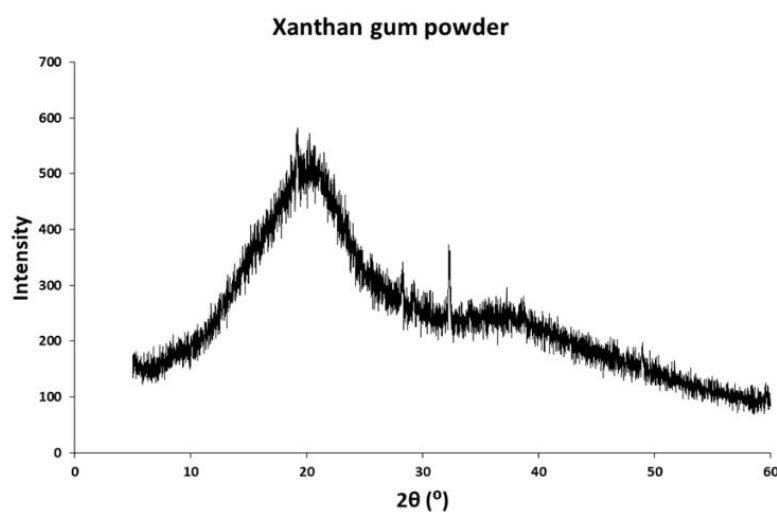


Figure A3.1. PXRD diffraction patterns of xanthan gum powder.

7.4 Appendix 4. The new crystal modification of electrospun poly (ethylene oxide) under stretching

Introduction

Polyethylene oxide is a semi-crystalline polymer that has two diffraction peaks at $2\theta = 19^\circ$ and 23° on powder X-ray diffraction (PXRD); and two well-known conformations, 7/2 helical conformation in the normal state [458] and planar zigzag conformation, stable only under tension [459]. It also has various helical conformations in crystalline complexes with urea [460], HgCl_2 [461, 462], NaI, NaSCN and KSCN [463, 464]. Takahashi et al. [459] showed the existence of a planar zigzag conformation for pure PEO. This conformation is stable only when stretched and is not characteristic in the absence of an applied stretching. On an X-ray diffraction, planar zigzag conformation is shown as a halo at $2\theta \approx 21^\circ$ and $2\theta \approx 24^\circ - 25^\circ$.

In this study, the new crystalline conformation of PEO in a stretched state is revealed, which is a finding that has not been previously reported. In the proposed discovery, PEO also underwent tension but the structural changes are different from the conformations known to date. The PEO nanofibers, obtained by electrospinning and stretched on a metal disk, showed the diffraction peaks at $2\theta = 19^\circ$, 23° (typical for semi-crystalline PEO) and $2\theta = 43.75^\circ$ (not typical for PEO) in an x-ray diffraction analysis. X-ray diffraction analysis was carried out using the powder X-ray diffraction, which showed an intense diffraction peak at $2\theta = 43.75^\circ$, previously not reported.

Initially, the effect of KIO_3 on the structural confirmation of PEO was investigated. The results show that KIO_3 has no impact on structural conformation or the degree of crystallinity of PEO. Then, PXRD analysis was conducted for KIO_3 to explore whether there are changes in the KIO_3 crystal structure after electrospinning. KIO_3 is an inorganic compound, which at atmospheric pressure undergoes five phase transitions with temperature change and all phases are ferroelectric, except phase I (**Figure A4.1**). It has a triclinic structure (P1) with very pronounced pseudorhombohedral symmetry at room temperature (phase III).

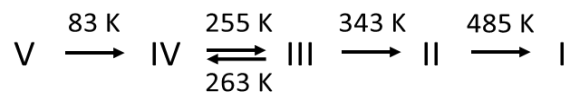


Figure A4.1. Five phase transitions of KIO_3 under atmospheric pressure with temperature change. The data was adopted from references.

The PXRD patterns of pure KIO_3 were compared with the simulated PXRD patterns of KIO_3 from the atomic positional parameters of KIO_3 using The Cambridge Crystallographic Data Centre (CCDC) Mercury 3.7 software. The atomic positional parameters of KIO_3 , which were determined by neutron powder-profile-structure refinement with wavelength 1.9090 \AA , were taken from the work of Lucas [170, 171] and Belokoneva [465]. The PXRD patterns of pure PEO were reconstructed from the crystallographic information file, which was downloaded from the CCDC official website, using CCDC Mercury 3.7 software. The obtained simulated PXRD pattern was then compared with the PXRD patterns of PEO used in this experiment.

Materials and methods

Materials and characterization techniques

PEO ($M_w = 6 \times 10^5 \text{ g/mol}$) and KIO_3 . Samples were characterized using SEM and PXRD.

Experimental part

PEO nanofibre preparation. PEO was dissolved in Milli Q water and electrospun subsequently. The concentration of the electrospun solution was 5 w/v %. The EPPs: 150 mm – 0.1 mL/h – 16-17kV.

PEO loaded KIO_3 nanofibre preparation. PEO and KIO_3 were dissolved in Milli Q water in different w/w % in order to produce solid fibres containing 0.4% – 43% w/w KIO_3 . The solid content concentration of the electrospun solutions were 5% and 7% w/v. The EPPs: 150 mm – 0.1 ml/h – 12 to 25 kV.

Placing samples in sample holder:

1) *To obtain its own, correct diffraction of poly (ethylene oxide) on an X-ray diffractogram.*

The nanofibre is removed from the aluminium foil carefully, without stretching the nanofibre mat, then folded into several layers with tweezers on a special metal sample holder (disk) with zero background and incorporated onto a spinner stage;

2) *To obtain a non-characteristic for poly (ethylene) oxide diffraction peak on an X-ray diffractogram when applying a tension force.* The nanofibre is removed from the aluminium foil carefully, without stretching the nanofibre mat, then stretched over the metal disc used for X-ray analysis into a single layer.

Results and Discussions

Figure A4.2 shows SEM images of electrospun nanofibres of PEO. As described in **Chapter 3**, PEO nanofibres have a uniform diameter range between 50 nm and 1.2 μm .

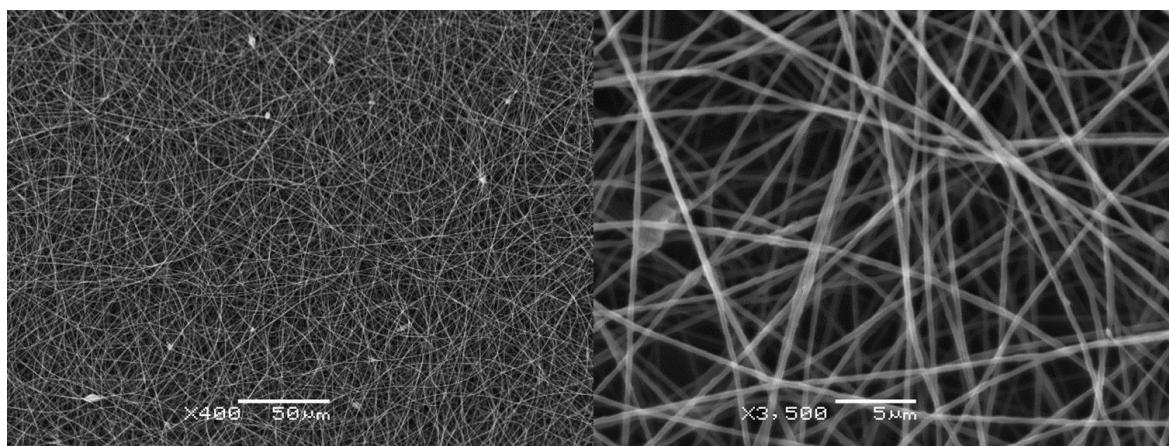


Figure A4.2. SEM images of electrospun PEO nanofibres (the right side is increased magnification).

Figure A4.3 shows the PXRD diffraction pattern of electrospun nanofibres of PEO. Under mechanical stretching, the conformations of PEO chains in the fibres show significant difference. As seen in **Figure A4.3b**, upon applying mechanical stretching to the PEO fibre mats, as indicated with a red arrow, an intensive peak at $2\theta = 43.75^\circ$ is clearly seen. After releasing the fibre mat from stretching, the relaxed fibre mat shows the absence of this peak

(Figure A4.3a). Although this peak has not been reported in the literature, we anticipated that this peak can be associated with the changes of structural conformation of the PEO chain.

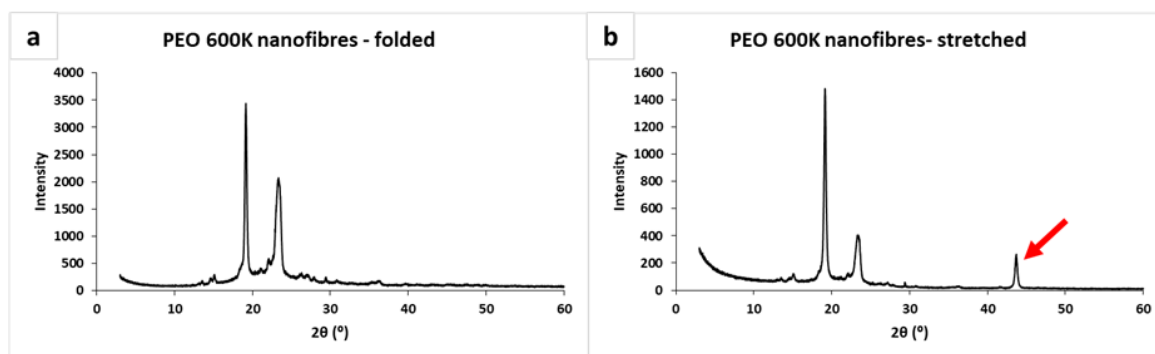


Figure A4.3. PXRD diffraction patterns of the electrospun nanofibres: a) folded; b) stretched.

At the beginning, we conducted PXRD analysis for PEO loaded with 0.4 w/w % of KIO_3 but with different polymer concentrations, namely 5 w/v % and 7 w/v %. As can be seen in **Figure A4.4**, the results show intensive peaks at $2\theta = 43.75^\circ$ and less intensive peaks at $2\theta = 19^\circ, 23^\circ$ for the sample with 5 w/v % solution concentration. In contrast, a less intensive peak at $2\theta = 43.75^\circ, 23^\circ$ and a very intensive peak at $2\theta = 19^\circ$ were shown for the sample with 7 w/v % solution concentration. We anticipated that potassium iodate might affect the conformational changes in PEO because the concentration of KIO_3 in the sample with 5 w/v % solution concentration is higher than in the sample with 7 w/v % solution concentration. Therefore, we conducted PXRD analysis for electrospun nanofibres loaded with KIO_3 in which the concentration was increased gradually from 0 to 43 w/w %.

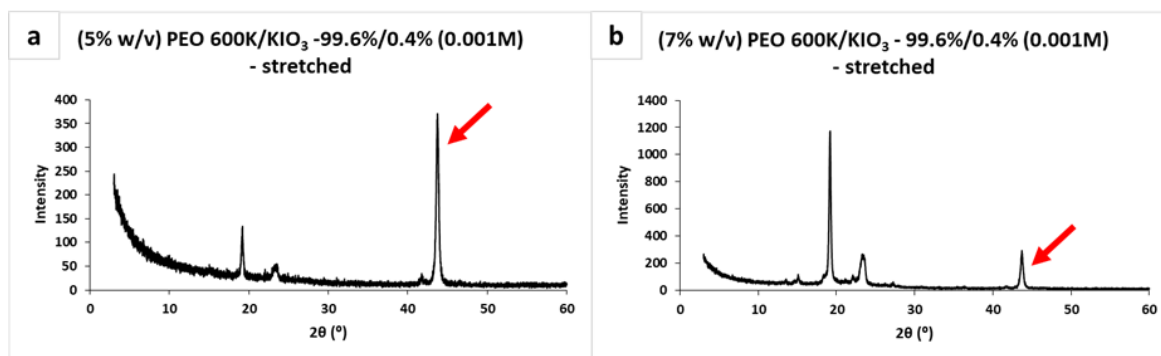


Figure A4.4. PXRD diffraction patterns of the stretched PEO electrospun nanofibres loaded with 0.4 w/w % KIO_3 : a) the solution concentration is 5 w/v %; b) the solution concentration is 7 w/v %.

Figures A4.5 represents PXRD diffraction patterns of the stretched electrospun nanofibres loaded with KIO_3 with the concentration ranging from 0 to 43 w/w % and the solution concentration is 5 w/v % for all samples. However, as can be seen from the obtained results, there is no correlation between KIO_3 content and the intensity of diffraction peaks. The intensity of diffraction peaks was not related to KIO_3 content. High content of KIO_3 did not result in strong or weak intensities, or vice versa. The intensities were random. In addition, it was not clear what caused the origin of the intensive peak at $2\theta = 43.75^\circ$, because the PEO powder does not exhibit it (**Figure A4.7**) and it does not exist in the literature. We anticipated that this might be due to electrospinning. Kim et al. [323] reported that PEO was transformed from 7/2 helical conformation in the normal state to planar zigzag conformation due to high extensional flow caused by electrospinning. However, in our case the ATR-FT IR analysis did not reveal such changes. In addition, Takahashi et al. [459] reported that planar zigzag conformation resulted in a halo at $2\theta \approx 21^\circ$ and $2\theta \approx 24^\circ$ - 25° in PXRD analysis. Then we anticipated that we might be destroying the PEO conformation by stretching the nanofibres onto the PXRD sample holder. Therefore, we conducted PXRD analysis for pure PEO electrospun nanofibres without KIO_3 for the stretched sample and folded sample: the results are shown in **Figure A4.3**, and we found that the intensive peak at $2\theta = 43.75^\circ$ is present in the stretched sample and absent in the folded sample. Additionally, we conducted PXRD analysis for PEO nanofibres loaded with 0.4 and 43 w/w % of KIO_3 and with one sample stretched onto the PXRD sample holder and another with the same formulations but accurately folded and placed in the PXRD sample holder. As can be seen in **Figures A4.6c, d**,

all diffraction patterns associated with PEO and KIO_3 exist. However, in **Figures A4.6b, d** there is one intensive peak at $2\theta = 43.75^\circ$ which is seen for the stretched sample and is not seen in **Figures A4.6a, c** for the folded sample. Therefore, we concluded that the origin of the diffraction peak at $2\theta = 43.75^\circ$ is associated with conformational changes during stretching, not because of electrospinning or KIO_3 presence. The degree of conformational changes is related to the force of applying stretching. The higher the force of applied stretching, the higher the degree of conformational changes. PXRD analysis for all samples studied in **Chapter 3** are given in Figure A4.7.

The reason we stretched the nanofibre onto the PXRD sample holder was because we wanted to have a plateau surface to get better results. However, it was a mistake; nanofibres should be folded and placed on a sample holder without stretching. Caution should be taken when peeling off the nanofibres from the Al foil to place in a sample holder to measure with PXRD, as weak stretching during peeling off may also cause conformational changes. Thus we anticipated that the other polymers that were presented in Takahashi et al. [459] work as polymers that undergo crystal transition due to stretching and may also exhibit new structural conformation changes if electrospun and tension force is applied. Additional experimental work needs to be conducted.

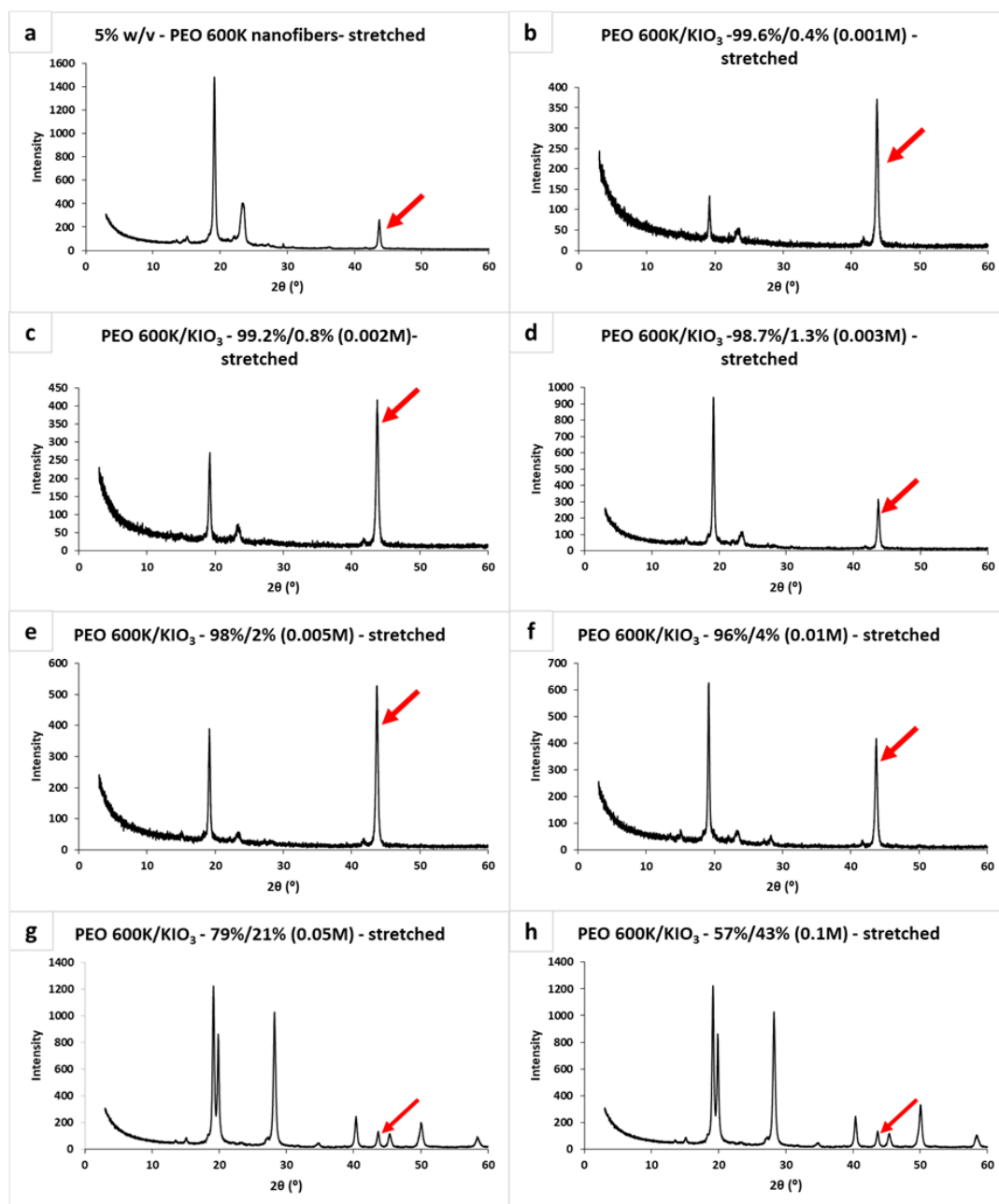


Figure A4.5. PXRD diffraction patterns of the stretched PEO electrospun nanofibres loaded with: a) 0 w/w % KIO_3 ; b) 0.4 w/w % KIO_3 ; c) 0.8 w/w % KIO_3 ; d) 1.3 w/w % KIO_3 ; e) 2 w/w % KIO_3 ; f) 4 w/w % KIO_3 ; g) 21 w/w % KIO_3 ; h) 43 w/w % KIO_3 . The solution concentration is 5 w/v %.

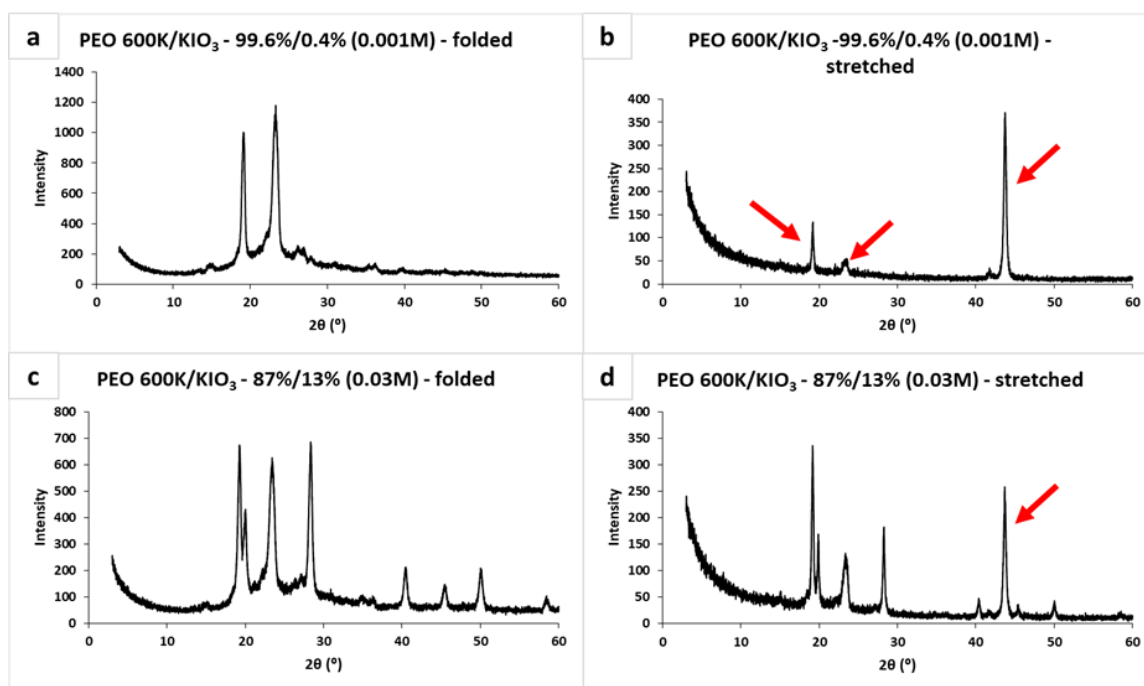


Figure A4.6. PXRD diffraction patterns of PEO electrospun nanofibres loaded with: a) 0.4 w/w % KIO_3 – folded; b) 0.4 w/w % KIO_3 – stretched; c) 13 w/w % KIO_3 – folded; d) 13 w/w % KIO_3 – stretched. The solution concentration is 5 w/v %.

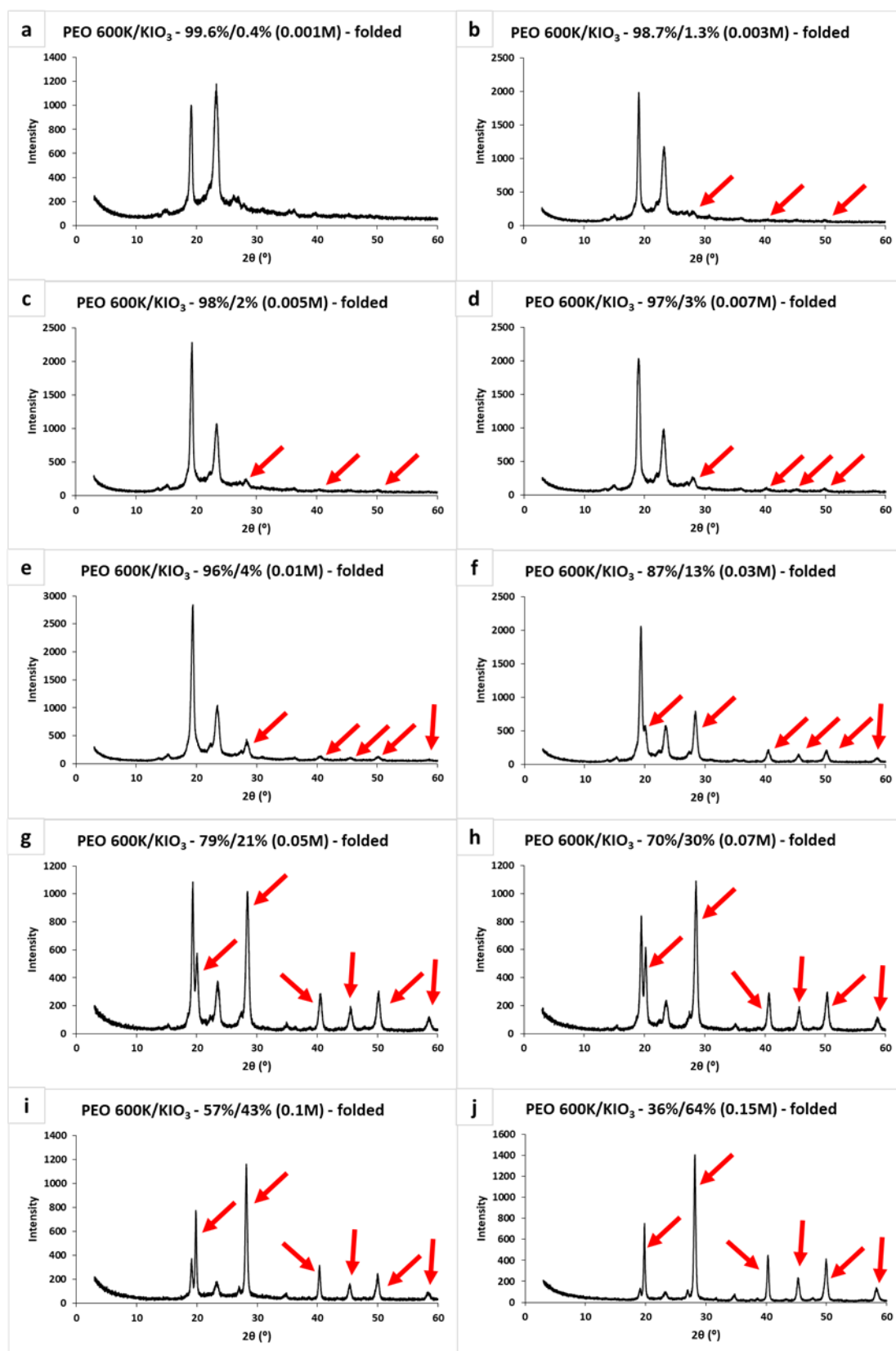


Figure A4.7. PXRD diffraction patterns of the folded PEO electrospun nanofibres loaded with: a) 0.4 w/w % KIO_3 ; b) 1.3 w/w % KIO_3 ; c) 2 w/w % KIO_3 ; d) 3 w/w % KIO_3 ; e) 4 w/w % KIO_3 ; f)

13 w/w % KIO_3 ; g) 21 w/w % KIO_3 ; i) 43 w/w % KIO_3 ; j) 64 w/w % KIO_3 . The solution concentration was 5 w/v %. The red arrows indicate the diffraction peaks of KIO_3 .

PEO has two PXRD diffraction patterns in CCDC: one has P1 space group and the other $\text{P2}_1/\text{a}$ space group (**Figures A4.7b, c**). Both were reported by Takahashi et al. [459, 466]. The PEO used in this study belongs to $\text{P2}_1/\text{a}$ space group as its PXRD pattern is similar to the PXRD pattern of PEO 600K (**Figure A4.7a**).

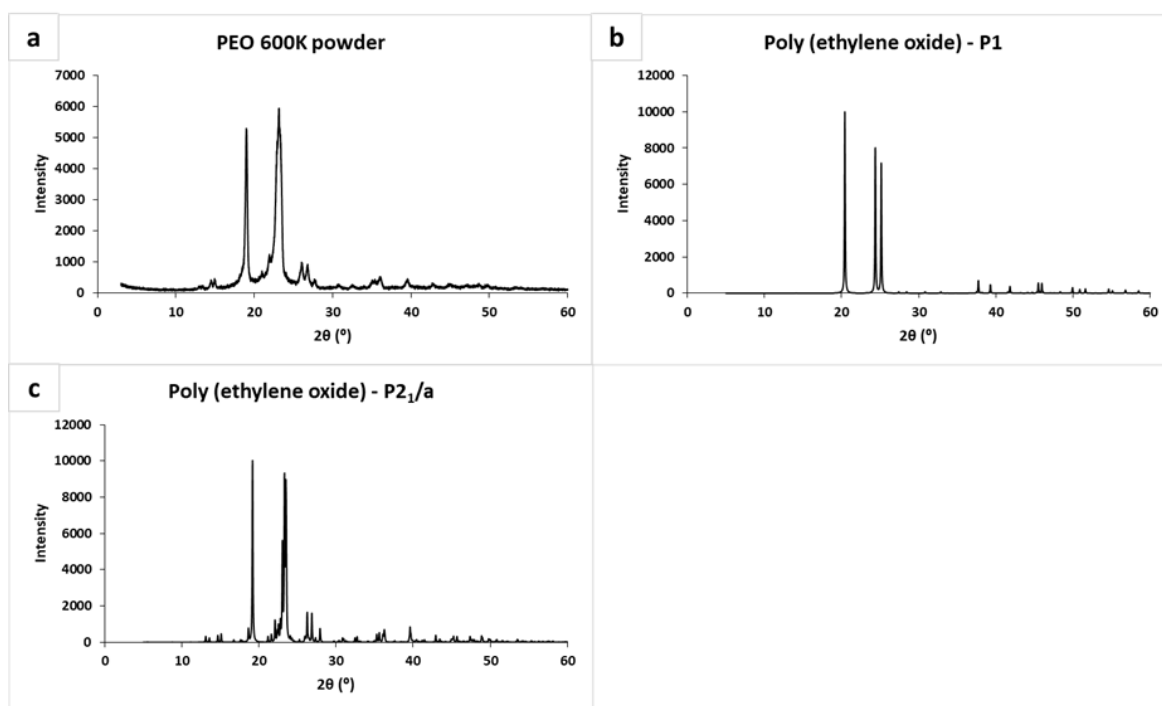


Figure A4.7. PXRD diffraction patterns of pure PEO 600K powder: a) PEO 600K used in this study; b) PEO with P1 space group reported by Takahashi et al. [459]; c) PEO with $\text{P2}_1/\text{a}$ space group reported by Takahashi et al. [466].

Various space groups have been reported for potassium iodate. The crystal systems, space groups and cell constant of KIO_3 were summarized by Crane in his work up until 1972 [467]. Lucas, in his work from 1984 and 1985, reported that phase III, IV and V belong to P1 (triclinic, $Z = 4$) space group [171]. In 1987, Byrom and Lucas suggested that the transition from phase III to phase I (from triclinic (pseudo-rhombohedral) to rhombohedral (pseudo-cubic)) is the only structural transition that occurs in the temperature range of 10K to 523K [468]. Kasatani et al. [469] reported that the space group of KIO_3 is as follows: the phase I belongs to R3m (rhombohedral, $Z = 2$), the phase II belongs to Cm (monoclinic, $Z = 8$), phase III belongs to P1

(triclinic, $Z = 4$). Belokoneva et al. [465] reported that KIO_3 belongs to R3 space group (trigonal crystal system) at 293K. Naray-Szabo and Kalman [470] reported that several modifications of KIO_3 can exist together at room temperature. Therefore, we reconstructed PXRD patterns of three phases (**Figure A4.8**) and found that the KIO_3 used in this study has the same PXRD pattern as the PXRD pattern of the trigonal crystal system at 293K reported by Belokoneva [465] and the triclinic crystal system at 100K reported by Lucas [171]. The KIO_3 used in this study belongs to R3 space group (trigonal crystal system) because the PXRD analysis of KIO_3 used in this study was obtained at room temperature and it cannot undergo any phase transitions (**Figure A4.8**). KIO_3 with an R3 space group has diffraction peaks at $2\theta = 19.8^\circ, 28^\circ, 35^\circ, 40^\circ, 45^\circ, 50^\circ, 58^\circ$. Phase IV KIO_3 has diffraction peaks at $2\theta = 19.9^\circ, 28^\circ, 35^\circ, 40^\circ, 45^\circ, 50^\circ, 59^\circ$. Phase III KIO_3 has diffraction peaks at $2\theta = 13.9^\circ, 19.8^\circ, 24^\circ, 28^\circ, 31.78^\circ, 35^\circ, 37.78^\circ, 40^\circ, 43^\circ, 45^\circ, 50^\circ, 58^\circ$. Phase V KIO_3 has diffraction peaks at $2\theta = 14^\circ, 19.9^\circ, 25^\circ, 28^\circ, 32^\circ, 35^\circ, 38^\circ, 40^\circ, 45^\circ, 50^\circ, 59^\circ$.

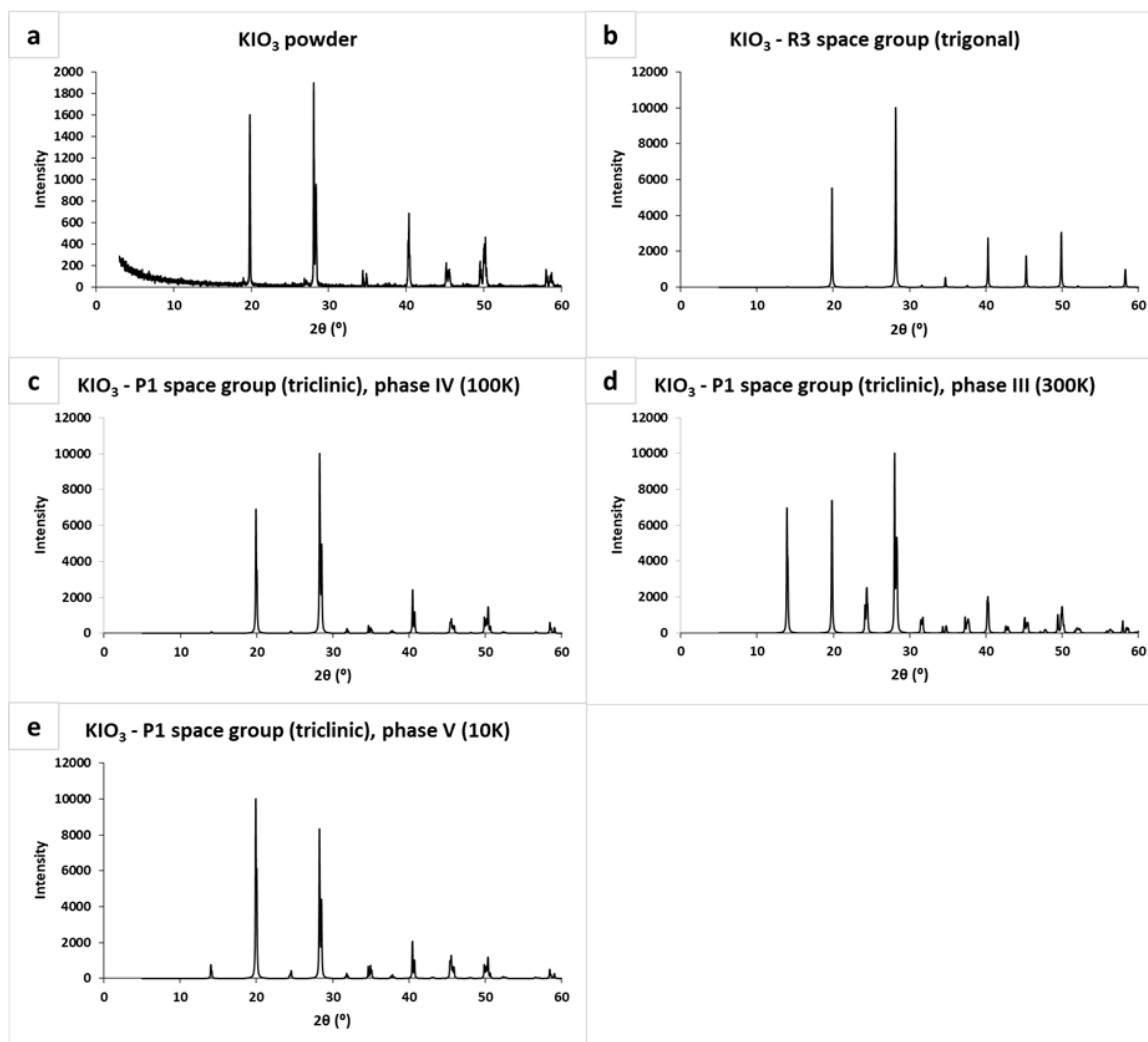


Figure A4.8. PXR D diffraction patterns of pure KIO_3 : a) used in this study; b) simulated PXR D diffraction patterns of pure KIO_3 from atomic positional parameters of KIO_3 taken from Belokoneva et al. [465]; c) simulated PXR D diffraction patterns of pure KIO_3 from atomic positional parameters of KIO_3 taken from Lucas [171]; d) simulated PXR D diffraction patterns of pure KIO_3 from atomic positional parameters of KIO_3 taken from Lucas [170]; e) simulated PXR D diffraction patterns of pure KIO_3 from atomic positional parameters of KIO_3 taken from Lucas [171].

We conducted PXR D analysis for a physical mixture of PEO and KIO_3 , 50/50 w/w % in order to see the difference in PXR D patterns of the physical mixture and the electrospun processed sample and to observe if there are any changes. As can be seen in **Figure A4.9**, there is no difference in the PXR D patterns of PEO and KIO_3 , except for the intensity, which is higher for

the electrospun sample. All characteristic peaks of PEO and KIO_3 exist in both the physical mixture and electrospun sample.

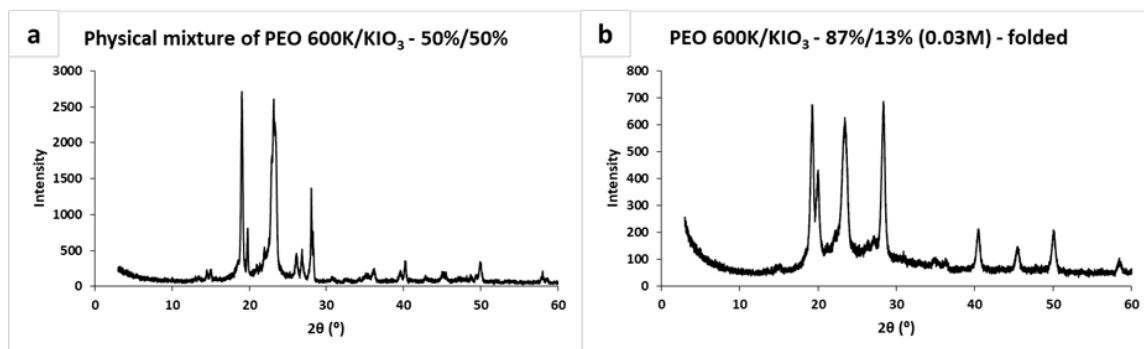


Figure A4.9. PXRD diffraction patterns of physical mixture of PEO 600K powder and KIO_3 powder, 50/50 w/w % compared with PEO loaded KIO_3 nanofibres.

Conclusion

The PXRD analysis of stretched PEO electrospun nanofibres show a sharp peak at $2\theta=43.75^\circ$, not typical for PEO. We anticipated that this is attributed to a new crystalline conformation of PEO in a stretched state, which is different from that reported by Takahashi et al. [459, 466]. In order to confirm the nature of confirmation, ATR FT-IR and scanning tunnelling microscopy should be further conducted.

8 Publication

Rustemkyzy, C., Belton, P. and Qi, S., 2015. Preparation and characterization of ultrarapidly dissolving orodispersible films for treating and preventing iodine deficiency in the pediatric population. *Journal of agricultural and food chemistry*, 63(44), pp.9831-9838

9 References

1. Nyaradi, A., et al., *The role of nutrition in children's neurocognitive development, from pregnancy through childhood*. *Frontiers in Human Neuroscience*, 2013. **7**(97).
2. Semba, R.D., *The Historical Evolution of Thought Regarding Multiple Micronutrient Nutrition*-. *The Journal of nutrition*, 2011. **142**: p. 143S-156S.
3. Moyer, V.A., *Vitamin, mineral, and multivitamin supplements for the primary prevention of cardiovascular disease and cancer: US Preventive Services Task Force recommendation statement*. *Annals of internal medicine*, 2014. **160**: p. 558-564.
4. Anonymous. *Micronutrients. What is the role of micronutrients in nutrition?* UNICEF 2018 [cited 2018, 11-Sep.]; Available from: https://www.unicef.org/nutrition/index_iodine.html.
5. Anonymous. *The global prevalence of anaemia in 2011*. WHO 2011 [cited 2018, 24-Sep.]; Available from: http://apps.who.int/iris/bitstream/handle/10665/177094/9789241564960_eng.pdf;jsessionid=D6D4581E3E30B13E17E9096D0909ACB7?sequence=1.
6. Anonymous. *World hunger and poverty facts and statistics*. World Hunger 2013 [cited 2013 02-Dec.]; Available from: https://www.worldhunger.org/articles/Learn/old/world%20hunger%20facts%202002_2012version.htm.
7. Wessells, K.R. and K.H. Brown, *Estimating the global prevalence of zinc deficiency: results based on zinc availability in national food supplies and the prevalence of stunting*. *PloS one*, 2012. **7**: p. e50568.
8. Mejia, L.A., *Fortification of foods: historical development and current practices*. *Food and Nutrition Bulletin (UNU)*. 1994.
9. Joint, F.A.O. and W.H. Organization, *Vitamin and mineral requirements in human nutrition*. 2005: Geneva: World Health Organization.
10. Zimmermann, M.B., *Iodine requirements and the risks and benefits of correcting iodine deficiency in populations*. *Journal of Trace Elements in Medicine and Biology*, 2008. **22**: p. 81-92.
11. Trentmann, C., I. Reinhard, and L. Vierck. *Supplementation, Food Fortification and Dietary Diversification: A Three-Pronged Approach to Reducing Hidden Hunger*. BMZ May 2012 [cited 2018, 10-Sep.]; Available from: https://www.bmz.de/en/zentrales_downloadarchiv/themen_und_schwerpunkte/ernaehrung/food_fortification.pdf.
12. Mason, P., *Dietary supplements*. 2012: Pharmaceutical Press.
13. Webster-Gandy, J., A. Madden, and M. Holdsworth, *Oxford handbook of nutrition and dietetics*. 2011.
14. Mason, P., *Nutrition and dietary advice in the pharmacy.*, no Ed. 2. 2000: Blakwell Science Ltd.
15. Campbell, B., M. Spano, and C. Association, *NSCA's Guide to Sport and Exercise Nutrition*. 2011: Human Kinetics.
16. Turley, J. and J. Thompson, *Nutrition your life science*. 2013: Cengage Learning.
17. Kapalka, G.M., *Nutritional and herbal therapies for children and adolescents: A handbook for mental health clinicians*. 2009: Academic Press.
18. Anonymous. *Dietary recommendations/Nutritional requirements list of publications*. WHO 2018 [cited 2018, 23-Sep.]; Available from: <http://www.who.int/nutrition/publications/nutrientrequirements/en/index.html>.
19. Anonymous. *Nutritional supplements*. *Medical Dictionary* 2018 [cited 2018, 23-Sep.]; Available from: <http://medical-dictionary.thefreedictionary.com/Nutritional+Supplements>.
20. Yen, P.M., *Physiological and molecular basis of thyroid hormone action*. *Physiological reviews*, 2001. **81**: p. 1097-1142.

21. Bürgi, H., *Iodine excess*. Best Practice & Research Clinical Endocrinology & Metabolism, 2010. **24**: p. 107-115.
22. Hess, S.Y., *Iodine: Physiology, Dietary Sources, and Requirements*, 2013, Encyclopedia of Human Nutrition. vol. 3, p. 33-38.
23. Andersson, M., V. Karumbunathan, and M.B. Zimmermann, *Global iodine status in 2011 and trends over the past decade*. The Journal of nutrition, 2012. **142**: p. 744-750.
24. Zimmermann, M.B., P.L. Jooste, and C.S. Pandav, *Iodine-deficiency disorders*. The Lancet, 2008. **372**: p. 1251-1262.
25. Vanderpump, M.P.J., et al., *Iodine status of UK schoolgirls: a cross-sectional survey*. The Lancet, 2011. **377**: p. 2007-2012.
26. Andersson, M., et al., *Iodine deficiency in Europe: a continuing public health problem*. 2007.
27. Bath, S.C., et al., *Iodine deficiency in pregnant women living in the South East of the UK: the influence of diet and nutritional supplements on iodine status*. British Journal of Nutrition, 2014. **111**: p. 1622-1631.
28. Williamson, C., M.E.J. Lean, and E. Combet, *Dietary recommendations and iodine awareness among mothers in the UK*. The Proceedings of the Nutrition Society, 2012. **71**.
29. Lampropoulou, M., M.E.J. Lean, and E. Combet, *Iodine status of women of childbearing age in Scotland*. The Proceedings of the Nutrition Society, 2012. **71**.
30. Bouga, M., et al., *Iodine intake and excretion are low in British breastfeeding mothers*. The Proceedings of the Nutrition Society, 2015. **74**.
31. Bath, S.C., et al., *Effect of inadequate iodine status in UK pregnant women on cognitive outcomes in their children: results from the Avon Longitudinal Study of Parents and Children (ALSPAC)*. The Lancet, 2013. **382**: p. 331-337.
32. Agarwal, S. and A. Greiner, *On the way to clean and safe electrospinning—green electrospinning: emulsion and suspension electrospinning*. Polymers for Advanced Technologies, 2011. **22**: p. 372-378.
33. Andersson, M. and M. Zimmermann, *Global iodine nutrition: a remarkable leap forward in the past decade*. IDD Newsletter, 2012. **40**: p. 1-5.
34. Anonymous. *Iodine supplements*. ICCIDD 2013 [cited 2013, 01-Dec.]; Available from: <http://www.ign.org/>.
35. Vishwanath, S., *Introduction to clinical nutrition*. 2012: CRC Press.
36. Holt, R.I.G. and N.A. Hanley, *Essential endocrinology and diabetes*. Vol. 41. 2012: John Wiley & Sons.
37. Stipanuk, M.H., *Biochemical, Physiological, Molecular Aspects of Human Nutrition, 2nd edn*, *Sunders*. 2006: Elsevier., St. Louis.
38. Mahan, L., S. Escott Stump, and J.L. Raymond, *Krause's Food & the Nutrition Care Process, (Krause's Food & Nutrition Therapy)*. Philadelphia: WB Saunders. 2012: Elsevier.
39. Taurog, A., E.M. Howells, and H.I. Nachimson, *Conversion of iodate to iodide in vivo and in vitro*. Journal of Biological Chemistry, 1966. **241**(20): p. 4686-4693.
40. Hess, S.Y., *The impact of common micronutrient deficiencies on iodine and thyroid metabolism: the evidence from human studies*. Best Practice & Research Clinical Endocrinology & Metabolism, 2010. **24**: p. 117-132.
41. Zimmermann, *Interactions of vitamin A and iodine deficiencies: effects on the pituitary-thyroid axis*. International journal for vitamin and nutrition research, 2007. **77**: p. 236-240.
42. Strain, J.J. and K.D. Cashman, *Minerals and trace elements*. Introduction to human nutrition. 2009: Blackwell Publishing Oxford, UK. 188-237.
43. Sarandöl, E., et al., *Oxidative stress and serum paraoxonase activity in experimental hypothyroidism: effect of vitamin E supplementation*. Cell Biochemistry and Function: Cellular biochemistry and its modulation by active agents or disease, 2005. **23**: p. 1-8.
44. Boccardi, V., et al., *Vitamin E family: role in the pathogenesis and treatment of Alzheimer's disease*. Alzheimer's & Dementia: Translational Research & Clinical Interventions, 2016. **2**: p.

- 182-191.
45. Peh, H.Y., et al., *Vitamin E therapy beyond cancer: Tocopherol versus tocotrienol*. Pharmacology & therapeutics, 2016. **162**: p. 152-169.
 46. Bartosińska, E., M. Buszewska-Forajta, and D. Siluk, *GC–MS and LC–MS approaches for determination of tocopherols and tocotrienols in biological and food matrices*. Journal of pharmaceutical and biomedical analysis, 2016. **127**: p. 156-169.
 47. Galli, F., et al., *Vitamin E: Emerging aspects and new directions*. Free Radical Biology and Medicine, 2017. **102**: p. 16-36.
 48. Guo, Y., et al., *The applications of Vitamin E TPGS in drug delivery*. European Journal of Pharmaceutical Sciences, 2013. **49**: p. 175-186.
 49. Zhang, Z., S. Tan, and S.-S. Feng, *Vitamin E TPGS as a molecular biomaterial for drug delivery*. Biomaterials, 2012. **33**: p. 4889-4906.
 50. Duhem, N., F. Danhier, and V. Préat, *Vitamin E-based nanomedicines for anti-cancer drug delivery*. Journal of Controlled Release, 2014. **182**: p. 33-44.
 51. Authority, E.F.S., *D-alpha-tocopheryl polyethylene glycol 1000 succinate (tpgs) in use for food for particular nutritional purposes*. EFSA J, 2007. **490**: p. 1-20.
 52. Beken, S. and E.U. Kabataş, *Fish Oil and The Retinopathy of Prematurity*, in *Fish and Fish Oil in Health and Disease Prevention*. 2016, Elsevier. p. 115-118.
 53. SanGiovanni, J.P. and E.Y. Chew, *The role of omega-3 long-chain polyunsaturated fatty acids in health and disease of the retina*. Progress in retinal and eye research, 2005. **24**(1): p. 87-138.
 54. Anonymous, *Dietary reference intakes for energy, carbohydrate, fiber, fat, fatty acids, cholesterol, protein and amino acids*. Institute of Medicine. 2002, Washington, D.C.: National Academies Press.
 55. Watson, R.R. and F. De Meester, *Handbook of lipids in human function: fatty acids*. 2015: Elsevier.
 56. Anonymous. *Omega-3 Fatty Acids. Fact Sheet for Health Professionals*. National Institute of Health: Office of Dietary Supplement. U.S. Department of Health and Human Services. 2018 [cited 2018, 10-Sep.]; Available from: <https://ods.od.nih.gov/factsheets/Omega3FattyAcids-HealthProfessional/>.
 57. Ruxton, C.H.S., et al., *The health benefits of omega-3 polyunsaturated fatty acids: a review of the evidence*. Journal of Human Nutrition and Dietetics, 2004. **17**: p. 449-459.
 58. Simopoulos, A.P., *The importance of the ratio of omega-6/omega-3 essential fatty acids*. Biomedicine & pharmacotherapy, 2002. **56**: p. 365-379.
 59. Ruiz Ruiz, J.C., E.D.L.L. Ortiz Vazquez, and M.R. Segura Campos, *Encapsulation of vegetable oils as source of omega-3 fatty acids for enriched functional foods*. Critical reviews in food science and nutrition, 2017. **57**: p. 1423-1434.
 60. Lane, K.E. and E.J. Derbyshire, *Omega-3 fatty acids—a review of existing and innovative delivery methods*. Critical reviews in food science and nutrition, 2018. **58**: p. 62-69.
 61. Anonymous. *WHO Collaboration Center for Drug Statistics Methodology*. WHOCC [cited 2018, 29-Aug.]; Available from: <https://www.whocc.no/>.
 62. Amidon, G.L., et al., *A theoretical basis for a biopharmaceutical drug classification: the correlation of in vitro drug product dissolution and in vivo bioavailability*. Pharmaceutical research, 1995. **12**: p. 413-420.
 63. Anonymous. *Anatomical Therapeutic Chemical (ATC) Classification*. WHO [cited 2018, 29-Aug.]; Available from: https://www.who.int/medicines/regulation/medicines-safety/toolkit_atc/en/.
 64. Dressman, J.B. and H. Lennernas, *Oral drug absorption: Prediction and assessment*. 2000: CRC Press.
 65. Baghel, S., H. Cathcart, and N.J. O'Reilly, *Polymeric amorphous solid dispersions: a review of amorphization, crystallization, stabilization, solid-state characterization, and aqueous solubilization of biopharmaceutical classification system class II drugs*. Journal of

- pharmaceutical sciences, 2016. **105**: p. 2527-2544.
66. Wu, C.-Y. and L.Z. Benet, *Predicting drug disposition via application of BCS: transport/absorption/elimination interplay and development of a biopharmaceutics drug disposition classification system*. *Pharmaceutical research*, 2005. **22**: p. 11-23.
 67. Kawabata, Y., et al., *Formulation design for poorly water-soluble drugs based on biopharmaceutics classification system: basic approaches and practical applications*. *International journal of pharmaceutics*, 2011. **420**: p. 1-10.
 68. Earll, M., *A Guide to log P and pKa Measurements and Their Use*. C chem MRS, 1999: p. 3-4.
 69. Pandey, M.M., et al., *Determination of pKa of felodipine using UV-Visible spectroscopy*. *Spectrochimica Acta Part A: Molecular and Biomolecular Spectroscopy*, 2013. **115**: p. 887-890.
 70. Bhal, S.K. *LogP—Making Sense of the Value*. Advanced Chemistry Development, Inc. 2011 [cited 2018 10-Sep.]; Available from: https://www.acdlabs.com/download/app/physchem/making_sense.pdf.
 71. Sagalowicz, L. and M.E. Leser, *Delivery systems for liquid food products*. *Current Opinion in Colloid & Interface Science*, 2010. **15**: p. 61-72.
 72. Hearnden, V., et al., *New developments and opportunities in oral mucosal drug delivery for local and systemic disease*. *Advanced drug delivery reviews*, 2012. **64**: p. 16-28.
 73. Vo, C.L.-N., C. Park, and B.-J. Lee, *Current trends and future perspectives of solid dispersions containing poorly water-soluble drugs*. *European Journal of Pharmaceutics and Biopharmaceutics*, 2013. **85**: p. 799-813.
 74. Zhou, L., et al., *Microsol-electrospinning for controlled loading and release of water-soluble drugs in microfibrinous membranes*. *RSC Advances*, 2014. **4**: p. 43220-43226.
 75. Khan, S., et al., *Formulation, characterisation and stabilisation of buccal films for paediatric drug delivery of omeprazole*. *AAPS PharmSciTech*, 2015. **16**: p. 800-810.
 76. Anonymous. *Report of the informal Expert Meeting on Dosage Forms of Medicines for Children*. WHO 2008 [cited 2018, 10-Sep.]; Available from: http://www.who.int/selection_medicines/committees/expert/17/application/paediatric/Dosage_form_reportDEC2008.pdf.
 77. Kalepu, S., M. Manthina, and V. Padavala, *Oral lipid-based drug delivery systems—an overview*. *Acta Pharmaceutica Sinica B*, 2013. **3**: p. 361-372.
 78. Mrsny, R.J., *Oral drug delivery research in Europe*. *Journal of controlled release*, 2012. **161**: p. 247-253.
 79. Gao, L., et al., *Application of drug nanocrystal technologies on oral drug delivery of poorly soluble drugs*. *Pharmaceutical research*, 2013. **30**: p. 307-324.
 80. Ensign, L.M., R. Cone, and J. Hanes, *Oral drug delivery with polymeric nanoparticles: the gastrointestinal mucus barriers*. *Advanced drug delivery reviews*, 2012. **64**: p. 557-570.
 81. Patel, V.F., F. Liu, and M.B. Brown, *Advances in oral transmucosal drug delivery*. *Journal of controlled release*, 2011. **153**: p. 106-116.
 82. Madhav, N.V.S., et al., *Orotransmucosal drug delivery systems: a review*. *Journal of controlled release*, 2009. **140**: p. 2-11.
 83. Anonymous. *Reflection paper: formulations of choice for the paediatric population*. European Medicine Agency, London 2006 [cited 2018, 10-Sep.]; Available from: https://www.ema.europa.eu/documents/scientific-guideline/reflection-paper-formulations-choice-paediatric-population_en.pdf.
 84. Vrana, K.E., K.D. Karpa, and M. Kester, *Elsevier's Integrated Review Pharmacology*. 2012: Elsevier Health Sciences.
 85. Leuner, C. and J. Dressman, *Improving drug solubility for oral delivery using solid dispersions*. *European journal of Pharmaceutics and Biopharmaceutics*, 2000. **50**: p. 47-60.
 86. Huang, Y. and W.-G. Dai, *Fundamental aspects of solid dispersion technology for poorly soluble drugs*. *Acta Pharmaceutica Sinica B*, 2014. **4**: p. 18-25.
 87. Yu, D.-G., et al., *Dissolution improvement of electrospun nanofiber-based solid dispersions for*

- acetaminophen*. *Aaps Pharmscitech*, 2010. **11**: p. 809-817.
88. Craig, D.Q.M., *The mechanisms of drug release from solid dispersions in water-soluble polymers*. *International journal of pharmaceutics*, 2002. **231**: p. 131-144.
 89. Huang, Z.-M., et al., *A review on polymer nanofibers by electrospinning and their applications in nanocomposites*. *Composites science and technology*, 2003. **63**: p. 2223-2253.
 90. Teo, W.E. and S. Ramakrishna, *A review on electrospinning design and nanofibre assemblies*. *Nanotechnology*, 2006. **17**: p. R89.
 91. Bhardwaj, N. and S.C. Kundu, *Electrospinning: a fascinating fiber fabrication technique*. *Biotechnology advances*, 2010. **28**: p. 325-347.
 92. Brettmann, B.K., A.S. Myerson, and B.L. Trout, *Solid-state nuclear magnetic resonance study of the physical stability of electrospun drug and polymer solid solutions*. *Journal of pharmaceutical sciences*, 2012. **101**: p. 2185-2193.
 93. Yu, D.-G., et al., *Oral fast-dissolving drug delivery membranes prepared from electrospun polyvinylpyrrolidone ultrafine fibers*. *Nanotechnology*, 2009. **20**: p. 55104.
 94. Dixit, R.P. and S.P. Puthli, *Oral strip technology: overview and future potential*. *Journal of controlled release*, 2009. **139**: p. 94-107.
 95. Persano, L., et al., *Industrial upscaling of electrospinning and applications of polymer nanofibers: a review*. *Macromolecular Materials and Engineering*, 2013. **298**: p. 504-520.
 96. Forward, K.M. and G.C. Rutledge, *Free surface electrospinning from a wire electrode*. *Chemical Engineering Journal*, 2012. **183**: p. 492-503.
 97. Sambaer, W., M. Zatloukal, and D. Kimmer, *3D modeling of filtration process via polyurethane nanofiber based nonwoven filters prepared by electrospinning process*. *Chemical Engineering Science*, 2011. **66**: p. 613-623.
 98. Wendorff, J.H., S. Agarwal, and A. Greiner, *Electrospinning: materials, processing, and applications*. 2012: John Wiley & Sons.
 99. Ramakrishna, S., et al., *An introduction to electrospinning and nanofibers*. 2005, Singapura: World Scientific.
 100. Jaeger, R., et al., *Electrospinning of ultra-thin polymer fibers*. *Macromolecular Symposia*, 1998. **127**: p. 141-150.
 101. Hu, X., et al., *Electrospinning of polymeric nanofibers for drug delivery applications*. *Journal of Controlled Release*, 2014. **185**: p. 12-21.
 102. Fong, H., I. Chun, and D.H. Reneker, *Beaded nanofibers formed during electrospinning*. *Polymer*, 1999. **40**: p. 4585-4592.
 103. Liu, H. and Y.L. Hsieh, *Ultrafine fibrous cellulose membranes from electrospinning of cellulose acetate*. *Journal of Polymer Science, Part B: Polymer Physics*, 2002. **40**: p. 2119-2129.
 104. Ghorani, B. and N. Tucker, *Fundamentals of electrospinning as a novel delivery vehicle for bioactive compounds in food nanotechnology*. *Food Hydrocolloids*, 2015. **51**: p. 227-240.
 105. Doshi, J. and D.H. Reneker, *Electrospinning process and applications of electrospun fibers*. *Journal of electrostatics*, 1995. **35**: p. 151-160.
 106. Zong, X., et al., *Structure and process relationship of electrospun bioabsorbable nanofiber membranes*. *Polymer*, 2002. **43**: p. 4403-4412.
 107. Huang, C., et al., *Electrospun polymer nanofibres with small diameters*. *Nanotechnology*, 2006. **17**: p. 1558.
 108. Deitzel, J.M., et al., *The effect of processing variables on the morphology of electrospun nanofibers and textiles*. *Polymer*, 2001. **42**: p. 261-272.
 109. Reneker, D.H. and I. Chun, *Nanometre diameter fibres of polymer, produced by electrospinning*. *Nanotechnology*, 1996. **7**: p. 216.
 110. Zhang, C., et al., *Study on morphology of electrospun poly (vinyl alcohol) mats*. *European polymer journal*, 2005. **41**: p. 423-432.
 111. Demir, M.M., et al., *Electrospinning of polyurethane fibers*. *Polymer*, 2002. **43**: p. 3303-3309.
 112. Larrondo, L. and R. St John Manley, *Electrostatic fiber spinning from polymer melts. I.*

- Experimental observations on fiber formation and properties.* Journal of Polymer Science Part B: Polymer Physics, 1981. **19**: p. 909-920.
113. Larrondo, L. and R. St John Manley, *Electrostatic fiber spinning from polymer melts. II. Examination of the flow field in an electrically driven jet.* Journal of Polymer Science Part B: Polymer Physics, 1981. **19**: p. 921-932.
114. Larrondo, L. and R. St John Manley, *Electrostatic fiber spinning from polymer melts. III. Electrostatic deformation of a pendant drop of polymer melt.* Journal of Polymer Science Part B: Polymer Physics, 1981. **19**: p. 933-940.
115. Buchko, C.J., et al., *Processing and microstructural characterization of porous biocompatible protein polymer thin films.* Polymer, 1999. **40**: p. 7397-7407.
116. Megelski, S., et al., *Micro- and nanostructured surface morphology on electrospun polymer fibers.* Macromolecules, 2002. **35**: p. 8456-8466.
117. Lee, J.S., et al., *Role of molecular weight of atactic poly (vinyl alcohol)(PVA) in the structure and properties of PVA nanofabric prepared by electrospinning.* Journal of Applied Polymer Science, 2004. **93**: p. 1638-1646.
118. Mo, X.M., et al., *Electrospun P (LLA-CL) nanofiber: a biomimetic extracellular matrix for smooth muscle cell and endothelial cell proliferation.* Biomaterials, 2004. **25**: p. 1883-1890.
119. Katti, D.S., et al., *Bioresorbable nanofiber-based systems for wound healing and drug delivery: Optimization of fabrication parameters.* Journal of Biomedical Materials Research Part B: Applied Biomaterials, 2004. **70**: p. 286-296.
120. Pawlowski, K.J., et al., *Biomedical nanoscience: electrospinning basic concepts, applications, and classroom demonstration.* MRS Proceedings, 2004. **827**: p. BB1.7.
121. Haghi, A.K. and M. Akbari, *Trends in electrospinning of natural nanofibers.* physica status solidi (a), 2007. **204**: p. 1830-1834.
122. Tan, S.H., et al., *Systematic parameter study for ultra-fine fiber fabrication via electrospinning process.* Polymer, 2005. **46**: p. 6128-6134.
123. Ki, C.S., et al., *Characterization of gelatin nanofiber prepared from gelatin-formic acid solution.* Polymer, 2005. **46**: p. 5094-5102.
124. Zhao, Z., et al., *Preparation and properties of electrospun poly (vinylidene fluoride) membranes.* Journal of applied polymer science, 2005. **97**: p. 466-474.
125. Yamashita, Y., A. Tanaka, and F. Ko, *Electrospinning for the industrial nanofiber technology, in Proceedings of International Fiber Conference, Seoul, Korea.* 2006.
126. Angeles, M., H.L. Cheng, and S.S. Velankar, *Emulsion electrospinning: composite fibers from drop breakup during electrospinning.* Polymers for Advanced Technologies, 2008. **19**: p. 728-733.
127. Xu, X., et al., *Preparation of core-sheath composite nanofibers by emulsion electrospinning.* Macromolecular Rapid Communications, 2006. **27**: p. 1637-1642.
128. Bazilevsky, A.V., A.L. Yarin, and C.M. Megaridis, *Co-electrospinning of core-shell fibers using a single-nozzle technique.* Langmuir, 2007. **23**: p. 2311-2314.
129. Sanders, E.H., et al., *Two-phase electrospinning from a single electrified jet: microencapsulation of aqueous reservoirs in poly (ethylene-co-vinyl acetate) fibers.* Macromolecules, 2003. **36**: p. 3803-3805.
130. Yu, D.-G., et al., *Solid dispersions in the form of electrospun core-sheath nanofibers.* International journal of nanomedicine, 2011. **6**: p. 3271.
131. Sun, Z., et al., *Compound core-shell polymer nanofibers by co-electrospinning.* Advanced materials, 2003. **15**: p. 1929-1932.
132. Kriegel, C., et al., *Nanofibers as carrier systems for antimicrobial microemulsions. Part I: fabrication and characterization.* Langmuir, 2008. **25**: p. 1154-1161.
133. Kriegel, C., et al., *Nanofibers as carrier systems for antimicrobial microemulsions. II. Release characteristics and antimicrobial activity.* Journal of applied polymer science, 2010. **118**: p. 2859-2868.

134. Camerlo, A., et al., *Fragrance encapsulation in polymeric matrices by emulsion electrospinning*. European Polymer Journal, 2013. **49**: p. 3806-3813.
135. Moomand, K. and L.-T. Lim, *Oxidative stability of encapsulated fish oil in electrospun zein fibres*. Food research international, 2014. **62**: p. 523-532.
136. Moomand, K. and L.-T. Lim, *Properties of encapsulated fish oil in electrospun zein fibres under simulated in vitro conditions*. Food and bioprocess technology, 2015. **8**: p. 431-444.
137. García-Moreno, P.J., et al., *Encapsulation of fish oil in nanofibers by emulsion electrospinning: Physical characterization and oxidative stability*. Journal of Food Engineering, 2016. **183**: p. 39-49.
138. García-Moreno, P.J., et al., *Development of carbohydrate-based nano-microstructures loaded with fish oil by using electrohydrodynamic processing*. Food Hydrocolloids, 2017. **69**: p. 273-285.
139. Jiang, Y.-N., H.-Y. Mo, and D.-G. Yu, *Electrospun drug-loaded core–sheath PVP/zein nanofibers for biphasic drug release*. International journal of pharmaceutics, 2012. **438**: p. 232-239.
140. Benschrit, R.C., et al., *Development of oral food-grade delivery systems: current knowledge and future challenges*. Food & function, 2012. **3**: p. 10-21.
141. Augustin, M.A. and Y. Hemar, *Nano-and micro-structured assemblies for encapsulation of food ingredients*. Chemical society reviews, 2009. **38**: p. 902-912.
142. McClements, D.J., *Food emulsions: principles, practices, and techniques*. 2015: CRC press.
143. McClements, D.J., *Non-covalent interactions between proteins and polysaccharides*. Biotechnology advances, 2006. **24**: p. 621-625.
144. Patino, J.M.R. and A.M.R. Pilosof, *Protein–polysaccharide interactions at fluid interfaces*. Food Hydrocolloids, 2011. **25**: p. 1925-1937.
145. Bouyer, E., et al., *Proteins, polysaccharides, and their complexes used as stabilizers for emulsions: alternatives to synthetic surfactants in the pharmaceutical field?* International journal of pharmaceutics, 2012. **436**: p. 359-378.
146. Tolstoguzov, V.B., *Protein-polysaccharide interactions*. FOOD SCIENCE AND TECHNOLOGY-NEW YORK-MARCEL DEKKER-. 1997: MARCEL DEKKER AG. 171-198.
147. Patel, A.R., et al., *Biopolymer-based structuring of liquid oil into soft solids and oleogels using water-continuous emulsions as templates*. Langmuir, 2014. **31**: p. 2065-2073.
148. Tang, X.C. and M.J. Pikal, *Design of freeze-drying processes for pharmaceuticals: practical advice*. Pharmaceutical research, 2004. **21**: p. 191-200.
149. Geidobler, R. and G. Winter, *Controlled ice nucleation in the field of freeze-drying: fundamentals and technology review*. European Journal of Pharmaceutics and Biopharmaceutics, 2013. **85**: p. 214-222.
150. Chan, M. *The global nutrition challenge: getting a healthy start*. WHO 2008 [cited 2018 10-Sep.]; Available from: <https://www.who.int/dg/speeches/2008/20080618/en/>.
151. Anonymous. *Nutrition. What are the challenges?* UNICEF 2003 [cited 2018, 10-Sep.]; Available from: https://www.unicef.org/nutrition/index_challenges.html.
152. Anonymous. *The world health report. Childhood and maternal undernutrition*. WHO 2002 [cited 2018 10-Sep.]; Available from: <https://www.who.int/whr/2002/chapter4/en/index3.html>.
153. Anonymous. *The problem: about iron deficiency*. UNICEF [cited 2018, 10-Sep.]; Available from: https://www.unicef.org/nutrition/23964_iron.html.
154. Stoltzfus, R.J., *Iron deficiency: global prevalence and consequences*. Food and nutrition bulletin, 2003. **24**: p. S99-S103.
155. Finney, E. *Children's medicines: A situational analysis*. WHO 2011 [cited 2018 10-Sep.]; Available from: https://www.who.int/childmedicines/progress/CM_analysis.pdf.
156. Anonymous. *Cancer*. WHO 2018 [cited 2018, 28-Dec.]; Available from: <https://www.who.int/news-room/fact-sheets/detail/cancer>.
157. Rowe, R.C., P.J. Sheskey, and M.E. Quinn, *Handbook of pharmaceutical excipients*. 2009:

- London-Chicago: Pharmaceutical Press.
158. Gao, P., et al., *Swelling of hydroxypropyl methylcellulose matrix tablets. 2. Mechanistic study of the influence of formulation variables on matrix performance and drug release*. Journal of pharmaceutical sciences, 1996. **85**: p. 732-740.
 159. Ma, D., et al., *Development of a HPMC-based controlled release formulation with hot melt extrusion (HME)*. Drug development and industrial pharmacy, 2013. **39**: p. 1070-1083.
 160. Sterling, J.B. and W.R. Heymann, *Potassium iodide in dermatology: a 19th century drug for the 21st century—uses, pharmacology, adverse effects, and contraindications*. Journal of the American Academy of Dermatology, 2000. **43**: p. 691-697.
 161. Kelly, F.C., *Studies on the stability of iodine compounds in iodized salt*. Bulletin of the World Health Organization, 1953. **9**: p. 217.
 162. Chmyrov, A., T. Sandén, and J. Widengren, *Iodide as a Fluorescence Quencher and Promoter - Mechanisms and Possible Implications*. The Journal of Physical Chemistry B, 2010. **114**: p. 11282-11291.
 163. Jeong, K.U., H.S. Lee, and J.S. Hwang, *Effects of short-term potassium iodide treatment for thyrotoxicosis due to Graves disease in children and adolescents*. Annals of pediatric endocrinology & metabolism, 2014. **19**: p. 197-201.
 164. Bahn, R.S., et al., *Hyperthyroidism and other causes of thyrotoxicosis: management guidelines of the American Thyroid Association and American Association of Clinical Endocrinologists*. Thyroid, 2011. **21**: p. 593-646.
 165. Organization, W.H., *Guidelines for iodine prophylaxis following nuclear accidents: update 1999*. Geneva: World Health Organization, 1999
 166. Costa, R.O., et al., *Use of potassium iodide in dermatology: updates on an old drug*. Anais brasileiros de dermatologia, 2013. **88**: p. 396-402.
 167. Organization, W.H., *Cough and cold remedies for the treatment of acute respiratory infections in young children*. 2001.
 168. Lawrence, J.C., *The use of iodine as an antiseptic agent*. Journal of wound care, 1998. **7**: p. 421-425.
 169. Secretariat, W.H.O., et al., *Prevention and control of iodine deficiency in pregnant and lactating women and in children less than 2-years-old: conclusions and recommendations of the Technical Consultation*. Public health nutrition, 2007. **10**: p. 1606-1611.
 170. Lucas, B.W., *Structure (neutron) of room-temperature phase III potassium iodate, KIO₃*. Acta Crystallographica Section C: Crystal Structure Communications, 1984. **40**: p. 1989-1992.
 171. Lucas, B.W., *Structure (neutron) of potassium iodate at 100 and 10 K*. Acta Crystallographica Section C: Crystal Structure Communications, 1985. **41**: p. 1388-1391.
 172. WHO, UNICEF, and ICCIDD, *Assessment of iodine deficiency disorders and monitoring their elimination: a guide for programme managers*. Geneva: World Health Organization, 2007.
 173. Zimmermann, M. and F. Delange, *Iodine supplementation of pregnant women in Europe: a review and recommendations*. European journal of clinical nutrition, 2004. **58**: p. 979.
 174. Wilderjans, E., et al., *Impact of potassium bromate and potassium iodate in a pound cake system*. Journal of agricultural and food chemistry, 2010. **58**: p. 6465-6471.
 175. Marcus, J.B., *Culinary nutrition: the science and practice of healthy cooking*. 2013: Academic Press.
 176. Jiang, X.M., et al., *Dynamics of environmental supplementation of iodine: four years' experience of iodination of irrigation water in Hotien, Xinjiang, China*. Archives of environmental health, 1997. **52**: p. 399-408.
 177. Ren, Q., et al., *An environmental approach to correcting iodine deficiency: supplementing iodine in soil by iodination of irrigation water in remote areas*. Journal of Trace Elements in Medicine and Biology, 2008. **22**: p. 1-8.
 178. Anonymous. *Potassium iodide*. 2008 [cited 2018, 24-Sep]; Available from: <http://www.drugsmarineaquaculture.com/pdf/DrGslodideMSDS.pdf>.

179. Anonymous. *Potassium Iodide*. Sparchem [cited 2018, 24-Sep.]; Available from: <http://www.sparchem.com/msds/7681-11-0.pdf>.
180. Young, J.A., *Potassium Iodate*. Journal of Chemical Education, 2008. **85**: p. 910.
181. Bürgi, H., T.H. Schaffner, and J.P. Seiler, *The toxicology of iodate: a review of the literature*. Thyroid, 2001. **11**: p. 449-456.
182. Chung, H., et al., *Oil components modulate physical characteristics and function of the natural oil emulsions as drug or gene delivery system*. Journal of Controlled Release, 2001. **71**: p. 339-350.
183. Roccia, P., et al., *Influence of spray-drying operating conditions on sunflower oil powder qualities*. Powder Technology, 2014. **254**: p. 307-313.
184. Gunstone, F., *Vegetable oils in food technology: composition, properties and uses*. 2011: John Wiley & Sons.
185. Isbell, T.A., T.P. Abbott, and K.D. Carlson, *Oxidative stability index of vegetable oils in binary mixtures with meadowfoam oil*. Industrial Crops and products, 1999. **9**: p. 115-123.
186. Pharmacopoeia, B., *British Pharmacopoeia* 2018.
187. Goyal, A., et al., *Flax and flaxseed oil: an ancient medicine & modern functional food*. Journal of food science and technology, 2014. **51**: p. 1633-1653.
188. Tonon, R.V., C.R.F. Grosso, and M.D. Hubinger, *Influence of emulsion composition and inlet air temperature on the microencapsulation of flaxseed oil by spray drying*. Food Research International, 2011. **44**: p. 282-289.
189. Tolkachev, O.N. and A.A. Zhuchenko, *Biologically active substances of flax: medicinal and nutritional properties (a review)*. Pharmaceutical Chemistry Journal, 2004. **34**: p. 360-367.
190. Carneiro, H.C.F., et al., *Encapsulation efficiency and oxidative stability of flaxseed oil microencapsulated by spray drying using different combinations of wall materials*. Journal of Food Engineering, 2013. **115**: p. 443-451.
191. Goyal, A., et al., *Development and physico-chemical characterization of microencapsulated flaxseed oil powder: A functional ingredient for omega-3 fortification*. Powder Technology, 2015. **286**: p. 527-537.
192. Karaca, A.C., M. Nickerson, and N.H. Low, *Microcapsule production employing chickpea or lentil protein isolates and maltodextrin: Physicochemical properties and oxidative protection of encapsulated flaxseed oil*. Food chemistry, 2013. **139**: p. 448-457.
193. Fioramonti, S.A., A.C. Rubiolo, and L.G. Santiago, *Characterisation of freeze-dried flaxseed oil microcapsules obtained by multilayer emulsions*. Powder Technology, 2017. **319**: p. 238-244.
194. Kaushik, P., et al., *Microencapsulation of flaxseed oil in flaxseed protein and flaxseed gum complex coacervates*. Food research international, 2016. **86**: p. 1-8.
195. Piroddi, M., et al., *Nutrigenomics of extra-virgin olive oil: A review*. Biofactors, 2017. **43**: p. 17-41.
196. Waterman, E. and B. Lockwood, *Active components and clinical applications of olive oil*. Alternative medicine review, 2007. **12**.
197. Yang, J. and O.N. Ciftci, *Encapsulation of fish oil into hollow solid lipid micro-and nanoparticles using carbon dioxide*. Food chemistry, 2017. **231**: p. 105-113.
198. Cleland, L.G., M.J. James, and S.M. Proudman, *The role of fish oils in the treatment of rheumatoid arthritis*. Drugs, 2003. **63**: p. 845-853.
199. García-Moreno, P.J., et al., *Physical and oxidative stability of fish oil-in-water emulsions stabilized with fish protein hydrolysates*. Food chemistry, 2016. **203**: p. 124-135.
200. Ghorbanzade, T., et al., *Nano-encapsulation of fish oil in nano-liposomes and its application in fortification of yogurt*. Food chemistry, 2017. **216**: p. 146-152.
201. Salminen, H., et al., *Tuning of shell thickness of solid lipid particles impacts the chemical stability of encapsulated ω -3 fish oil*. Journal of colloid and interface science, 2017. **490**: p. 207-216.
202. Ilyasoglu, H. and S.N. El, *Nanoencapsulation of EPA/DHA with sodium caseinate–gum arabic*

- complex and its usage in the enrichment of fruit juice*. LWT-Food Science and Technology, 2014. **56**: p. 461-468.
203. Encina, C., et al., *Conventional spray-drying and future trends for the microencapsulation of fish oil*. Trends in Food Science & Technology, 2016. **56**: p. 46-60.
204. Fox, C.B., *Squalene emulsions for parenteral vaccine and drug delivery*. Molecules, 2009. **14**: p. 3286-3312.
205. Abd Ghani, A., et al., *Effects of oil-droplet diameter on the stability of squalene oil in spray-dried powder*. Drying technology, 2016. **34**: p. 1726-1734.
206. Spanova, M. and G. Daum, *Squalene–biochemistry, molecular biology, process biotechnology, and applications*. European journal of lipid science and technology, 2011. **113**: p. 1299-1320.
207. Vogel, F.R. and M.F. Powell, *A compendium of vaccine adjuvants and excipients*, in *Vaccine Design*. 1995, Springer: Boston, MA. p. 141-228.
208. Tagliabue, A. and R. Rappuoli, *Vaccine adjuvants: the dream becomes real*. Human Vaccines, 2008. **4**: p. 347-349.
209. Schultze, V., et al., *Safety of MF59™ adjuvant*. Vaccine, 2008. **26**: p. 3209-3222.
210. Reddy, L.H. and P. Couvreur, *Squalene: A natural triterpene for use in disease management and therapy*. Advanced Drug Delivery Reviews, 2009. **61**: p. 1412-1426.
211. Huang, Z.-R., Y.-K. Lin, and J.-Y. Fang, *Biological and pharmacological activities of squalene and related compounds: potential uses in cosmetic dermatology*. Molecules, 2009. **14**: p. 540-554.
212. Viseras, C., et al., *The effect of recrystallization on the crystal growth, melting point and solubility of ketoconazole*. Thermochimica acta, 1995. **268**: p. 143-151.
213. Pawar, B., M. Kanyalkar, and S. Srivastava, *Search for novel antifungal agents by monitoring fungal metabolites in presence of synthetically designed fluconazole derivatives using NMR spectroscopy*. Biochimica et Biophysica Acta (BBA)-Biomembranes, 2010. **1798**: p. 2067-2075.
214. Esclusa-Diaz, M.T., et al., *Characterization and in vitro dissolution behaviour of ketoconazole/ β - and 2-hydroxypropyl- β -cyclodextrin inclusion compounds*. International journal of pharmaceutics, 1996. **143**: p. 203-210.
215. Männistö, P.T., et al., *Impairing effect of food on ketoconazole absorption*. Antimicrobial agents and chemotherapy, 1982. **21**: p. 730-733.
216. Van den Mooter, G., et al., *Physical stabilisation of amorphous ketoconazole in solid dispersions with polyvinylpyrrolidone K25*. European journal of pharmaceutical sciences, 2001. **12**: p. 261-269.
217. Gupta, A.K. and D.C.A. Lyons, *The rise and fall of oral ketoconazole*. Journal of cutaneous medicine and surgery, 2015. **19**: p. 352-357.
218. Papadopoulos, D.P. and V. Papademetriou, *Metoprolol succinate combination in the treatment of hypertension*. Angiology, 2009. **60**: p. 608-613.
219. Wang, Y., et al., *Novel ethylcellulose-coated pellets for controlled release of metoprolol succinate without lag phase: characterization, optimization and in vivo evaluation*. Drug development and industrial pharmacy, 2015. **41**: p. 1120-1129.
220. Dongre, V.G., et al., *Simultaneous determination of metoprolol succinate and amlodipine besylate in pharmaceutical dosage form by HPLC*. Journal of pharmaceutical and biomedical analysis, 2008. **46**: p. 583-586.
221. Anonymous, *Safety Data Sheet*. United States Pharmacopeia, 2006. **6**: p. 1-6.
222. Quinten, T., et al., *Preparation and evaluation of sustained-release matrix tablets based on metoprolol and an acrylic carrier using injection moulding*. AAPS PharmSciTech, 2012. **13**: p. 1197-1211.
223. Malode, V.N., A. Paradkar, and P.V. Devarajan, *Controlled release floating multiparticulates of metoprolol succinate by hot melt extrusion*. International journal of pharmaceutics, 2015. **491**: p. 345-351.
224. Paoli, P., et al., *Similar but Different: The Case of Metoprolol Tartrate and Succinate Salts*. Crystal Growth & Design, 2016. **16**: p. 789-799.

225. Appelgren, C.H. and E.C. Eskilsson, *Metoprolol succinate*. 1992, Google Patents.
226. Hariharan, P., M. Palani, and M. Vaiyapuri, *An Evaluation of Antioxidant Potential of Flavonoid Eriodictyol in Isoproterenol-Induced Myocardial Infarction in Rats*. INDIAN JOURNAL OF PHARMACEUTICAL EDUCATION AND RESEARCH, 2017. **51**: p. 603-612.
227. Ravishankar, H., et al., *Modulated release metoprolol succinate formulation based on ionic interactions: in vivo proof of concept*. Journal of controlled release, 2006. **111**: p. 65-72.
228. Sandberg, A., et al., *Pharmacokinetic and pharmacodynamic properties of a new controlled-release formulation of metoprolol: a comparison with conventional tablets*. European journal of clinical pharmacology, 1988. **33**: p. S9-S14.
229. Tangeman, H.J. and J.H. Patterson, *Extended-release metoprolol succinate in chronic heart failure*. Annals of Pharmacotherapy, 2003. **37**: p. 701-710.
230. Sandberg, A., B. Abrahamsson, and J. Sjögren, *Influence of dissolution rate on the extent and rate of bioavailability of metoprolol*. International journal of pharmaceutics, 1991. **68**: p. 167-177.
231. Jobin, G., et al., *Investigation of drug absorption from the gastrointestinal tract of man. I. Metoprolol in the stomach, duodenum and jejunum*. British journal of clinical pharmacology, 1985. **19**.
232. Yu, F., et al., *Plasticized-starch/poly (ethylene oxide) blends prepared by extrusion*. Carbohydrate polymers, 2013. **91**: p. 253-261.
233. Crowley, M.M., et al., *Stability of polyethylene oxide in matrix tablets prepared by hot-melt extrusion*. Biomaterials, 2002. **23**: p. 4241-4248.
234. Ignatious, F., et al., *Electrospun nanofibers in oral drug delivery*. Pharmaceutical research, 2010. **27**: p. 576-588.
235. Son, W.K., et al., *The effects of solution properties and polyelectrolyte on electrospinning of ultrafine poly (ethylene oxide) fibers*. polymer, 2004. **45**: p. 2959-2966.
236. Brady, J., et al., *Polymer properties and characterization*, in *Developing Solid Oral Dosage Forms (Second Edition)*. 2017, Elsevier. p. 181-223.
237. Chen, Q., et al., *Preferential facet of nanocrystalline silver embedded in polyethylene oxide nanocomposite and its antibiotic behaviors*. The Journal of Physical Chemistry C, 2008. **112**: p. 10004-10007.
238. Wongsasulak, S., S. Pathumban, and T. Yoovidhya, *Effect of entrapped α -tocopherol on mucoadhesivity and evaluation of the release, degradation, and swelling characteristics of zein-chitosan composite electrospun fibers*. Journal of Food Engineering, 2014. **120**: p. 110-117.
239. Anonymous. *EU approved additives and their E Numbers*. Food Standard Agency, London 2010 [cited 2018, 24-Sep.]; Available from: <https://www.food.gov.uk/print/pdf/node/847>.
240. Callahan, J.C., et al., *Equilibrium moisture content of pharmaceutical excipients*. Drug Development and Industrial Pharmacy, 1982. **8**: p. 355-369.
241. Kvamme, B.B., G. Huseby, and O.K. Forrisdahl, *Molecular dynamics simulations of PVP kinetic inhibitor in liquid water and hydrate/liquid water systems*. Molecular Physics, 1997. **90**: p. 979-992.
242. Vasanthavada, M., et al., *Phase behavior of amorphous molecular dispersions II: Role of hydrogen bonding in solid solubility and phase separation kinetics*. Pharmaceutical research, 2005. **22**: p. 440-448.
243. Winter, S., et al., *Back to the roots: photodynamic inactivation of bacteria based on water-soluble curcumin bound to polyvinylpyrrolidone as a photosensitizer*. Photochemical & Photobiological Sciences, 2013. **12**: p. 1795-1802.
244. Tipduangta, P., *Crystallisation of amorphous fenofibrate and potential of the polymer blend electrospun matrices to stabilise in its amorphous form*. 2016, University of East Anglia.
245. Yu, D.-G., et al., *Solid dispersions of ketoprofen in drug-loaded electrospun nanofibers*. Journal of Dispersion Science and Technology, 2010. **31**: p. 902-908.

246. De Vrieze, S., et al., *The effect of temperature and humidity on electrospinning*. Journal of materials science, 2009. **44**: p. 1357.
247. Mu, L. and S.-S. Feng, *Vitamin E TPGS used as emulsifier in the solvent evaporation/extraction technique for fabrication of polymeric nanospheres for controlled release of paclitaxel (Taxol®)*. Journal of Controlled Release, 2002. **80**: p. 129-144.
248. Repka, M.A. and J.W. McGinity, *Influence of vitamin E TPGS on the properties of hydrophilic films produced by hot-melt extrusion*. International journal of pharmaceutics, 2000. **202**: p. 63-70.
249. Shah, A.R. and R. Banerjee, *Effect of d- α -tocopheryl polyethylene glycol 1000 succinate (TPGS) on surfactant monolayers*. Colloids and Surfaces B: Biointerfaces, 2011. **85**: p. 116-124.
250. Yan, A., et al., *Tocopheryl polyethylene glycol succinate as a safe, antioxidant surfactant for processing carbon nanotubes and fullerenes*. Carbon, 2007. **45**: p. 2463-2470.
251. Khalf, A. and S.V. Madihally, *Recent advances in multiaxial electrospinning for drug delivery*. European Journal of Pharmaceutics and Biopharmaceutics, 2017. **112**: p. 1-17.
252. Esteghlal, S., et al., *Gelatin-hydroxypropyl methylcellulose water-in-water emulsions as a new bio-based packaging material*. International journal of biological macromolecules, 2016. **86**: p. 242-249.
253. Yakimets, I., et al., *Mechanical properties with respect to water content of gelatin films in glassy state*. Polymer, 2005. **46**: p. 12577-12585.
254. Ge, Y., et al., *Gelatin-assisted fabrication of water-dispersible graphene and its inorganic analogues*. Journal of Materials Chemistry, 2012. **22**(34): p. 17619-17624.
255. Arvanitoyannis, I.S., A. Nakayama, and S.-i. Aiba, *Chitosan and gelatin based edible films: state diagrams, mechanical and permeation properties*. Carbohydrate polymers, 1998. **37**: p. 371-382.
256. Saraogi, G.K., et al., *Gelatin nanocarriers as potential vectors for effective management of tuberculosis*. International journal of pharmaceutics, 2010. **385**: p. 143-149.
257. Tayade, P.T. and R.D. Kale, *Encapsulation of water-insoluble drug by a cross-linking technique: Effect of process and formulation variables on encapsulation efficiency, particle size, and in vitro dissolution rate*. AAPS PharmSci, 2004. **6**: p. 112-119.
258. Xiao, J., et al., *Impact of melting point of palm oil on mechanical and water barrier properties of gelatin-palm oil emulsion film*. Food Hydrocolloids, 2016. **60**: p. 243-251.
259. Li, M., et al., *Electrospinning polyaniline-contained gelatin nanofibers for tissue engineering applications*. Biomaterials, 2006. **27**: p. 2705-2715.
260. Bueno, V.B., et al., *Synthesis and swelling behavior of xanthan-based hydrogels*. Carbohydrate polymers, 2013. **92**(2): p. 1091-1099.
261. Kumar, A., K.M. Rao, and S.S. Han, *Application of xanthan gum as polysaccharide in tissue engineering: A review*. Carbohydrate polymers, 2017.
262. Shalviri, A., et al., *Novel modified starch-xanthan gum hydrogels for controlled drug delivery: Synthesis and characterization*. Carbohydrate Polymers, 2010. **79**: p. 898-907.
263. Habibi, H. and K. Khosravi-Darani, *Effective variables on production and structure of xanthan gum and its food applications: A review*. Biocatalysis and Agricultural Biotechnology, 2017. **10**: p. 130-140.
264. Yoshida, T., et al., *Annealing induced gelation of xanthan/water systems*. Polymer, 1998. **39**: p. 1119-1122.
265. Fujiwara, J., et al., *Structural change of xanthan gum association in aqueous solutions*. Thermochimica acta, 2000. **352**: p. 241-246.
266. Guru, G.S., et al., *Miscibility studies of polysaccharide xanthan gum/PVP blend*. Journal of Polymers and the Environment, 2010. **18**: p. 135-140.
267. Argin-Soysal, S., P. Kofinas, and Y.M. Lo, *Effect of complexation conditions on xanthan-chitosan polyelectrolyte complex gels*. Food hydrocolloids, 2009. **23**: p. 202-209.
268. Katzbauer, B., *Properties and applications of xanthan gum*. Polymer degradation and Stability,

1998. **59**: p. 81-84.
269. Sinha, V.R., et al., *Compression coated systems for colonic delivery of 5-fluorouracil*. Journal of pharmacy and pharmacology, 2007. **59**: p. 359-365.
270. Sinha, V.R., et al., *Colonic drug delivery of 5-fluorouracil: an in vitro evaluation*. International Journal of Pharmaceutics, 2004. **269**: p. 101-108.
271. Chen, H., et al., *Microemulsion-based hydrogel formulation of ibuprofen for topical delivery*. International Journal of Pharmaceutics, 2006. **315**: p. 52-58.
272. Iijima, M., et al., *AFM studies on gelation mechanism of xanthan gum hydrogels*. Carbohydrate polymers, 2007. **68**: p. 701-707.
273. Camino, N.A., et al., *Hydroxypropylmethylcellulose- β -lactoglobulin mixtures at the oil-water interface. Bulk, interfacial and emulsification behavior as affected by pH*. Food Hydrocolloids, 2012. **27**: p. 464-474.
274. Siepmann, J. and N.A. Peppas, *Modeling of drug release from delivery systems based on hydroxypropyl methylcellulose (HPMC)*. Advanced drug delivery reviews, 2001. **48**: p. 139-157.
275. Nakayama, S., K. Ihara, and M. Senna, *Structure and properties of ibuprofen-hydroxypropyl methylcellulose nanocomposite gel*. Powder Technology, 2009. **190**: p. 221-224.
276. Camino, N.A. and A.M.R. Pilosof, *Hydroxypropylmethylcellulose at the oil-water interface. Part II. Submicron-emulsions as affected by pH*. Food Hydrocolloids, 2011. **25**: p. 1051-1062.
277. Burdock, G.A., *Safety assessment of hydroxypropyl methylcellulose as a food ingredient*. Food and Chemical Toxicology, 2007. **45**: p. 2341-2351.
278. Hiremath, P.S. and R.N. Saha, *Controlled release hydrophilic matrix tablet formulations of isoniazid: design and in vitro studies*. Aaps Pharmscitech, 2008. **9**: p. 1171-1178.
279. Mason, L.M., et al., *The influence of polymer content on early gel-layer formation in HPMC matrices: the use of CLSM visualisation to identify the percolation threshold*. European Journal of Pharmaceutics and Biopharmaceutics, 2015. **94**: p. 485-492.
280. Pigliacelli, C., *Polymer-bile salts interaction and its impact on the solubilisation and intestinal uptake of poorly water-soluble drugs*. 2014, University of East Anglia.
281. Jain, A.K., et al., *The influence of hydroxypropyl methylcellulose (HPMC) molecular weight, concentration and effect of food on in vivo erosion behavior of HPMC matrix tablets*. Journal of Controlled Release, 2014. **187**: p. 50-58.
282. Viridén, A., B. Wittgren, and A. Larsson, *The consequence of the chemical composition of HPMC in matrix tablets on the release behaviour of model drug substances having different solubility*. European Journal of Pharmaceutics and Biopharmaceutics, 2011. **77**: p. 99-110.
283. Futamura, T. and M. Kawaguchi, *Characterization of paraffin oil emulsions stabilized by hydroxypropyl methylcellulose*. Journal of colloid and interface science, 2012. **367**: p. 55-60.
284. van den Berg, M., F.L. Jara, and A.M.R. Pilosof, *Performance of egg white and hydroxypropylmethylcellulose mixtures on gelation and foaming*. Food Hydrocolloids, 2015. **48**: p. 282-291.
285. Patel, A.R. and K. Dewettinck, *Comparative evaluation of structured oil systems: Shellac oleogel, HPMC oleogel, and HIPE gel*. European journal of lipid science and technology, 2015. **117**: p. 1772-1781.
286. Patel, A.R., et al., *Edible oleogels based on water soluble food polymers: preparation, characterization and potential application*. Food & function, 2014. **5**: p. 2833-2841.
287. Su, J.-F., et al., *Structure and properties of carboxymethyl cellulose/soy protein isolate blend edible films crosslinked by Maillard reactions*. Carbohydrate Polymers, 2010. **79**: p. 145-153.
288. Yadav, M., K.Y. Rhee, and S.J. Park, *Synthesis and characterization of graphene oxide/carboxymethylcellulose/alginate composite blend films*. Carbohydrate polymers, 2014. **110**: p. 18-25.
289. Ghannam, M.T. and M.N. Esmail, *Rheological properties of carboxymethyl cellulose*. Journal of applied polymer science, 1997. **64**: p. 289-301.
290. Saha, D. and S. Bhattacharya, *Hydrocolloids as thickening and gelling agents in food: a critical*

- review. *Journal of food science and technology*, 2010. **47**: p. 587-597.
291. El-Sayed, S., et al., *DSC, TGA and dielectric properties of carboxymethyl cellulose/polyvinyl alcohol blends*. *Physica B: Condensed Matter*, 2011. **406**: p. 4068-4076.
292. Wang, J., M. Feng, and H. Zhan, *Preparation, characterization, and nonlinear optical properties of graphene oxide-carboxymethyl cellulose composite films*. *Optics & Laser Technology*, 2014. **57**: p. 84-89.
293. Chen, R.-N., et al., *Development of swelling/floating gastroretentive drug delivery system based on a combination of hydroxyethyl cellulose and sodium carboxymethyl cellulose for Losartan and its clinical relevance in healthy volunteers with CYP2C9 polymorphism*. *European Journal of Pharmaceutical Sciences*, 2010. **39**: p. 82-89.
294. Agarwal, T., et al., *Calcium alginate-carboxymethyl cellulose beads for colon-targeted drug delivery*. *International journal of biological macromolecules*, 2015. **75**: p. 409-417.
295. Ugwoke, M.I., et al., *Scintigraphic evaluation in rabbits of nasal drug delivery systems based on carbopol 971p[®] and carboxymethylcellulose*. *Journal of controlled release*, 2000. **68**: p. 207-214.
296. Fekete, T., et al., *Synthesis of carboxymethylcellulose/acrylic acid hydrogels with superabsorbent properties by radiation-initiated crosslinking*. *Radiation Physics and Chemistry*, 2016. **124**: p. 135-139.
297. Rasoulzadeh, M. and H. Namazi, *Carboxymethyl cellulose/graphene oxide bio-nanocomposite hydrogel beads as anticancer drug carrier agent*. *Carbohydrate polymers*, 2017. **168**: p. 320-326.
298. Ruusunen, M., et al., *Effect of sodium citrate, carboxymethyl cellulose and carrageenan levels on quality characteristics of low-salt and low-fat bologna type sausages*. *Meat science*, 2003. **64**: p. 371-381.
299. Lu, W., et al., *Synthesis of Au nanoparticles decorated graphene oxide nanosheets: Noncovalent functionalization by TWEEN 20 in situ reduction of aqueous chloroaurate ions for hydrazine detection and catalytic reduction of 4-nitrophenol*. *Journal of hazardous materials*, 2011. **197**: p. 320-326.
300. Majid, A.A.A., et al., *Measurement of the water droplet size in water-in-oil emulsions using low field nuclear magnetic resonance for gas hydrate slurry applications*. *Canadian Journal of Chemistry*, 2015. **93**: p. 1007-1013.
301. Kim, C. and Y.-L. Hsieh, *Wetting and absorbency of nonionic surfactant solutions on cotton fabrics*. *Colloids and Surfaces A: Physicochemical and engineering aspects*, 2001. **187**: p. 385-397.
302. Peltonen, L., J. Hirvonen, and J. Yliruusi, *The behavior of sorbitan surfactants at the water–oil interface: straight-chained hydrocarbons from pentane to dodecane as an oil phase*. *Journal of colloid and interface science*, 2001. **240**: p. 272-276.
303. Omokawa, Y., et al., *In vitro and in vivo anti-tumor effects of novel Span 80 vesicles containing immobilized Eucheuma serra agglutinin*. *International journal of pharmaceutics*, 2010. **389**: p. 157-167.
304. Anonymous. *IKA Dispersers and Shakers. An ideal solution for research laboratories!* Laboratory-Equipment [cited 2018, 02-Sep.]; Available from: https://www.laboratory-equipment.com/uploads/tech_resources/ika_disperser_success_story_white_paper_111717_130409.pdf.
305. Anonymous. *IKA Dispersers*. [cited 2018, 02-Sep.]; Available from: <http://www.thermofishersci.in/lit/IKA%20Disperser.pdf>.
306. Ratti, C., *Hot air and freeze-drying of high-value foods: a review*. *Journal of food engineering*, 2001. **49**: p. 311-319.
307. Dudkiewicz, A., et al., *Characterization of nanomaterials in food by electron microscopy*. *TrAC Trends in Analytical Chemistry*, 2011. **30**: p. 28-43.
308. Davidson, M.W. and M. Abramowitz, *Optical microscopy*. *Encyclopedia of imaging science and*

- technology, 2002. **2**: p. 120.
309. Talwar, P., *Manual of Cytogenetics in Reproductive Biology*. 2014: JP Medical Ltd.
310. Leboffe, M.J. and B.E. Pierce, *A photographic atlas for the microbiology laboratory*. 2012: Morton Publishing Company.
311. Tran, P.T., A. Paoletti, and F. Chang, *Imaging green fluorescent protein fusions in living fission yeast cells*. *Methods*, 2004. **33**: p. 220-225.
312. Łasińska, A., *Selected imaging techniques applied in forensic science*. *Przegląd Bezpieczeństwa Wewnętrznego*, 2018. **10**: p. 283-309.
313. Brakenhoff, G.J., et al., *Three-dimensional confocal fluorescence microscopy*. *Methods Cell Biol*, 1989. **30**: p. 379-398.
314. Prasad, V., D. Semwogerere, and E.R. Weeks, *Confocal microscopy of colloids*. *Journal of Physics: Condensed Matter*, 2007. **19**: p. 113102.
315. Hickey, C.D., et al., *Growth and location of bacterial colonies within dairy foods using microscopy techniques: a review*. *Frontiers in microbiology*, 2015. **6**: p. 99.
316. Sondej, F., A. Bück, and E. Tsotsas, *Comparative analysis of the coating thickness on single particles using X-ray micro-computed tomography and confocal laser-scanning microscopy*. *Powder Technology*, 2016. **287**: p. 330-340.
317. Egerton, R.F., *Physical principles of electron microscopy*. 2005: Springer.
318. Bogner, A., et al., *A history of scanning electron microscopy developments: towards "wet-STEM" imaging*. *Micron*, 2007. **38**: p. 390-401.
319. Vernon-Parry, K.D., *Scanning electron microscopy: an introduction*. *III-Vs Review*, 2000. **13**: p. 40-44.
320. Kaminskyj, S.G.W. and T.E.S. Dahms, *High spatial resolution surface imaging and analysis of fungal cells using SEM and AFM*. *Micron*, 2008. **39**: p. 349-361.
321. Klang, V., C. Valenta, and N.B. Matsko, *Electron microscopy of pharmaceutical systems*. *Micron*, 2013. **44**: p. 45-74.
322. Luo, H., L.E. Scriven, and L.F. Francis, *Cryo-SEM studies of latex/ceramic nanoparticle coating microstructure development*. *Journal of colloid and interface science*, 2007. **316**: p. 500-509.
323. Kim, G.-M., et al., *One-dimensional arrangement of gold nanoparticles by electrospinning*. *Chemistry of materials*, 2005. **17**: p. 4949-4957.
324. Li, D. and Y. Xia, *Fabrication of titania nanofibers by electrospinning*. *Nano letters*, 2003. **3**: p. 555-560.
325. Vrignaud, S., et al., *Reverse micelle-loaded lipid nanocarriers: a novel drug delivery system for the sustained release of doxorubicin hydrochloride*. *European journal of pharmaceutics and biopharmaceutics*, 2011. **79**: p. 197-204.
326. Auty, M.A.E., et al., *The application of microscopy and rheology to study the effect of milk salt concentration on the structure of acidified micellar casein systems*. *Food Hydrocolloids*, 2005. **19**: p. 101-109.
327. Nam, Y.S., et al., *Tocopheryl acetate nanoemulsions stabilized with lipid-polymer hybrid emulsifiers for effective skin delivery*. *Colloids and Surfaces B: Biointerfaces*, 2012. **94**: p. 51-57.
328. Lammertyn, J., et al., *MRI and X-ray CT study of spatial distribution of core breakdown in 'Conference' pears*. *Magnetic Resonance Imaging*, 2003. **21**: p. 805-815.
329. Agrawal, A.K., et al., *Application of X-ray micro-CT for micro-structural characterization of APCVD deposited SiC coatings on graphite conduit*. *Applied Radiation and Isotopes*, 2016. **108**: p. 133-142.
330. Miguélez-Morán, A.M., et al., *Characterisation of density distributions in roller-compacted ribbons using micro-indentation and X-ray micro-computed tomography*. *European Journal of Pharmaceutics and Biopharmaceutics*, 2009. **72**: p. 173-182.
331. Chang, H.-H., et al., *Application of scanning electron microscopy and X-ray microanalysis: FE-SEM, ESEM-EDS, and EDS mapping for studying the characteristics of topographical*

- microstructure and elemental mapping of human cardiac calcified deposition*. Analytical and bioanalytical chemistry, 2014. **406**: p. 359-366.
332. Dinnebier, R.E. and S.J.L. Billinge, *Powder diffraction: theory and practice*. 2008: Royal Society of Chemistry.
333. Rohrer, G.S., *Structure and Bonding in Crystalline Materials: A Textbook for Materials Science and Engineering Students*. JOURNAL OF MATERIALS EDUCATION, 1998. **20**: p. 135-150.
334. Stanjek, H. and W. Häusler, *Basics of X-ray Diffraction*. Hyperfine Interactions, 2004. **154**: p. 107-119.
335. Connolly, J.R., *Introduction quantitative X-ray diffraction methods*. Fundamentals of X-ray Powder Diffraction, 2010.
336. Akbari, B., M.P. Tavandashti, and M. Zandrahimi, *Particle size characterization of nanoparticles—a practical approach*. Iranian Journal of Materials Science and Engineering, 2011. **8**: p. 48-56.
337. Harris, K.D.M., M. Tremayne, and B.M. Kariuki, *Contemporary advances in the use of powder X-ray diffraction for structure determination*. Angewandte Chemie International Edition, 2001. **40**: p. 1626-1651.
338. Smith, B.C., *Fundamentals of Fourier transform infrared spectroscopy*. 2011: CRC press.
339. Salari, A. and R.E. Young, *Application of attenuated total reflectance FTIR spectroscopy to the analysis of mixtures of pharmaceutical polymorphs*. International journal of pharmaceutics, 1998. **163**: p. 157-166.
340. Vlachos, N., et al., *Applications of Fourier transform-infrared spectroscopy to edible oils*. Analytica chimica acta, 2006. **573**: p. 459-465.
341. Lii, C.-y., et al., *Carboxymethyl cellulose–gelatin complexes*. Carbohydrate Polymers, 2002. **50**: p. 19-26.
342. Lii, C.-Y., et al., *Xanthan gum–gelatin complexes*. European Polymer Journal, 2002. **38**: p. 1377-1381.
343. Craig, D.Q.M. and M. Reading, *Thermal analysis of pharmaceuticals*. 2006: CRC press.
344. Garbett, N.C., et al., *Differential scanning calorimetry of blood plasma for clinical diagnosis and monitoring*. Experimental and Molecular Pathology, 2009. **86**: p. 186-191.
345. Polini, A. and F. Yang, *Physicochemical characterization of nanofiber composites*, in *Nanofiber Composites for Biomedical Applications*. 2017, Elsevier. p. 97-115.
346. Estellé, P., et al., *On the optimisation of a texture analyser in squeeze flow geometry*. Measurement, 2006. **39**: p. 771-777.
347. Jones, D.S., A.D. Woolfson, and A.F. Brown, *Textural, viscoelastic and mucoadhesive properties of pharmaceutical gels composed of cellulose polymers*. International journal of pharmaceutics, 1997. **151**: p. 223-233.
348. Chandra, M.V. and B.A. Shamasundar, *Texture profile analysis and functional properties of gelatin from the skin of three species of fresh water fish*. International journal of food properties, 2015. **18**: p. 572-584.
349. Lau, M.H., J. Tang, and A.T. Paulson, *Texture profile and turbidity of gellan/gelatin mixed gels*. Food Research International, 2000. **33**: p. 665-671.
350. Shekunov, B.Y., et al., *Particle size analysis in pharmaceuticals: principles, methods and applications*. Pharmaceutical research, 2007. **24**: p. 203-227.
351. Allahyari, E., et al., *Dynamic Light Scattering (DLS)*, in *Thermal and Rheological Measurement Techniques for Nanomaterials Characterization*. 2017, Elsevier. p. 37-49.
352. Rawle, A., *Basic of principles of particle-size analysis*. Surface coatings international. Part A, Coatings journal, 2003. **86**(2): p. 58-65.
353. Storti, F. and F. Balsamo, *Particle size distributions by laser diffraction: sensitivity of granular matter strength to analytical operating procedures*. Solid Earth, 2010. **1**: p. 25-48.
354. Horiba Instruments, I.N.C., *A guidebook to particle size analysis*. 2014, USA.
355. Anonymous. *In Vitro Dissolution Testing For Solid Oral Dosage Forms*. Particle science -

- Technical Brief: Volume 5 2010 [cited 2018, 27-Jun.]; Available from: https://www.particlesciences.com/docs/technical_briefs/TB_2010_5.pdf.
356. FDA, U.S., *Guidance for Industry: Dissolution testing of immediate-release solid oral dosage forms*. Food and Drug Administration, Center for Drug Evaluation and Research (CDER), 1997.
357. USP, G.C., *711> Dissolution*. United States Pharmacopeia, 2011.
358. Anonymous. *Introduction to Ultraviolet -Visible Spectroscopy (UV)*. Royal Society of Chemistry 2009 [cited 2018, 27-Jun.]; Available from: http://www.rsc.org/learn-chemistry/content/filerepository/CMP/00/001/304/UV-Vis_Student%20resource%20pack_ENGLISH.pdf.
359. Richard-Lacroix, M. and C. Pellerin, *Molecular orientation in electrospun fibers: from mats to single fibers*. *Macromolecules*, 2013. **46**: p. 9473-9493.
360. Garg, K. and G.L. Bowlin, *Electrospinning jets and nanofibrous structures*. *Biomicrofluidics*, 2011. **5**: p. 13403.
361. Teo, W.-E., R. Inai, and S. Ramakrishna, *Technological advances in electrospinning of nanofibers*. *Science and technology of advanced materials*, 2011. **12**: p. 13002.
362. Frenot, A. and I.S. Chronakis, *Polymer nanofibers assembled by electrospinning*. *Current opinion in colloid & interface science*, 2003. **8**: p. 64-75.
363. Zamani, M., M.P. Prabhakaran, and S. Ramakrishna, *Advances in drug delivery via electrospun and electrosprayed nanomaterials*. *International journal of nanomedicine*, 2013. **8**: p. 2997.
364. Bhushani, J.A. and C. Anandharamakrishnan, *Electrospinning and electrospraying techniques: Potential food based applications*. *Trends in food science & technology*, 2014. **38**: p. 21-33.
365. Arroyave, G., O. Pineda, and N.S. Scrimshaw, *The stability of potassium iodate in crude table salt*. *Bulletin of the World Health Organization*, 1956. **14**: p. 183.
366. Van den Mooter, G., *The use of amorphous solid dispersions: A formulation strategy to overcome poor solubility and dissolution rate*. *Drug Discovery Today: Technologies*, 2012. **9**: p. e79-e85.
367. Gupta, R.K. and H.-W. Rhee, *Plasticizing effect of K⁺ ions and succinonitrile on electrical conductivity of [poly (ethylene oxide)-succinonitrile]/KI-I₂ redox-couple solid polymer electrolyte*. *The Journal of Physical Chemistry B*, 2013. **117**: p. 7465-7471.
368. Kalaigan, G.P. and M.-S. Kang, *Effects of compositions on properties of PEO-KI-I₂ salts polymer electrolytes for DSSC*. *Solid State Ionics*, 2006. **177**: p. 1091-1097.
369. Agarwala, S., et al., *Co-existence of LiI and KI in filler-free, quasi-solid-state electrolyte for efficient and stable dye-sensitized solar cell*. *Journal of Power Sources*, 2011. **196**: p. 1651-1656.
370. Reddy, M.J. and P.P. Chu, *Optical microscopy and conductivity of poly (ethylene oxide) complexed with KI salt*. *Electrochimica acta*, 2002. **47**: p. 1189-1196.
371. Sill, T.J. and H.A. von Recum, *Electrospinning: applications in drug delivery and tissue engineering*. *Biomaterials*, 2008. **29**: p. 1989-2006.
372. Wannatong, L., A. Sirivat, and P. Supaphol, *Effects of solvents on electrospun polymeric fibers: preliminary study on polystyrene*. *Polymer International*, 2004. **53**: p. 1851-1859.
373. Kessick, R., J. Fenn, and G. Tepper, *The use of AC potentials in electrospraying and electrospinning processes*. *Polymer*, 2004. **45**: p. 2981-2984.
374. Piburn, G. and A.R. Barron, *An introduction to energy dispersive X-ray spectroscopy*. *Physical methods in chemistry and nano science*. Connexions/Rice University, Houston, 2013: p. 90-98.
375. Wollman, D.A., et al., *High-resolution, energy-dispersive microcalorimeter spectrometer for X-ray microanalysis*. *Journal of Microscopy*, 1997. **188**: p. 196-223.
376. Li, Z. and C. Wang, *One-dimensional nanostructures: electrospinning technique and unique nanofibers*. 2013: Springer.
377. Mit-uppatham, C., M. Nithitanakul, and P. Supaphol, *Effects of Solution Concentration, Emitting Electrode Polarity, Solvent Type, and Salt Addition on Electrospun Polyamide-6 Fibers: A Preliminary Report*. *Macromolecular Symposia*, 2004. **216**: p. 293-300.

378. Qin, X.H., et al., *Effect of different salts on electrospinning of polyacrylonitrile (PAN) polymer solution*. Journal of applied polymer science, 2007. **103**: p. 3865-3870.
379. Arayanarakul, K., et al., *Effects of poly (ethylene glycol), inorganic salt, sodium dodecyl sulfate, and solvent system on electrospinning of poly (ethylene oxide)*. Macromolecular Materials and Engineering, 2006. **291**: p. 581-591.
380. Liu, Y., et al., *Controlling numbers and sizes of beads in electrospun nanofibers*. Polymer International, 2008. **57**: p. 632-636.
381. Yu, D.-G., et al., *PVP nanofibers prepared using co-axial electrospinning with salt solution as sheath fluid*. Materials Letters, 2012. **67**: p. 78-80.
382. Nartetamrongsutt, K. and G.G. Chase, *The influence of salt and solvent concentrations on electrospun polyvinylpyrrolidone fiber diameters and bead formation*. Polymer, 2013. **54**: p. 2166-2173.
383. Arumugam, G.K., S. Khan, and P.A. Heiden, *Comparison of the effects of an ionic liquid and other salts on the properties of electrospun fibers, 2-poly (vinyl alcohol)*. Macromolecular Materials and Engineering, 2009. **294**: p. 45-53.
384. Barakat, N.A.M., et al., *Spider-net within the N6, PVA and PU electrospun nanofiber mats using salt addition: novel strategy in the electrospinning process*. Polymer, 2009. **50**: p. 4389-4396.
385. Ding, W., et al., *Manipulated electrospun PVA nanofibers with inexpensive salts*. Macromolecular Materials and Engineering, 2010. **295**: p. 958-965.
386. Yoshihara, T., H. Tadokoro, and S. Murahashi, *Normal Vibrations of the Polymer Molecules of Helical Conformation. IV. Polyethylene Oxide and Polyethylene-d 4 Oxide*. The Journal of Chemical Physics, 1964. **41**(9): p. 2902-2911.
387. Yang, S., et al., *Effect of molecular weight on conformational changes of PEO: an infrared spectroscopic analysis*. Journal of materials science, 2015. **50**: p. 1544-1552.
388. Bergeron, C., et al., *A study of the deformation, Network, and aging of polyethylene oxide films by infrared spectroscopy and calorimetric measurements*. International Journal of Spectroscopy, 2012. **2012**.
389. Pucić, I. and T. Jurkin, *FTIR assessment of poly (ethylene oxide) irradiated in solid state, melt and aqueous solution*. Radiation Physics and Chemistry, 2012. **81**: p. 1426-1429.
390. Tang, Z., et al., *A novel PEO-based composite polymer electrolyte with absorptive glass mat for Li-ion batteries*. Electrochimica acta, 2007. **52**: p. 6638-6643.
391. Nakamoto, K., *Infrared and Raman spectra of inorganic and coordination compounds*. 1986, USA: Wiley Online Library.
392. Miller, F.A. and C.H. Wilkins, *Infrared spectra and characteristic frequencies of inorganic ions*. Analytical chemistry, 1952. **24**(8): p. 1253-1294.
393. Cosco, D., et al., *Liposomes as multicompartamental carriers for multidrug delivery in anticancer chemotherapy*. Drug delivery and translational research, 2011. **1**: p. 66-75.
394. Chen, Y., et al., *Sterically stabilized spongosomes for multidrug delivery of anticancer nanomedicines*. Journal of Materials Chemistry B, 2015. **3**: p. 7734-7744.
395. Xu, X., et al., *Ultrafine PEG-PLA fibers loaded with both paclitaxel and doxorubicin hydrochloride and their in vitro cytotoxicity*. European Journal of Pharmaceutics and Biopharmaceutics, 2009. **72**: p. 18-25.
396. Zimmermann, M.B., et al., *The effects of vitamin A deficiency and vitamin A supplementation on thyroid function in goitrous children*. The Journal of Clinical Endocrinology & Metabolism, 2004. **89**: p. 5441-5447.
397. Liu, W., et al., *Formation and stability of paraffin oil-in-water nano-emulsions prepared by the emulsion inversion point method*. Journal of colloid and interface science, 2006. **303**: p. 557-563.
398. Americas, I.C.I., *The HLB System: A Time-saving Guide to Emulsifier Selection*. 1984: ICI Americas, Incorporated.
399. McClements, D.J., *Critical review of techniques and methodologies for characterization of*

- emulsion stability*. Critical reviews in food science and nutrition, 2007. **47**: p. 611-649.
400. Al-Shannaq, R., et al., *Emulsion stability and cross-linking of PMMA microcapsules containing phase change materials*. Solar Energy Materials and Solar Cells, 2015. **132**: p. 311-318.
401. Wooster, T.J., M. Golding, and P. Sanguansri, *Impact of oil type on nanoemulsion formation and Ostwald ripening stability*. Langmuir, 2008. **24**: p. 12758-12765.
402. Bouchemal, K., et al., *Nano-emulsion formulation using spontaneous emulsification: solvent, oil and surfactant optimisation*. International journal of pharmaceutics, 2004. **280**: p. 241-251.
403. Pal, R., *A novel method to correlate emulsion viscosity data*. Colloids and Surfaces A: Physicochemical and Engineering Aspects, 1998. **137**: p. 275-286.
404. Orafidiya, L.O. and F.A. Oladimeji, *Determination of the required HLB values of some essential oils*. International Journal of Pharmaceutics, 2002. **237**: p. 241-249.
405. Yuan, Y., et al., *Characterization and stability evaluation of β -carotene nanoemulsions prepared by high pressure homogenization under various emulsifying conditions*. Food Research International, 2008. **41**: p. 61-68.
406. Mahdi Jafari, S., Y. He, and B. Bhandari, *Nano-emulsion production by sonication and microfluidization—a comparison*. International Journal of Food Properties, 2006. **9**: p. 475-485.
407. White, J.G., W.B. Amos, and M. Fordham, *An evaluation of confocal versus conventional imaging of biological structures by fluorescence light microscopy*. The Journal of cell biology, 1987. **105**: p. 41-48.
408. Sun, C. and S. Gunasekaran, *Effects of protein concentration and oil-phase volume fraction on the stability and rheology of menhaden oil-in-water emulsions stabilized by whey protein isolate with xanthan gum*. Food Hydrocolloids, 2009. **23**: p. 165-174.
409. Tan, C.P. and M. Nakajima, *β -Carotene nanodispersions: preparation, characterization and stability evaluation*. Food Chemistry, 2005. **92**: p. 661-671.
410. Chen, G. and D. Tao, *An experimental study of stability of oil–water emulsion*. Fuel processing technology, 2005. **86**: p. 499-508.
411. Flourey, J., A. Desrumaux, and J. Lardieres, *Effect of high-pressure homogenization on droplet size distributions and rheological properties of model oil-in-water emulsions*. Innovative Food Science & Emerging Technologies, 2000. **1**: p. 127-134.
412. Binks, B.P. and J.A. Rodrigues, *Types of phase inversion of silica particle stabilized emulsions containing triglyceride oil*. Langmuir, 2003. **19**: p. 4905-4912.
413. Abbas, S., et al., *An overview of ultrasound-assisted food-grade nanoemulsions*. Food Engineering Reviews, 2013. **5**: p. 139-157.
414. Guo, Q. and T.H. Mu, *Emulsifying properties of sweet potato protein: effect of protein concentration and oil volume fraction*. Food Hydrocolloids, 2011. **25**: p. 98-106.
415. Schubert, H., K. Ax, and O. Behrend, *Product engineering of dispersed systems*. Trends in Food Science & Technology, 2003. **14**: p. 9-16.
416. Bhattacharyya, A. and M. Bajpai, *Development and oral bioavailability of self emulsifying formulation of ketoconazole*. Int J Pharm Sci Nanotechnol, 2013. **5**: p. 1858-1865.
417. Yang, Y.-Y., T.-S. Chung, and N.P. Ng, *Morphology, drug distribution, and in vitro release profiles of biodegradable polymeric microspheres containing protein fabricated by double-emulsion solvent extraction/evaporation method*. Biomaterials, 2001. **22**: p. 231-241.
418. Vladislavljević, G.T. and H. Schubert, *Preparation of emulsions with a narrow particle size distribution using microporous α -alumina membranes*. Journal of dispersion science and technology, 2003. **24**: p. 811-819.
419. Desplanques, S., et al., *Impact of chemical composition of xanthan and acacia gums on the emulsification and stability of oil-in-water emulsions*. Food Hydrocolloids, 2012. **27**: p. 401-410.
420. Bais, D., et al., *Rheological characterization of polysaccharide–surfactant matrices for cosmetic O/W emulsions*. Journal of colloid and interface science, 2005. **290**: p. 546-556.

421. Trabelsi, S. and D. Langevin, *Co-adsorption of Carboxymethyl-Cellulose and Cationic Surfactants at the Air– Water Interface*. Langmuir, 2007. **23**: p. 1248-1252.
422. Bain, C.D., et al., *Complexes of surfactants with oppositely charged polymers at surfaces and in bulk*. Advances in Colloid and Interface Science, 2010. **155**: p. 32-49.
423. Bao, H., et al., *Interactions between ionic surfactants and polysaccharides in aqueous solutions*. Macromolecules, 2008. **41**: p. 9406-9412.
424. Grant, J., J. Cho, and C. Allen, *Self-assembly and physicochemical and rheological properties of a polysaccharide– surfactant system formed from the cationic biopolymer chitosan and nonionic sorbitan esters*. Langmuir, 2006. **22**: p. 4327-4335.
425. Dickinson, E., J. Ma, and M.J.W. Povey, *Creaming of concentrated oil-in-water emulsions containing xanthan*. Food Hydrocolloids, 1994. **8**: p. 481-497.
426. Song, S.H., et al., *Novel hybrid immobilization of microorganisms and its applications to biological denitrification*. Enzyme and Microbial Technology, 2005. **37**: p. 567-573.
427. Rahn, H., et al., *Microcomputed tomography analysis of ferrofluids used for cancer treatment*. Journal of Physics: Condensed Matter, 2008. **20**: p. 204152.
428. Awaja, F., et al., *An investigation of the accelerated thermal degradation of different epoxy resin composites using X-ray microcomputed tomography and optical coherence tomography*. Polymer Degradation and Stability, 2009. **94**: p. 1814-1824.
429. Mackay, D. and S. Paterson, *Calculating fugacity*. Environmental Science & Technology, 1981. **15**: p. 1006-1014.
430. Madyira, D.M., Z. Nkomo, and E.T. Akinlabi, *Characterizing sunflower oil biodiesel blends as alternatives to fossil diesel*, in *Proceedings of the World Congress on Engineering*. 2012. **3**: p. 4-6.
431. Guillén, M.D. and N. Cabo, *Usefulness of the frequency data of the Fourier transform infrared spectra to evaluate the degree of oxidation of edible oils*. Journal of Agricultural and Food Chemistry, 1999. **47**: p. 709-719.
432. Xu, J., et al., *Mechanical enhancement of nanofibrous scaffolds through polyelectrolyte complexation*. Nanotechnology, 2012. **24**: p. 25701.
433. Guo, J., et al., *Periodate oxidation of xanthan gum and its crosslinking effects on gelatin-based edible films*. Food Hydrocolloids, 2014. **39**: p. 243-250.
434. Hazirah, M.N., M.I.N. Isa, and N.M. Sarbon, *Effect of xanthan gum on the physical and mechanical properties of gelatin-carboxymethyl cellulose film blends*. Food Packaging and Shelf Life, 2016. **9**: p. 55-63.
435. Su, L., et al., *Chemical modification of xanthan gum to increase dissolution rate*. Carbohydrate polymers, 2003. **53**: p. 497-499.
436. Mu, C., et al., *Freezing/thawing effects on the exfoliation of montmorillonite in gelatin-based bionanocomposite*. Journal of Applied Polymer Science, 2013. **128**: p. 3141-3148.
437. Enagbare, B.O., *Characterization of metoprolol succinate coated with Surelease™ polymer and fluid bed monitoring using NIR*. 2009, Howard University.
438. Ochiuz, L.c.m., et al., *Microencapsulation of metoprolol tartrate into chitosan for improved oral administration and patient compliance*. Industrial & Engineering Chemistry Research, 2013. **52**: p. 17432-17441.
439. Macêdo, R., et al., *Application of thermal analysis in the characterization of anti-hypertensive drugs*. Journal of Thermal Analysis and Calorimetry, 2000. **59**: p. 657-661.
440. Wang, R., Q. Wang, and L. Li, *Evaporation behaviour of water and its plasticizing effect in modified poly (vinyl alcohol) systems*. Polymer international, 2003. **52**: p. 1820-1826.
441. Chaisawang, M. and M. Suphantharika, *Effects of guar gum and xanthan gum additions on physical and rheological properties of cationic tapioca starch*. Carbohydrate Polymers, 2005. **61**: p. 288-295.
442. Banerjee, J., et al., *Synthesis and characterization of xanthan gum-g-N-vinyl formamide with a potassium monopersulfate/Ag (I) system*. Journal of Applied Polymer Science, 2006. **101**: p.

- 1637-1645.
443. Chen, C.-H., et al., *Studies of chitosan: II. Preparation and characterization of chitosan/poly (vinyl alcohol)/gelatin ternary blend films*. International Journal of Biological Macromolecules, 2008. **43**: p. 37-42.
444. Asha, S., et al., *Spectroscopic and thermal studies of 8 MeV electron beam irradiated HPMC films*. Nuclear Instruments and Methods in Physics Research Section B: Beam Interactions with Materials and Atoms, 2009. **267**: p. 2385-2389.
445. Yin, J., et al., *Miscibility studies of the blends of chitosan with some cellulose ethers*. Carbohydrate Polymers, 2006. **63**: p. 238-244.
446. Hosseini, S.F., et al., *Preparation and functional properties of fish gelatin–chitosan blend edible films*. Food chemistry, 2013. **136**: p. 1490-1495.
447. Gupta, A.K., et al., *Effect of cellular uptake of gelatin nanoparticles on adhesion, morphology and cytoskeleton organisation of human fibroblasts*. Journal of Controlled Release, 2004. **95**: p. 197-207.
448. Choi, Y.S., et al., *Study on gelatin-containing artificial skin: I. Preparation and characteristics of novel gelatin-alginate sponge*. Biomaterials, 1999. **20**: p. 409-417.
449. Feeney, O.M., et al., *50 years of oral lipid-based formulations: provenance, progress and future perspectives*. Advanced drug delivery reviews, 2016. **101**: p. 167-194.
450. Onoue, S., et al., *Inhalable dry-emulsion formulation of cyclosporine A with improved anti-inflammatory effects in experimental asthma/COPD-model rats*. European Journal of Pharmaceutics and Biopharmaceutics, 2012. **80**: p. 54-60.
451. Guillén, M.D. and N. Cabo, *Relationships between the composition of edible oils and lard and the ratio of the absorbance of specific bands of their Fourier transform infrared spectra. Role of some bands of the fingerprint region*. Journal of Agricultural and Food Chemistry, 1998. **46**: p. 1788-1793.
452. Mundargi, R.C., S.A. Patil, and T.M. Aminabhavi, *Evaluation of acrylamide-grafted-xanthan gum copolymer matrix tablets for oral controlled delivery of antihypertensive drugs*. Carbohydrate Polymers, 2007. **69**: p. 130-141.
453. Kumar, A., K. Singh, and M. Ahuja, *Xanthan-g-poly (acrylamide): microwave-assisted synthesis, characterization and in vitro release behavior*. Carbohydrate Polymers, 2009. **76**: p. 261-267.
454. Faria, S., et al., *Characterization of xanthan gum produced from sugar cane broth*. Carbohydrate Polymers, 2011. **86**: p. 469-476.
455. Yahoum, M.M., N. Moulai-Mostefa, and D. Le Cerf, *Synthesis, physicochemical, structural and rheological characterizations of carboxymethyl xanthan derivatives*. Carbohydrate polymers, 2016. **154**: p. 267-275.
456. Izawa, H. and J.-i. Kadokawa, *Preparation and characterizations of functional ionic liquid-gel and hydrogel materials of xanthan gum*. Journal of Materials Chemistry, 2010. **20**: p. 5235-5241.
457. Lad, M., et al., *On the origin of sharp peaks in the X-ray diffraction patterns of xanthan powders*. Food chemistry, 2013. **139**: p. 1146-1151.
458. Tadokoro, H., et al., *Structural studies on polyethers, [-(CH₂)_m-O-]_n. II. Molecular structure of polyethylene oxide*. Macromolecular Chemistry and Physics, 1964. **73**: p. 109-127.
459. Takahashi, Y., I. Sumita, and H. Tadokoro, *Structural studies of polyethers. IX. Planar zigzag modification of poly (ethylene oxide)*. Journal of Polymer Science Part B: Polymer Physics, 1973. **11**: p. 2113-2122.
460. Tadokoro, H., et al., *A preliminary report of structural studies on polyethylene oxide-urea complex*. Journal of Polymer Science Part C: Polymer Letters, 1964. **2**: p. 363-368.
461. Iwamoto, R., et al., *Structure of poly (ethylene oxide) complexes. II. Poly (ethylene oxide)–mercuric chloride complex*. Journal of Polymer Science Part B: Polymer Physics, 1968. **6**: p. 1509-1525.
462. Yokoyama, M., et al., *Structure of poly (ethylene oxide) complexes. III. Poly (ethylene oxide)-*

- mercuric chloride complex. Type II.* *Macromolecules*, 1969. **2**: p. 184-192.
463. Fenton, D.E., J.M. Parker, and P.V. Wright, *Complexes of alkali metal ions with poly (ethylene oxide).* *Polymer*, 1973. **14**: p. 589.
464. Chatani, Y. and S. Okamura, *Crystal structure of poly (ethylene oxide)—sodium iodide complex.* *Polymer*, 1987. **28**: p. 1815-1820.
465. Belokoneva, E.L., S.Y. Stefanovich, and O.V. Dimitrova, *New nonlinear optical potassium iodate $K [IO_3]$ and borates $K_3 [B_6O_{10}] Br$, $KTa [B_4O_6(OH)_4(OH)_2 \cdot 1.33 H_2O$ —Synthesis, structures and relation to the properties.* *Journal of Solid State Chemistry*, 2012. **195**: p. 79-85.
466. Takahashi, Y. and H. Tadokoro, *Structural studies of polyethers, $-(CH_2 mO)_n$. X. Crystal structure of poly (ethylene oxide).* *Macromolecules*, 1973. **6**: p. 672-675.
467. Crane, G.R., *The relation of physical properties to the symmetry of potassium iodate.* *Journal of Applied Crystallography*, 1972. **5**: p. 360-365.
468. Byrom, P. and B. Lucas, *Structure (neutron) of high-temperature phase I potassium iodate at 523 K.* *Acta Crystallographica Section C*, 1987. **43**(9): p. 1649-1651.
469. Kasatani, H., et al., *Study of crystal structure at high temperature phase in KIO_3 crystal by synchrotron powder X-ray diffraction.* *Nuclear Instruments and Methods in Physics Research Section B: Beam Interactions with Materials and Atoms*, 2003. **199**: p. 49-53.
470. Naray-Szabo, I. and A. Kalman, *On the structure and polymorphism of potassium iodate, KIO_3 .* *Acta Crystallographica*, 1961. **14**: p. 791-792.